Development of a Test Resonator for Investigations of the RF Properties of Superconducting Materials

Dissertation

zur Erlangung des Doktorgrades

an der Fakultät für Mathematik, Informatik und Naturwissenschaften

Fachbereich Physik

der Universität Hamburg

vorgelegt von

Ricardo Monroy Villa

Hamburg

2023

Gutachter/innen der Dissertation:	Prof. Dr. Wolfgang Hillert Dr. Marc Wenskat
Zusammensetzung der Prüfungskommission:	Jun.-Prof. Dr. Simon Adrian Prof. Dr. Wolfgang Hillert Prof. Dr. Daniela Pfannkuche Dr. Hans Weise Dr. Marc Wenskat
Vorsitzende/r der Prüfungskommission:	Prof. Dr. Daniela Pfannkuche
Datum der Disputation:	11.12.2023
Vorsitzender des Fach-Promotionsausschusses PHYSIK:	Prof. Dr. Markus Drescher
Leiter des Fachbereichs PHYSIK:	Prof. Dr. Wolfgang J. Parak
Dekan der Fakultät MIN:	Prof. Dr.-Ing. Norbert Ritter

Declaration on oath

I hereby declare in lieu of oath that I have written this dissertation myself and that I have not used any auxiliary materials or sources other than those indicated.

Hamburg, 31.01.2024

Signature of the doctoral student

Abstract

Pushing the limits of the accelerating field and quality factor of superconducting radiofrequency (SRF) cavities beyond pure niobium requires the implementation of specific inner surface treatments and the development of alternative materials, which are yet to be studied and optimized. One of the fundamental challenges in investigating alternative materials is that only samples or cavity cut-outs can be fully characterized from a material science point of view. In contrast, complete cavities enable the SRF characterization of the inner surface, while samples can usually only be analysed using surface characterization, mechanical testing, and direct current methods. To overcome this problem, a test resonator for samples called "Quadrupole Resonator" (QPR) was designed and operated at Conseil Européen pour la Recherche Nucléaire (CERN), and another one was developed later at Helmholtz-Zentrum Berlin (HZB). In a collaborative effort between Universität Hamburg (UHH) and Deutsches Elektronen-Synchrotron (DESY), an improved QPR has been designed, successfully commissioned, and is currently being operated at DESY. This QPR allows for the full RF characterization of samples at frequencies of 0.42 GHz, 0.86 GHz, and 1.3 GHz, within a temperature range of 1.8-20 K, and at designed applied magnetic fields up to 120 mT, as will be demonstrated.

This work presents the UHH QPR design, which incorporated improvements motivated by mechanical and RF studies and experimental experience. The results from both room temperature and cryogenic commissioning are discussed as well. More importantly, the results for the RF tests conducted on a Nb sample after undergoing a series of chemical surface treatments are detailed. The RF characterization data include surface resistance as a function of temperature and applied magnetic field and frequency and thermal conductivity as a function of temperature of the sample. These results show an overall good agreement with theoretical models describing superconductivity. Furthermore, material parameters, such as London penetration depth, mean free path, superconducting gap and Dynes parameter, derived from the experimental data in general align closely with values reported in literature. Finally, an outlook of the further improvements and usage of the QPR is presented.

Zusammenfassung

Die Optimierung des Grenzen des Beschleunigungsfeldes und des Gütefaktors von supraleitenden Hochfrequenz (SRF) Hohlraumresonatoren über reines Niob hinaus erfordert die Umsetzung spezifischer Oberflächenbehandlungen und die Entwicklung alternativer Materialien, die noch untersucht und optimiert werden müssen. Eine der grundlegenden Herausforderungen bei der Untersuchung alternativer Materialien besteht darin, dass nur Proben oder Oberflächenausschnitte aus materialwissenschaftlicher Sicht vollständig charakterisiert werden können. Im Gegensatz dazu ermöglichen vollständige Hohlraumresonatoren die SRF-Charakterisierung der inneren Oberfläche, während Proben in der Regel nur durch Oberflächencharakterisierung, mechanischen Tests und Gleichstrom-Methoden analysiert werden können. Um dieses Problem zu überwinden, wurde ein Testresonator für Proben namens "Quadrupolresonator" (QPR) entwickelt und am Conseil Européen pour la Recherche Nucléaire (CERN) betrieben, und später wurde ein weiterer am Helmholtz-Zentrum Berlin (HZB) entwickelt. In einer Zusammenarbeit zwischen der Universität Hamburg (UHH) und dem Deutschen Elektronen-Synchrotron (DESY) wurde ein verbesserter QPR entworfen, erfolgreich in Betrieb genommen und derzeit bei DESY betrieben. Dieser QPR ermöglicht die vollständige HF-Charakterisierung von Proben bei Frequenzen von 0,42 GHz, 0,86 GHz und 1,3 GHz, in einem Temperaturbereich von 1,8-20 K und bei geplanten angelegten Magnetfeldern von bis zu 120 mT.

Diese Arbeit präsentiert das UHH-QPR-Design, das Verbesserungen aufgrund von mechanischen und HF-Studien sowie experimentellen Erfahrungen beinhaltet. Die Ergebnisse sowohl der Raumtemperatur- als auch der kryogenen Inbetriebnahme werden ebenfalls diskutiert. Zu dem werden die Ergebnisse der HF-Tests an einer Nb-Probe nach einer Reihe von chemischen Oberflächenbehandlungen diskutiert. Die HF-Charakterisierungsdaten umfassen den Oberflächenwiderstand als Funktion von Temperatur und angelegtem Magnetfeld, sowie jeweils die Frequenz und die Wärmeleitfähigkeit als Funktion der Temperatur der Probe. Diese Ergebnisse zeigen insgesamt eine gute Übereinstimmung mit theoretischen Modellen zur Beschreibung der Supraleitfähigkeit. Darüber hinaus stimmen die aus den experimentellen Daten abgeleiteten Materialparameter wie London-Eindringtiefe, mittlere freie Weglänge, supraleitende Lücke und Dynes-Parameter im Allgemeinen eng mit in der Literatur berichteten Werten überein. Abschließend wird ein Ausblick auf weitere Verbesserungen und die Verwendung des QPR präsentiert.

Contents

Chapter 1

Introductory Overview

Niobium is widely recognized as the optimal material to construct superconducting radio frequency (SRF) cavities for their use in modern particle accelerators. However, as the accelerating fields within these SRF cavities are approaching their theoretical limit, researchers have been exploring alternative material and treatments to enhance the cavity performance. Currently, radiofrequency (RF) cavities made of superconducting materials are capable of attaining accelerating fields up to 50 MV/m and quality factors of 10^{11}. Materials such as Nb_3Sn and MgB_2 and multilayer structures like superconductor-insulator-superconductor films, as well as treatments including nitrogen doping, nitrogen infusion, and medium temperature (mid-T) annealing of bulk Nb cavities, have shown promising results in increasing quality factors and for maximizing achievable fields. For instance, the industrialization of N-doping cavity preparation has been successful for Linac Coherent Light Source (LCLS)-II production at SLAC National Accelerator Laboratory. However, further investigations are necessary before cavities manufactured or treated with alternative recipes can be implemented in accelerators.

To expedite studies on alternative materials, there is a growing interest in the scientific community to characterize small samples of superconducting materials due to the significant cost and time associated with producing and measuring full-scale cavities. Therefore, the development of sample test devices with easier preparation and fast turnaround times are highly valuable for investigating these materials. To satisfy this need, research laboratories around the world have developed a variety of setups to measure the surface resistance R_s of samples under controlled conditions, such as frequency, temperature, and peak magnetic field. These devices cover operational frequencies from the megahertz to a few gigahertz, temperatures ranging from 2 K to 20 K, and magnetic fields up to 400 mT. Sample diameters are on the centimetre scale, and their shapes consist of flat discs, rods, or thin-films. Examples of these setups include host cavities, sapphire loaded cavities, surface impedance characterization (SIC) systems, hemispherical cavities, QPRs, and a rapid superconductor test apparatus. These setups also aid in the development and testing of theoretical models of the surface resistance due to the wide space defined by their parameters.

QPRs have been developed and used at various research institutes, including CERN and HZB, allowing for testing superconducting samples with a 75 mm radius under cavity-like conditions. These resonators operate at frequencies of approximately 400, 800, and 1300 MHz and peak magnetic fields up to 120 mT. An additional attractive aspect of this device is the possibility to study the same sample with advanced surface and RF characterization techniques. The simple geometry of the samples allows for easier preparation, and exchange is possible at lower costs compared to cavities. With the extensive space of parameters, the QPR can investigate loss mechanisms attributed to the surface resistance with a dependency on frequency.

This work presents the status of a new QPR designed, developed, and operated at Universität Hamburg and DESY. The thesis starts with Chapter 2, introducing fundamental concepts of electrodynamics that establish the basis of the operating principle of RF cavities. Chapter 3 focuses on the introductory concepts of superconductivity, briefly reviewing the main theories and demonstrating their application to RF cavities made of superconducting materials. Cavity testing techniques and their common operational limitations are also discussed. In Chapter 4, a detailed description of the QPR is provided, as well as a forensic study of the existing QPRs and the strategies employed to address operational challenges. The unique features of the UHH QPR design, which is based on the successful HZB system, are described. Chapter 5 outlines the commissioning of the UHH QPR at the fabrication company Zanon Research & Innovation Srl (Zanon) and at DESY. This commissioning phase consisted of a series of tests performed at room temperature and another series carried out at cold temperatures. Furthermore, it contains a description of the chemical surface treatment applied to the QPR and the RF system used for the measurements. In Chapter 6, the first measurements of a sample at cold temperatures are discussed. The sample studied with the UHH QPR is a Nb sample that belongs to HZB and underwent a polishing process to remove 150 µm as a last treatment. It was characterized by obtaining its surface resistance and resonant frequency as a function of temperature and the thermal conductivity of the sample tube. These results enabled the determination of material parameters such as mean free path, superconducting gap, effective penetration depth, and more, showing good agreement with literature values of Nb. The final chapter, Chapter 7, presents the conclusions, highlighting the robust capabilities of the QPR and its valuable role in SRF accelerator research and development (R&D).

Chapter 2

Radiofrequency Cavity Fundamentals

In particle accelerators, the electromagnetic force is used to interact with a group of charged particles, also known as "beam" [1]. On the one hand, magnetic fields, generated by either electromagnets or permanent magnets, are utilized to modify the trajectory of the beam. On the other hand, electric fields are responsible for accelerating, or increasing the kinetic energy, of the beam. Modern advancements have made it possible to create powerful electric fields and confine the beam within a small volume of space using a specialized structure called "RF cavity" [2]. This chapter serves as an introduction to the fundamental concepts of electrodynamics that form the basis of the operating principle of SRF cavities.

2.1 Basic Concepts of Microwave Engineering

RF cavities are hollow metallic structures designed to resonate with electromagnetic waves at a microwave frequency and are used to accelerate the beam. The behaviour of electromagnetic phenomena within an RF cavity is described using classical electrodynamics, beginning with an analysis of a cylindrical pill-box cavity [3]. This study focuses on understanding the distribution of electromagnetic energy inside the cavity, and the resonance frequencies of such a structure are determined by the eigenvalues of the Helmholtz equation.

2.1.1 Electromagnetic Fields in a Waveguide

To begin the analysis of the fields inside an RF cavity, an infinitely long cylindrical waveguide is considered. The behaviour of electromagnetic waves within this waveguide is described using time-dependent Maxwell equations. This set of equations in vacuum, with charge and current sources, can be written as:

$$\nabla \cdot \vec{\mathcal{D}} = \rho \tag{2.1}$$

$$\nabla \cdot \vec{\mathcal{B}} = 0 \tag{2.2}$$

$$\nabla \times \vec{\mathcal{E}} = -\frac{\partial \vec{\mathcal{B}}}{\partial t} \tag{2.3}$$

$$\nabla \times \vec{\mathcal{H}} = \vec{\mathcal{J}} + \frac{\partial \vec{\mathcal{D}}}{\partial t}, \tag{2.4}$$

where $\vec{\mathcal{D}} = \epsilon_0 \vec{\mathcal{E}}$ is the electric flux density, $\vec{\mathcal{B}} = \mu_0 \vec{\mathcal{H}}$ is the magnetic flux density, $\vec{\mathcal{E}}$ is the electric field in volts per metre, and $\vec{\mathcal{H}}$ is the magnetic field in amperes per metre. The vacuum permittivity and permeability have the values of $\epsilon_0 = 8.85 \cdot 10^{-12}\,\mathrm{C^2/Nm^2}$ and $\mu_0 = 4\pi \cdot 10^{-7}\,\mathrm{Tm/A}$, respectively. Since RF power is applied to the structure and waves inside the cavity will resonate, resulting in solutions with harmonic time dependence, it is convenient to use the phasor notation. For example, the electric field $\vec{\mathcal{E}}$ in real space can be obtained as

$$\vec{\mathcal{E}}\,(\vec{r},\, t) = \mathrm{Re}\left[\vec{E}\,(\vec{r})\, e^{i\omega t}\right], \tag{2.5}$$

where $\vec{E}$ is the electric field in the complex space, $\vec{r}$ is an arbitrary vector in space, and t represents time. Replacing the harmonic solutions of the electric and magnetic field in Eqs. 2.1-2.4 yields to the complex representation of Maxwell equations. Since the behaviour of the waves is only of interest in the region enclosed by the waveguide walls, which is an empty space, the Maxwell equations in the source-free region of the waveguide with $\rho = 0$ and $\vec{J} = \vec{0}$ are considered. With these previous expressions, and by making use of the vector triple product, Eqs. 2.1-2.4 are reduced to two Helmholtz equations [4]:

$$\nabla^2 \vec{E} + k^2 \vec{E} = 0 \tag{2.6}$$

$$\nabla^2 \vec{H} + k^2 \vec{H} = 0, \tag{2.7}$$

where $k = \omega\sqrt{\epsilon_0 \mu_0} = 2\pi/\lambda$ is the wave number in vacuum.

Typically, RF cavities are manufactured from materials that are considered good conductors, such as copper [2, 5], and thus, for the development of the following analysis, they are considered as lossless materials, also called "perfect conductors". To find the solutions of Eqs. 2.6 and 2.7, boundary conditions for perfect conductors must be satisfied. These boundaries are given by:

$$\hat{n} \times \vec{E} = 0 \tag{2.8}$$

$$\hat{n} \cdot \vec{H} = 0, \tag{2.9}$$

where $\hat{n}$ is the normal unit vector pointing out of the conductor walls.

2.1.2 Transverse Electric Modes

In order to simplify the calculations of the problem at hand, the cylindrical waveguide is placed along the z-axis and has a radius a, see Fig. 2.1. With this geometry, and by choosing a cylindrical coordinate system (ρ, ϕ, z), it is possible to obtain two distinct wave modes that can exist in waveguides, which are the transverse electric (TE) and the transverse magnetic (TM). In this section the solutions for the TE modes are obtained.

TE modes are characterized by the absence of a longitudinal electric field component, which for the selected reference system is the z-coordinate. Thus, $E_z\,(\vec{r}) = 0$, where $\vec{r} = (\rho,\, \phi,\, z)$ denotes an arbitrary vector in space. Since $H_z\,(\vec{r}) \neq 0$, this component can be calculated through Eq. 2.7. The separation of variables method is then used to split the problem into three simpler differential equations. It assumed that the solution takes the form of a product of three functions, i.e.

$$H_z(\rho, \phi, z) = R(\rho) P(\phi) S(z). \tag{2.10}$$

Two of the equations obtained describe a harmonic-oscillator-like behaviour:

$$\frac{d^2S}{dz^2} + \beta^2 S = 0 \tag{2.11}$$

$$\frac{d^2P}{d\phi^2} + k_\phi^2 P = 0, \tag{2.12}$$

where β and k_ϕ are two constants in the real space. Due to the cylindrical geometry of the waveguide, it is reasonable to assume that the angular solution P will be periodic in the angle coordinate ϕ. Therefore, $k_\phi = n$, where n is an integer.

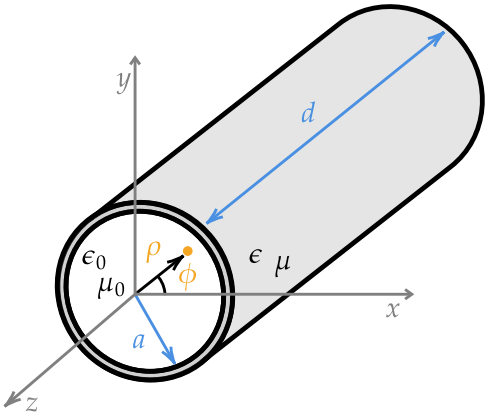

Figure 2.1: Cylindrical waveguide. Here, a is the inner radius of the waveguide and d the length.

The third equation is given by:

$$\rho^2 \frac{d^2R}{d\rho^2} + \rho \frac{dR}{d\rho} + \left(\rho^2 k_c^2 - n^2\right) R = 0, \tag{2.13}$$

where $k_c = \sqrt{k^2 - \beta^2}$ is the cut off wave number and β is the propagation constant. It is clear from this equation why the term "cut off" is given to k_c: when $k > k_c$, β is a real number, indicating that the wave propagates only when this condition is satisfied. On the contrary, for wave numbers $k < k_c$, the propagation constant becomes imaginary, leading to an exponential decay of the fields. Such modes are referred to as "cut off" or "evanescent" modes.

Eq. 2.13 is known as "Bessel differential equation", and its general solution is a linear combination of the Bessel functions [6] of the first kind J_n and the second kind Y_n. However, considering that the Bessel function of the second kind $Y_n(\rho = 0) \to \infty$, this results in a solution R only involving the term $J_n(k_c\rho)$. This restriction is important to ensure a finite energy inside the waveguide. In addition to this, the boundary condition stated in Eq. 2.8 must be considered in the analysis. Accordingly, at the radius $\rho = a$, the tangential components of the electric field must be zero, particularly the angular part $E_\phi(a, \phi, z) = 0$. By applying this condition, a requirement for k_c must be met, given by:

$$J_n'(k_c a) = 0 \quad \Rightarrow \quad k_c a = p'_{nm}, \tag{2.14}$$

where p'_{nm} is the mth root of the first derivative of J_n.

However, an RF cavity is actually a finite metallic structure that can be formed from a closed section of a waveguide. Then, conducting plates, whose face is perpendicular to the z-axis, separated by a distance d, see Fig. 2.1, are included in the previous waveguide description to simulate a standing wave inside a pill-box-like cavity. Therefore, due to the boundary condition given in Eq. 2.8, the transverse components of field $\vec{E}_t\,(\rho,\,\phi,\,z)$ must be zero at $z = 0,\,d$. Applying this condition yields to

$$\beta d = \ell\pi, \quad \text{for } \ell = 0,\,1,\,2,\,3,\,\ldots \tag{2.15}$$

Using these conditions, the resonant frequency of the TE modes $f_{nm\ell}$ can be obtained employing the expression of the speed of an electromagnetic wave in vacuum $c = 1/\sqrt{\epsilon_0\mu_0}$, along with the relation of the angular frequency $\omega = 2\pi f$ and the wave number k, which is $\omega = ck$:

$$f_{nm\ell} = \frac{1}{2\pi\sqrt{\epsilon_0\mu_0}}\sqrt{\left(\frac{p'_{nm}}{a}\right)^2 + \left(\frac{\ell\pi}{d}\right)^2}. \tag{2.16}$$

Finally, the TE modes inside a pill-box cavity are derived:

$$E_z\,(\vec{r}\,) = 0 \tag{2.17}$$

$$H_z\,(\vec{r}\,) = H_0 J_n\left(\frac{p'_{nm}}{a}\rho\right)\cos\left(n\phi\right)\sin\left(\frac{\ell\pi}{d}z\right) \tag{2.18}$$

$$H_\rho\,(\vec{r}\,) = \frac{\beta}{k_c}H_0 J'_n\left(\frac{p'_{nm}}{a}\rho\right)\cos\left(n\phi\right)\cos\left(\frac{\ell\pi}{d}z\right) \tag{2.19}$$

$$H_\phi\,(\vec{r}\,) = -\frac{\beta n}{k_c^2\rho}H_0 J_n\left(\frac{p'_{nm}}{a}\rho\right)\sin\left(n\phi\right)\cos\left(\frac{\ell\pi}{d}z\right) \tag{2.20}$$

$$E_\rho\,(\vec{r}\,) = \frac{i\omega\mu_0 n}{k_c^2\rho}H_0 J_n\left(\frac{p'_{nm}}{a}\rho\right)\sin\left(n\phi\right)\sin\left(\frac{\ell\pi}{d}z\right) \tag{2.21}$$

$$E_\phi\,(\vec{r}\,) = \frac{i\omega\mu_0}{k_c}H_0 J'_n\left(\frac{p'_{nm}}{a}\rho\right)\cos\left(n\phi\right)\sin\left(\frac{\ell\pi}{d}z\right), \tag{2.22}$$

where H_0 is the maximum attainable magnetic field.

2.1.3 Transverse Magnetic Modes

Transverse magnetic modes are calculated in a similar procedure as the TE modes. In the TM modes, the z-component of the magnetic field, $H_z\,(\vec{r}\,)$, is zero; thus $E_z\,(\vec{r}\,)$ is calculated from the same-axis component of Eq. 2.6. The boundary condition in Eq. 2.8 requires that the component $E_z\,(a,\,\phi,\,z) = 0$. Additionally, the z-component of Eq. 2.1 shows that $\frac{\partial E_z}{\partial z}\,(\rho,\,\phi,\,z) = 0$ for all values of z.

Given these constraints, the resonant frequency of the TM modes is given by:

$$f_{nm\ell} = \frac{1}{2\pi\sqrt{\epsilon_0\mu_0}}\sqrt{\left(\frac{p_{nm}}{a}\right)^2 + \left(\frac{\ell\pi}{d}\right)^2}, \tag{2.23}$$

where p_{nm} is the mth root of J_n. Therefore, the TM modes can be described by the following set of field components:

$$H_z\,(\vec{r}\,) = 0 \tag{2.24}$$

$$E_z(\vec{r}) = E_0 J_n\left(\frac{p_{nm}}{a}\rho\right)\cos(n\phi)\cos\left(\frac{\ell\pi}{d}z\right) \tag{2.25}$$

$$H_\rho(\vec{r}) = -\frac{i\omega\epsilon_0 n}{k_c^2\rho}E_0 J_n\left(\frac{p_{nm}}{a}\rho\right)\sin(n\phi)\cos\left(\frac{\ell\pi}{d}z\right) \tag{2.26}$$

$$H_\phi(\vec{r}) = -\frac{i\omega\epsilon_0}{k_c}E_0 J_n'\left(\frac{p_{nm}}{a}\rho\right)\cos(n\phi)\cos\left(\frac{\ell\pi}{d}z\right) \tag{2.27}$$

$$E_\rho(\vec{r}) = -\frac{\beta}{k_c}E_0 J_n'\left(\frac{p_{nm}}{a}\rho\right)\cos(n\phi)\sin\left(\frac{\ell\pi}{d}z\right) \tag{2.28}$$

$$E_\phi(\vec{r}) = \frac{\beta n}{k_c^2\rho}E_0 J_n\left(\frac{p_{nm}}{a}\rho\right)\sin(n\phi)\sin\left(\frac{\ell\pi}{d}z\right), \tag{2.29}$$

where E_0 is the maximum attainable electric field.

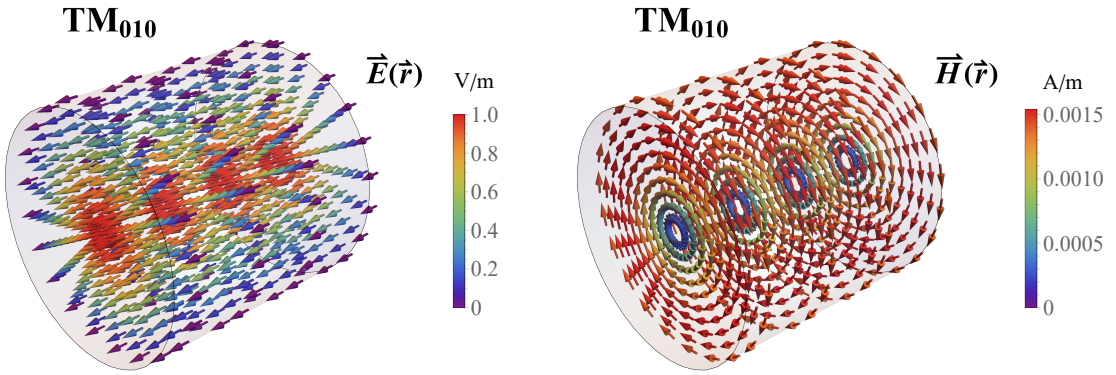

Figure 2.2: Electric $\vec{E}$ (left) and magnetic fields $\vec{H}$ (right) of the TM_{010} mode. These results were simulated in Mathematica 13® [7].

2.1.4 TM_{010} Mode of the Pill-Box Cavity

The TM_{010} mode is of particular interest in RF cavities because it provides a maximum electric field along the centre of the structure. Note that with the indices values ℓ, $n = 0$, all the components of the electric and magnetic field become zero except E_z and H_ϕ. In this case, these field components can be expressed as

$$E_z(\vec{r}, t) = E_0 J_0\left(\frac{2.405}{a}\rho\right)e^{i\omega t} \tag{2.30}$$

$$H_\phi(\vec{r}, t) = -\frac{i\omega\epsilon_0}{k_c}E_0 J_0'\left(\frac{2.405}{a}\rho\right)e^{i\omega t} = ic\epsilon_0 E_0 J_1\left(\frac{2.405}{a}\rho\right)e^{i\omega t}. \tag{2.31}$$

The operational frequency of the TM_{010} mode of a pill-box cavity is given by:

$$f_{010} = \frac{1}{2\pi\sqrt{\epsilon_0\mu_0}}\frac{2.405}{a}. \tag{2.32}$$

Fig. 2.2 illustrates the electric and magnetic fields of the TM_{010} mode described with the real part of Eqs. 2.30 and 2.31. It is observed that the z-component of the electric field is maximum at the centre of the cavity, while the magnetic field is maximum at the radius $r = 0.77a$ due to the behaviour of the Bessel functions. As is demonstrated in Sec. 2.2, the modes calculated for a pill-box cavity, such as the TM_{010} mode shown in Eqs. 2.30 and 2.31, provide a reliable approximation to the actual field distribution observed in RF cavities.

2.1.5 Energy Dissipation

So far, the analysis of the electromagnetic fields in a waveguide or cavity has been limited to their empty region. However, because cavities are made of good conductors, the fields actually penetrate their inner surface, but they decay exponentially because the electrons in the material try to shield the fields from the bulk of the metal [8]. Therefore, an analysis of the electromagnetic fields inside the surface of this metallic structure is discussed in the present section.

If the material of the cavity is considered to be a lossy or conductive medium with a conductivity σ, complex permittivity ϵ, and complex permeability μ, the presence of an electric field within its near-surface region results in the appearance of electron conduction current given by:

$$\vec{\mathcal{J}} = \sigma\vec{\mathcal{E}}, \tag{2.33}$$

which is Ohm's law [9]. Note that in real space the current density is given by $\vec{\mathcal{J}} = \mathrm{Re}\left[\vec{J}e^{i\omega t}\right]$, provided that the RF fields exciting the electrons in the metal have an harmonic behaviour. Considering this non-zero current density $\vec{\mathcal{J}}$ changes the expression of Maxwell equations given by Eqs. 2.1-2.4. Using the vector triple product, the following differential equations are obtained for the electromagnetic fields inside the metal:

$$\nabla^2\vec{E} - \gamma^2\vec{E} = 0 \tag{2.34}$$

$$\nabla^2\vec{H} - \gamma^2\vec{H} = 0, \tag{2.35}$$

where $\gamma = i\sqrt{\mu\epsilon\omega^2\left(1 + \frac{\sigma}{i\omega\epsilon}\right)}$ is the complex propagation constant.

In a good conductor, the conductive current is significantly larger than the displacement current, resulting in $\sigma \gg \omega\epsilon$, and also $\mu \approx \mu_0$. Thus, γ becomes

$$\gamma \simeq \sqrt{i\omega\mu_0\sigma} = (1+i)\,\frac{1}{\delta_\mathrm{s}}, \tag{2.36}$$

where the skin depth δ_s is defined as

$$\delta_\mathrm{s} = \sqrt{\frac{2}{\omega\mu_0\sigma}}. \tag{2.37}$$

Eq. 2.40 gives the depth below the conductor surface at which the AC current density decreases by $1/e$ (approximately 0.37) with respect to the maximum value at the surface. For instance, in Fig. 2.3, a harmonic magnetic field $H_0e^{i\omega t}\hat{y}$ is applied to a semi-infinite good conductor positioned perpendicular to the x-axis. Inside the material, the magnetic field $\vec{H}\,(x,\,t) = H_0e^{-x/\delta_\mathrm{s}}e^{-i(x/\delta_\mathrm{s}-\omega t)}\hat{y}$ oscillates, but it also decays by a factor of $1/e$ after travelling a distance equal to δ_s. With this, the intrinsic impedance of the medium η is given by:

$$\eta = \frac{i\omega\mu_0}{\gamma} \simeq (1+i)\,\frac{1}{\sigma\delta_s}. \tag{2.38}$$

Understanding that the electromagnetic fields decay exponentially inside a good conductor makes it possible to obtain an expression for the surface resistance. When RF power is supplied to a cavity, a portion of that power P_c will be dissipated through its walls due to the interaction of the field with the free electrons, which occurs over a distance δ_s. If S is the surface of the cavity wall, the surface resistance is defined as

$$R_s = \frac{2}{H^2}\frac{dP_c}{dS}, \tag{2.39}$$

where H is the local magnetic field. However, another expression of R_s involves the intrinsic impedance of the medium η and, consequently, the skin depth, which is given by:

$$R_s = \mathrm{Re}\,[\eta] = \sqrt{\frac{\omega\mu_0}{2\sigma}}. \tag{2.40}$$

For example, consider the pill-box cavity made of copper operating at 1.5 GHz and at 300 K. Given that the electrical conductivity of copper at this temperature is $\sigma = 5.96 \cdot 10^7\, 1/(\Omega\mathrm{m})$, the cavity would have a skin depth of $\delta_s = 1.7\,\mu\mathrm{m}$ and a surface resistance of $R_s = 10\,\mathrm{m}\Omega$.

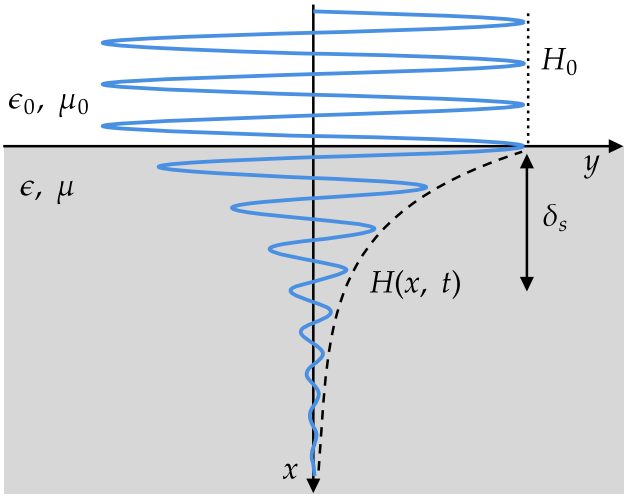

Figure 2.3: A magnetic field H_0 of constant amplitude enters the resonator surface. Inside the conductor, the magnetic field $H\,(x,\,t)$ decays exponentially.

2.2 Radiofrequency Cavities

A real RF cavity has, however, a more complex geometry than a simple pill-box. Fig. 2.4 shows a 1.3 GHz TESLA (TeV-Energy Superconducting Linear Accelerator)-shaped nine-cell SRF cavity designed for the acceleration of ultra-relativistic ($\beta = v/c = 1$, where v is the velocity of the beam and c is the speed of light) electrons. The electric and magnetic fields described by the TM_{010} mode in Eqs. 2.30 and 2.31 offer a good approximation to the actual field distribution found in these cavities.

In the SRF community, more precise calculations of the electromagnetic fields inside more complicated geometries are performed using simulation tools like CST Microwave Studio® (CST) [11] or Ansoft HFSS® (HFSS) [12].

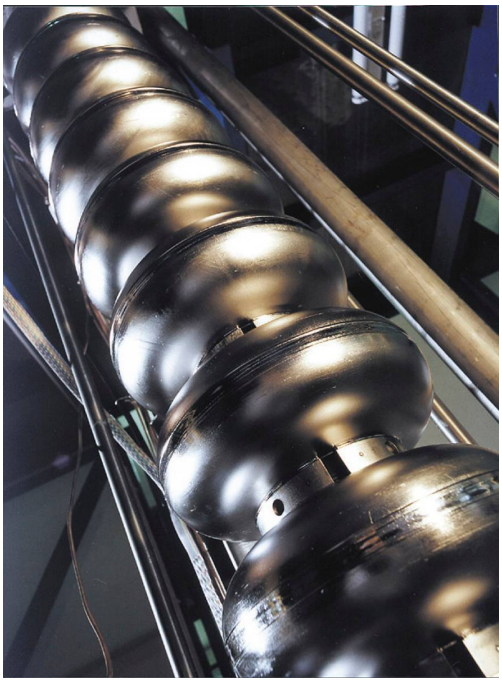

Figure 2.4: 1.3 GHz TESLA-shaped nine-cell SRF cavity employed in the European XFEL. Figure taken from [10].

For example, Fig. 2.5 shows a 1.3 GHz TESLA-shaped single-cell cavity drawn from CST preloaded database. The electromagnetic fields are calculated with the eigenmode solver, and the resulting fields are shown in Fig. 2.6. It is observed that the classical electrodynamics analysis of the pill-box cavity in which the TM_{010} mode equations were obtained provides a good approximation to the mode field distribution within an actual TESLA cavity with a resonant mode at 1.3 GHz.

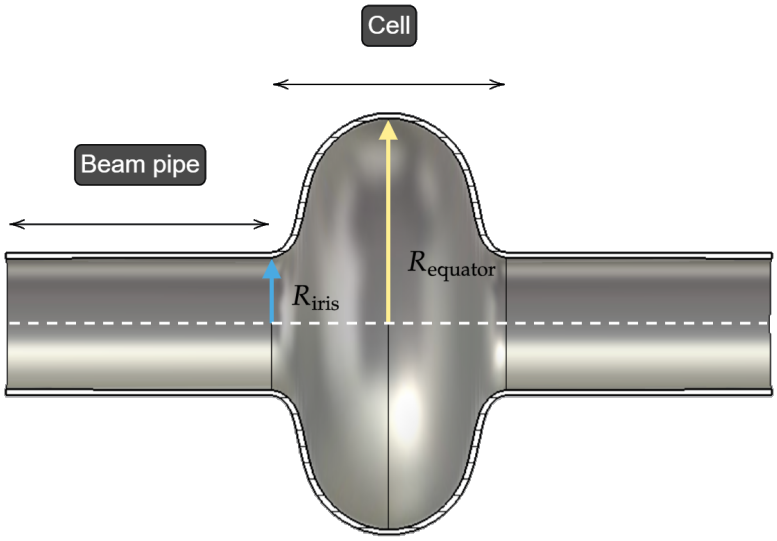

Figure 2.5: Schematic diagram of the parts of a 1.3 GHz TESLA-shaped single-cell SRF cavity.

However, it is important to note that the electromagnetic fields in an operational RF cavity change sign in time, as expressed, for example, in Eq. 2.30, with a period $T = 2\pi/\omega_{mnl}$. In order to be able to accelerate charged particles, there must be synchronization between the time-varying electric field and the incoming charged particles in such a way that they always see the field pointing in the same direction.

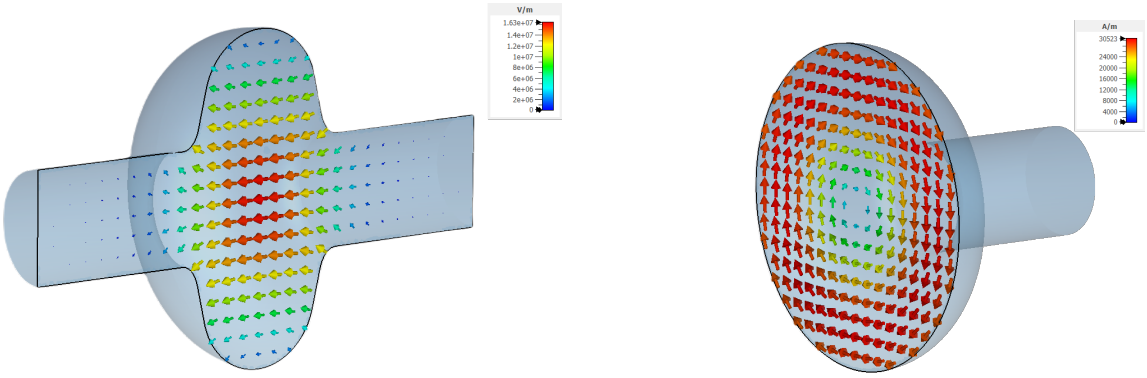

Figure 2.6: CST simulation of the electric $\vec{E}$ (left) and magnetic fields $\vec{H}$ (right) of the TM_{010} mode of a TESLA-shaped single-cell SRF cavity at 1.3 GHz.

If a charged particle travelling almost at the speed of light c enters the cavity at position $z = 0$ and at time $t = 0$, and leaves from $z = d$ at time $t = t_{\text{out}}$, then the synchronization condition says that the time it takes the charged particle to cross the cavity, denoted as t_{out}, must be equal to half the RF period of the electromagnetic fields. This condition gives the relation for the time t_{out} with the frequency of the cavity ω_{mnl} as follows:

$$t_{\text{out}} = \frac{d}{c} = \frac{\pi}{\omega_{mnl}}. \tag{2.41}$$

Additionally, cavities are designed to have the charged particles travelling along the symmetry axis of the structure, which refers to the radius $\rho = 0$. The energy gained by the beam after leaving the cavity is calculated from the accelerating voltage V_{c}, which is defined as the integral of electric field component E_z as seen by the particle. Therefore, the accelerating voltage is

$$V_{\text{c}} = \left| \int_0^d E_z\,(0,\,\phi,\,z)\, e^{-i\frac{\omega z}{c}}\, dz \right|, \tag{2.42}$$

where $E_z\,(0,\,\phi,\,z)$ takes the form of the previously calculated TM mode shown in Eq. 2.25. The exponential function in Eq. 2.42, which depends on the z-coordinate, accounts for the displacement of the particle as it moves through the cavity at the speed of light c. Then, the accelerating field E_{acc} is

$$E_{\text{acc}} = \frac{V_{\text{c}}}{d}. \tag{2.43}$$

Naturally, there is a limit for the electric field that can be maintained inside a cavity, and it depends on the maximum magnetic field on the surface of the resonator. For RF cavities made of normal conducting materials, such as copper, the accelerating fields typically achieved are on the order of 10^6-10^8 V/m [13].

2.2.1 Figures of Merit of RF Cavities

Over time, the designs of RF cavities and the materials they are made of have undergone many changes in order to further increase the maximum accelerating field they can withstand [14]. For the purpose of comparing the iterations of the improvement process, the scientific community has introduced various figures of merit. One such figure is the accelerating field E_{acc}. Two others are defined as the ratio of the peak surface electric and magnetic fields on the resonator surface, denoted as E_{pk} and H_{pk} respectively, to the accelerating field E_{acc}. The goal of a cavity design is to minimize these ratios to maximize the accelerating field.

Another figure of merit is the quality factor, denoted as Q_0. As was mentioned in the previous section, the RF electromagnetic fields inside the cavity penetrate the surface of the material a few micrometres, causing the movement of charge carriers, which later scatter with material lattice imperfections and vibrating lattice ions, resulting in a dissipation of energy. The quality factor quantifies the energy efficiency of any oscillator and is proportional to the ratio of energy stored in the resonator to the energy losses per electromagnetic field cycle. It is formally defined as:

$$Q_0 = \frac{\omega U}{P_\mathrm{c}}, \tag{2.44}$$

where ω is the angular frequency, U is the stored energy, and P_c is the power lost in the cavity walls.

Due to the oscillatory nature of the RF power, the total energy inside the cavity [4] can be determined using

$$U = \frac{1}{2}\mu_0 \int H^2 dV \tag{2.45}$$

or

$$U = \frac{1}{2}\epsilon_0 \int E^2 dV. \tag{2.46}$$

From the integral of Eq. 2.39, the power dissipated through the cavity walls can be derived as

$$P_\mathrm{c} = \frac{1}{2} \int R_\mathrm{s} H^2 dS. \tag{2.47}$$

Therefore, the quality factor takes another form:

$$Q_0 = \frac{\omega_0 \mu_0 \int H^2 dV}{R_\mathrm{s} \int H^2 dS} = \frac{G}{R_\mathrm{s}}, \tag{2.48}$$

where G is the geometry factor and is determined by

$$G = \frac{\omega_0 \mu_0 \int H^2 dV}{\int H^2 dS}. \tag{2.49}$$

The geometry factor G is a ratio dependent only on the shape of the resonator and is used for comparison of cavity designs because it gives information about their effectiveness in providing an accelerating field.

Another figure of merit is the shunt impedance of the cavity, R_a, which is a measure of the strength of the interaction of the operational mode with charged particles along the cavity symmetry axis [15]. In accelerators, it is defined as follows:

$$R_\mathrm{a} = \frac{V_\mathrm{c}^2}{P_\mathrm{c}}. \tag{2.50}$$

However, in circuit theory, this figure is defined as

$$R_\mathrm{a}^\mathrm{c} = \frac{V_\mathrm{c}^2}{2P_\mathrm{c}} \tag{2.51}$$

and in linear accelerators (LINACs) as

$$r_\mathrm{a} = \frac{V_\mathrm{c}^2}{P_\mathrm{c}^{'}}, \tag{2.52}$$

where $P_\mathrm{c}^{'}$ is the power dissipated per unit length.

In cavity design, it is desirable to have R_a with a large value, meaning that the dissipated power through the cavity walls is minimized. Interestingly, the ratio

$$\frac{R_\mathrm{a}}{Q_0} = \frac{V_\mathrm{c}^2}{\omega_0 U}, \tag{2.53}$$

known as the "geometric shunt impedance", is independent of R_s and the cavity size, meaning that it only depends on its geometry. To maximize the ratio R_a/Q_0, a common approach consists of making a smaller hole for the beam pipe. This measure can lower the peak electric and magnetic fields in the cavity, resulting in a reduction of P_c. However, this approach represents a potential risk, as it also maximizes the ratio R_a/Q_0 of high-order modes. Consequently, the beam can interact more strongly with these high-order modes, degrading the beam and limiting the maximum possible bunch charge. In summary, this ratio measures how efficient the cavity is in reaching a certain voltage across the cavity gap per unit of stored energy for a given frequency.

Chapter 3

Superconducting RF Cavities

Particle accelerators, such as SACLA (SPring-8 Angstrom Compact free-electron LAser) X-ray free-electron laser (XFEL), use normal conducting cavities operating at 300 K to produce accelerating gradients of 38 MV/m and quality factors of 10^5 [16]. To reach higher quality factors, SRF cavities are cooled to a temperature of a few Kelvins in a liquid helium (LHe) bath, causing it to change from the normal conducting state to the superconducting state. Modern linear accelerators that employ superconducting cavities, such as the European XFEL (Eu-XFEL) [17], operate them at 23.5 MV/m and quality factors of 10^{10} at 2 K. Superconducting cavities have an average quality factor that is approximately 10^5 times higher than that of normal conducting cavities, resulting in significantly lower power dissipation in the cavity walls (see Eq. 2.48).

The operational cost of superconducting cavities is then much lower than that of normal conducting cavities. To illustrate this, consider a pill-box cavity with a radius of $a = 7.65\,\text{cm}$ and a length of $d = 10\,\text{cm}$, operating at 1.5 GHz and at 2 K with $V_\text{c} = 1\,\text{MV}$. A cavity with these parameters would produce an accelerating field of $E_\text{acc} = 10\,\text{MV/m}$ and dissipate a power of $P_\text{c} = 0.4\,\text{W}$. Nevertheless, there is an energetic price paid in the refrigeration system that maintains the LHe at low temperatures required for superconducting cavities. Typically, the power consumption of this refrigeration system is 750 times the dissipated RF power P_c [14]. Therefore, for a superconducting cavity with $R_\text{s} = 20\,\text{n}\Omega$, the refrigerator AC power would be 300 W.

In contrast, a normal conducting cavity made of copper operating at 300 K and operating at the same frequency, typically showing a $R_\text{s} = 3\,\text{m}\Omega$, would dissipate a power of 60 kW. However, since RF power sources, such as klystrons, are employed to supply power to these kinds of cavities, the AC power cost can go up to 120 kW. Therefore, the use of superconducting cavities reduces the AC power by a factor of 400.

3.1 Advantages of Superconductivity in RF Cavities

Superconducting RF cavities offer several advantages over normal conducting cavities, including the reduction of the energetic cost of operation. In addition, these kinds of resonators offer the following benefits [18]:

Since normal conducting cavities present higher power losses on their walls, small beam pipe apertures are required to reduce this power dissipation and effectively concentrate the electric field. However, choosing such a small aperture may increase the shunt impedance (see Eq. 2.50), not only for the operational one but also for other high-order modes. This rise in shunt impedance increases the amount of

generated wake fields and limits the achievable bunch charge. Conversely, SRF cavities can be designed with larger beam pipe apertures without inducing excitations of other high-order modes. Moreover, due to high power losses occurring in normal conducting cavities, they cannot operate continuously or with high duty cycles for more than a few microseconds, otherwise the heat produced would damage the structure. In contrast, minimal heat dissipation in SRF cavities allows for operation in continuous wave (CW) mode, resulting in enhanced luminosity for a collider or brilliance for a light source. Furthermore, beams accelerated with SRF cavities in CW or long pulse operation exhibit a small energy spread, as the accelerating field remains undisturbed due to the low losses. On the contrary, normal conducting cavities with higher dissipation require short pulses to reduce the beam energy spread.

As mentioned earlier, the two outstanding characteristics of superconducting accelerating cavities are their average accelerating field E_{acc} and intrinsic quality factor Q_0. Ideally, a cavity is expected to operate at a high Q_0 that remains constant as E_{acc} increases and abruptly decays at a maximum accelerating field. R&D have further exploited and expanded these unique features of Nb-based SRF cavities. For example, certain treatments, such as a 120 °C annealing for 48 hours [19], nitrogen infusion, or nitrogen doping at 800 °C [20], have enabled cavities to achieve record accelerating fields E_{acc} between 40 and 50 MV/m and quality factors in the range of 10^{10} to 10^{11}, respectively. In order to have a better understanding of SRF cavities, a review of the theory of superconductivity is presented in the next section, followed by a study of its specific application in RF cavities.

3.2 Introduction to Superconductivity

Superconductivity was discovered by H. Kamerlingh Onnes in 1911 while measuring the electrical conductivity of pure metals, such as gold, mercury, and lead, at low temperatures [21]. Prior to this discovery, Kamerlingh Onnes and his team successfully liquified hydrogen in 1906 [22] and helium [23] in 1908, which enabled them to perform investigations into the resistivity of metals as low as 3 K. During their experiments with mercury, they observed a sudden drop to zero in its resistivity at 4.2 K. This temperature at which the resistance of a conductor vanished was named the "critical temperature". The important breakthrough of the disappearance of resistivity in certain metals at specific temperatures, which H. Kamerlingh called "superconductivity", announced the birth of a new experimental field.

Nowadays, superconducting metals have found various applications, for example, in medicine [24], means of transportation [25], power lines [26], and quantum computers [27], and they are still the subject of modern research. One goal of these investigations is to create new materials with a higher critical temperature as close as possible to room temperature [28], which would drastically reduce the cost of operation of cryogenic equipment in optimal conditions. When looking at and analysing the elements of the periodic table, Nb has the highest critical temperature at $T_{\mathrm{c}} = 9.27\,\mathrm{K}$, while metal alloys like Nb_3Sn show a T_{c} of 18.3 K [29].

Currently, two properties are used to define superconductors and to differentiate them from other conductors: perfect conductivity and perfect diamagnetism. As mentioned above, perfect conductivity was reported by Kamerlingh Onnes in 1911, while perfect diamagnetism was found in 1933 by W. Meissner and R. Ochsenfeld [30].

Perfect diamagnetism, which is currently referred to as the "Meissner effect", is a fundamental feature found in superconducting materials. When these materials are cooled down below T_{c}, not only is any magnetic field excluded from entering the volume, but also the field originally present inside the bulk is expelled. This occurs because the electromagnetic fields induce a supercurrent inside the bulk of the superconductor, up to a characteristic length λ, cancelling or "screening" and "expelling" the fields. In

1914, Kamerlingh Onnes aimed to use superconducting wires to build electromagnets to produce high magnetic fields. However, later it was discovered that a limit to the production of high currents exists because, for a certain magnetic field value resulting from the same current, superconductivity breaks down. This phenomenon is referred to as “quench”.

The DC magnetic field limit has a temperature dependency, which is empirically described by the equation

$$H_{\mathrm{c}}(T) = H_0 \left[1 - \left(\frac{T}{T_{\mathrm{c}}}\right)^2\right], \tag{3.1}$$

where H_0 is the critical magnetic field at zero Kelvin. This equation is plotted in Fig. 3.1.

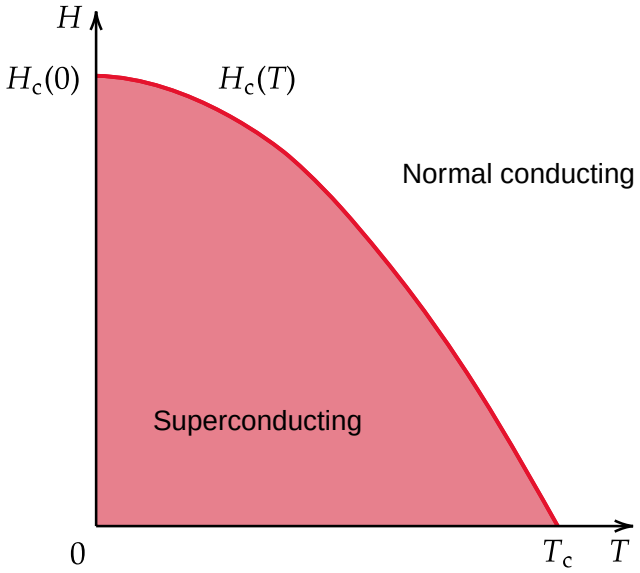

Figure 3.1: Critical magnetic field $H_{\mathrm{c}}(T)$ as a function of temperature.

The critical magnetic field H_{c} exists because the system has to do work proportional to the magnetic field strength to expel it from the inside of the bulk during the transition from the normal to the superconducting states. Without this limit, an indefinite increase of the magnetic field would produce an unstable superconducting state with respect to the normal state of the conductor. The critical magnetic field is thermodynamically related to the free energy density of the system [31] as follows:

$$F_N(T, 0) - F_S(T, 0) = \frac{\mu_0}{2} H_{\mathrm{c}}^2(T), \tag{3.2}$$

where $F(T, 0)$ is the free energy density of the normal conducting (N) and superconducting (S) states in the absence of an external magnetic field. In a more general form, for any existing external magnetic field in the superconductor, the free energy is given by:

$$F_N(T, H) - F_S(T, H) = \frac{\mu_0}{2} H_{\mathrm{c}}^2(T) - \frac{\mu_0}{2} H^2. \tag{3.3}$$

Eq. 3.3 shows that the equilibrium condition for normal and superconducting states is met when $H = H_{\mathrm{c}}$. The previous description of H_{c} only corresponds to one class of superconductors, called “Type I”. However, a second class, “Type II”, was discovered in 1935 by L. V. Shubnikov [32]. The term “Type II” was later given by A. Abrikosov [33] in a work published in 1957, where he characterized superconductors according to the ideas described in the Ginzburg–Landau theory [34]. The phenomenon

of superconductivity remained unexplained on the microscopic level four decades after the discovery of Kamerlingh Onnes until the BCS theory was established by J. Bardeen, L. Cooper, and R. Schrieffer [35]. In the following sections, two models that established the basis for the development of the BCS and Ginzburg–Landau theories of superconductivity are reviewed.

3.2.1 Two-Fluid Model

The first model is the two-fluid model, which was formulated in 1934 by C. Gorter and H. Casimir [36], and was proposed to explain the behaviour of superconductors. The model states that in the superconductor there is a fluid of normal electrons n_N mixed with a fluid of superconducting electrons n_S. These two parts interpenetrate each other, but do not interact, and together form the constant total current carrier density n.

Let $x = n_N/n$ represent the fraction of electrons in the normal fluid and $1 - x = n_S/n$ the ones in the superfluid. Note that $x = 1$ for temperatures $T \geq T_\mathrm{c}$ and $x = 0$ for $T = 0\,\mathrm{K}$. The free energy density of the superconducting state $F(x, T)$ proposed by C. Gorter and H. Casimir is given by:

$$F_S(x, T) = \sqrt{x} f_N(T) + (1 - x) f_S(T), \tag{3.4}$$

where $f_N(T)$ corresponds to the free energy density of the electrons in the normal state and $f_S(T)$ to the condensation energy of the superfluid [37]. Minimizing Eq. 3.4 with respect to x yields an expression for the number of superconducting electrons n_S:

$$\frac{n_S(T)}{n} = 1 - \left(\frac{T}{T_\mathrm{c}}\right)^4. \tag{3.5}$$

Considering that the total number of electrons is

$$n = n_S(T) + n_N(T) = \begin{cases} n_S(0) & \text{at } T = 0\,\mathrm{K} \\ n_N(T) & \text{for } T \geq T_\mathrm{c} \end{cases}, \tag{3.6}$$

the expression of n_S in Eq. 3.5 can be rewritten as

$$n_S(T) = n_S(0) \left[1 - \left(\frac{T}{T_\mathrm{c}}\right)^4\right]. \tag{3.7}$$

The two-fluid model provides a good analytical approach from a thermodynamics point of view, and it is helpful in qualitatively understanding the microscopic theories of superconductivity. Lastly, a two-fluid model consisting of normal and superfluid atoms was also postulated to describe superfluid helium ^{4}He below its lambda point ($\sim 2.17\,\mathrm{K}$ at $1\,\mathrm{atm}$) [38].

3.2.2 London Theory

H. London and F. London [39] postulated their theory in 1935, which provides a phenomenological description of superconductivity. They proposed a scheme based on the two-fluid model and assumed the total current density $\vec{J}$ can be written as the sum of a supercurrent $\vec{J}_S$, corresponding to the superfluid, and a normal current $\vec{J}_N$, so that

$$\vec{J} = \vec{J}_N + \vec{J}_S. \tag{3.8}$$

This implies that a density of normal charge carriers n_N coexist in the metal with a density of superconducting charge carriers n_S, without interacting with each other, and associated with the velocities

$\vec{v}_N$ and $\vec{v}_S$, respectively. The sum of the densities constitutes the average number of electrons per unit volume n. The Drude model [40], which describes the behaviour of the normal conducting electrons, makes it possible to obtain an expression for the electrical normal conductivity σ_N. Conversely, the London theory provides a framework for obtaining a representation for the superconductivity σ_S. According to Drude model, the average velocity of the normal conducting electrons $\vec{v}_N$ is given by Newton's second law as follows:

$$m\frac{d\vec{v}_N}{dt} = -e\vec{E} - \frac{m}{\tau}\vec{v}_N, \tag{3.9}$$

where τ is the mean free time between collisions, also called the "relaxation time". For harmonic behaviour, the normal conducting current density is represented as $\vec{J}_N(t) = \vec{J}_{0_N} e^{i\omega t} = -en_N\vec{v}_N$ and the electric field as $\vec{E}(t) = \vec{E}_0 e^{i\omega t}$. Then, by substituting these expressions into Eq. 3.9, the following relation of the maximum current density $\vec{J}_{0_N}$ is obtained:

$$\vec{J}_{0_N} = \frac{n_N e^2 \tau}{m}\left(\frac{1}{i\omega\tau + 1}\right)\vec{E}_0. \tag{3.10}$$

Typically, good conductors at microwave frequencies satisfy the following condition: $\omega\tau \ll 1$. For example, the relaxation time of Nb is $\tau = 0.42 \cdot 10^{-14}$ s and most cavities operate at $\omega \sim 10^9$ Hz [14]. Comparing Ohm's law to Eq. 3.10, the normal conductivity σ_N is given by:

$$\sigma_N = \frac{n_N e^2 \tau}{m}. \tag{3.11}$$

In the case of the supercurrent charge carriers, which move with an average velocity $\vec{v}_S$, their dynamics follow a similar expression as in the normal state case. These charge carriers move frictionlessly in the bulk of the metal with an equation of motion given by

$$m\frac{d\vec{v}_S}{dt} = -e\vec{E}. \tag{3.12}$$

Note that Eq. 3.12 is obtained when considering $\tau \to \infty$ in the normal fluid equation displayed in Eq. 3.9. The supercurrent in the harmonic regime, which is $\vec{J}_S(t) = \vec{J}_{0_S} e^{i\omega t} = -en_S\vec{v}_S$, satisfies the first London equation:

$$\frac{\partial \vec{J}_S}{\partial t} = \frac{n_S e^2}{m}\vec{E}. \tag{3.13}$$

The first London equation can be reduced to an expression analogous to Ohm's law:

$$\vec{J}_{0_S} = \frac{n_S e^2}{i\omega m}\vec{E}_0, \tag{3.14}$$

where the superconducting conductivity σ_S is defined as follows:

$$\sigma_S = \frac{n_S e^2}{\omega m}. \tag{3.15}$$

The total current in the framework of the two-fluid model is $\vec{J} = (\sigma_N - i\sigma_S)\vec{E}$.

The second London equation is obtained by assuming that the wave function describing the superfluid does not change due to the absence of an electromagnetic field, having the ground state with a zero-net momentum. This results in a supercurrent described by

$$\vec{J}_S = -\frac{n_S e^2}{m}\vec{A}, \tag{3.16}$$

where $\vec{A}$ is the magnetic vector potential, which satisfies $\vec{B} = \nabla \times \vec{A}$. Taking the curl of $\vec{J_S}$ leads to the second London equation:

$$\nabla \times \vec{J_S} = -\frac{n_S e^2}{m}\vec{B}. \tag{3.17}$$

Using Ampere's law for the case $\nabla \times \vec{H} = \vec{J}$ in Eq. 3.17 leads to

$$\nabla^2 \vec{H} = \frac{1}{\lambda_{\mathrm{L}}^2}\vec{H}, \tag{3.18}$$

where λ_{L} is the London penetration depth, which is defined as:

$$\lambda_{\mathrm{L}}(0) = \sqrt{\frac{m}{\mu_0 n_S(0)\, e^2}}. \tag{3.19}$$

Eq. 3.19 is analogous to the concept of skin depth, but it applies specifically to superconductors. It represents the characteristic penetration depth of electromagnetic fields into superconducting materials and typically ranges from 50 to 500 nm. It is worth noting that the frictionless movement of the supercurrent charge carriers, which is described by Eq. 3.12, occurs at 0 K. However, the temperature dependence of λ_{L} is introduced according to Eq. 3.7:

$$\lambda_{\mathrm{L}}(T) = \frac{\lambda_{\mathrm{L}}(0)}{\sqrt{1-\left(\frac{T}{T_{\mathrm{c}}}\right)^4}}. \tag{3.20}$$

In this framework, the skin depth δ_{s}, given by Eq. 2.37, takes a different form. Using the conductivity of the two-fluid model $\sigma = \sigma_N - i\sigma_S$ and assuming that $\sigma_N \ll \sigma_S$ for $T \ll T_{\mathrm{c}}$, leads to

$$\delta_{\mathrm{s}} \simeq \sqrt{\frac{1}{\mu_0 \omega \sigma_S}}\left(1 + i\frac{\sigma_N}{2\sigma_S}\right). \tag{3.21}$$

With this approximation, the propagation constant γ becomes

$$\gamma \simeq \sqrt{\frac{1}{\mu_0 \omega \sigma_S}}(1+i)\left(1 - i\frac{\sigma_N}{2\sigma_S}\right). \tag{3.22}$$

Finally, the intrinsic impedance of the medium $\eta = i\omega\mu_0/\gamma$ is roughly

$$\eta \simeq \frac{1}{2}\mu_0^2\omega^2\sigma_N\lambda_{\mathrm{L}}^3 + i\mu_0\omega\lambda_{\mathrm{L}}. \tag{3.23}$$

The surface resistance is obtained by taking the real part of Eq. 3.23, i.e.

$$R_{\mathrm{s}} = \mathrm{Re}[\eta] = \frac{1}{2}\mu_0^2\omega^2\sigma_N\lambda_{\mathrm{L}}^3. \tag{3.24}$$

Note that according to Eq. 2.40, the surface resistance R_{s} in the normal conducting state is proportional to $\sqrt{\omega}$, while in the superconducting state it is $R_{\mathrm{s}} \propto \omega^2$, see Eq. 3.24. Additionally, the normal conductivity σ_N is proportional to the relaxation time τ, which is defined as the mean free time that charge carries travel before scattering with the lattice or with another particle. This leads to the definition of the mean free path ℓ, which is the distance covered during the mean free time by the charge carriers. Therefore, as R_{s} is proportional to the normal conductivity σ_N in the superconducting state, and since σ_N is proportional to ℓ, the surface resistance has the following dependency:

$$R_{\mathrm{s}} \propto \ell. \tag{3.25}$$

In SRF cavities, typically made of Nb, penetration of RF fields into the structure is on the order of nanometres, resulting in a surface resistance of just a few nano-ohms [41].

3.2.3 Pippard Nonlocal Electrodynamics

RF fields penetrate the surface of a good conductor up to a distance equal to the skin depth δ_s, as given by Eq. 2.37. In principle, this distance can be reduced by increasing the frequency and normal conductivity, which is achieved by decreasing the temperature. According to Eq. 2.40, this reduction in skin depth should result in a corresponding decrease in surface resistance. However, experiments often show a higher R_s than expected, indicating a departure from this expression [42]. This phenomenon is known as the "anomalous skin effect", and it occurs when the mean free path of the charge carriers is larger than the skin depth. Under these conditions, the electrons are exposed to the field for only a small fraction of time, resulting in a poor capacity to shield the field penetrating into the bulk. Consequently, the surface resistance increases more than the expression given by Eq. 2.40.

To account for the anomalous skin effect, Ohm's law is generalized to a nonlocal expression. Ohm's law describes the local dynamics and is given by:

$$\vec{J}(\vec{r}) = \sigma(\ell)\,\vec{E}(\vec{r}), \tag{3.26}$$

which is only valid when $\vec{E}(\vec{r})$ varies slowly within a vicinity of distance ℓ around $\vec{r}$. In contrast, when there is a nonlocal relation between the current and the field, $\vec{J}(\vec{r})$ depends on the electric field in the region of size ℓ around the point $\vec{r}$, so it can be expressed as

$$\vec{J}(\vec{r}) \propto \frac{\sigma}{\ell}\int \frac{\vec{R}\left[\vec{R}\cdot\vec{E}(\vec{r}')\right]e^{-R/\ell}}{R^4}d\vec{r}', \tag{3.27}$$

where $\vec{R} = \vec{r} - \vec{r}'$ and $\vec{r}'$ is a vector pointing out at the charge.

A. B. Pippard [43] introduced the concept of coherence length, denoted by ξ, when he proposed a nonlocal generalization of the London equations similar to what R. G. Chambers [44] and G. E. Reuter and E. H. Sondheimer [45] did with the nonlocal generalization of Ohm's law. In the quantum description, the electrons are described by the wave function ψ that propagates throughout the lattice of the metal. Pippard argued that the wave function should have a characteristic dimension ξ_0, named "coherence length", analogous to the mean free path in the nonlocal dynamics of normal conducting metals, which is the typical distance an electron propagates before scattering with an impurity. For a pure or clean metal, the coherence length ξ_0 is estimated by an argument based on the uncertainty principle, as follows: the electrons that become the superconducting charge carriers are those within the energy range of $k_B T_c$ of the Fermi energy, which have a momentum range of $\Delta p \approx k_B T_c / v_F$. Thus, the spatial extent of the electrons is

$$\xi_0 = \Delta x \gtrsim \frac{\hbar}{\Delta p} = \frac{\hbar v_F}{k_B T_c}, \tag{3.28}$$

where k_B is Boltzmann's constant and v_F is the Fermi velocity. Pippard then proposed a generalization of Eq. 3.16 through the following phenomenological relation:

$$\vec{J}_S(\vec{r}) = -\frac{3 n_S e^2}{4\pi\xi_0 m}\int \frac{\vec{R}\left[\vec{R}\cdot\vec{A}(\vec{r}')\right]e^{-R/\xi}}{R^4}d\vec{r}'. \tag{3.29}$$

In the previous equation, ξ is the coherence length in the presence of scattering, which would correspond to the description of a dirty metal, and it is related to the mean free path by

$$\frac{1}{\xi} = \frac{1}{\xi_0} + \frac{1}{\ell}. \tag{3.30}$$

In the presence of impurities, the mean free path is reduced and ξ is expected to be short, not exceeding the electronic mean free path. Thus, in a dirty metal, both are comparable in size. Further discussion on impurities is given in the following sections. The ideas of Pippard described the concepts of a superconductor that were later justified with a microscopic description, anticipating the BCS theory.

3.2.4 BCS Theory

The microscopic description of superconductivity was provided by the BCS theory, developed in 1957 by J. Bardeen, L. Cooper, and J. Robert Schrieffer. At low temperatures, an electron-lattice interaction causes a weak net attraction between pairs of electrons with equal and opposite momentum and spin. In the BCS framework, these superconducting charge carriers are called "Cooper pairs" and they behave as bosons, following the Bose-Einstein statistics [31, 46]. As a result, the Cooper pairs condense in a state of minimum energy or, in other words, in a quantum state with the same centre-of-mass energy described by a wave function that extends over a distance of order ξ_0. Due to this pairing mechanism and the fact that the extension of each pair ξ_0 is larger than the atoms and imperfections in the lattice, the electrical resistance of a superconductor goes to zero when a DC field is applied.

The simplest model considered in the BCS theory to describe the ground state of the system consists of N electrons added to the Fermi sea at $T = 0\,\mathrm{K}$, forming Cooper pairs represented with N-electron antisymmetrized product functions. In the second quantization, this corresponds to a singlet wavefunction given by:

$$|\psi_0\rangle = \sum_{k>k_F} g_{\vec{k}} c^*_{\vec{k}\uparrow} c^*_{-\vec{k}\downarrow} |F\rangle\,, \tag{3.31}$$

where $|F\rangle$ represents the Fermi Sea with all states filled up to k_F, $c^*_{\vec{k}\uparrow}$ is the creation operator that forms an electron of momentum $\vec{k}$ and spin up, $c^*_{-\vec{k}\downarrow}$ is another creation operator that forms an electron of momentum $-\vec{k}$ and spin down, and $g_{\vec{k}}$ are weighting coefficients. The annihilation operators, such as $c_{\vec{k}\uparrow}$, exist to empty the corresponding state.

The formation of Cooper pairs in the Fermi sea leads to a separation of the ground state and the next excited state, known as the "energy gap" Δ. This gap appears because at $T = 0\,\mathrm{K}$ the electrons with an energy $E < E_\mathrm{F}$ form pairs with electrons with energy $E > E_\mathrm{F}$, where E_F is the Fermi energy, and therefore, the total energy of a pair is $2E < 2E_\mathrm{F}$. This means that there is a minimum energy required to break a Cooper pair, which is $2\Delta\,(T)$. One of the predictions of the BCS theory is the relation between the energy gap and T_c at temperatures $T \ll T_\mathrm{c}$, which is given by:

$$\Delta\,(0\,\mathrm{K}) = \Delta_0 = 1.764 \cdot k_\mathrm{B} T_\mathrm{c}. \tag{3.32}$$

The gap $\Delta\,(T)$ has a dependency on the temperature of the superconductor and is related to the density of normal electrons n_N, as described in the two-fluid model. At temperatures $T \leq T_\mathrm{c}$, the unpaired electrons move independently from each other, behaving more like a classical gas. Thus, as the temperature goes to zero, the number of electrons is expected to decay according to the following expression:

$$n_N \propto \exp\left[-\frac{\Delta\,(T)}{k_\mathrm{B} T}\right]. \tag{3.33}$$

J. Turneaure and I. Weissman [41] observed that the surface resistance in the same temperature range is proportional to the normal conductivity, which, in turn, is proportional to the number of electrons, as shown in Eqs. 3.23 and 3.11. This is given by:

$$R_{\mathrm{s}} \propto \sigma_N \propto n_N. \tag{3.34}$$

They also noted that in the BCS theory the surface resistance has a dependency on the temperature T, the frequency f, the Fermi velocity v_{F}, the electron density of states $N(0)$, the electron mean free path ℓ, and the gap $\Delta(T)$. In 1968, Turneaure and Weissman published a simplified version of the surface resistance that takes all of these parameters into account, which is valid for temperatures $T < T_{\mathrm{c}}/2$ and frequencies $f < 10^{12}$ Hz and is given by:

$$R_{\mathrm{BCS}}(T) = A \cdot \frac{f^2}{T} \cdot \exp\left[-\frac{\Delta_0}{k_{\mathrm{B}} T}\right], \tag{3.35}$$

where A is a free parameter dependent on the normal conductivity σ_N, the mean free path ℓ, and the effective penetration depth λ (see Eq. 3.38). Here, Δ_0 is called the "superconducting gap". The surface resistance R_{BCS} of Nb at 2.5 K as a function of the mean free path for 424, 857, and 1298 MHz is illustrated in Fig. 3.2, assuming a London penetration depth of 39 nm and a coherence length of 38 nm. It is observed that the minimum R_{BCS} is obtained at approximately $\ell \sim \xi_0/2$.

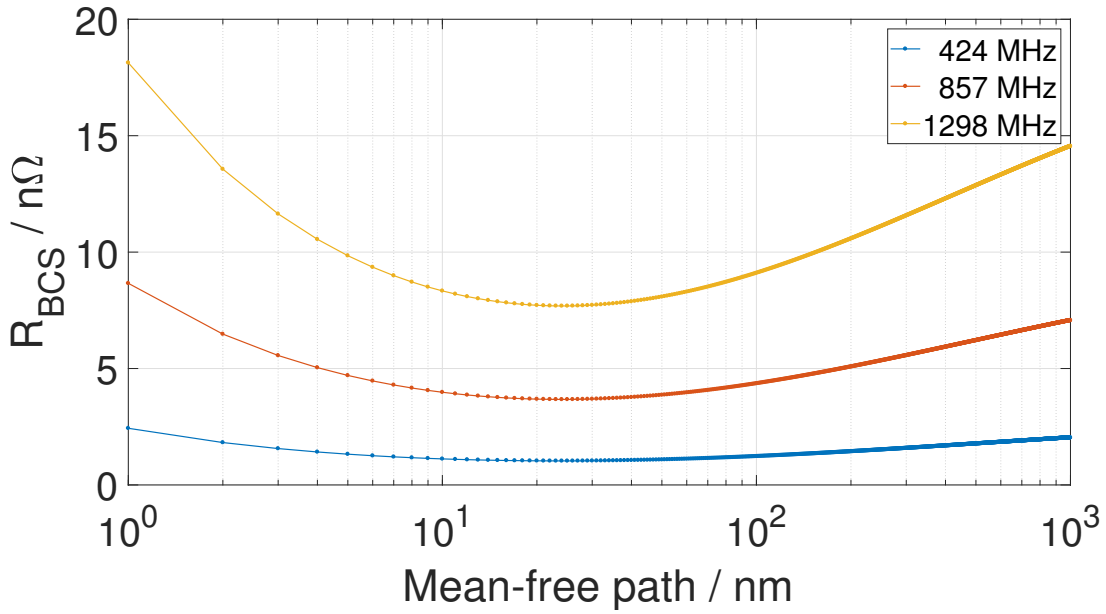

Figure 3.2: Calculated BCS surface resistance as a function of the mean free path for standard Nb at 2.5 K.

The presence of a non-zero surface resistance below T_{c} originates from the fact that Cooper pairs have mass, and therefore, inertia. This mass prevents the pairs from effectively shielding the RF fields, which accelerates the electrons, causing dissipation. From Eq. 3.35 it is trivial to check that at 0 K:

$$R_{\mathrm{BCS}}(T \to 0) = 0. \tag{3.36}$$

However, in experiments, it is observed that the surface resistance close to 0 K stays constant or even at a higher value than the one calculated with R_{BCS}. This is because the expression of the BCS theory does not consider other scattering effects, such as lattice imperfections, impurities, or magnetic impurities where magnetic flux pinning takes place [47] (the latter is discussed in Sec. 3.2.5). If these

contributions exist within the lattice of a superconductor, some Cooper pairs will eventually scatter, leading to a minimum value of the R_s called "residual resistance" R_res. Therefore, the total surface resistance is expressed as

$$R_\mathrm{s}(T) = R_\mathrm{BCS}(T) + R_\mathrm{res}. \tag{3.37}$$

The consideration of impurities changes other expressions of material properties calculated up until now. For example, the London penetration depth displayed in Eq. 3.20 is only valid in the clean limit or, in other words, when conductors have a short coherence length or a large mean free path ($\xi_0 \ll \ell$). For the case of impurities, the condition is reversed, the so-called "dirty limit" $\xi_0 \gg \ell$, and the penetration depth results in:

$$\lambda(T, \ell) = \lambda_\mathrm{L}(T)\sqrt{1 + \frac{\xi_0}{\ell}}. \tag{3.38}$$

This expression shows that the effective size of superconducting carriers and the penetration depth can be influenced by the purity of the material. Finally, it is worth mentioning that the purity of the material is determined by the residual-resistance ratio (RRR), which is usually defined as the ratio of the resistivity of a material at 300 K and at 4.2 K [48].

3.2.5 Ginzburg–Landau Theory

In 1950, seven years before the publication of the BCS theory, V. Ginzburg and L. Landau presented their phenomenological theory to describe superconductors on a macroscopic level. The Ginzburg-Landau (GL) theory served as a generalization of the London theory, offering a study of superconductors with existing spatial inhomogeneities. This was in contrast to the microscopic description of the BCS theory, where the gap Δ does not change over space. The GL theory introduces the pseudo-wavefunction $\psi(\vec{r})$ to represent the density of superconducting electrons n_S, as defined in the two-fluid model, given by:

$$n_S(\vec{r}) = |\psi(\vec{r})|^2. \tag{3.39}$$

Note that in the framework of this theory, the density of superconductors n_S has a spatial dependency to account for the inhomogeneities and fields strong enough to change it. Using a variational principle of the free energy of the system in the superconducting state, and assuming a small $\psi(\vec{r})$ with a slow variation in space, the following differential equation can be derived:

$$\frac{1}{2m^*}\left[\frac{\hbar}{i}\nabla - e^*\vec{A}(\vec{r})\right]^2 \psi(\vec{r}) + \beta|\psi(\vec{r})|^2\psi(\vec{r}) = -\alpha\psi(\vec{r}), \tag{3.40}$$

where α and β are expansion coefficients, e^* is the effective charge, m^* is the effective mass, and $\vec{A}(\vec{r})$ is the magnetic potential. It is worth noting that Eq. 3.40 has a similar form to the Gross–Pitaevskii equation, which describes the ground state of the Bose-Einstein condensate [49].

Despite its publication, this theory remained almost unnoticed until 1959 when L. Gor'kov [50] proved that the GL theory can be derived as a limiting case of the BCS theory. This is applicable for small spatial variations of $\psi(\vec{r})$ and $\vec{A}(\vec{r})$ and for temperatures near T_c. This theory introduces the GL coherence length $\xi(T)$, which characterizes the extension of $\psi(\vec{r})$. The ratio of this characteristic length and the penetration depth $\lambda(T, \ell)$, obtained in Eq. 3.38, defines the GL parameter:

$$\kappa_\mathrm{GL} = \frac{\lambda(T, \ell)}{\xi(T)}. \tag{3.41}$$

In pure or type I superconductors it is found that $\kappa_{\mathrm{GL}} \ll 1$. A. Abrikosov investigated dirty superconductors in a paper published in 1957. He studied the properties of materials with $\kappa_{\mathrm{GL}} > 1$ and demonstrated that the limit that divides type I and type II superconductors occurs at $\kappa_{\mathrm{GL}} = 1/\sqrt{2}$, where $\kappa_{\mathrm{GL}} < 1/\sqrt{2}$ corresponds to type I and $\kappa_{\mathrm{GL}} > 1/\sqrt{2}$ to type II. In contrast to type I superconductors, where there is a spontaneous phase transition between the normal and superconducting states, in Type II superconductors, this phase transition is not spontaneous, and a "mixed state" exists characterized by the penetration of the magnetic field in the form of an array of flux tubes, each carrying a quantum flux of

$$\Phi_0 = \frac{h}{2e} = 2.07 \cdot 10^{-15}\,\mathrm{Wb}. \tag{3.42}$$

In other words, in type II superconductors, there is a lower critical magnetic field H_{c1} below which there is total expulsion of the field, referred to as the "Meissner state", as would happen in a Type I superconductor. Then, above H_{c1} there is a continuous increase in magnetic flux penetration in the bulk of the metal until reaching H_{c2}, where superconductivity is destroyed. The previous process is depicted in Fig. 3.3.

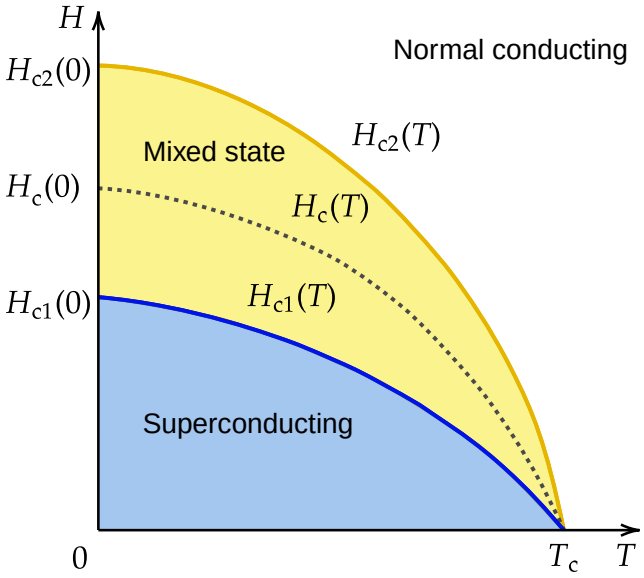

Figure 3.3: Lower, thermodynamic, and upper critical magnetic fields, H_{c1}, H_{c}, and H_{c2} respectively, of Type II superconductors as functions of temperature.

In general, the upper critical magnetic field H_{c2} can be expressed in terms of the GL parameter as

$$H_{\mathrm{c2}} = \sqrt{2}\kappa_{\mathrm{GL}} H_{\mathrm{c}}, \tag{3.43}$$

where H_{c} is the thermodynamic critical magnetic field. In type I superconductors, $H_{\mathrm{c2}} < H_{\mathrm{c}}$, which means that the conductor remains in the normal state even below H_{c} and until reaching H_{c2} when exposed to a decreasing magnetic field. Conversely, in type II superconductors, $H_{\mathrm{c2}} > H_{\mathrm{c}}$, and the material becomes superconducting at H_{c2}, entering the mixed state.

Up to this point, these critical fields mentioned are under equilibrium conditions. Before a phase transition takes place, an energy cost exists associated with nucleating a fluxoid, which leads to the possibility of a metastable "superheated" superconducting state persisting at $H > H_{\mathrm{c}}$. In this state, the energetically favourable transition has not occurred due to the activation energy barrier. This barrier,

represented by the surface energy per unit area, vanishes at the superheating field H_{sh}:

$$\frac{\mu_0}{2}\left(\xi H_{\mathrm{c}}^2 - \lambda H_{\mathrm{sh}}^2\right) = 0. \tag{3.44}$$

Therefore, superconductivity cannot persist beyond $H = H_{\mathrm{sh}}$. For pure Nb at 0 K, with $\kappa_{\mathrm{GL}} \approx 1$, the critical magnetic fields are: $H_{\mathrm{c1}} = 180\,\mathrm{mT}$, $H_{\mathrm{c}} = 200\,\mathrm{mT}$, $H_{\mathrm{sh}} = 1.2H_{\mathrm{c}} = 240\,\mathrm{mT}$, and $H_{\mathrm{c2}} = 280\,\mathrm{mT}$ [51]. Finally, in the mixed state, an array of unit cells formed by magnetic flux tubes appears, with each cell containing a vortex supercurrent that concentrates the field flux towards its centre. Each of these individual unit cells, which are constituted by a magnetic flux concentration, is simply referred to as a "vortex". When a magnetic field is applied to a type II superconductor with sufficient strength to cause vortices to appear, and a current density $\vec{J}$ is present, the vortices move due to the Lorentz force $\vec{J} \times \vec{\Phi}_0$, causing energy dissipation. However, material defects serve as pinning sites for vortices, reducing their movement and, therefore, the dissipation of energy. In the case of an applied RF field, even though the vortices are pinned, they oscillate around its centre point, generating heat that can potentially cause a quench [52]. Nowadays, R&D efforts are dedicated to preventing vortex formation in cavities in order to achieve high Q_0.

3.2.6 Materials Beyond Nb

Current research in SRF materials aims to increase the quality factor and accelerating field per unit length in Nb cavities. Various surface treatments, such as N-doping [53], N-infusion [54], and mid-T annealing [55], have been implemented to push their quality factors and accelerating gradients up to approximately 10^{11} and 50 MV/m, respectively. However, since these gradients are approaching their theoretical limit of approximately 55 MV/m [56], the scientific community has been developing and investigating coating techniques involving materials, such as Nb_3Sn [29, 57] and MgB_2 [58], and multilayer structures [59], which have the potential to minimize the losses and increase the maximum electromagnetic fields they can achieve.

Alternative materials for SRF applications should possess a critical temperature T_{c}, lower critical magnetic field H_{c1}, thermodynamic critical magnetic field H_{c}, and superheating field H_{sh} higher than those of Nb, and low resistivity in the normal state. Tab. 3.4 presents a few materials that have the potential to be candidates for this kind of application.

Material	T_{c} (K)	ρ_{n} ($\mu\Omega$ cm)	$H_{\mathrm{c}}(0)$ (T)	$H_{\mathrm{c1}}(0)$ (T)	$H_{\mathrm{c2}}(0)$ (T)	λ (nm)	Δ (meV)	ξ (nm)
Nb	9.23	2	0.2	0.18	0.28	40	1.5	35
NbN	16.2	70	0.23	0.02	15	200–350	2.6	3–5
NbTiN	17.3	35		0.03	15	150–200	2.8	5
Nb_3Sn	18	8–20	0.54	0.05	28	80–100	3.1	4
V_3Si	17	4	0.72	0.072	24.5	179	2.5	3.5
Nb_3Al	18.7	54			33	210	3	
Mo_3Re	15	10–30	0.43	0.03	3.5	140		
MgB_2	40	0.1–10	0.43	0.03	3.5–60	140	2.3 /7.2	5
Pnictides	30–55		0.5–0.9	30	50–135	200	10–20	2

Figure 3.4: Superconducting parameters for candidate materials considered for SRF applications. Image taken from [57].

In the following sections, examples of these alternative materials are briefly described and their advantages and limitations are discussed.

Nb_3Sn

Inter-metallic A15 compounds, such as Nb_3Sn, have been studied for accelerator technology applications since their critical temperature can achieve values of nearly two times that of Nb. However, they are employed only in the form of thin-films because of their fragile composition. Nb_3Sn as a coating material for cavities is an attractive option due to its potential to achieve high quality factors and accelerating fields at 4.2 K [29]. To fabricate Nb_3Sn thin-films, a developed technique called "vapor diffusion" is commonly employed, where a Nb substrate is place in an ultra-high-vacuum (UHV) furnace with a tin source inside. A controlled heating process causes the Sn to evaporate and to diffuse into the Nb, forming nucleation sites. The coating takes place when tin diffuses into the Nb along with alloying to Nb_3Sn.

An Nb-Sn intermetallic alloy has a stable composition from 18 to 25 at.% Sn, where T_c changes from 6 K to 18 K, Δ_0 from 1 to 3.4 meV, and $\mu_0 H_{c2}$ ranges from 6 to 30 T. Therefore, a bulk Nb cavity coated with Nb_3Sn, operating at 2 K, may exhibit a Q_0 comparable to that of a Nb cavity under the same conditions. Moreover, at 4.2 K, the Q_0 would be almost two orders of magnitude larger than that of an operating Nb cavity at 2 K. The performance of this alloy also depends on how close it is to stoichiometry after fabrication. In the case of close-to-stoichiometry Nb_3Sn coated cavities fabricated using the Sn vapour technique, a $R_{BCS} < 2\,n\Omega$ is expected at 4.2 K and 500 MHz, which is much lower than the 55 nΩ found in Nb cavities. Theoretically, the thermodynamic critical magnetic field of Nb_3Sn is 520 mT [60], which is more than double that of Nb. Therefore, the expected accelerating field would be $E_{acc} > 100$ MV/m.

Nb_3Sn thin-films basically consist of coating bulk Nb cavities with a film of thickness d, which provides them with an enhanced H_{c1} compared to that of the Nb substrate. This configuration is often referred to as a "superconductor-superconductor" structure. Considering a film with thickness $d < \lambda$, where λ is the effective penetration depth, as shown in Eq. 3.38, the resulting lower critical magnetic field H_{c1} of the thin-film is given by:

$$\mu_0 H_{c1} = \frac{2\Phi_0}{\pi d^2} \ln\left(\frac{d}{1.074 \cdot \xi_{GL}}\right). \tag{3.45}$$

For instance, using Eq. 3.45 for a thin-film made of Nb_3Sn with $d = 20$ nm gives $\mu_0 H_{c1} = 5.7$ T, surpassing the lower critical magnetic field of 200 mT for pure Nb (see Tab. 3.4). Nevertheless, the larger H_{c1} value of the film enables it to shield the bulk Nb from vortex penetration.

As a next step in the improvement process of this technique, depositing multiple thin-films has also been proven to increase the lower critical magnetic field. For example, if a Nb cavity that achieves a maximum magnetic field up to 150 mT is coated with an insulating layer, and a $d = 50$ nm Nb_3Sn layer is deposited on top of it, the applied RF field can be approximately 320 mT. This configuration could enable an attainable accelerating field $E_{acc} > 75$ MV/m. Despite these predictions and advancements, Nb_3Sn cavity performance has yet to be fully realized.

MgB_2

In 2001, an endeavour to raise the critical temperature of superconductors led to the discovery of the compound MgB_2, a material that becomes superconducting at 39 K [61]. The understanding of MgB_2 properties has been facilitated by the use of theoretical models, revealing that this material has two superconducting gaps (2.7 meV and 6.7 meV). The resistivity in the normal state remains low, with the best values found below 1 μΩcm. Additionally, this material has high lower, thermodynamic, and upper critical magnetic fields. For instance, upper critical magnetic field $\mu_0 H_{c2}$ limits of approximately 74 T have been reported for thin-films alongside a T_c of 35 K [62]. These properties position MgB_2 as

a promising candidate for applications in SRF cavities. Many efforts have been invested within the scientific community to develop MgB_2 thin-films on cavities. However, the fabrication of these films presents challenges due to the material vulnerability to moisture, which causes degradation and increases the surface resistance. A potential solution for this issue may involve the implementation of protective measures during the cleaning process of a coated cavity with this material.

S-I-S Thin-Films

The implementation of alternative materials, such as Nb_3Sn, has the potential to significantly enhance the accelerating fields and quality factors of SRF cavities. Furthermore, thin-films coatings of these materials can further boost cavity performance by enabling them to withstand higher external fields, see Eq. 3.45. However, a different approach to achieve this was proposed by A. Gurevich [59], involving the coating of bulk Nb cavities (S) with multilayer structures constituted of alternating superconducting (S) layers with higher critical magnetic field H_c and dielectric (I) layers, as depicted in Fig. 3.5. Both the S and I layers should have a thickness d_S and d_I, respectively, that are smaller than the effective penetration depth λ. Additionally, d_I needs to be sufficiently large to avoid Josephson junction effects.

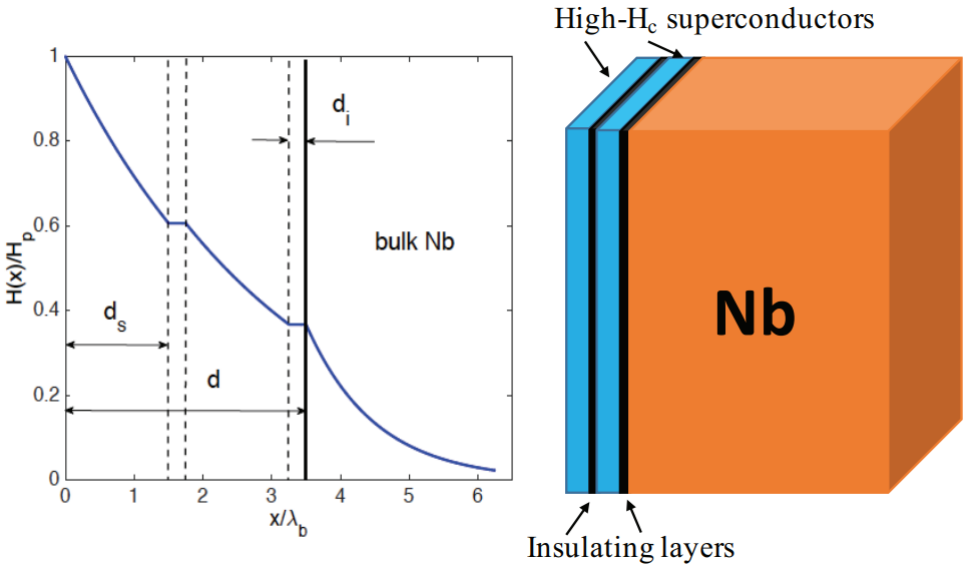

Figure 3.5: Multilayer coating consisting of thin ($d < \lambda$) layers of superconductors with high B_s separated by thin dielectric layers deposited on the inner surface of the Nb cavity. Left panel shows screened magnetic field in a multilayer. Figure taken from [60].

The most commonly studied form of this bulk-layers arrangement is the superconductor-insulator-superconductor (SIS) structure. However, the optimal number of SI layers is determined by a balance between minimizing vortex dissipation, superconductivity suppression at the SI interfaces, and maintaining effective thermal conductivity. The candidate materials considered for coating Nb cavities include AlN or Al_2O_3 for the insulating layer. On top of the insulator, materials such as NbN, NbTiN, or Nb_3Sn are employed as the S-layer [63]. By implementing this approach, the SIS layers act as a magnetic shield of the bulk, stopping the propagation of local vortices at the insulating layer and preventing avalanches, reducing the risk of cavity quenching. The predicted Q_0 of these multi-layered cavities at 4.2 K is expected to surpass Nb values by two orders of magnitude and increase the sustainable external magnetic field. Moreover, this technology has the potential to increase E_{acc} by 20 to 100% in comparison to Nb.

For example, applying a NbN thin-film ($\xi_0 = 5\,\text{nm}$) with a thickness $d = 20\,\text{nm}$ on a Nb cavity may result in a lower critical magnetic field $\mu_0 H_{c1} = 4.2\,\text{T}$, as calculated with Eq. 3.45 [60]. Current

research has demonstrated significant progress in SIS coatings through their study on samples. Using a technique called "atomic layer deposition", these coatings have achieved a critical temperature of 15.9 K and $\mu_0 H_{c1} = 213\,\mathrm{mT}$, surpassing the values obtained for Nb [64]. The choice of such materials has shown promising results both theoretically and experimentally, as they enhance the cavity performance by increasing the onset of vortex penetration and the thermal breakdown field above the critical magnetic field H_c of Nb.

It is evident that the materials presented in this section still require further R&D before they can be applied to operating cavities. To accelerate this progress, material characterization tools such as the QPR can prove to be invaluable.

3.3 Superconducting RF Cavity Testing

In order to evaluate the performance of a cavity, microwave engineering techniques are employed to measure its electric and magnetic fields, resonant frequency, and intrinsic quality factor Q_0. From these results material properties of the cavity can be obtained using the theory shown in chapter 3.2. In general, it is desired for a cavity to have as high an accelerating field and as high a quality factor as possible. The most commonly used technique to characterize a cavity is based on the measurement of its response to RF fields, which allows for determining the quality factor as a function of the peak electric field.

This section introduces the commonly used techniques in SRF cavity testing. These techniques can also be used with the QPR by making minor changes to the data-acquisition system.

3.3.1 RF Measurements

To excite the modes of a cavity, RF power needs to flow into the structure to drive it. This is typically achieved by directing the RF power in the form of transverse electromagnetic waves (TEM) from the source into the cavity. These waves then enter the resonator through an input antenna. The antenna couples with the electric fields, and its coupling strength, simply referred to as "coupling", depends on its penetration within the cavity. The coupling β is a measure of the overlap between the cavity fields and the fields that leak into the cut-off region from the input coupler. Another antenna, known as the "pick-up antenna", is employed to obtain more information about the resonator, such as the stored energy U or the transmission coefficient S_{21}. Fig. 3.6 shows a 1.3 GHz TESLA-shaped single-cell cavity with its corresponding input and pick-up antennas, as well as the electric field distribution of the operating TM_{010} mode.

When studying the behaviour of a cavity operating at its resonant frequency, a scenario is first considered in which the cavity has its RF power switched off at a certain time. Consequently, the energy stored in the cavity is dissipated through the cavity walls and antennas. The total power within the cavity, P_{tot}, can be formally described by the following equation:

$$P_{\mathrm{tot}} = P_{\mathrm{c}} + P_{\mathrm{refl}} + P_{\mathrm{tran}}, \tag{3.46}$$

where P_{c} is the power dissipated through the cavity walls, P_{refl} is the power leaking back out of the input coupler, and P_{tran} is the power coming out of the probe antenna. As the cavity is left to "ring down", its stored energy U satisfies the following differential equation:

$$\frac{dU}{dt} = -P_{\mathrm{tot}} = -\frac{\omega U}{Q_{\mathrm{L}}}, \tag{3.47}$$

where Q_{L} is the loaded quality factor, defined as

$$Q_{\mathrm{L}} = \frac{\omega U}{P_{\mathrm{tot}}}. \tag{3.48}$$

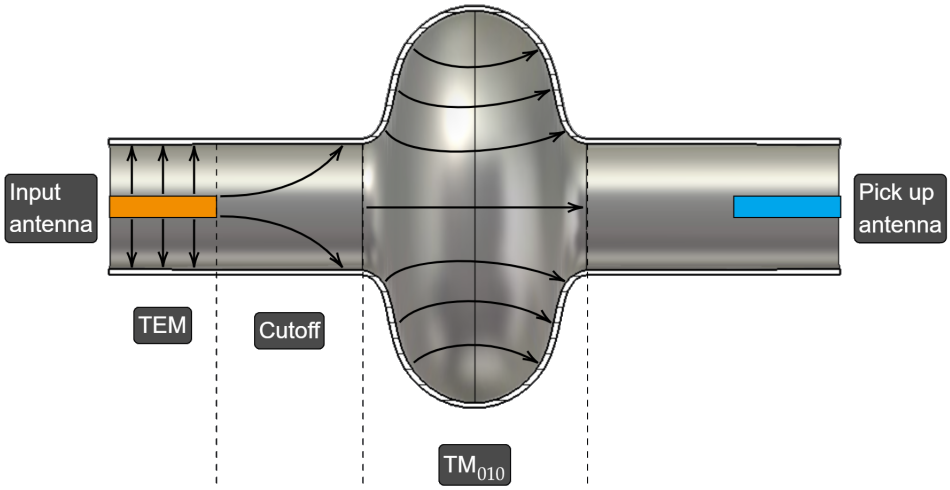

Figure 3.6: Diagram of a 1.3 GHz single-cell cavity with input and pick-up antennas. The electric field distribution inside the cell corresponds to that of the TM_{010} mode.

It is worth emphasizing that while the quality factor Q_0, given by (see Eq. 2.44):

$$Q_0 = \frac{\omega U}{P_{\mathrm{c}}}, \tag{3.49}$$

is an intrinsic property of the cavity, Q_{L} characterizes the cavity with the couplers. In the simplest case, when no field emission (see Sec. 3.4) or other anomalous losses take place, the solution to Eq. 3.47 is

$$U(t) = U_0 \exp\left(-\frac{\omega}{Q_{\mathrm{L}}} t\right), \tag{3.50}$$

where U_0 is the stored energy at $t = 0$. The energy stored in the cavity thus dissipates exponentially with a decay time constant τ_{L} defined as

$$\tau_{\mathrm{L}} = \frac{Q_{\mathrm{L}}}{\omega}. \tag{3.51}$$

The loaded quality factor can then be determined by measuring the decay time. However, the main interest lies in obtaining the intrinsic properties of the cavity, i.e. Q_0, instead of the whole system. Substituting Eq. 3.46 into the inverse of Eq. 3.48 gives the quality factor for each loss mechanism:

$$\frac{1}{Q_{\mathrm{L}}} = \frac{P_{\mathrm{tot}}}{\omega U} = \frac{1}{Q_0} + \frac{1}{Q_{\mathrm{ext}}^{\mathrm{inp}}} + \frac{1}{Q_{\mathrm{ext}}^{\mathrm{pro}}}, \tag{3.52}$$

where the external quality factors for the couplers, $Q_{\mathrm{ext}}^{\mathrm{inp}}$ and $Q_{\mathrm{ext}}^{\mathrm{pro}}$, are defined as:

$$Q_{\mathrm{ext}}^{\mathrm{inp}} = \frac{\omega U}{P_{\mathrm{refl}}} \tag{3.53}$$

$$Q_{\mathrm{ext}}^{\mathrm{pro}} = \frac{\omega U}{P_{\mathrm{tran}}}. \tag{3.54}$$

The coupling constant of the input and pick-up antennas are defined as

$$\beta_{\mathrm{inp}} = \frac{Q_0}{Q_{\mathrm{ext}}^{\mathrm{inp}}} \tag{3.55}$$

$$\beta_{\mathrm{pro}} = \frac{Q_0}{Q_{\mathrm{ext}}^{\mathrm{pro}}}. \tag{3.56}$$

The coupling constant or coupling strength provides information on how strongly the antennas interact with the resonator. For instance, a $\beta_{\mathrm{inp}} > 1$ means that the power leaking out of the input coupler is larger than the power dissipated in the cavity. Finally, the unloaded quality factor is

$$Q_0 = Q_{\mathrm{L}} \cdot (1 + \beta_{\mathrm{inp}} + \beta_{\mathrm{pro}}) \,. \tag{3.57}$$

Basically, to obtain the quality factor of the cavity, it is required to measure the coupling constants and the loaded quality factor.

3.3.2 Driven Cavity

The RF characterization of a driven cavity, which is discussed in the this section, is then carried out considering only the input antenna connected to the cavity with an external quality factor $Q_{\mathrm{ext}} = Q_{\mathrm{ext}}^{\mathrm{inp}}$ and a coupling constant $\beta_{\mathrm{inp}} = \beta$. The coupling constant of the probe antenna is generally chosen such that $\beta_{\mathrm{pro}} \ll 1$, which minimizes any possible field perturbation caused by the presence of this antenna. To drive a cavity and excite one of its resonance modes, P_{forw} is transferred to the cavity. However, not all of the power provided flows into the resonator, and a reflected power P_{refl} exists, also called "reverse travelling power", which is given by:

$$P_{\mathrm{refl}} = |\Gamma|^2 \, P_{\mathrm{forw}}, \tag{3.58}$$

where Γ is the reflection coefficient [3].

While it is not simple to excite a single mode in a real cavity, and the same applies to the transmission line, an analysis performed by H. Padamsee and J. Knobloch [14] considers a one-mode excitation to obtain the cavity response to the input RF power in continuous-mode operation or steady state. The cavity-coupler system is modelled by a nonlinear harmonic oscillator driven by an RF power, making it possible to predict the cavity steady-state behaviour and the transient response through a differential equation describing the stored energy in the resonator:

$$\frac{d\sqrt{U}}{dt} = \frac{1}{2\tau_{\mathrm{L}}} \left(\sqrt{U_0} - \sqrt{U} \right), \tag{3.59}$$

where U_0 is the stored energy in the steady state for the given RF power.

An expression for the reflected power is also obtained, which provides information about the coupling strength β. The general form of the reflected power is:

$$P_{\mathrm{ref}} = \left(\sqrt{\frac{\omega U}{Q_{\mathrm{ext}}}} - \sqrt{P_{\mathrm{forw}}} \right)^2 . \tag{3.60}$$

Eq. 3.60 describes the reflected power in the driven cavity as a sum of the part of the forward power reflected at the antenna and the power emitted from the cavity. The following sections study the transient responses for the cases of turning on and off the RF power and steady state.

Switch RF On

Consider an empty cavity where at $t = 0$, the P_{forw} is switched on. The internal energy of the cavity is then expected to increase from zero to U_0, which corresponds to its constant energy value during continuous wave operation. The time period from turning on until reaching the steady state is known as the "filling phase" [65]. The behaviour of the energy is described by Eq. 3.59, and its solution takes the form

$$U(t) = U_0 \left[1 - \exp\left(-\frac{t}{2\tau_{\text{L}}}\right)\right]^2. \tag{3.61}$$

The coupling constant β between the cavity and the input antenna determines the efficiency of power transmission to the resonator. The power reflected, which is the forwarded power minus the energy flowing into the cavity, can be obtained with Eqs. 3.60 and 3.61. They give the relation

$$P_{\text{refl}} = \left\{1 - \frac{2\beta}{1+\beta}\left[1 - \exp\left(-\frac{t}{2\tau_{\text{L}}}\right)\right]\right\}^2 P_{\text{forw}}. \tag{3.62}$$

Steady State

Once the filling phase is complete, the cavity reaches steady-state operation. At this point, the internal energy of the cavity no longer changes with time and is constant at its maximum value U_0. Under these conditions, the reflected power stays constant, and this part of the curves is referred to as the "flat top". The power reflected from the cavity can be obtained by taking the limit of Eq. 3.62 as $t \to \infty$, which yields

$$P_{\text{refl}} = \left(\frac{\beta - 1}{\beta + 1}\right)^2 P_{\text{forw}}. \tag{3.63}$$

Conversely, Eq. 3.63 can be used to determine the coupling β, using the following relation:

$$\beta = \frac{1 \pm \sqrt{\frac{P_{\text{refl}}}{P_{\text{forw}}}}}{1 \mp \sqrt{\frac{P_{\text{refl}}}{P_{\text{forw}}}}}, \tag{3.64}$$

where the upper signs correspond to the over-coupled case, and the lower signs for the under-coupled case[1].

Switch RF Off

Switching off the RF power is a common method used in laboratories worldwide to determine the value of $Q_0(E_{\text{acc}})$ [2, 66, 67], which involves measuring the decay-time constant. In this procedure, the RF power that is flowing into the cavity is turned off, and the cavity is left to ring down while the reflected power or the transmitted power is recorded. To understand the behaviour of the stored energy, consider a cavity operating in continuous mode, and at time $t = 0$, the RF power is switched off, causing the forwarded power P_{forw} to immediately drop to zero. This results in U_0 also going to zero. Then, the energy U is described by the following differential equation:

$$\frac{d\sqrt{U}}{dt} = -\frac{1}{2\tau_{\text{L}}}\sqrt{U}, \tag{3.65}$$

which has a solution given by Eq. 3.50.

[1] The over-couple case corresponds to $\beta > 1$ and, reciprocally, the under-couple case to $\beta < 1$.

In this situation, the reflected power is equal to all the power leaking out of the cavity. Hence, Eq. 3.60 gives the relation:

$$P_{\text{refl}} = \frac{4\beta^2 P_{\text{forw}}}{(1+\beta)^2} \cdot \exp\left(-\frac{t}{\tau_{\text{L}}}\right), \tag{3.66}$$

where P_{forw} takes the value of the power just before the RF was turned off. At $t = 0$, an expression of the coupling strength that does not distinguish whether the input antenna is under or over coupled is obtained:

$$\beta = \frac{1}{2\sqrt{\frac{P_{\text{forw}}}{P_{\text{refl}}}} - 1}. \tag{3.67}$$

However, instead of a signal in continuous mode, modern laboratories typically use rectangular pulse-shaped forwarded powers P_{forw}. For example, facilities using normal conducting cavities, such as LCLS, require pulse lengths on the order of a few microseconds. Conversely, accelerators employing superconducting cavities, such as FLASH (Free Electron LASer in Hamburg) and Eu-XFEL, can use longer pulse lengths on the order of $10^2\,\mu$s [68]. Notably, at DESY, vertical testing of 1.3 GHz TESLA-shaped nine-cell cavities at approximately 2 K is conducted with pulse lengths as long as 1 s, which is possible due to the high quality factors of approximately 10^{10}. In general, the pulse length must be long enough to drive the cavity to near equilibrium. Fig. 3.7 shows the shape of the reflected and transmitted powers as a response to rectangular pulses for different coupling constants. The measurement of the forwarded, transmitted, and reflected powers, P_{forw}, P_{refl}, and P_{tran} respectively, are typically carried out using an oscilloscope.

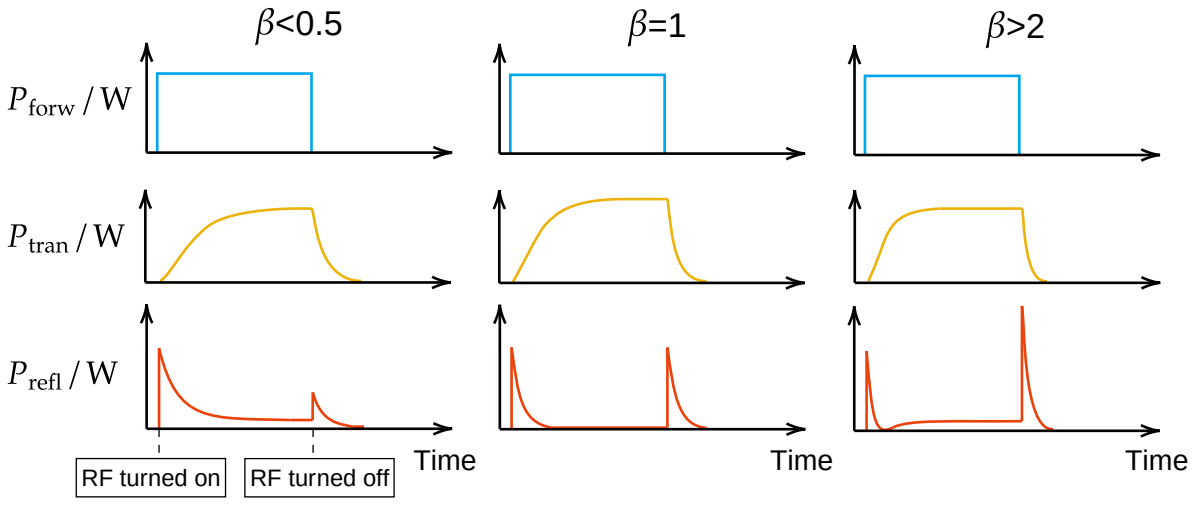

Figure 3.7: Cavity response to a rectangular pulse shape for different coupling constants. The forward, reflected, and transmitted powers, P_{forw}, P_{refl}, and P_{tran} respectively, show distinct shapes depending on the coupling of the input antenna.

As was discussed before, cavities are subject to various limitations that can affect their performance, such as material contamination, operating parameters, or intrinsic material limits. The next section reviews the most common problems encountered when operating cavities.

3.4 Limitations of SRF Cavities

3.4.1 Quench

Quench is a phenomenon where a cavity transitions from the superconducting to the normal conducting state. When a cavity quenches, there is a sudden drop in its intrinsic quality factor, caused by an increase in the surface resistance of the material. One of the mechanisms that can trigger a quench is called "thermal breakdown", referred to as "thermal quench". This occurs when RF field-induced heat at hot spots on the surface, also called "defects", is large enough to rise the local temperature above T_c. Therefore, a portion of the surface becomes normal conducting. If the heat generated at the defect cannot be transferred to the helium bath, the normal conducting region grows, increasing the power dissipation until the thermal instability takes place and the cavity quenches.

Another mechanism to break down superconductivity is called "magnetic quench". In this case, geometric defects in the form of a convex or concave protrusion enhance the local magnetic field above the upper critical magnetic field, thus destroying the Meissner state [69]. The type of defects that raise the local magnetic field include impurity inclusions, grain boundaries, pits, bumps, or scratches, which may form during cavity preparation. To avoid triggering this magnetic breakdown, a preventive measure is to conduct eddy-current scanning of the material sheets to identify and exclude those that do not meet the standard. Additionally, choosing high-purity Nb for cavity fabrication helps in stabilizing defect heating due to its high thermal conductivity [70].

3.4.2 Multipactor Discharge

Devices that operate with RF fields at low pressures are susceptible to experiencing multipacting, also known as the "multipactor effect". Multipacting in RF cavities is the rapid multiplication of electrons caused by a few seed electrons that gain energy from the fields and collide with the walls of the structure. When the kinetic energy and the impact angle of the seed electrons are within a specific range, secondary electrons may be emitted from the cavity surface. In addition, if the trajectory of these secondary electrons is synchronized with the RF field, they can impact with the same or another area inside the cavity. An exponential growth of electrons takes place if the yield secondary emission[2] δ of the subsequent collisions is $\delta > 1$ and the timing of these impacts is synchronized with the RF fields.

The avalanche of electrons created absorbs energy from the RF fields, which they transfer to the cavity walls through collisions, leading to an increase of the temperature of the walls to a point that can trigger a thermal quench. In elliptical cavities, such as 1.3 GHz TESLA-shaped cavities, multipacting occurs at accelerating fields between 17 MV/m and 22 MV/m [71] and is observed at the equatorial region as a result of the force caused by the electric field distribution of the TM_{010}-like mode. Multipacting can be simulated as a 2D problem showing reliable results [72, 73, 74] because the electric field of this mode has only the components ρ and z of the cylindrical coordinate system.

There are different techniques to reduce or eliminate multipacting. One technique consists of changing the cavity design. For example, since the trajectories of the secondary electrons tend to congregate around the equator, a slight deformation of this area might change the field distribution, affecting the growth rate of multipacting. Another technique is referred to as "processing the cavity", which consists of allowing multipacting to start and develop for several minutes while increasing the RF power [75]. This process enables the electrons to clean the cavity surface, ensuring that $\delta < 1$. As long as the cavity is kept under vacuum, this approach cures multipacting.

[2]The yield of secondary emission δ is defined as the ratio of the number of secondary electrons N_s to the number of primary electrons N_p, i.e. $\delta = N_s/N_p$ [72].

3.4.3 Field Emission

While the cavity design allows for the production of the desirable TM_{010}-like field distribution when driven, it also results in the existence of high electric field concentrations on its inner surface, which can cause problems. Field emission is the phenomenon in which electrons are emitted from certain spots, called "emitters", on the surface exposed to RF fields. These electrons then get accelerated and may collide with the cavity walls, depositing heat on it and increasing the local temperature to a level that can induce a thermal quench [76]. This heat deposition is also accompanied by the generation of X-rays through "Bremsstrahlung" [40]. High-field regions are located at the irises of 1.3 GHz TESLA-shaped cavities with $\beta = 1$, as depicted in Fig. 2.5. Therefore, particulate contaminants or geometrical defects, such as scratches or needle-tip-like shaped protrusions, exposed to a high-field area, are most likely emitting sites. On a microscopic level, the UHV environment inside the cavity, together with the electric field, increases the probability of electrons to tunnelling through the potential barrier that prevents them from escaping the metal, thereby initiating field emission.

To avoid field emission in operating cavities and achieve higher accelerating fields, surface cleanliness is essential. Improving the cleanliness conditions of the preparation process of the inner surface of the cavity and the clean room environment during the assembly process can mitigate field emission. In addition to these requirements, an advanced cleaning technique known as "high-pressure water rinsing" (HPR) has been implemented since it reduces field emission more effectively. Even after the HPR, cavities still display field emission, but at higher accelerating fields.

3.4.4 Q-Disease

In 1990, after the introduction of high-purity Nb for cavity fabrication, a systematic quality factor degradation by up to three orders of magnitude was observed when cavities were cooled down at rates slower than 1 K/min [77]. This anomalous loss mechanism, known as "Q-disease", is attributed to the absorption of hydrogen by bulk Nb. This hydrogen bonds to the atoms and imperfections of the lattice, precipitating as hydrides at the Nb surface at temperatures between 100 and 150 K.

Based on these observations, it was established to cool down cavities rapidly (at a rate of < 1 K/min) from room temperature to 4.2 K to prevent hydride formation. The impact that two different cooldown speeds have on the cavity quality factor Q_0 is shown in Fig. 3.8. It can be observed that slow cooldowns lead to a reduced quality factor up to one order of magnitude and that the quality factor decreases further with increasing accelerating field.

It was also found that typical cavity preparation procedures after fabrication can lead to the possibility of hydrogen uptake into the material. The hydrogen density is greater near the Nb surface than in the bulk, particularly if the surface has undergone a chemical treatment like buffered chemical polishing (BCP)[3] or electropolishing (EP)[4] [80]. While the oxide layer is estimated to be around 6 nm in depth, the hydrogen content covers a layer of 10 nm. However, the near-surface volume also contains defects such

[3] BCP is a technique employed to remove material from the inner surface of cavities to remove damage and contamination after the mechanical fabrication and to improve their performance. A 1:1:2 mixure of the chemicals HF, HNO_3, and H_3PO_4 can remove 1 µm per minute from the cavity surface. To prevent the difussion of hydrogen into the bulk, the mixure is cooled to 15 °C during the application process [78].

[4] EP is a technique that uses a 1:9 mixure of the chemicals HF and H_2SO_4, as well as an electric current flowing through it to remove and smooth the sharp edges present in the inner surface of cavities. In the setup, the anode (cavity) is placed horizontally, and a cathode is introduced along its center, which includes a nozzle to fill the resonator with the acids. When a voltage within the range ΔV_1 is applied to the electrodes, a thin, viscous film appears on the anode surface. The thickness of the anodic film varies due to the protrusions and valleys present on the rough surface of the cavity. Once the corresponding current for a voltage in the range $\Delta V_2 > \Delta V_1$ flows across the electrolyte, the viscous film has a higher viscosity and electrical resistivity than the rest of the acid. Since the film is thinner in protrusions, it presents a higher resistivity than in the valleys. This results in a higher current density at these protrusions, causing them to dissolve faster [79]. With this setup, typical removal rates ranging from 0.3 to 0.5 µm/min can be achieved.

as vacancies, vacancy clusters, interstitial impurities, or dislocations, which facilitate the precipitation of hydrogen into different phases of hydrides [81]. The Q-disease is more severe for slow cooldowns because the longer the cavity stays in the temperature range from 150 K to 75 K, the greater the number and size of hydrides that form, including islands with dimensions larger than 100 nm [82]. Moreover, these islands become superconducting below 1.3 K [83], turning into potential scattering sites that increase the residual resistance, as cavities operate at 2 K. In order to get rid of this "disease", a rapid cooling is required, but a more effective preventive measure is degassing the cavity in UHV at a temperature between 700 °C and 900 °C for 2 to 3 hours.

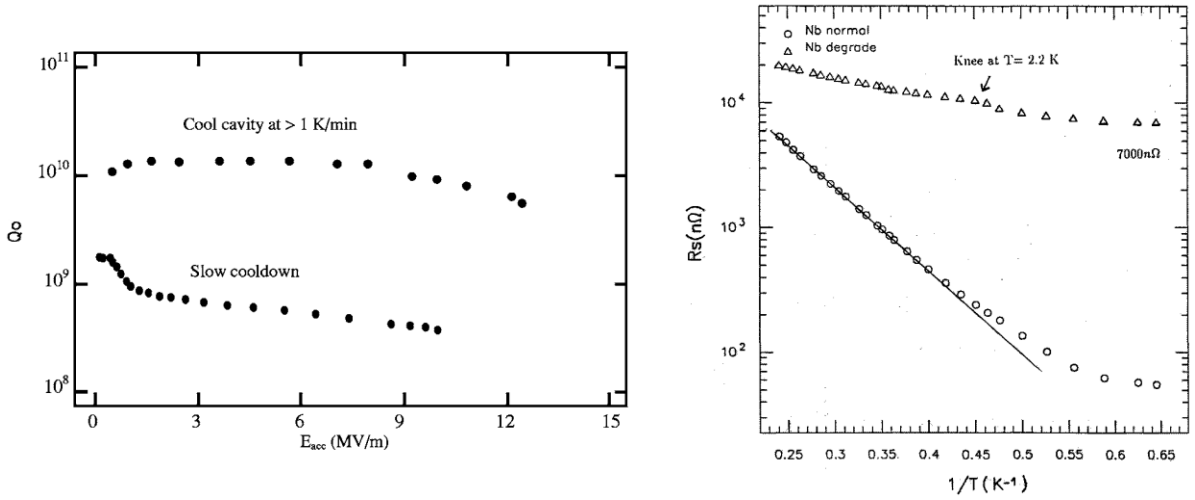

Figure 3.8: Left: Comparison of Q_0 vs E_{acc} curves measured after a slow and a fast cooldown. Right: Surface resistance R_{s} of a "healthy" and a Q-diseased cavity versus temperature. Image taken from [77].

Chapter 4

The Quadrupole Resonator

4.1 RF-Based Superconducting Sample Characterization Instruments

The scientific community has an interest in characterizing small samples of superconducting materials due to the cost and time associated with producing and measuring full-scale cavities. Additionally, certain film deposition techniques and thermal treatments require further R&D before they can be effectively applied in cavities. Therefore, sample test devices with faster turnaround times and lower costs compared to cavities are highly valuable for investigating these materials. To satisfy this need, laboratories worldwide have developed a variety of setups to measure the surface resistance R_s of samples under controlled conditions that are typical for SRF cavities. These conditions include parameters such as RF frequency f, cryogenic temperature T, and applied magnetic field B.

These setups cover operational frequencies from the ultra-high-frequency range to the W-band, temperatures ranging from 2 K to at least 20 K, and magnetic fields up to 400 mT. Sample diameters can range from 1 cm to 17 cm, and notable examples of these setups include host cavities, sapphire loaded cavities, SIC systems, hemispherical cavities, and QPRs. These setups can also aid in the development and testing of theoretical models for the surface resistance by providing a diverse parameter space for investigation.

The shapes of the samples typically consist of flat discs, rods, or thin-films. Two measurement techniques are applied to determine the surface resistance of samples depending on the setup used. The first technique is the end-plate replacement, which requires a resonator with a reference sample, both of which are surface treated in the same way. The resonant structure is excited while exposing the sample to the RF fields, and the quality factor is measured. Finally, the sample of interest is then mounted in place of the reference, and the change in quality factor with respect to the reference determines the surface resistance [84].

The second technique involves directly mounting the sample of interest onto the resonant structure without the need for a reference sample. This technique is known as “calorimetric measurement”, explained in more detail in Sec. 4.5, because it employs a DC heater, which is usually a resistor, and temperature sensors attached to the side of the sample that are not exposed to the RF fields. The heater sets the temperature of the sample, and the sensors track this value using a closed-loop. The power change of the heater when the RF power is turned on relates to the power dissipated on the sample, which then allows for the determination of the surface resistance.

Device	Frequency (GHz)	Sample diameter (mm)	Sensitivity	B_{max} (mT)	B_{max} sample/B_{max} cavity
SIC	7.4	50	Sub nΩ	14	1.04
Quadrupole resonator (CERN)	0.4/0.8/1.2	75	Sub nΩ	70	1.18
Quadrupole resonator (HZB)	0.433/0.866/1.3	75	Sub nΩ	120	0.89
Orsay	4/5.6	126	Few nΩ	16	
SLAC mushroom	11.4	50	0.1 mΩ Cu cavity/10 μΩ Nb cavity	400	2.5
Cornell mushroom	4.78/6.16	100		106	1.24/1.57
TAMU sapphire-loaded	2.2	178			9.02
Choked resonator	7.8	100	Few nΩ (est.)	10 (@4.2 K)	1.18

Figure 4.1: Comparison of the different and alternative devices for RF characterization of samples. Table taken from [84].

At present, sample characterization devices offer the advantage of studying small samples with a fairly simple geometry. The design of a test device aims to have a resonance frequency f_0 in a typical range of operating cavities, a high peak magnetic field B_{pk} on the sample, a high ratio of peak magnetic field on the sample to the same on the cavity $B_{\mathrm{sample,\,pk}}/B_{\mathrm{cavity,\,pk}}$ and a high sensitivity. Fig. 4.1 compares various devices used in different laboratories around the world.

4.2 Advantages of the QPR

Compared to other sample-characterization systems, the QPR offers several advantages. It enables direct measurement of the surface resistance through the use of the calorimetric measurement technique. For instance, the QPR allows for the study of the surface resistance of samples at 1.3 GHz, which is the operational frequency of Nb SRF TESLA-shaped cavities in superconducting LINACs for free-electron lasers [85, 86, 87, 88]. The QPR facilitates easier sample preparation and exchange with shorter turnaround times and lower cost compared to the same study conducted with multiple cavities operating at different frequencies. This device also enables the investigation of residual and BCS resistance contributions on the same sample RF surface [14] at applied fields below 120 mT and at two other frequencies: 400 and 800 MHz. The investigation of samples at these two frequencies is of interest as they fall within the operational range of SRF accelerators like the ESS (European Spallation Source) [89], CEPC (Circular Electron Positron Collider) [90], or Large Hadron Collider (LHC) [91]. In addition, the QPR allows for measurements of the frequency f, critical magnetic field H_{c}, and thermal conductivity κ as a function of temperature of the sample to determine material parameters, such as the London penetration depth λ_{L}, critical temperature T_{c}, mean free path ℓ, superconducting gap Δ_0, and residual resistance R_{res}. Finally, the QPR can accommodate a magnet system to determine the efficiency and sensitivity to trapped flux of a sample and study flux pinning effects [92].

4.3 Quadrupole Resonator

The first QPR was developed at CERN (CERN QPR) in 1997 [93]. In the mid-2010s, HZB [94] reported the results of an optimized QPR (HZB QPR). A redesign of the first CERN QPR (CERN QPR II) was announced in 2017 [95] and was presented in 2019 [96]. Building upon these advancements, a collaborative effort involving Universität Hamburg (UHH), DESY, and Universität Rostock [97] has further refined and recently constructed an improved version of the resonator (UHH QPR). A fourth QPR is currently under

development at Jefferson Lab and construction is being carried out at CERN [98]. The following sections review the QPR and the different systems developed and operated at CERN, HZB, and DESY.

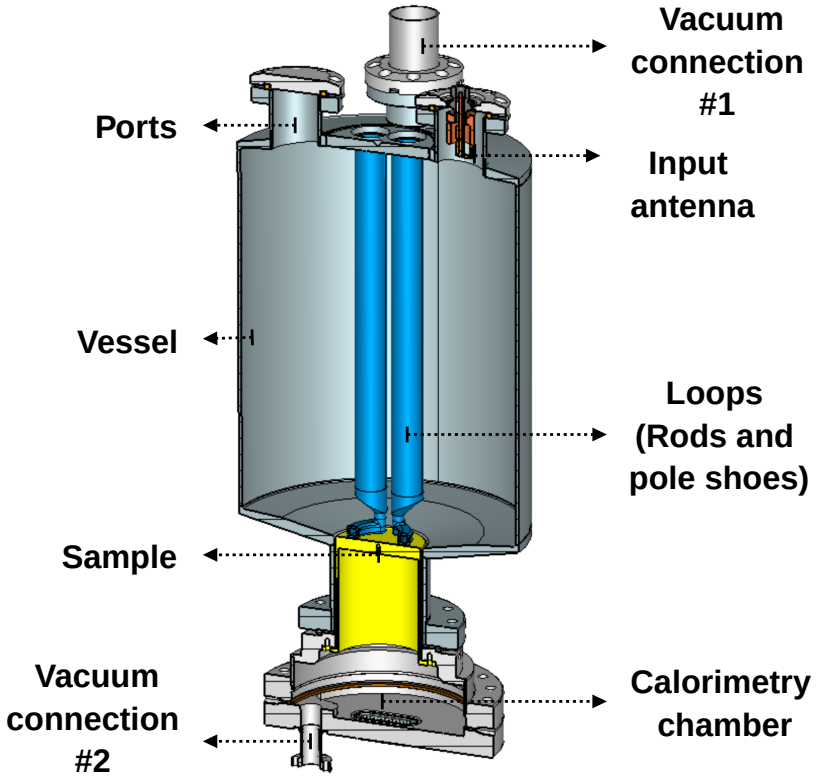

Figure 4.2: Cross-sectional view of the UHH QPR.

All of the existing QPRs have a similar geometry and utilize similar components. The QPR (depicted in Fig. 4.2) consists of a high *RRR* Nb screening vessel and four hollow Nb tubes that form a four-wire transmission line, which is welded to the top part of the vessel. These tubes are enclosed pairwise with Nb hollow half rings, known as "pole shoes", at the bottom of the rods (highlighted in blue). The rods themselves are hollow to allow for the flow of LHe and to prevent them from warming up during operation. The sample (yellow) consists of a disc welded to a sample tube and is mounted to the vessel with a so-called "sample flange", forming a coaxial gap, as shown in Fig. 4.3. Fig. 4.4 provides an example of a QPR sample, where the area exposed to the RF fields is referred to as the "RF surface".

The top of the QPR has four ports used to install input and pick-up loop antennas (positions A and B, respectively, as depicted in Fig. 4.5) and connect it to the vacuum system. The details of this port selection are explained in Sec. 4.7.3. The enclosed volume within the vessel is typically evacuated to a pressure of 10^{-9} mbar. Below the sample, there is a volume that is not exposed to the RF fields and is sealed at the bottom of the sample flange with a sub-D connector feed-through flange. This section forms the calorimetry chamber (see Fig. 4.3), which serves to create thermal isolation of the sample from the rest of the resonator and ensures an adjustable stable sample temperature.

The calorimetry chamber, which is independent from the vessel volume, is evacuated to a pressure between $10^{-7} - 10^{-4}$ mbar. This chamber is equipped with four CERNOX$^{\text{TM}}$ temperature sensors and a DC heater (a 50 Ω resistor). Two of those sensors are positioned on the bottom sample surface, while two more are placed at a lower height on the sample tube. The heater is located at the centre of the sample. These auxiliary devices are employed to carry out a calorimetric measurement technique for determining the sample surface resistance (see Sec. 4.4).

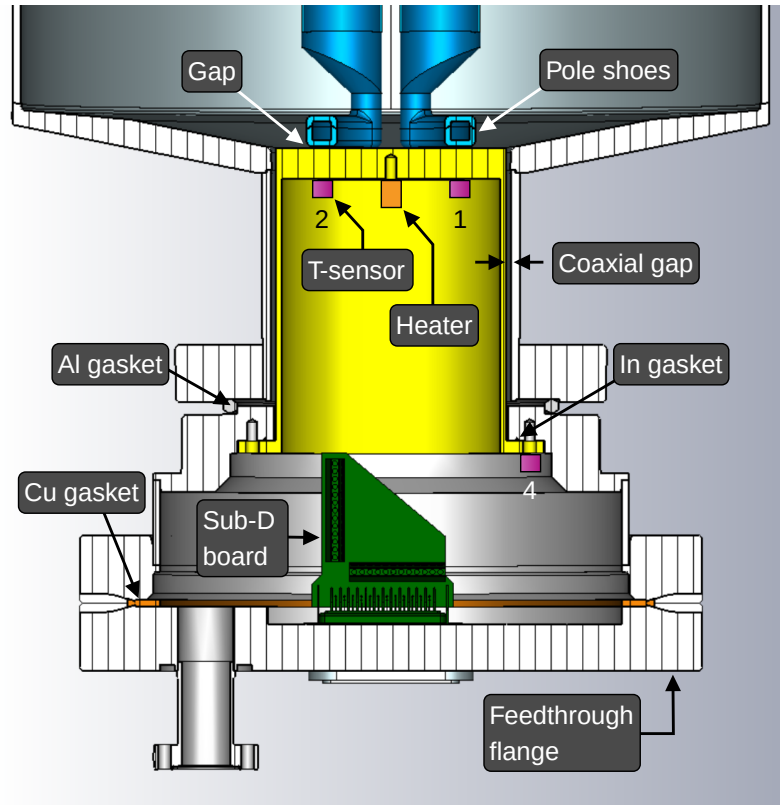

Figure 4.3: Cross-sectional view of the calorimetry chamber.

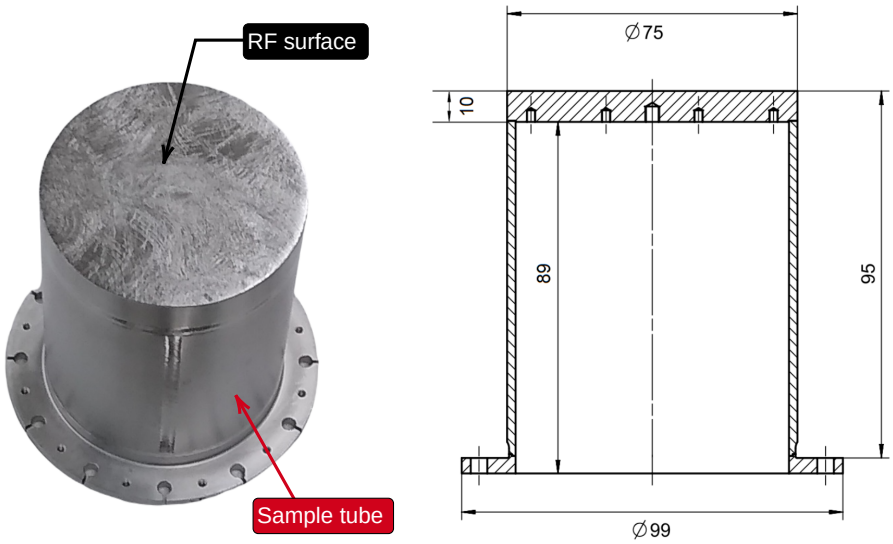

Figure 4.4: Left: Flat cylindrical QPR sample, with the RF surface ideally being the only part exposed to the electromagnetic field. Right: Cross-sectional view of a QPR sample, with units indicated in millimetres.

At a temperature of 2 K, the QPR has an unloaded quality factor Q_0 of about 10^9. However, since the QPR has a higher sensitivity to microphonics, the external quality factor of the input antenna $Q_{\text{ext}}^{\text{inp}}$ is set to approximately 10^7 to achieve a coupling β_{inp} of about 100, which increases the bandwidth of the resonance peak. The phenomenon of microphonics in the QPR is discussed in detail in Sec. 4.6.2. In contrast, the external quality factor of the pick-up antenna $Q_{\text{ext}}^{\text{pro}}$ is fixed between 10^{10} and 10^{11}, resulting

in a coupling β_{pro} in the range of 0.01-0.1. These values allow the phase lock loop (PLL), which is reviewed in Sec. 5.4, to maintain the lock of the resonance peak of the QPR. It is worth mentioning that the coupling of these loop antennas is determined by the scalar product of the magnetic field and the unit vector normal to the loop face. This coupling can be varied by changing the antenna orientation with respect to its symmetry axis.

The QPR operates as follows: RF fields are introduced into the QPR through the input antenna. These fields resonate within the vessel, resulting in the formation of quadrupole-like mode distributions of the electromagnetic field. Thus, a current is induced in the pole shoes, generating an image current on the sample located a fraction of millimetres below. Notably, the RF fields of the quadrupole modes (operational modes) exhibit exponential decay within the coaxial gap up to 2.5 GHz. Therefore, operating below this frequency value ensures that the maximum field density takes place on the sample RF surface, as can be seen in Fig. 4.6.

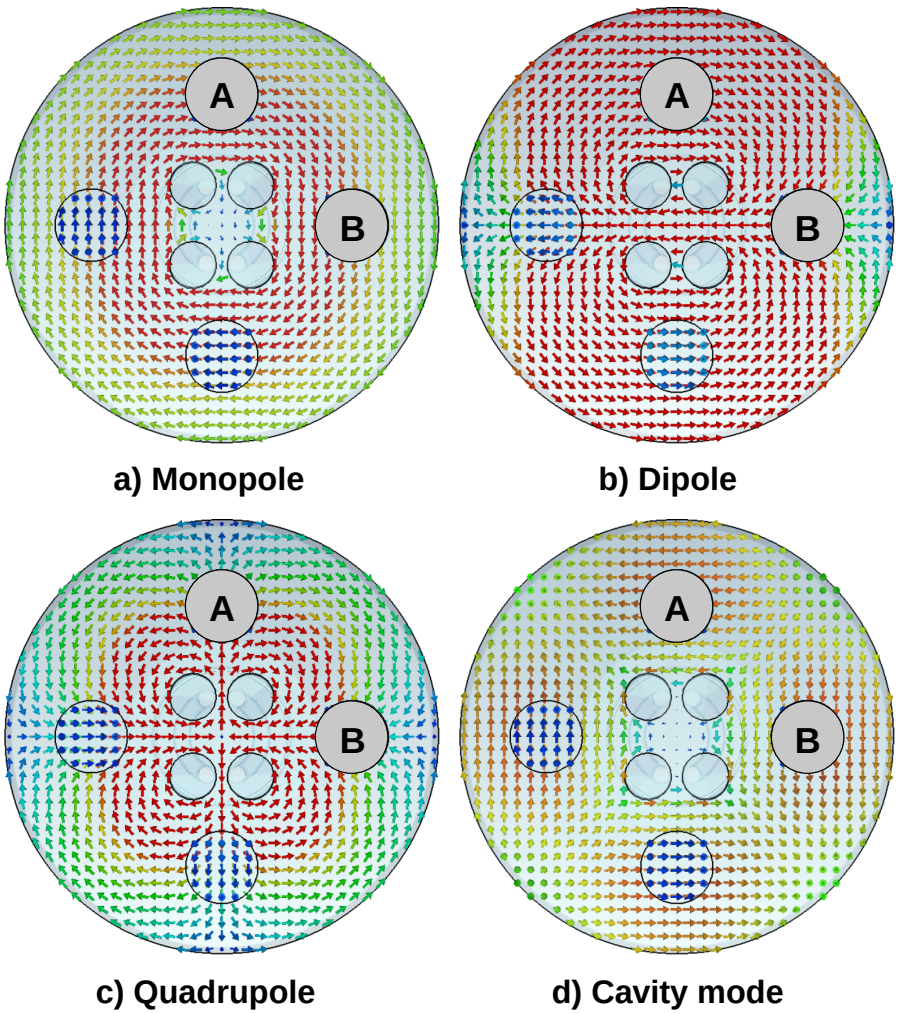

Figure 4.5: RF magnetic field configuration for different resonant mode types within a horizontal plane of the QPR. The input and pick-up antennas are typically installed in port positions A and B, respectively, on top of the resonator.

However, other configurations of the field can get excited within this structure, such as monopole, dipole, and various higher-order modes of the four-wire transmission line, as well as the modes of the vessel, as shown in Fig. 4.5. The modes of the vessel, which exhibit a pill-box cavity TE_{210}-mode field distribution, are referred to as “cavity modes”. It has been demonstrated that dipole modes are inevitably

excited in all QPR devices due to the presence of the pole shoes, which disrupt the symmetry of the QPR [99]. This results in a considerable fraction of dipole modes and even monopole modes propagating through the coaxial gap, reaching the sample flange. Consequently, parasitic fields around the bottom area, especially at the gasket, cause a temperature rise of the sample RF surface. This temperature rise is then included in the determination of the Joule heating, leading to an overestimation of the surface resistance.

To address this issue, HZB has applied a 45 µm Nb coating to the area of the sample flange exposed to the fields, significantly reducing these parasitic losses by 24 nΩ at the first quadrupole mode and at 2 K. In the case of the UHH QPR, a modified geometry of the sample flange has been implemented (refer to Sec. 4.7.1), allowing for the flow of LHe near the region with the highest concentration of RF field, reducing the systematic bias of surface resistance.

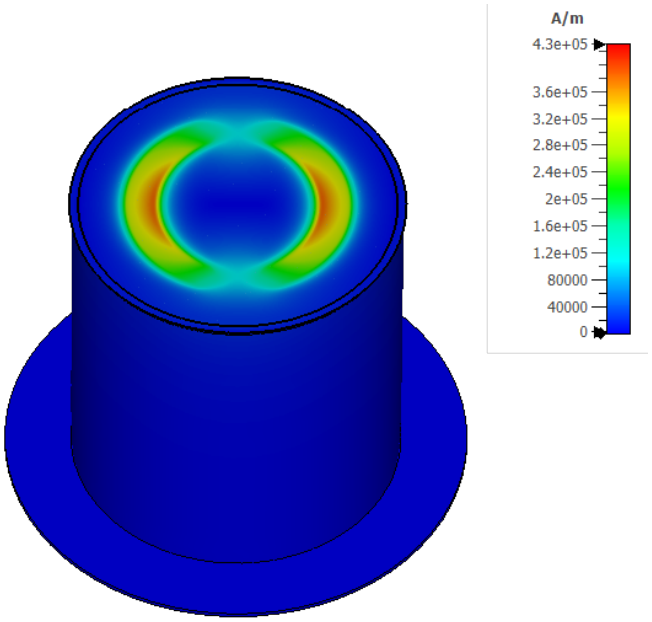

Figure 4.6: Magnitude of the magnetic field $\vec{H}$ focused on the RF surface of the sample, as simulated in CST Microwave Studio®.

4.4 Calorimetric Measurement Principle

The auxiliary devices shown in Fig. 4.3 are interconnected in a closed-loop controller that performs an RF-DC power compensation measurement technique to obtain the surface resistance of the sample. The technique operates as follows: first, the heater increases the sample temperature from the temperature of the LHe bath T_{bath} to a desired higher temperature T_{int}. The required heating power P_{DC1} is recorded. Then, the RF power is turned on, and RF dissipation leads to a further increase in the sample temperature due to Joule heating. The controller decreases the power to compensate for this increase in heat until the temperature of the sample returns to T_{int}. Finally, the new power P_{DC2} is recorded (see Fig. 4.7).

Integrating Eq. 2.39 and assuming a spatially constant R_{s} across the sample, and considering that the power lost in the sample RF surface is given by $P_{\mathrm{c}} = \Delta P_{\mathrm{DC}} = P_{\mathrm{DC1}} - P_{\mathrm{DC2}}$, the process above can be described by Eq. 4.1:

$$R_s = \frac{2 * (P_{DC1} - P_{DC2})}{\int\limits_{\text{sample}} |H|^2 \, dA} = 2c_1\mu_0^2 \frac{\Delta P_{DC}}{B^2_{\text{sample, pk}}}. \tag{4.1}$$

In the expression displayed in Eq. 4.1, $B_{\text{sample, pk}}$ denotes the peak magnetic field on the sample surface, analogous to the figure of merit $B_{pk} = \mu_0 H_{pk}$ defined for cavities in Sec. 2.2.1. The constants c_1 and c_2 are derived from simulations by calculating the expressions:

$$c_1 = \frac{B^2_{\text{sample, pk}}}{\int\limits_{\text{sample}} |B|^2 \, dA} \tag{4.2}$$

$$c_2 = \frac{B^2_{\text{sample, pk}}}{U}. \tag{4.3}$$

The stored energy U is measured using the principle that when the input antenna is over coupled, and the RF power is switched off, all energy decays as reflected power through it. This is explained in more detail in Sec. 5.4. The peak magnetic field on the sample surface can be calculated using the transmitted power P_{tran}:

$$B_{\text{sample, pk}} = \sqrt{c_2 \tau_L P_{\text{tran}}}, \tag{4.4}$$

where $\tau_L$is the decay time constant, as shown in Eq. 3.51.

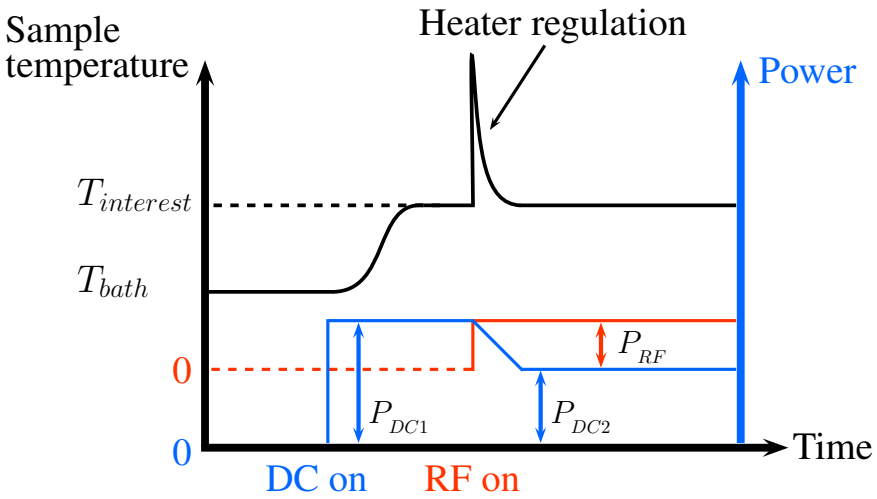

Figure 4.7: Illustration of the calorimetric measurement principle. Diagram taken from [100].

In Sec. 2.2.1, the geometric factor G was introduced as a cavity parameter. However, it is defined in the same manner for the QPR, considering only the losses that occur on the sample surface. Therefore, it is defined for the QPR as:

$$G_{\text{sample}} = R_s Q_{\text{sample}} = 2\omega\mu_0^2 \frac{c_1}{c_2}. \tag{4.5}$$

As observed in the term on the right side of Eq. 4.5, the geometric factor of the sample can also be determined using the constants in Eqs. 4.2 and 4.3.

Overall Surface Resistance Accuracy

The propagation of uncertainties using Eq. 4.1 leads to an expression for the relative error of the surface resistance given by:

$$\left(\frac{\sigma_{R_\mathrm{s}}}{R_\mathrm{s}}\right)^2 = 2\left(\frac{\sigma_{P_\mathrm{DC}}}{\Delta P_\mathrm{DC}}\right)^2 + \frac{1}{2}\left(\frac{\sigma_\mathrm{RF}}{\mathrm{RF}}\right)^2, \tag{4.6}$$

where the second term, RF, corresponds to the relative error of the reflected or transmitted power measurement.

4.5 CERN QPR

The CERN QPR (shown in Fig. 4.8) was developed in 1997 to measure the surface resistance of Nb film samples at 400 MHz. This QPR was reported to operate at 800 MHz and 1200 MHz in 2012 by T. Junginger [100]. This thin-film technology was applied to samples processed as the LHC [91] and LEP (Large Electron–Positron Collider) [101] cavities, which consisted of RF cavities made of Cu with a micrometre thin Nb film sputtered on their inner surface.

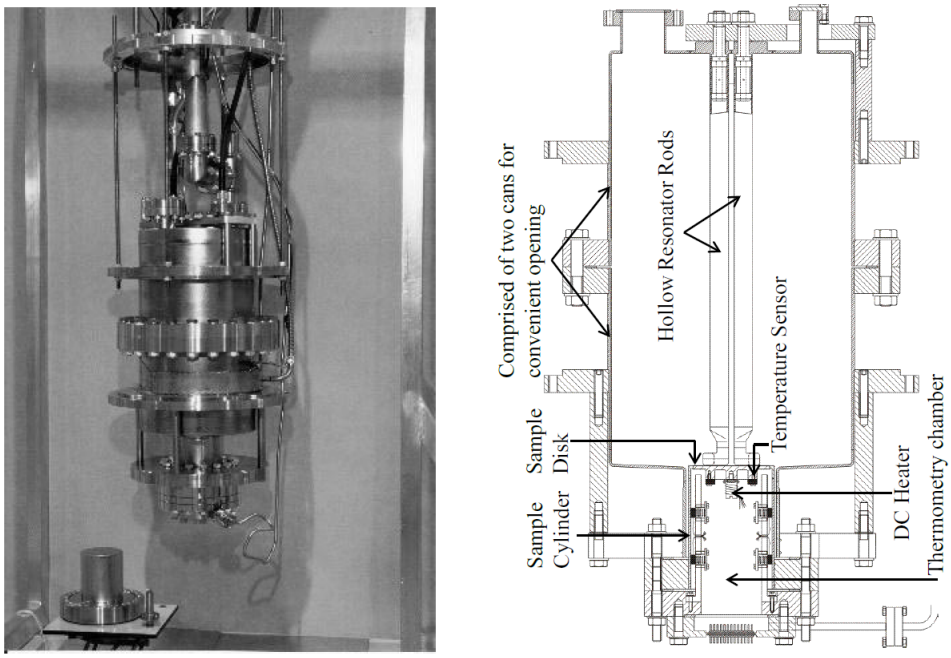

Figure 4.8: Left: Photograph of the QPR, an additional sample, and an antenna. Right: Technical drawing of the device. Images taken from [100].

4.5.1 Overview

Several models were considered for the initial design of the first QPR, with the near-final version resembling the "dipole resonator" shown in Fig. 4.9. The dipole resonator consists of a sample holder (grey) and a Nb resonator (blue). Initially, a current-carrying wire (green) was constructed with the same dimensions as the sample. However, since the sample holder and the resonator form a coaxial line, the dimensions of this line need to be modified to ensure the electromagnetic fields decay exponentially, i.e. are cut-off. The main problem with the dipole resonator was that, given its dimensions, the cut off frequency would be below 1200 MHz. To increase the cut-off frequency by a factor of two, the diameter

of the current-carrying wire was reduced, and a second wire was added, as shown in the "quadrupole resonator" model in Fig. 4.9.

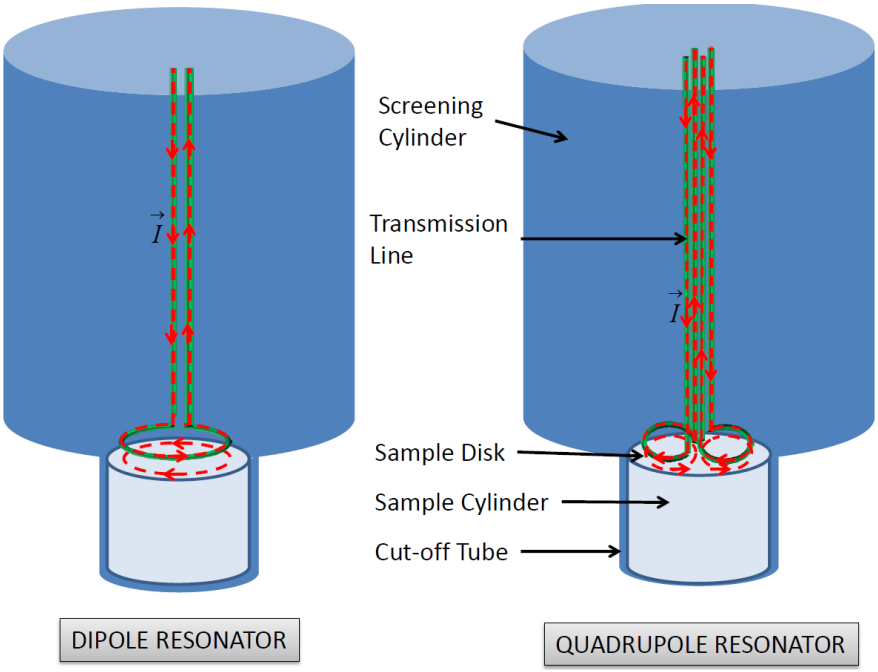

Figure 4.9: Left: Dipole Resonator. Right: Quadrupole Resonator. Figure taken from [100].

The final QPR design consists of a *RRR* 50 Nb screening cylinder with a thickness of 2 mm, a diameter of 210 mm, and a height of 361 mm. The four-wire transmission line consists of four hollow *RRR* 100 Nb tubes, each with a diameter of 16 mm, welded to the top part of the cylinder. At the bottom of the rods, each pair is enclosed with *RRR* 250 Nb hollow half rings with a radius of 25 mm. When RF power is provided to the QPR, a current is induced in these half rings, generating an image current on the sample disc located 1 mm below them. The sample disc has a diameter of 75 mm. This configuration forms a coaxial gap or cut-off tube of 1 mm.

Junginger reported that the QPR operates at the quadrupole modes corresponding to the harmonics of 400 MHz. Fig. 4.10 shows the different modes of the CERN QPR measured and simulated at room temperature in the range of 200 to 1400 MHz. The dipole and quadrupole modes agree within 5% regarding the frequency. The maximum difference of 50 MHz is found between the simulation and measurement for the dipole mode of the highest frequency.

4.5.2 Calorimetric Measurement Setup

The thermometry chamber in the CERN QPR (see Fig. 4.8) includes six calibrated silicon diodes and a heater, i.e. a resistor. Four of those diodes are placed on the bottom sample surface, while the other two are installed at a lower height on the sample holder, and the heater is located at the centre of the sample. To determine the sample surface resistance, the DC power compensation measurement, as discussed in Sec. 4.4, is employed with the use of the auxiliary devices connected in a closed-loop controller. Additionally, the QPR is equipped with a critically coupled input antenna ($\beta = 1$) and an under-coupled pick-up antenna ($\beta \ll 1$) to determine the stored energy.

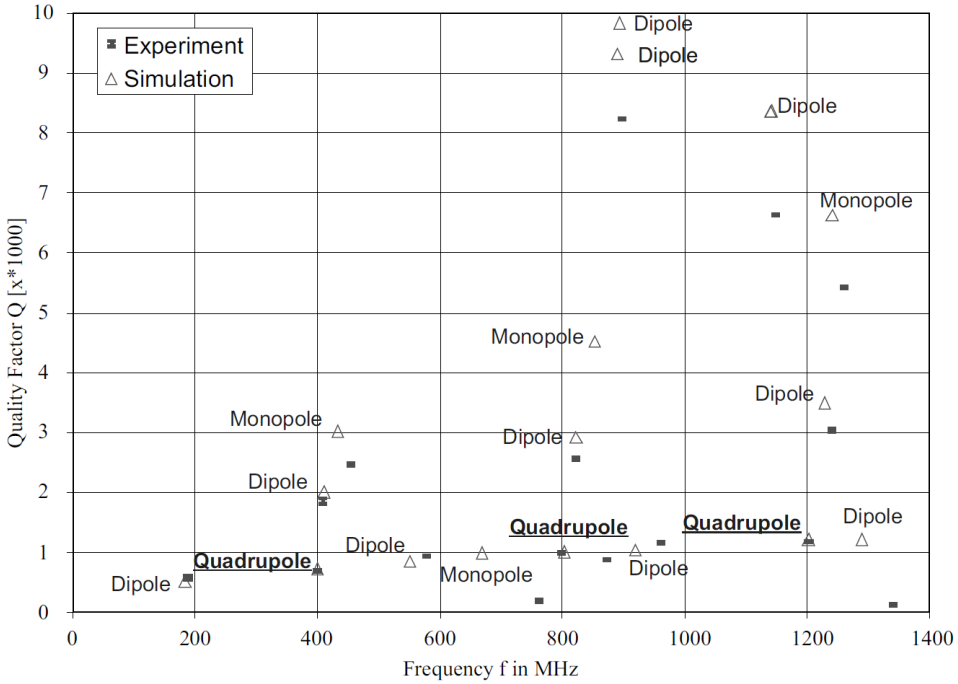

Figure 4.10: Quality factor versus frequency of the CERN QPR at room temperature. Experimental and simulated results are included. Plot taken from [100].

The constants c_1, c_2, and G_{sample} were derived from two different computer programs: CST and HFSS. The results obtained from these two programs are shown in Fig. 4.11. The values of c_1 and c_2 obtained with CST agree within 6% with the constants obtained using HFSS.

f in MHz	c_1 in m^{-2}	c_2 in T^2/J	G_{Sample}
399.6/399.4	1408/1431	0.105/0.104	106.3/109.1
803.1/803.2	1403/1488	0.105/0.105	212.9/225.9
1211.1/1208.8	1569/1540	0.121/0.116	311.6/318.5

Figure 4.11: Field parameters of the CERN QPR calculated with CST Microwave Studio® and Ansoft HFSS®. Table taken from [100].

Pulsed Operation

The QPR operates in continuous wave mode whenever possible. However, at high fields, low temperatures, and/or high surface resistance, the power dissipated may heat up the sample above T_{int}, see Fig. 4.7. In such cases, the RF signal must be modulated in a rectangular pulse. Since the quality factor of the QPR is on the order of 10^9, the decay times are typically a few hundred microseconds, but this depends on the operating mode. For standard operation, pulse periods between 5 ms and 25 ms and duty factors down ranging from 10% and 50% are used for R_{s} measurements. However, for critical RF fields, 1 ms pulses are applied.

4.5.3 Electric and Magnetic Field Configuration

The QPR can expose SRF samples to electric and magnetic fields at the same time. For an applied peak magnetic field of 10 mT, the peak electric field inside the QPR is 0.52, 1.04, and 1.56 MV/m at 400, 800,

and 1200 MHz, respectively. Although the values of these peak electric fields in the QPR are smaller than those inside elliptical cavities, the high field area is relatively larger. In elliptical cavities operating in the TM_{010} mode, the surface electric field is mainly concentrated at the cavity iris. In the QPR, the electric and magnetic fields are concentrated over nearly the same area on the sample RF surface.

However, comparable values of the mean electric and magnetic field ratios ($E_{\text{mean}}/B_{\text{mean}}$) of elliptical cavities and the QPR justify using the latter for studying SRF samples for their application in SRF cavities. With the QPR, the surface resistance is calculated as the magnetic surface resistance. If losses caused by an electric field are to be considered, the surface resistance in this case is defined in a manner similar to Eq. 4.5,

$$G^E_{\text{sample}} = R^E_{\text{s}} Q_{\text{sample}}, \tag{4.7}$$

where the electric geometry factor G^E_{sample} is given by:

$$G^E_{\text{sample}} = \frac{\mu_0}{\epsilon_0} \frac{2\omega U}{\int\limits_{\text{sample}} |E|^2 \, dA}. \tag{4.8}$$

4.5.4 Field Limitations

When the CERN QPR operates at the frequency of 400 MHz, the maximum magnetic field on the sample surface is approximately 60 mT, which corresponds to a maximum field of 70 mT on the pole shoes and a peak electric field of approximately 15 MV/m on the rods. The quench mechanism has been identified as either field emission or multipacting. At this level of electric field strength, field emission was known to occur in cavities that underwent a BCP, making it also possible to occur in the QPR. At 800 MHz, no multipacting was observed, while at 1200 MHz, multipacting occurred at 15 mT. Despite the appearance of multipacting at the last mode, the QPR was processed by turning on the CW RF field below 15 mT for several minutes. However, the resonator quenched at the 60 mT barrier at 400 MHz and could not be processed further.

Operation at 1200 MHz presents challenges as the measured surface resistance has been observed to have values higher than anticipated, exceeding the f^2 scaling (see Eq. 3.35). This issue is attributed to microphonics originating from the excitation of the rods. Therefore, R_{s} measurements at this mode are reliable at low fields, typically up to 15 mT.

4.5.5 Mechanical Vibrations

At high fields, the power transmitted can be strongly modulated in amplitude. The worst case of this modulation occurs when the QPR operates at 1200 MHz. The modulation is 69 Hz when it is operated at 800 Hz and 1200 MHz, but not at 400 MHz, at which it is 278 Hz instead. While the origin of these oscillations could be external sources, such as vacuum pumps, piezoelectric accelerometers mounted outside the cryostat showed peaks only at 75 Hz and at 96 Hz, indicating that the 69 Hz is not excited from outside.

When the QPR was outside the cryostat, the piezoelectric accelerometers were used to measure oscillation of the rods, which showed a peak at 69 Hz. This indicated that the 69 Hz oscillation of the amplitude signal came from the excitation of the rods. To solve this problem, a faster feedback system was used to keep up with the cavity on resonance, including the vibration of the rods.

4.5.6 Accuracy and Resolution

The resolution of surface resistance measurements is limited by the minimum detectable heat. The Lake Shore 340 controller is used to measure the temperature of the sample with a resolution of 0.1 mK, which corresponds to a heating of 2.5 µW at 2 K and 12.5 µW at 8 K for a bulk Nb sample with a $RRR \approx 70$. The minimum surface resistance corresponding to the minimum detectable heating is calculated using Eq. 4.1. For a field of $B_{\mathrm{sample,\,pk}} = 5\,\mathrm{mT}$, the minimum resolvable surface resistance is $R_\mathrm{s} = 0.44\,\mathrm{n\Omega}$ at 2 K and 2.2 nΩ at 8 K. However, the resolution is better for higher magnetic fields, while for materials with higher thermal conductivity, such as Nb films on Cu substrates, it is comparatively worse.

When measuring R_s as a function of temperature at a fixed magnetic field value, statistical error sources need to be considered. For instance, the stability of the LHe bath has a direct influence in the heater power and in the frequency of the QPR. The temperature of the bath at CERN could only be stabilized to approximately ±0.3 mK, which yields an uncertainty three times higher than the minimum detectable temperature. The current source of the heater has a noise of 50 µW+0.001% of its value, resulting in a power of 0.05 nW. The voltmeter used to measure this was operated in the 200 V range, resulting in a resolution of 10 µW, which is well below the current source noise. Only at low fields did the statistical uncertainties described above dominate the overall uncertainty.

4.6 HZB QPR

At HZB, a QPR based on the resonator developed by CERN in 1997 was built and operated. R. Kleindienst [94, 102, 103] reported the first commissioning and optimization process of the HZB QPR, which led to the current design [104].

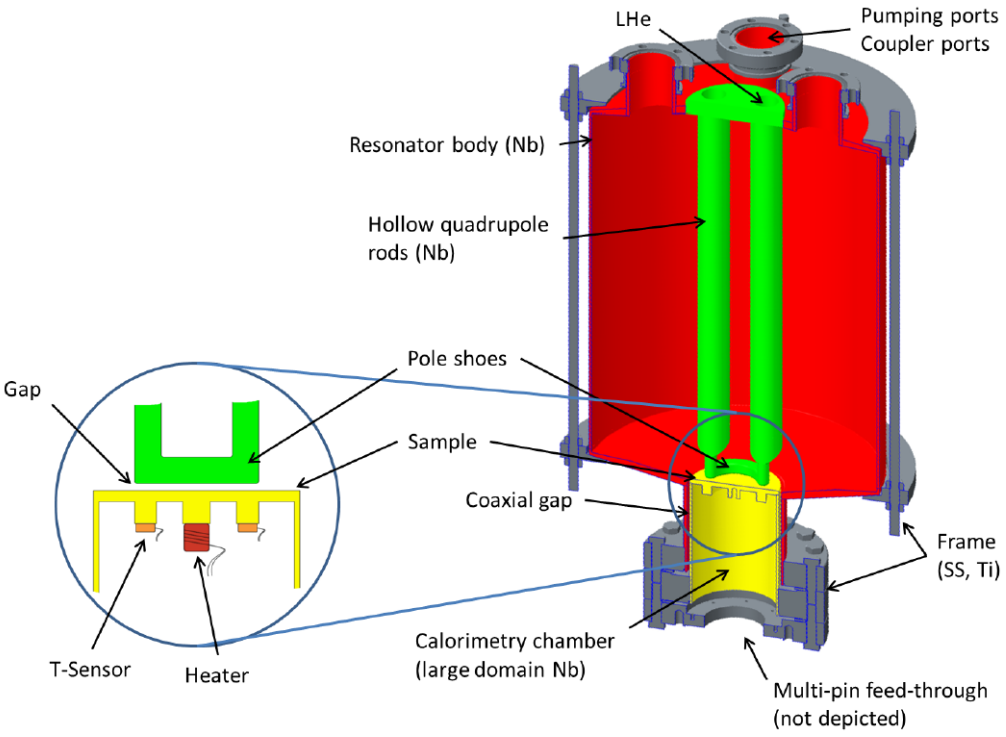

Figure 4.12: Schematic view of the QPR at HZB. Image taken from [104].

4.6.1 Overview

The HZB QPR, shown in Fig. 4.12, has slightly shifted operational resonant frequencies of 415 MHz, 850 MHz, and 1285 MHz, and optimized measurement resolution and maximum achievable field strength. By maintaining a gap of 0.5 mm between the sample surface and pole shoes surface, a field on the sample is achievable that is 89% of the maximum field present on the pole shoes surface.

The QPR is closed at the bottom with a feed-through flange and is evacuated to reach a pressure $p < 5{\cdot}10^{-9}$ mbar at 1.8 K. Inside the calorimetry chamber, the vacuum conditions range from 10^{-7}–10^{-4} mbar, depending on the cleanliness of the gaskets. As explained in Sec. 4.3, to operate the QPR, the external quality factor of the input antenna $Q_{\mathrm{ext}}^{\mathrm{inp}}$ is fixed for strong over coupling ($\beta_{\mathrm{inp}} = 100$). In contrast, the pick-up antenna has an external quality factor $Q_{\mathrm{ext}}^{\mathrm{pro}}$ that satisfies the condition $Q_{\mathrm{ext}}^{\mathrm{inp}} \approx Q_{\mathrm{L}} \ll Q_0 \ll Q_{\mathrm{ext}}^{\mathrm{pro}}$, resulting in an under-coupled antenna ($\beta_{\mathrm{pro}} = 0.01 - 0.1$). To investigate the coupling of the antennas placed in positions "A" and "B", as depicted in Fig. 4.5, simulations were performed using CST.

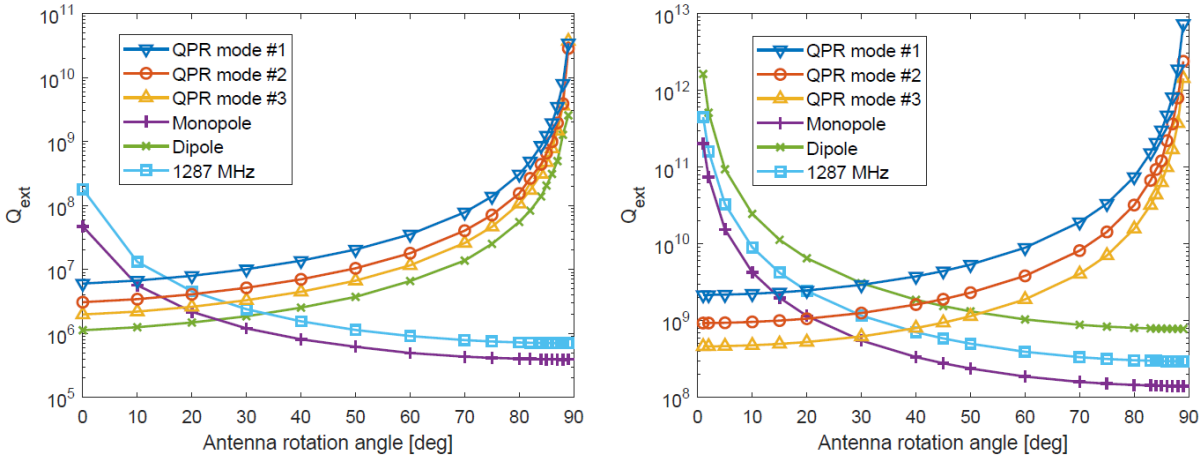

(a) *Initial loop coupler, mounted on port "B".* **(b)** *New dedicated pickup coupler, port "A".*

Figure 4.13: Q_{ext} of initial loop coupler (left) and new dedicated pickup coupler (right) as a function of rotational angle for all three quadrupole modes and the other two modes. Only angles between 0° and 90° are plotted due to rotational symmetry. Both couplers show qualitatively comparable behaviour if installed on the same port location. Note that the ordinates of plots (a) and (b) differ by several orders of magnitude. Figure taken from [104].

The results of these simulations are shown in Fig. 4.13. Due to cylindrical symmetry of the antennas, the curves were calculated only for angles ranging from 0° to 90°. From these curves, it can be observed that the external quality factor of the pick-up antenna needs be oriented at least at 80° to achieve values of $10^{10} - 10^{11}$. Consequently, the development of a new pick-up antenna was necessary to ensure that $Q_{\mathrm{ext}}^{\mathrm{pro}}$ fell in this range in a less-steep region of the coupling curve, making it less sensitive to mechanical tolerances and vibrations.

The current input antenna, which is the same as the old pick-up antenna, and the new dedicated pick-up antenna are shown in Fig. 4.14. It can be seen that the new pick-up antenna (right) does not have a protruding loop, and the open diameter of the coaxial line had to be reduced in order to achieve the desirable external quality factor. The simulations revealed that the Q_{ext} is higher for antennas in port A. This is attributed to the electromagnetic field configuration since port A is closer to the pole shoes where the magnetic field density is higher. Additionally, the external quality factors obtained for antennas in position B are 1.7 times higher than those in A for all quadrupole modes.

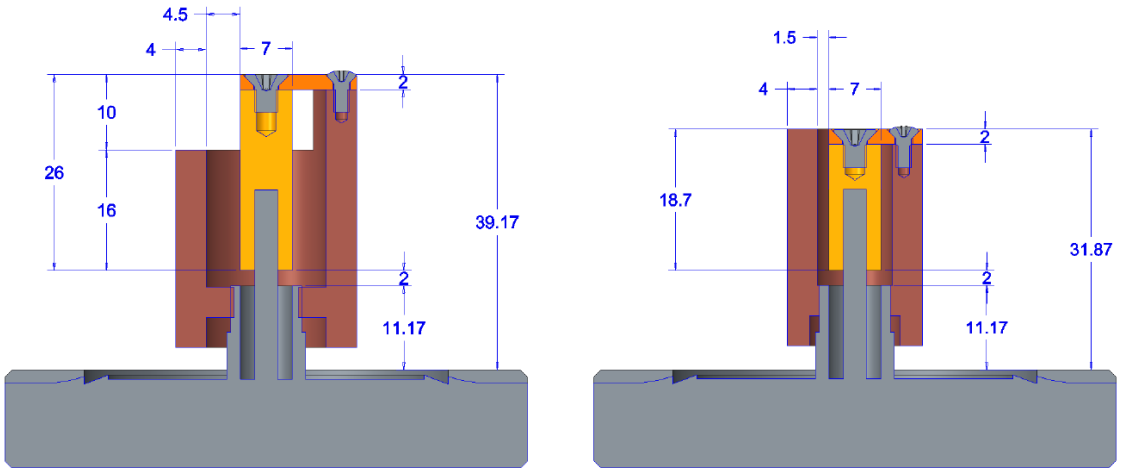

Figure 4.14: Sectional drawings of initial loop coupler (left) and new dedicated pick-up coupler (right). The initial design is still used as an input antenna. Image taken from [104].

4.6.2 Dynamic Detuning

Microphonics refers to unwanted RF noise induced by mechanical vibrations, which can trigger the dynamic detuning of the QPR. During the commissioning phase at HZB, a modulation on top of the driving RF signal was observed when the applied magnetic field exceeded 30 mT (see left side of Fig. 4.15). The corresponding spectrogram of this event (centre) demonstrated that the frequency components of the detuning changed in time, with the main component observed at 100 Hz. Since the mechanical eigenmode of the Nb rods also lies at 100 Hz (right), they were excited, leading to a detuning build up until the data-acquisition system lost the lock of the resonance peak.

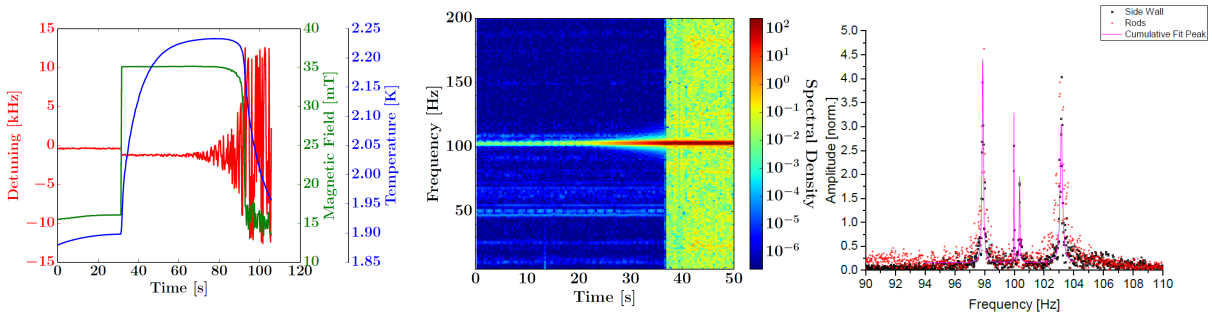

Figure 4.15: Left: Runaway build-up of microphonics with subsequent loss of field due to the finite bandwidth of phased-lock loop. Centre: Normalized fast Fourier transform versus Frequency. Right: Mechanical spectrum of HZB's QPR measured with a geophone. Vibrational eigenmodes at and around 100 Hz are observed. Figures taken from [103].

The RF modulation of the input signal was originated from a 100 Hz component within the electronic devices of the measurement setup. Therefore, in the event shown above, the 100 Hz modulation of the RF signal led to the excitation of the mechanical modes of the rods through Lorentz forces. Subsequently, the problematic devices were replaced, and the coupling of the input antenna was increased to broaden the QPR bandwidth.

4.6.3 Measurement Technique

To determine the surface resistance of SRF samples, the QPR at HZB employs the calorimetric measurement technique established for the QPR at CERN, as discussed in Sec. 4.4. The HZB QPR can achieve

a maximum magnetic field of $B_{\max} = 120\,\mathrm{mT}$, almost double the maximum achieved by the QPR at CERN, thanks to the use of RF power pulses. However, the pulses must satisfy specific requirements for the accurate characterization of the sample: The pulse period must be short enough to ensure the sample remains at a stable temperature. The initial transition part and the tail of the pulse must be shorter than the constant part. Since the rods have a natural frequency of 100 Hz, the pulse repetition rate should not have the same frequency in order to avoid exciting this mechanical mode. For standard operation, a pulse period of 133 ms and duty factors of up to 30% are used.

Kleindienst and S. Keckert determined the dependency of constants c_1 and c_2 on the pole shoes-sample gap, as depicted in Fig. 4.16, which is necessary because the gasket used to mount the sample to the QPR or a sample surface treatment, such as a thin-film coating or a BCP, might modify this distance.

Q1:

$$\begin{aligned} c_1\left[\tfrac{1}{\mathrm{m}^2}\right] &= 1318.5 - 344\,\Delta g + 204\,(\Delta g)^2 \\ c_2\left[\tfrac{\mathrm{T}^2}{\mathrm{J}}\right] &= 0.14827 - 0.1355\,\Delta g + 0.088\,(\Delta g)^2 \\ G\,[\Omega] &= 74.89 + 46.69\,\Delta g \end{aligned}$$

Q2:

$$\begin{aligned} c_1\left[\tfrac{1}{\mathrm{m}^2}\right] &= 1399 - 364\,\Delta g + 209\,(\Delta g)^2 \\ c_2\left[\tfrac{\mathrm{T}^2}{\mathrm{J}}\right] &= 0.1394 - 0.137\,\Delta g + 0.088\,(\Delta g)^2 \\ G\,[\Omega] &= 170.94 + 125\,\Delta g \end{aligned}$$

Q3:

$$\begin{aligned} c_1\left[\tfrac{1}{\mathrm{m}^2}\right] &= 1542.9 - 403\,\Delta g + 229\,(\Delta g)^2 \\ c_2\left[\tfrac{\mathrm{T}^2}{\mathrm{J}}\right] &= 0.1577 - 0.171\,\Delta g + 0.112\,(\Delta g)^2 \\ G\,[\Omega] &= 252.94 + 217.8\,\Delta g \end{aligned}$$

Figure 4.16: RF calibration constants are obtained using polynomial fits with values of g in mm. Figure taken from [104].

In the previous equations, Δg is the deviation from the nominal gap g_0 of 500 µm, and it is given by:

$$\Delta g = \frac{418.3\,\mathrm{MHz} - f_{\mathrm{Q1}}}{0.95} \cdot 100\,\mu\mathrm{m} - 75\,\mu\mathrm{m}. \tag{4.9}$$

Here, f_{Q1} is the frequency of the first quadrupole mode measured at room temperature with the same pressure conditions inside and outside the QPR. Eq. 4.9 was derived from simulations in which the frequency sensitivity to gap changes $df/d\mathrm{gap}$ for Q_1 was determined. This expression serves as a calibration method for calculating the gap.

4.6.4 Identification of the QPR Operational Modes

Although the QPR is designed to operate with the quadrupole mode, it is still possible for other monopole and dipole modes to be accidentally excited due to static or dynamic detuning of the resonator. For instance, a problematic scenario caused by detuning is mode order swapping, as observed at HZB with the neighbouring modes of the third quadrupole mode. These modes are as close as 400 kHz to Q_3. To identify these operational modes, a procedure reported by Keckert involves tracking the frequency of the neighbouring modes in a region around the quadrupole modes during the evacuation and after LHe refill of the cryostat. The modes with the highest sensitivity to ambient pressure $^{df}/_{dp}$ are identified as the quadrupole modes, as shown in Fig. 4.17.

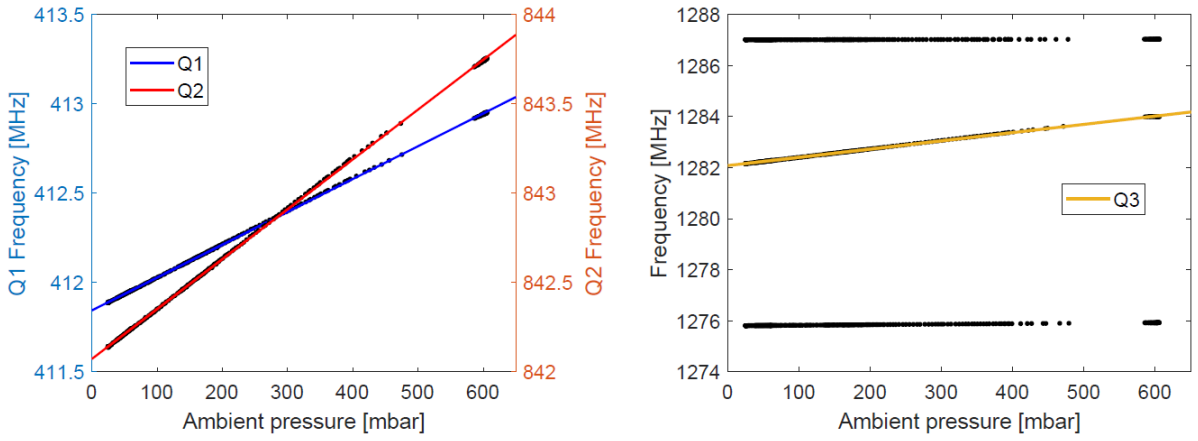

(a) *df/dp of Q1 and Q2* **(b)** *df/dp of Q3 and neighboring modes*

Figure 4.17: Shift of resonant frequencies with ambient pressure. Data is obtained from vector network analyser measurements during pump-down after helium refill. The abscissae contain both gas pressure and hydrostatic pressure acting on the cavity. Linear fits are shown for the quadrupole modes only; the hydrostatic pressure is calculated relative to the cavity centre. Plots taken from [104].

With the frequency data recorded during the cooldown, it was possible to determine the sensitivity of the QPR to ambient pressure $^{df}/_{dp}$ for each mode quantitatively, as shown in Fig. 4.18.

Frequency [MHz]		412 (Q1)	842 (Q2)	1275	1282 (Q3)	1278
$^{df}/_{dp}$	[Hz/mbar]	1836 ± 1	2789 ± 2	204 ± 1	3226 ± 3	40.1 ± 0.2
$^{df}/_{dl}$	[Hz/%]	399.2 ± 0.2	606.3 ± 0.4	44.4 ± 0.2	701.3 ± 0.7	8.72 ± 0.04

Figure 4.18: Sensitivity of resonant frequency to ambient pressure and LHe level for different RF modes. Error bars give statistical fit uncertainty only. Table taken from [104].

The sensitivity of the QPR operational modes is between 180 and 320 times higher than that of TESLA-shaped cavities, which have $^{df}/_{dp} = 10\,\mathrm{Hz/mbar}$. However, the values reported in Fig. 4.18 correspond to the conditions obtained during the assembly of the QPR for a specific test. Therefore, it is necessary to measure $^{df}/_{dp}$ for every run for data correction.

4.6.5 Resolution, Accuracy, and Precision

Resolution of the Surface Resistance

At low temperatures, the resolution of the surface resistance is limited by the heater power change resulting from the LHe stability. At 2 K, this power corresponds to 12 µW, which yields $R_\mathrm{s} = 0.5\,\mathrm{n\Omega}$ at $B_{\mathrm{sample,\,pk}} = 10\,\mathrm{mT}$ for mode Q_1. The best resolution is obtained at the magnetic quench limit of $B_{\mathrm{sample,\,pk}} = 120\,\mathrm{mT}$, giving $R_\mathrm{s} = 0.003\,\mathrm{n\Omega}$. For higher quadrupole modes, the minimum resolvable surface resistance increases by about 20%, as the constants c_1 and c_2 increase with respect to the increasing frequency.

However, the resolution of the surface resistance depends on the properties of the sample being investigated. In cases where the sample has a low thermal conductivity, the heat transfer between the sample and the helium becomes less efficient. As a result, the required heater power to compensate for temperature fluctuations of the helium bath is reduced. In such cases, the resolution is ultimately limited by the temperature sensor resolution of 0.1 mK.

Measurement Bias Due to Parasitic Losses

Kleindienst reported that the lowest surface resistance measured with the QPR was 8 nΩ at 2.25 K and Q_1 on a *RRR* 300 Nb sample. However, consistent results could not be obtained for Q_3, possibly due to RF heating of the coaxial gap and the stainless steel (SS304) sample flange. In Sec. 4.3, it was explained that RF losses in this region can increase the temperature of the sample RF surface, leading to the overestimation of R_s. Simulations in his work predicted that RF losses at this flange can cause a systematic bias of 4.6 nΩ at Q_1 [103]. To investigate the effect of this unwanted RF-induced heating on the RF surface, Keckert analysed the field of the quadrupole modes on three areas of the sample chamber: sample surface, the coaxial gap wall, and the sample flange. Simulations in CST were conducted to determine the damping coefficient δ, defined as:

$$\delta_i = \frac{\int\limits_{\text{sample}} |H|^2 \, dA}{\int\limits_{i} |H|^2 \, dA}, \tag{4.10}$$

where index i refers to the integral of the H-field being performed on the coaxial gap wall and on the surface of the sample flange. The dissipated power P_i in each region is given by:

$$P_i = \frac{1}{\delta_i} \frac{R_i}{R_{\text{sample}}} P_{\text{sample}}, \tag{4.11}$$

where R_i is the surface resistance in the selected area, and R_{sample} and P_{sample} are the surface resistance and power lost in the sample surface, respectively. The damping coefficient values for the quadrupole modes are displayed in Fig. 4.19. In these results, the surface resistance of the stainless steel flange $R_{\text{s, SS304}}$ is calculated using Eq. 2.40 with $\sigma_N = 2{\cdot}10^6\ 1/(\Omega\text{m})$.

	Q1 (433 MHz)	Q2 (866 MHz)	Q3 (1315 MHz)
δ_{coax}	207.7	212.1	217.0
δ_{flange}	$1.4 \cdot 10^6$	$1.0 \cdot 10^6$	$5.7 \cdot 10^5$
$R_{\text{S, SS304}}$	29 mΩ	41 mΩ	51 mΩ
γ_{flange}	21.2 nΩ	40.7 nΩ	89.0 nΩ

Figure 4.19: RF parameters describing the additional losses on coaxial wall and bottom flange. The surface resistance of stainless steel flange $R_{\text{s, SS304}}$ is calculated using the normal skin effect with $\sigma_N = 2{\cdot}10^6\ 1/(\Omega\text{m})$ at cryogenic temperatures. Table taken from [104].

An analysis, considering R_{sample} calculated with the BCS theory for Nb 300 and $R_{\text{res}} = 10\,\text{n}\Omega$, revealed that the dissipated power in the coaxial gap wall P_{coax}, when compared with P_{flange}, can be neglected: R_{coax} is calculated in a similar manner to R_{sample}, but with $R_{\text{res}} = 100\,\text{n}\Omega$. The ratio of the power lost in the sample and coaxial gap is $P_{\text{coax}}/P_{\text{sample}} = 5\%$ at low temperatures, and 0.5% as the temperature approaches T_c. Similarly, $P_{\text{flange}}/P_{\text{sample}} = 500\%$ at approximately 2 K and 5% close to T_c.

However, this study needed additional simulations in COMSOL Multiphysics® to determine the temperature distribution on the sample induced by the heating from the heater and RF power and understand their contribution to R_s. The results showed a systematic error above 10 nΩ at low temperatures and Q_1, attributed to the power dissipation at the sample flange, contrasting with the observed error in measurement results [99]. Consequently, a decision was made to coat the sealing surface area of the sample flange with 45 µm Nb, leading to a reduction of the measured $R_s(T)$ by 24 nΩ at the first quadrupole mode. This improvement currently allows for measurements of R_{res} smaller than 5 nΩ at 2 K and Q_1.

RF Measurement Accuracy and Overall Surface Resistance Accuracy

The relative error of the surface resistance is expressed in Eq. 4.6. For the R_s measurements with the HZB QPR, the relative error of the transmitted power P_{tran} and heater power difference ΔP_{DC} are assumed to have the following values:

$$\frac{\sigma_{RF}}{RF} = 9.2\% \tag{4.12}$$

$$\frac{\sigma_{P_{DC}}}{\Delta P_{DC}} \leq \frac{1}{2}\frac{\sigma_{RF}}{RF}. \tag{4.13}$$

Eq. 4.13 establishes a lower boundary on ΔP_{DC} and, consequently, the minimum RF field required for a R_s measurement.

4.7 UHH QPR

In this section, the unique features of the UHH QPR design are discussed.

4.7.1 Overview

The UHH QPR [105, 106], depicted in Fig. 4.20, an optimized version of the successful HZB QPR, was fabricated at Zanon [107]. The QPR vessel, rods, and pole shoes are made of Nb (RRR=300). The port flanges and the bottom flange, where the sample is attached, are fabricated from an alloy composed of 45% Nb and 55% Ti (NbTi55). The design (nominal) gap between the surface of the pole shoes and the sample RF surface is (0.50 ± 0.07) mm. Samples investigated with the UHH QPR consist of a disc with a diameter of 75 mm and a thickness of 10 mm, welded to a tube with a height of 85 mm and a thickness of 2 mm.

The vessel volume is evacuated at room temperature, aiming to achieve a pressure at low temperatures better than 10^{-9} mbar[1]. The vacuum connection is made through the "snorkel" pipe at one of the top ports, as shown in Fig. 4.20. The input and pick-up antennas are installed in two different ports, as illustrated in Fig. 4.5, in an ISO 4 clean room. The fourth port has no measurement instrument, and hence a blind flange is installed to ensure the leak tightness condition. The frame is used to install the QPR in a dedicated insert, which can also support up to three additional 1.3 GHz single-cell cavities.

The calorimetry chamber of the UHH QPR differs from those in the CERN and HZB QPRs. At DESY, the calorimetry chamber provides more space for the circuit of the auxiliary devices, such as the board, temperature sensors, heater, and coils (in the future), as seen in Fig. 4.3. Inside the calorimetry chamber, shown in Fig. 4.21, four temperature sensors (T-sensors) and a heater[2] are typically positioned as follows: one T-sensor is placed on the bottom surface of the sample at the centre of each pole shoe (T_1 and T_2); another T-sensor is positioned at the same radius but at a 90° angle with respect to any of the previous ones (T_3); one T-sensor is positioned near the radius of the sensor 1 but at the height of the indium wire, which means that it is installed on the barrels at the bottom of the sample tube (T_4); and the heater is placed at the centre of the sample.

T-sensors 1 and 2 are located below the centre of each pole shoe because at this region, but on the top surface of the sample, the maximum concentration of magnetic field occurs, as depicted in Fig. 4.6. This region is also where the maximum temperature change occurs. T-sensor 1 is used for all measurements.

[1] It is also required to have a leak rate better than 10^{-11} mbar·L/s.

[2] The heater consists of a Cu body with a resistance of 50 Ω (including the pin connection cables).

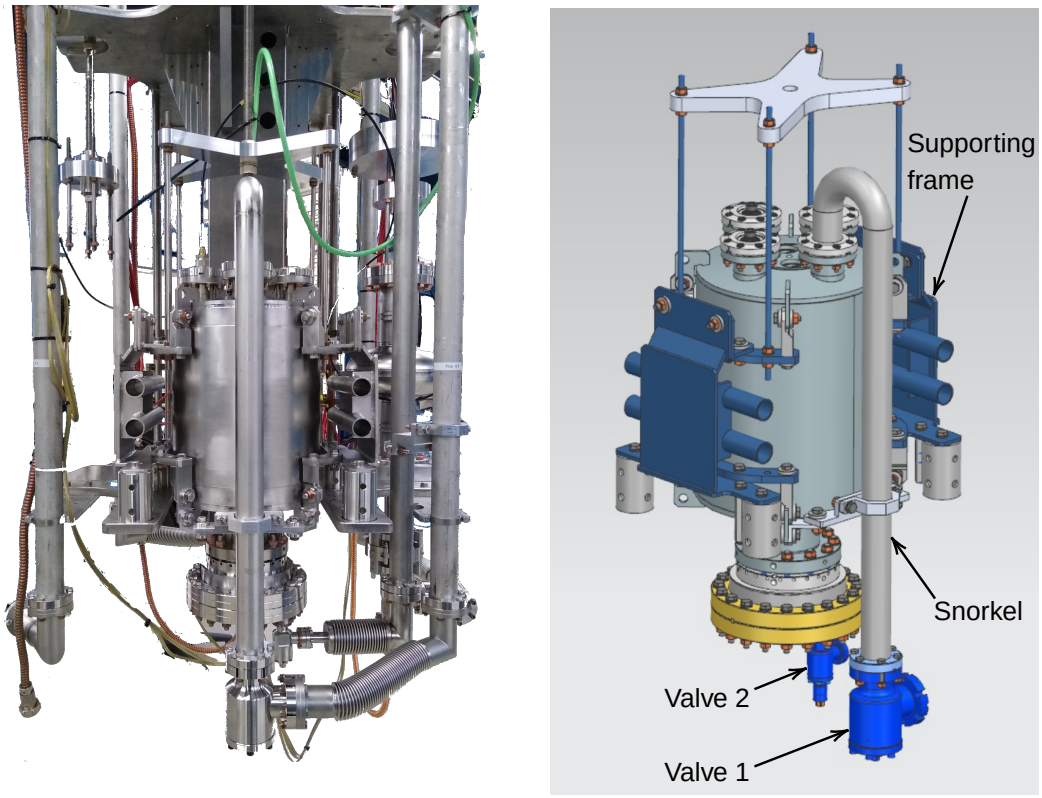

Figure 4.20: Left: UHH QPR installed in its dedicated insert. Right: Schematic view of the QPR with frame.

T-sensors 2, 3, and 4 are used for control purposes. In addition, T-sensor 4 is used to determine the thermal conductivity of samples. The heater is located at the centre to achieve a homogenous temperature on the sample during operation. Valve 2, shown in Fig. 4.20, is connected to the feed-through flange and used to evacuate the calorimetry chamber, targeting a pressure between $10^{-7} - 10^{-4}$ mbar.

Changes in the design were made due to material availability, such as an increase of the antenna ports' radial position by 2 mm and enlargement of their size from 36 mm to 40 mm. The inner diameter of the outer wall of the coaxial or cut-off tube was reduced by 0.5 mm, which decreased the coaxial gap from 2 mm to 1.5 mm. These changes did not impact the performance of the QPR. Changes in design also led to operational improvements. In Sec. 4.6.2, it was mentioned that at HZB, the rods have a mechanical resonance frequency of 100 Hz, which is why the RF pulse repetition rate should not have the same frequency to prevent their excitation or have a 100 Hz signal mixed to the carrier frequency. To avoid this issue in the UHH QPR, a rectangular bar made of high purity Nb was welded to the hollow section of the rods to enhance their stiffness. Consequently, this shifts the mechanical resonances of the rods away from the frequency of 100 Hz, as it is the first harmonic of the European power grid operating at 50 Hz. This modification is shown in Fig. 4.22. The results of these changes are discussed in Sec. 5.2.3.

To address the issue of the parasitic dipole field, as discussed in Sec. 4.3, the sample flange design was optimized by adding cooling channels around the Al gasket area (see Fig. 4.23). This modification effectively mitigates the RF surface heating caused by the dipole mode, leading to a significant reduction of the adverse effects of dipole modes on the QPR performance.

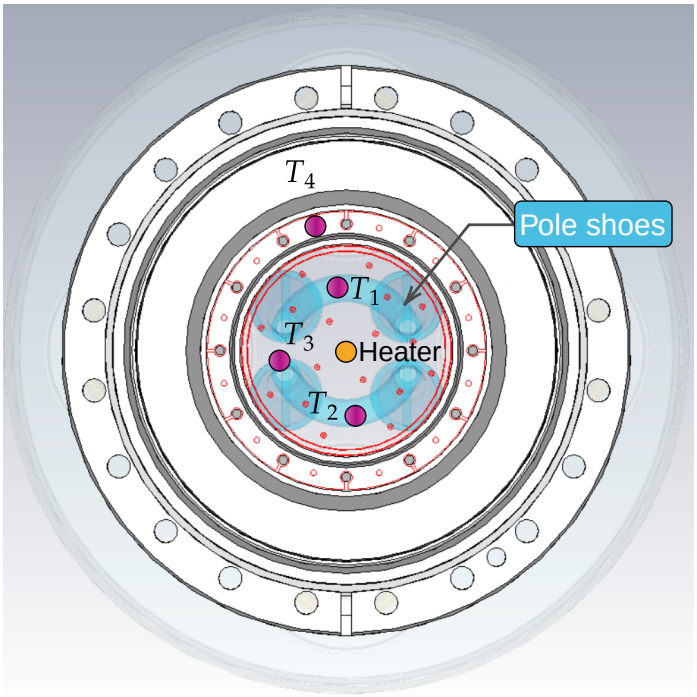

Figure 4.21: Position of temperature sensors and heater below the sample inside the calorimetry chamber.

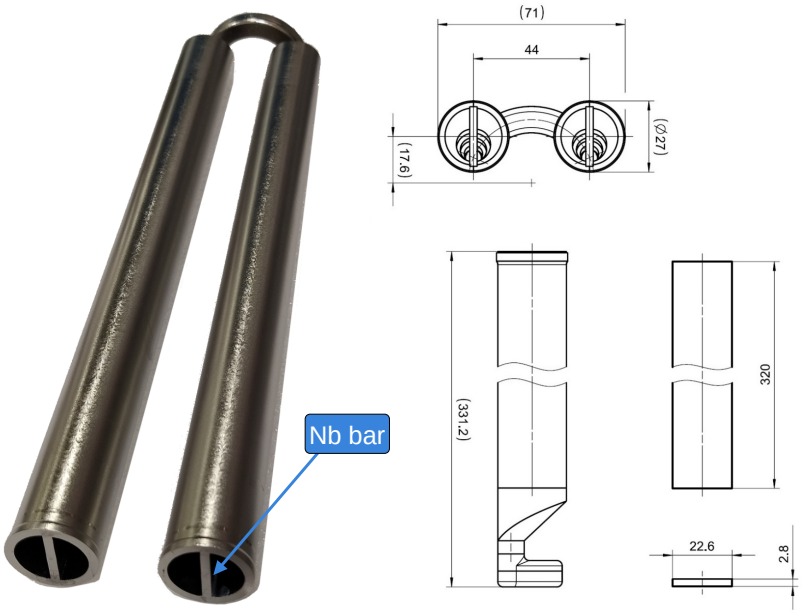

Figure 4.22: Left: A pair of rods with a pole shoe and an added Nb bar inside each of them to increase their rigidity. Right: Diagram of the rods with pole shoes; dimensions are indicated in millimetres.

4.7.2 QPR Modes

In order to avoid incorrect mode excitation, identifying the resonant modes of the QPR is crucial. Mode order swapping has been observed at HZB when the QPR is cooled down to 1.8 K, leading to ambiguity errors [104]. A model with nominal dimensions and a tetrahedral mesh was created to run simulations in CST to obtain the eigenmodes of the resonator and to check their frequency difference between neigh-

bouring modes. The spectrum has been obtained in the frequency range of 400 MHz to 1400 MHZ and at room temperature, where 20 modes were identified as monopoles, dipoles, quadrupoles, and cavity modes. These modes are plotted as a function of their Q_0, as shown in Fig. 4.24. These modes are compared to experimental results in Sec. 5.2.5.

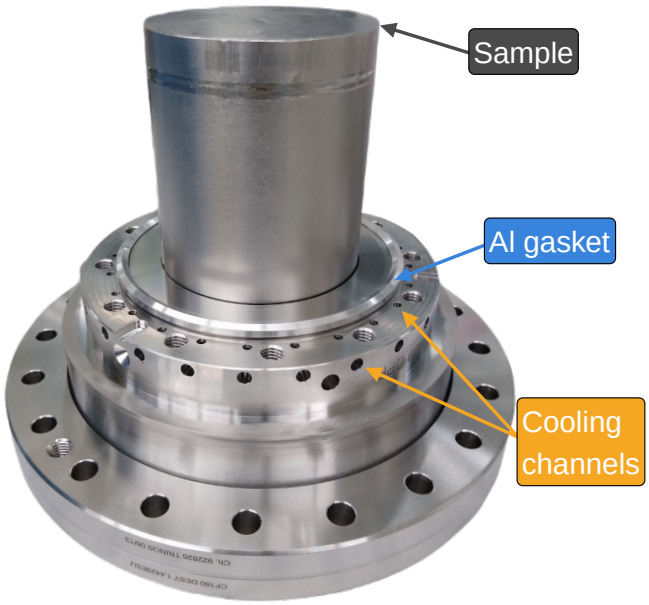

Figure 4.23: The sample flange incorporates cooling channels to effectively reduce the parasitic heat generated by field propagation within the coaxial gap.

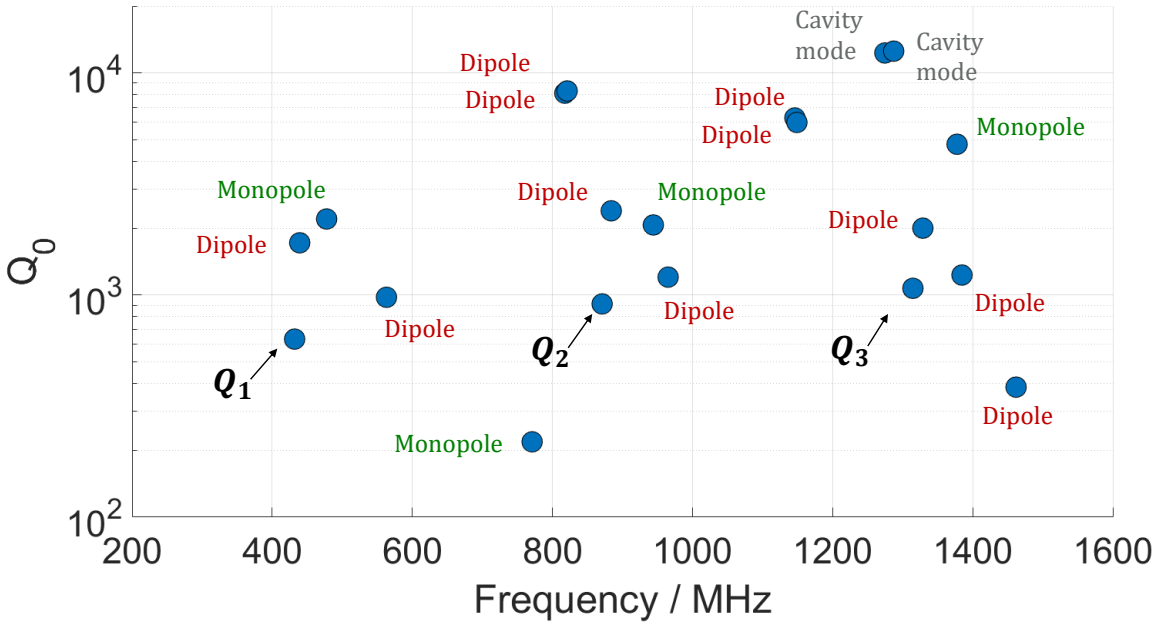

Figure 4.24: Quality factor versus frequency of the modes of the QPR at room temperature. Simulated values were calculated in CST Microwave Studio®.

The mode spectrum of the UHH QPR is similar to that of the CERN QPR, as depicted in Fig. 4.10. While the distribution of the modes across the frequency range is similar, a significant frequency shift can be observed between the two spectra. Moreover, the quality factor values of the monopoles and dipoles

differ, and the two cavity modes present in the UHH QPR spectrum around 820 MHz are absent in the CERN QPR. Using this CST model, three quadrupole modes were identified in the previous frequency range, as well as their quality factor Q_0 at 2 K, with the values[3] as shown in Tab. 4.1.

Table 4.1: Simulated intrinsic quality factors Q_0 and field parameters, c_1, c_2, and G, of the three quadrupole modes at 2 K. The results were calculated through simulations using CST Microwave Studio®.

Mode	f / MHz	Q_0 (2 K)	c_1 / $1/\mathrm{m}^2$	c_2 / T^2/J	G / Ω
Q_1	431.99	$1.01{\cdot}10^9$	1453.03	0.2313	53.81
Q_2	870.99	$1.45{\cdot}10^9$	1545.66	0.2430	109.67
Q_3	1314.69	$1.70{\cdot}10^9$	1709.48	0.3007	147.95

Simulation results confirm that in the quadrupole modes, the maximum field density occurs on the sample surface. For example, Fig. 4.25 shows the absolute value of the magnetic field of Q_1 on the sample surface for a stored energy of 1 J, where the ratio of the maximum H-field on the pole shoes and sample surfaces is

$$\frac{H_{\text{sample, pk}}}{H_{\text{pole shoes, pk}}} = \frac{3.85 \cdot 10^3\ \mathrm{A/m}}{4.29 \cdot 10^3\ \mathrm{A/m}} \cdot 100\% = 89.70\%. \tag{4.14}$$

Furthermore, the ratio of the peak magnetic field on the sample to the store energy inside the QPR is given by:

$$\frac{B_{\text{sample, pk}}}{\sqrt{U}} = \frac{484\ \mathrm{mT}}{\sqrt{1\ \mathrm{J}}}. \tag{4.15}$$

which is close to the ratio of HZB QPR of $440\ \mathrm{mT}/\sqrt{1\ \mathrm{J}}$ [103], as expected due to the design similarities.

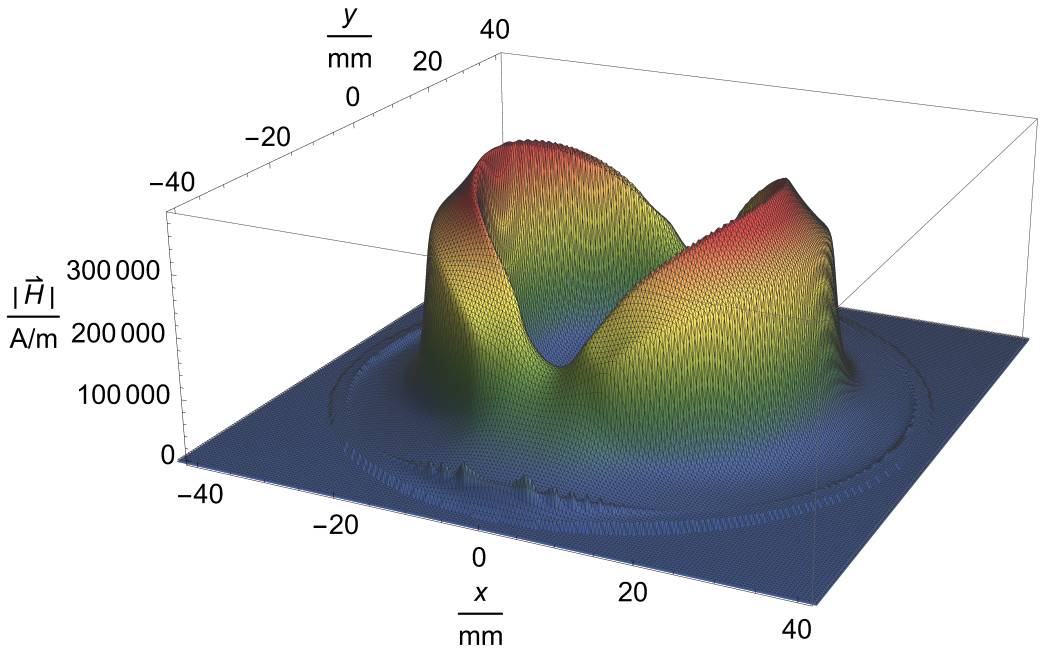

Figure 4.25: Calculated absolute magnitude of the $\vec{H}$-field on the sample for a stored energy of 1 J with $5 \cdot 10^6$ tetrahedrons.

[3]Selecting this temperature directly in CST is not possible. Hence, to calculate the quality factor at 2 K, the material is modeled in the simulations as a perfect electric conductor with an electrical conductivity of $10^{20}\ 1/(\Omega\mathrm{m})$.

For the determination of constants c_1 and c_2 in CST, a model consisting of a global mesh of one million tetrahedrons covering the entire structure was employed. Additionally, a small volume was incorporated to fill the pole-shoes-sample gap with a finer mesh, using an overall mesh with five million tetrahedrons. The QPR constants of the nominal design determined for the quadrupole modes are shown in Tab. 4.1.

4.7.3 Simulation Study of the Antennas

The input and pick-up antennas of the UHH QPR were also constructed based on the latest antenna designs used at HZB, as shown in Sec. 4.6.1. Both antennas are of the square loop type, which couples the magnetic field to the resonator and probes it, respectively [108]. These antennas, shown in Fig. 4.26, have a similar design, with the difference being the shorter loop length of the pick-up antenna.

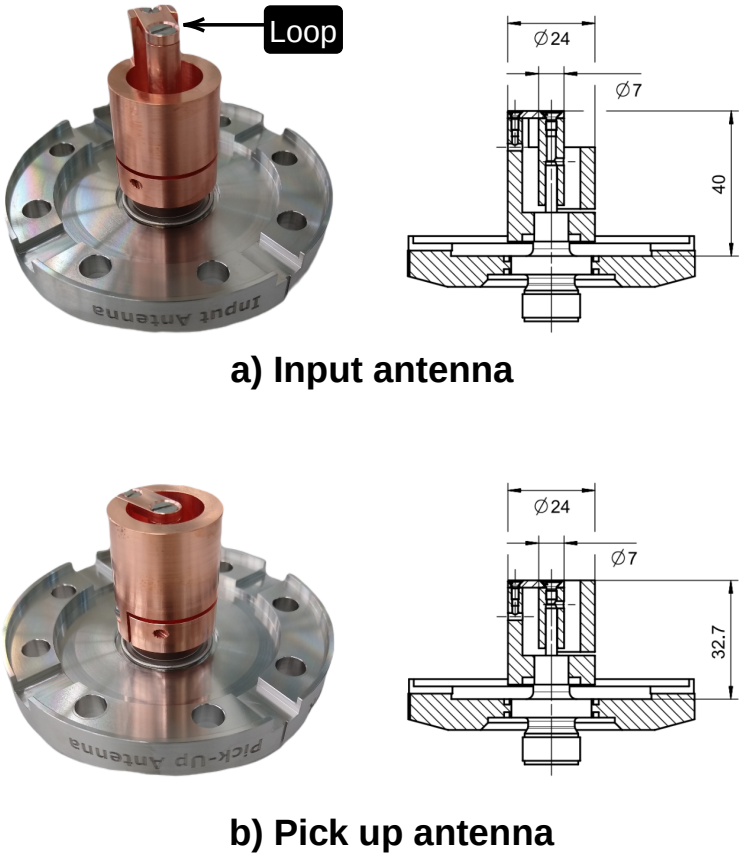

Figure 4.26: a) Input and b) pick-up antennas are designed to control the coupling by adjusting the angle between the loop area and the field orientation.

The behaviour of the antennas was studied in CST in order to determine their external quality factor Q_{ext}. First, the differences in port position are examined. Fig. 4.27 shows the top view of the magnetic field of mode Q_1 at the ports, where the input and pick-up antennas are installed in position A and B, respectively. The orientation of their loop is also important as the value of Q_{ext} shows a dependency on it. However, for the investigations of port position, the areas defined by the antenna loops were oriented perpendicular to the magnetic field. This orientation is known as the “zero-degree” position and is only valid for the field distribution of the quadrupole modes.

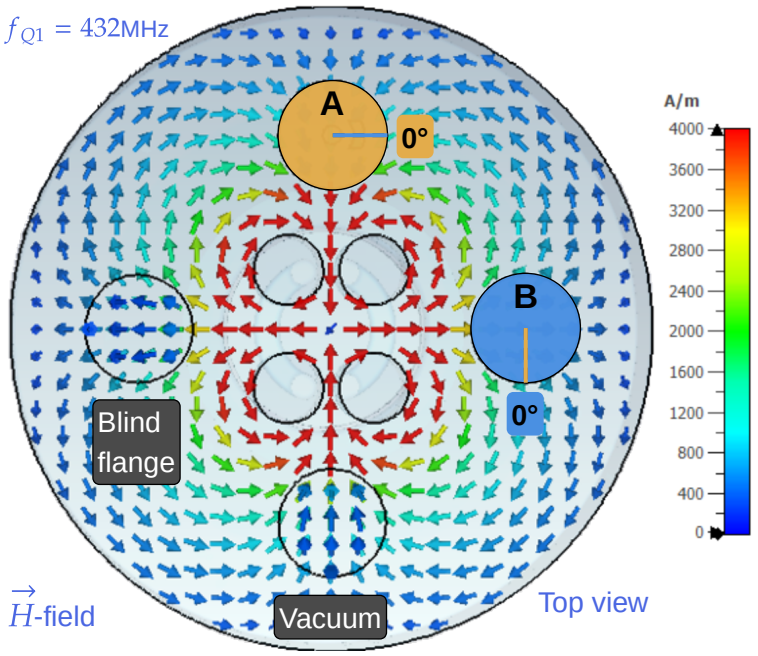

Figure 4.27: Cutting plane of the QPR normal to the z-axis at the height of the ports, showing the field distribution of the first quadrupole mode Q_1. The input antenna loop area in port position A and the probe oriented in B were fixed at 0°.

Table 4.2: Comparison of the external quality factors Q_{ext} for the different configuration of the antennas in port positions A and B, calculated using CST Microwave Studio®.

Antenna	Port pos.	Angle / deg	Q_{ext}
Input	A	0	$5.77{\cdot}10^6$
Input	B	0	$9.34{\cdot}10^6$
Pick-up	A	0	$0.93{\cdot}10^8$
Pick-up	B	0	$1.53{\cdot}10^8$

The obtained results for Q_{ext} in the previous configuration and in the reverse case, where the input and pick-up antennas are installed in position B and A, respectively, are summarized in Tab. 4.2. From these results, it is observed that the external quality factor of both antennas satisfies the following expressions:

$$Q_{\text{ext}}^{\text{inp}}(B) = 1.62 \cdot Q_{\text{ext}}^{\text{inp}}(A) \tag{4.16}$$

$$Q_{\text{ext}}^{\text{pro}}(B) = 1.65 \cdot Q_{\text{ext}}^{\text{pro}}(A)\,. \tag{4.17}$$

These findings demonstrate that the Q_{ext} of any antenna at position B is approximately 1.6 times higher compared to the same in A. These values are close to the reported results for the HZB QPR of 1.7, as expected. Considering that designs of both QPRs are similar, the slight discrepancy may be attributed to the fact that the ports of the UHH QPR are located at a radius from the centre 2 mm larger compared to the resonator at HZB. To have a higher value of Q_{ext} for the pick-up antenna, the final position of the antennas is chosen as follows: the pick-up antenna is placed at B and the input antenna at A.

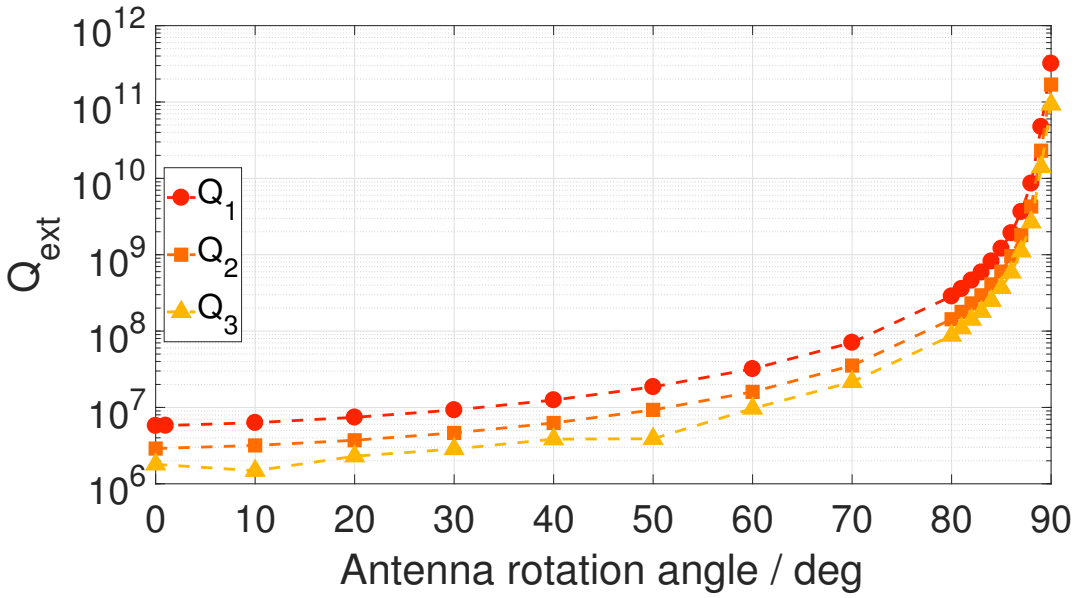

Figure 4.28: External quality factors Q_{ext} of the input antenna in port position A for all quadrupole modes.

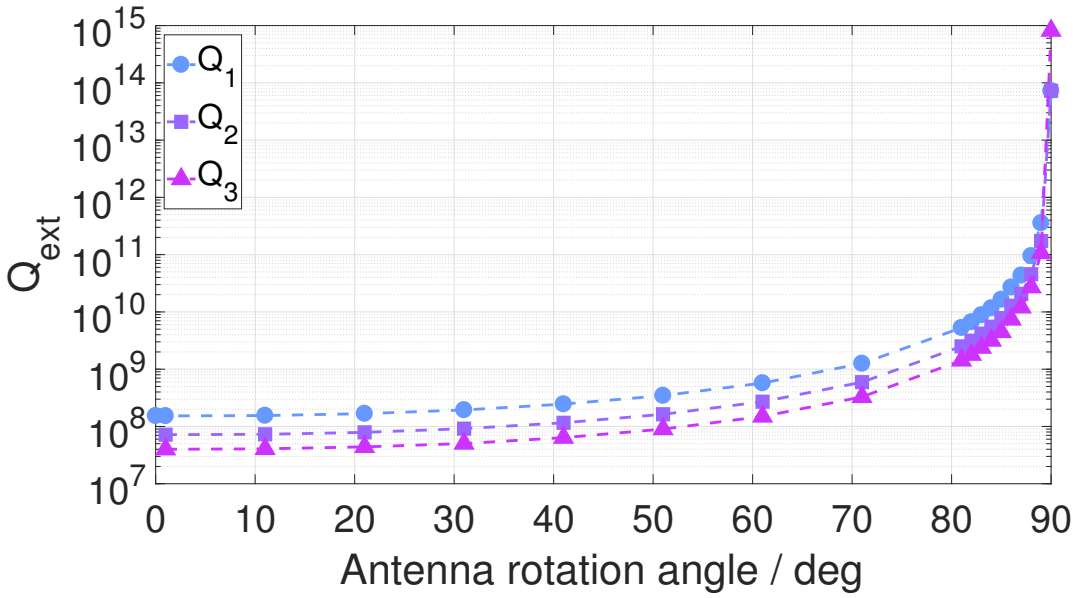

Figure 4.29: External quality factors of the pick-up antenna Q_{ext} in port position B for all quadrupole modes.

The Q_{ext} values of both antennas are then characterized as a function of the rotation angle from 0° to 90° around their respective symmetry axes. The results of the external quality factor for the input $Q_{\text{ext}}^{\text{inp}}$ and the pick-up $Q_{\text{ext}}^{\text{pro}}$ antennas are shown in Figs. 4.28 and 4.29, respectively. The QPR operates with $Q_{\text{ext}}^{\text{inp}} = 10^7$ and $Q_{\text{ext}}^{\text{pro}} = 10^{10} - 10^{11}$ for mode Q_1. As observed from Figs. 4.28 and 4.29, these target values can be achieved by rotating the input antenna by an angle of 22° and the pick-up antenna by 85°.

4.7.4 Frequency Sensitivity to Gap Changes

As discussed in Sec. 4.6.3, a calibration method was derived at HZB from simulations and measurements to calculate the gap between the sample surface and the pole shoes surface. Kleindienst and Keckert reported a dependence of the first quadrupole mode frequency Q_1 on the gap, given by $df/d\text{gap} = -0.95\,\text{MHz}/100\,\mu\text{m}$. The same constant was calculated for all the quadrupole modes of the UHH QPR in CST by moving the sample along the z-axis, increasing the pole-shoes-sample gap. Fig. 4.30 illustrates the dependency of Q_1on the gap. The dependencies of mode Q_2 and Q_3 on the gap are shown in Appx. II.

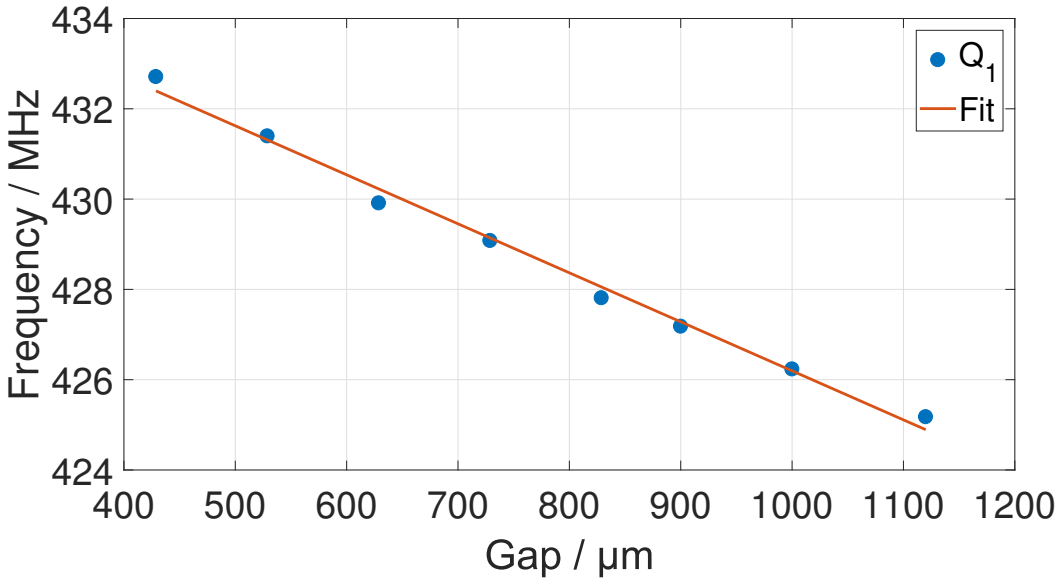

Figure 4.30: Quadrupole mode Q_1 frequency versus gap. Simulated frequencies obtained in CST Microwave Studio®.

Considering the linear behaviour of the frequencies, a linear regression was applied to these plots to obtain the following expressions:

$$Q_1 = \left(-0.01\,\frac{\text{MHz}}{\mu\text{m}}\right)\cdot \text{gap} + 437.05\,\text{MHz} \tag{4.18}$$

$$Q_2 = \left(-0.02\,\frac{\text{MHz}}{\mu\text{m}}\right)\cdot \text{gap} + 881.80\,\text{MHz} \tag{4.19}$$

$$Q_3 = \left(-0.03\,\frac{\text{MHz}}{\mu\text{m}}\right)\cdot \text{gap} + 1329.36\,\text{MHz}. \tag{4.20}$$

Tab. 4.3 provides the values of the sensitivity to gap change.

Table 4.3: Calculated $df/d\text{gap}$ for the quadrupole modes as a result of the linear regression applied to the simulated frequencies.

Mode	$df/d\text{gap}$ / $\text{MHz}/100\,\mu\text{m}$
Q_1	-1.09
Q_2	-2.23
Q_3	-3.05

Therefore, Eq. 4.21 is an expression to calculate the gap deviation from the nominal value of 500 µm:

$$\Delta\text{gap} = \left(\frac{437.05\,\text{MHz} - Q_1}{1.09}\right) \cdot 100\,\frac{\mu\text{m}}{\text{MHz}} - 434.22\,\mu\text{m}, \tag{4.21}$$

where Q_1 is the measured frequency of the first quadrupole mode.

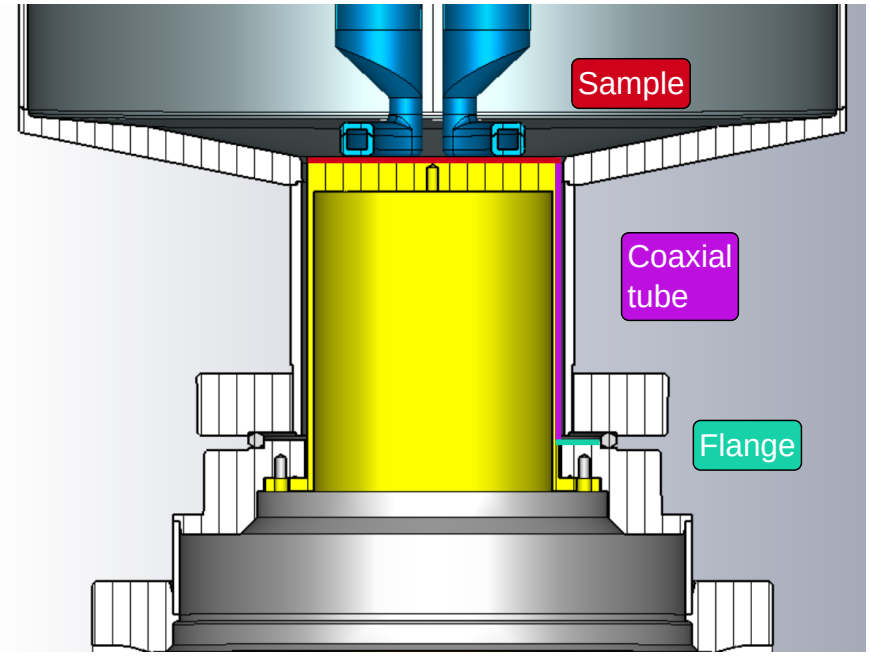

Figure 4.31: The magnetic field is integrated on the sample, coaxial tube, and flange to obtain the damping coefficients δ_i.

4.7.5 Parasitic Fields

In Sec. 4.6.5, it was mentioned that the presence of parasitic fields in the coaxial gap can lead to the overestimation of the sample surface resistance. For the purpose of characterizing the dissipated power P produced from RF-induced heating on the sample surface of the UHH QPR, the damping coefficient δ was calculated from simulations. This calculation follows the definition of δ_i employed in the HZB QPR, see Eq. 4.10, where index i refers to the integral of the H-field being performed on the coaxial tube and on the surface of the sample flange, as illustrated in Fig. 4.31. The values of the damping coefficients for the all of the quadrupole modes are presented in Tab. 4.4.

Table 4.4: Damping coefficients δ_i of the coaxial gap wall and sample flange, and the sum of magnetic field H on the sample surface.

f / MHz	δ_{coax}	δ_{flange}	$\int_{\text{sample}} \lvert H\rvert^2\, dA$ / A^2
Q_1	174.72	$1.31{\cdot}10^6$	$1.02{\cdot}10^8$
Q_2	179.88	$0.92{\cdot}10^6$	$1.01{\cdot}10^8$
Q_3	187.14	$0.49{\cdot}10^6$	$1.13{\cdot}10^8$

The damping coefficients of the coaxial gap and the sample flange of the UHH QPR are 15% lower compared to the results of the HZB QPR. Considering that the sample flange is also made of stainless steel, it is expected that the RF fields will produce a considerable loss contribution on the sample flange and a relatively small loss on the coaxial gap wall. This could potentially result in an overestimation of R_s by $36\,n\Omega$. However, as mentioned earlier, the cooling channels in the sample unit are designed to effectively mitigate any RF-induced parasitic heat contribution. Further investigations are required to determine the impact of the cooling channels on reducing this parasitic heating.

Chapter 5

Commissioning of the UHH QPR

After the fabrication of the QPR at Zanon, the following tests were conducted at room temperature for quality-control purposes during the commissioning phase at DESY: Ultrasonic wall thickness measurements were performed on the vessel and pole shoe surfaces, which were crucial for the BCP treatment of the QPR inner surface. Although fabrication tolerances were chosen carefully, measurements with a bridge coordinate measurement machine (CMM) were conducted to verify the parallelism of the vessel and the sample flange. Mechanical excitation tests were carried out to identify and analyse the spectrum of the response of the QPR to mechanical stimuli. RF spectrum measurements were conducted to identify three quadrupole modes in the range of 400 to 1400 MHz. Finally, the spectrum was remeasured after evacuating the resonator to compare mechanical simulations and quantify the impact of the mechanical deformation on the RF spectrum.

Subsequently, the QPR then returned to Zanon to undergo chemical and thermal (surface) treatments. This chapter presents the results of those measurements and provides a description of the surface treatment applied to the QPR after fabrication, a procedure typical of SRF cavities.

The chapter also covers the procedure for preparing the QPR for the measurements at cold temperatures, along with the series of tests conducted while immersed in LHe. These tests included the following: the installation of the antennas in an ISO 4 clean room; the installation of the sample in the QPR in a local clean room; the identification of the quadrupole modes during the cooldown process, following the method established at HZB; the analysis of the pressure stability of the cryostat, which is important for accounting for uncertainties in frequency and heater power values. Furthermore, this chapter explains in detail the RF system used for the measurements and the methods employed to determine the material parameters.

5.1 Surface Treatment

The QPR underwent a sequence of standard surface treatments at Zanon, a procedure typical for Nb SRF cavities. This procedure aims to ensure both high quality factors and high magnetic fields [2, 109, 110] and involved the following steps: *i*) A coarse BCP [78] to remove a total of 100-130 µm from the Nb walls. This step guarantees the removal of the inner damaged layer of the Nb lattice, which is on the order of 100 µm after forming and fabrication. *ii*) An 800 °C annealing for 3 hours to prevent the Q-disease and release mechanical stress. *iii*) Fine BCP to remove an additional 40 µm from the Nb wall's surface. Finally, *iv*) a 120 °C annealing for 48 hours to reduce the QPR's surface resistance and eliminate the sudden drop in quality factor (referred to as "Q-drop") at high fields.

Metrology, RF, and mechanical deformation tests were performed iteratively in between the different steps of the treatment until the resonator was finalized. The details of these experiments are discussed in the following sections.

5.2 Room Temperature Tests

5.2.1 Ultrasonic Thickness Measurements

The commissioning of the QPR began at DESY with measurements of the wall thickness of the vessel and the pole shoe surfaces. These values served as a baseline for the resonator undergoing the standard surface treatment common for TESLA-shaped SRF cavities. The initial measurement involved determining the thickness d_0 at four points around the upper and lower parts of the outer side of the vessel, as shown in Fig. 5.1.

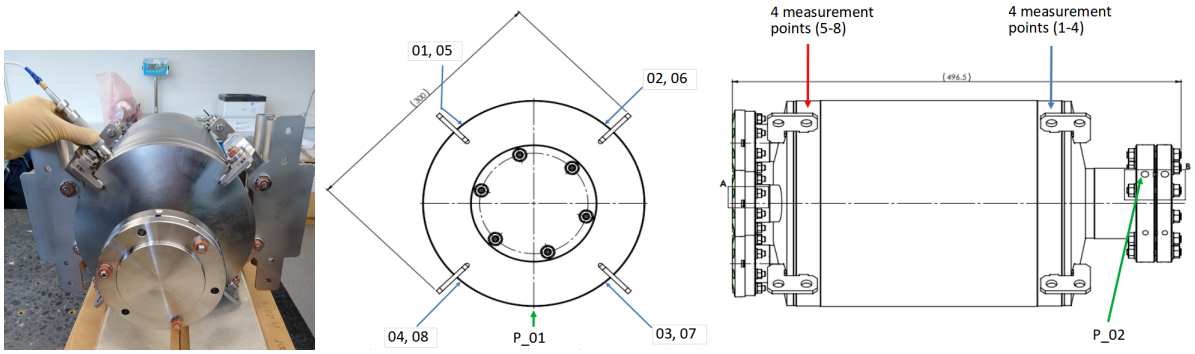

Figure 5.1: Ultrasonic thickness measurements at four points around the top and other four around the bottom area of the vessel.

Subsequently, the QPR underwent a BCP process three times at Zanon, with the aim of removing a total of 150 µm - 50 µm in each step - from its inner surface. However, to prevent contamination or damage to the internal surface of the QPR after the final BCP step, the wall thickness was measured only after the first two steps, corresponding to d_1 and d_2, respectively. Tab. 5.1 presents the initial wall thickness value, the thickness after each step, as well as the stepwise removal, $\Delta d_1 = d_1 - d_0$ and $\Delta d_2 = d_2 - d_1$, and total material removal $\Delta d_\mathrm{T} = d_2 - d_0$.

Table 5.1: Wall thickness of the vessel d, stepwise BCP removal Δd, and total removal Δd_T.

Point	d_0 / µm	d_1 / µm	Δd_1 / µm	d_2 / µm	Δd_2 / µm	Δd_T / µm
1	3121	3094	27	3018	76	103
2	3038	3018	20	2956	62	82
3	3040	3023	17	2951	72	89
4	3067	3055	12	2999	56	68
5		3004		2919	85	
6		3019		2958	61	
7		3023		2956	67	
8		3046		2968	78	

In Tab. 5.1, the values of points 5 to 8 are missing because they were not considered before the first measurement step. It was also observed that the material removal was much more uniform in step two compared to step one. On average, a total of 85.5 µm of material was removed from points 1 to 4. The third and final coarse removal step was skipped to let the fine BCP remove an additional 40 µm of material, resulting in an average total removal of 125 µm.

The next step in the procedure was to measure the wall thickness at three equidistant points at each of the pole shoe surfaces (see Fig. 5.2). Tab. 5.2 shows the results of the wall thickness test of the pole shoes.

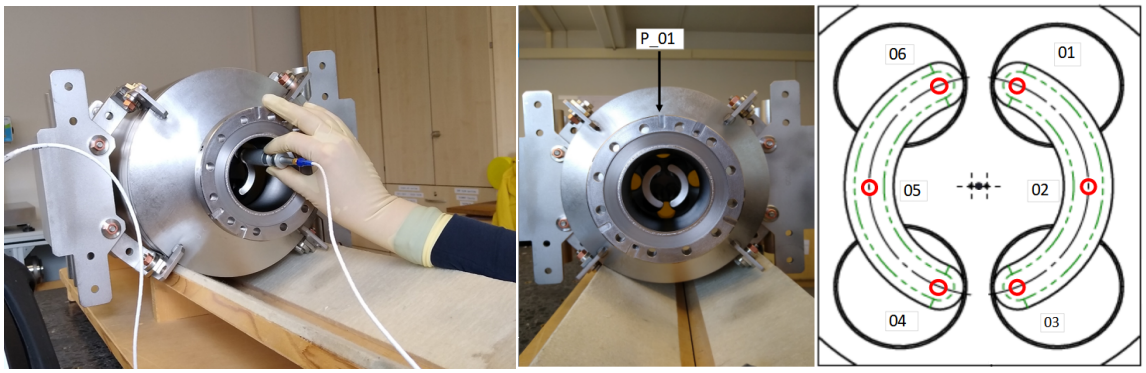

Figure 5.2: Ultrasonic wall thickness measurements on the pole shoes surface.

Table 5.2: Wall thickness of the pole shoes w, stepwise BCP removal Δw, and total removal Δw_{T}.

Point	w_0 / µm	w_1 / µm	Δw_1 / µm	w_2 / µm	Δw_2 / µm	Δw_{T} / µm
1	1800	1712	88	1529	183	271
2	1737	1626	111	1474	152	263
3	1700	1551	149	1345	206	355
4	1959	1779	180	1589	190	370
5	1977	1804	173	1590	214	387
6	1986	1806	180	1628	178	358

As was observed, much more material was removed from the surface of the pole shoes, but it happened more uniformly than on the vessel. The fact that more material was removed from the surface of the pole shoes validated the decision of skipping the third coarse BCP step. This is because the final chemistry step (fine BCP) also removed material, resulting in a total surface removal of the whole surface in accordance with the specified requirements.

5.2.2 Bridge Coordinate Measurement Machine Data

The QPR is designed to have a nominal gap of 500 µm between the sample surface and the pole shoes surface. However, variations of this gap can occur during the evacuation and cooldown processes of the QPR. Ultimately, this distance is determined by the sample height, the deformation of the gasket used at the bottom flange, and the sample flange dimensions. In addition, fabrication deviations from the nominal design of these components or the pole shoes can modify the gap, thereby causing a shift in the operational frequency and potentially the excitation of a dipole mode. Therefore, it is required that

the different parts of the QPR maintain a high level of parallelism, closely meeting the nominal design specifications.

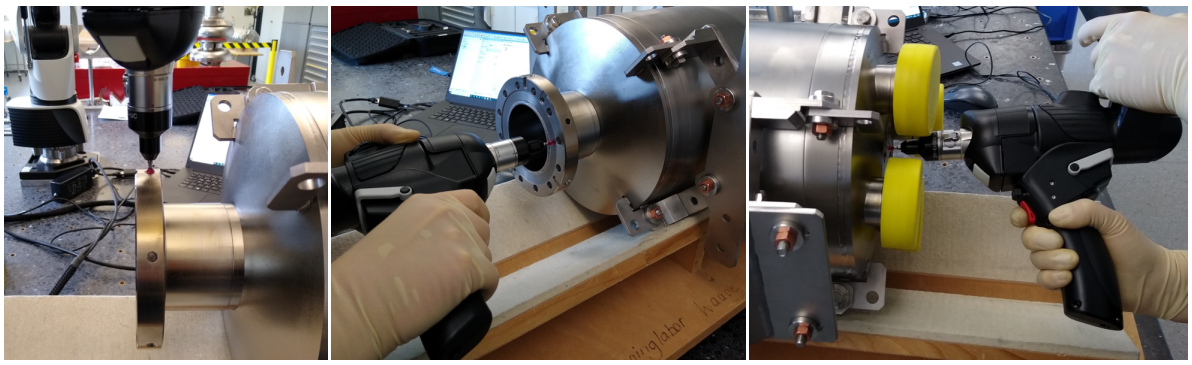

Figure 5.3: Measurements with the bridge coordinate measurement machine (CMM) on the outer surface of the QPR bottom flange (left), the gasket area on the QPR bottom flange (centre), and on point P_{05} (right).

To assess this parallelism, the procedure described in Appx. V was implemented with the CMM. Fig. 5.3 show pictures of the measurements conducted on the QPR using the CMM at DESY.

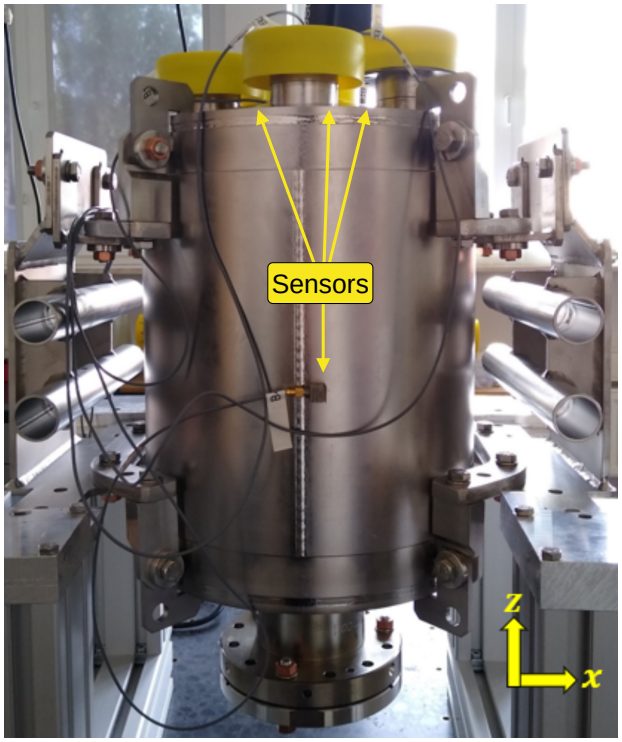

Figure 5.4: Mechanical resonances setup: four piezoelectric accelerometer sensors mounted on the QPR surface to measure vibrations in the x-, y-, and z-axes.

The results indicated that each rod exhibited a bending angle of approximately 0.06° around the y-axis, corresponding to a separation of 0.66 mm along the x-axis between them (see Appx. III for more details about the angle to on-axis displacement relationship). This displacement modified the gap between the sample and the pole shoe surfaces, introducing a deviation of 19.38 µm from its nominal value. This information was incorporated in the CST model used for the simulations. It was observed that this deviation does not significantly impact the performance of the QPR.

5.2.3 Mechanical Spectrum

In Sec. 4.6.2, the impact of microphonics on the operation of the QPR was discussed. At HZB, the excitation of the 100 Hz mechanical mode of the rods resulted in a detuning build up until the RF system could no longer lock the resonance frequency. In order to identify the mechanical spectrum of the UHH QPR, several piezoelectric accelerometer sensors were mounted on this resonator and stimuli were applied on top of it. The measurement setup used for this test is depicted in Fig. 5.4.

As anticipated from the modifications made to the rods design, as discussed in Sec. 4.7, when hitting the resonator on the top part where the rods are welded to the vessel, the mode at 100 Hz is no longer present (see Fig. 5.5). The two modes right below and above 100 Hz do not pose a problem, as the power grid operates at 50 Hz.

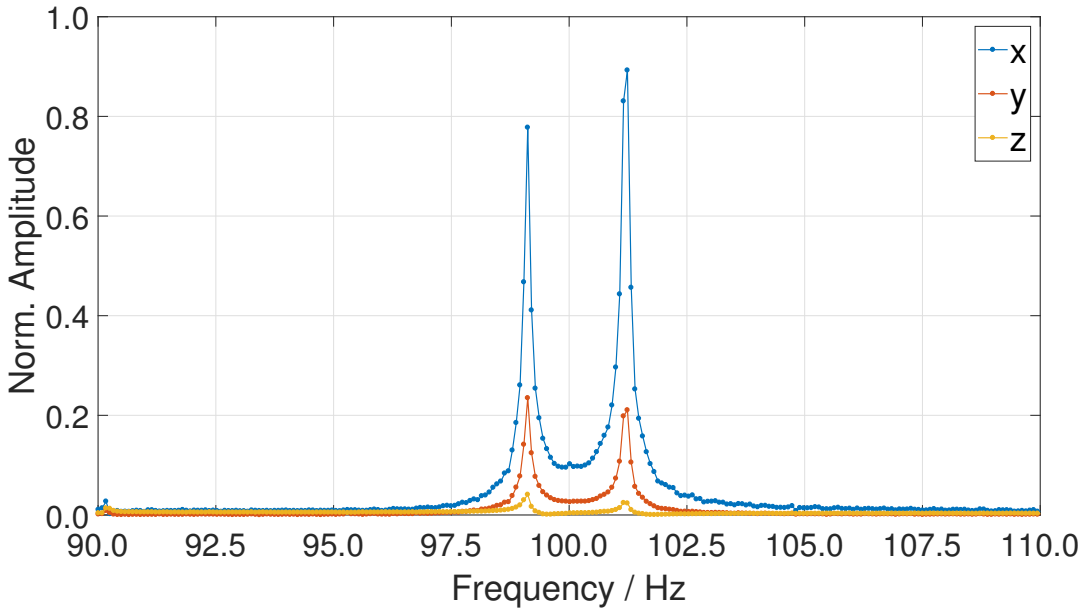

Figure 5.5: Normalized fast Fourier transform versus frequency. Three piezoelectric accelerometers mounted on the top part of the QPR measured vibrations in the three dimensions when hitting it in the vicinity of the sensors.

This measurement proves that the QPR exhibits improved stability against microphonics. The previous results also represent a significant achievement in both the design and manufacturing processes conducted at DESY and Zanon, respectively.

5.2.4 Measurement of the Frequency Sensitivity to Gap Changes

The frequency sensitivity to gap changes $df/d\text{gap}$ was determined through simulations and presented in Sec. 4.7.4. In the commissioning phase, $df/d\text{gap}$ for all of the quadrupole modes was measured. To achieve this, an Al gasket was utilized at the bottom flange and sample flange connection to vary the gap. Deformation studies have shown that when this type of gasket is mounted and the nuts are loosely tightened by hand (0 Nm) until reaching a torque of 30 Nm, the gasket undergoes a total deformation of (420±50) µm, see Appx. IV. After loosely mounting the gasket, each quadrupole-mode frequency was recorded for a duration of ten minutes[1]. Subsequently, the nuts were gradually tightened up to a torque of 30 Nm. During this process, only Q_1 was recorded, see Fig. 5.6, and after a few additional minutes, Q_1, Q_2, and Q_3 were measured again for ten minutes.

[1] The measurement was performed with a resolution of 6.24 kHz.

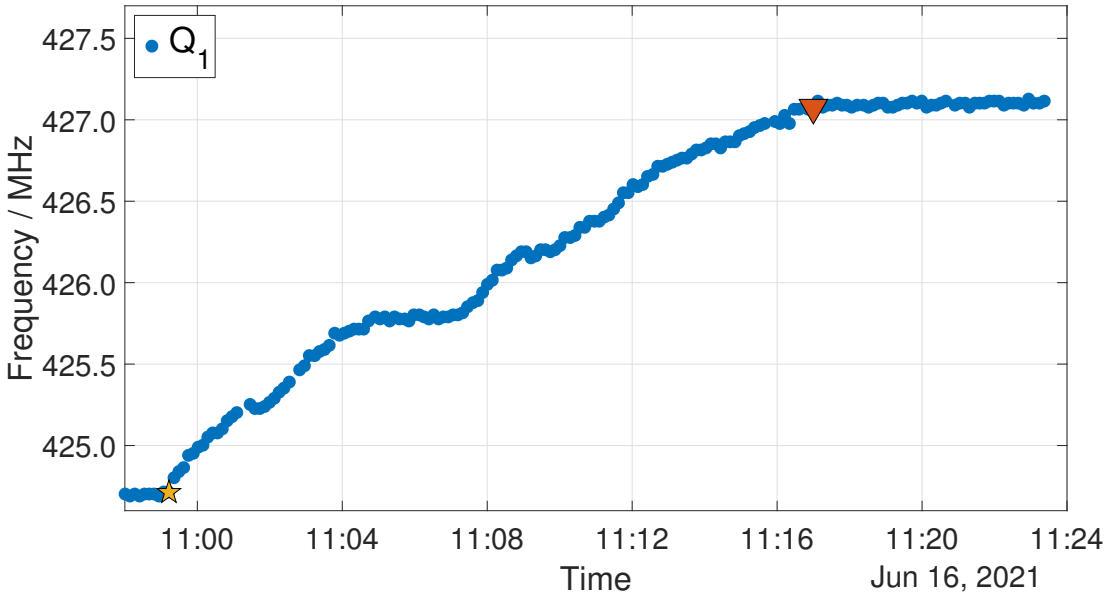

Figure 5.6: Quadrupole mode Q_1 frequency versus time. This mode was tracked while tightening the nuts from 0 Nm to 30 Nm. The yellow star indicates the time at which the tightening procedure started and the red triangle when the 30 Nm were achieved.

The frequency change of Q_1 quadrupole modes at different torques is reported in Fig. 5.7. The changes in frequency of modes Q_2 and Q_3 are reported in Appx. II. Tab. 5.3 provides the sensitivity $df/d\text{gap}$ obtained for the quadrupole modes. These values were calculated by averaging each data set at 0 Nm and at 30 Nm and then dividing the frequency difference by the corresponding gap change, which corresponded to the gasket deformation.

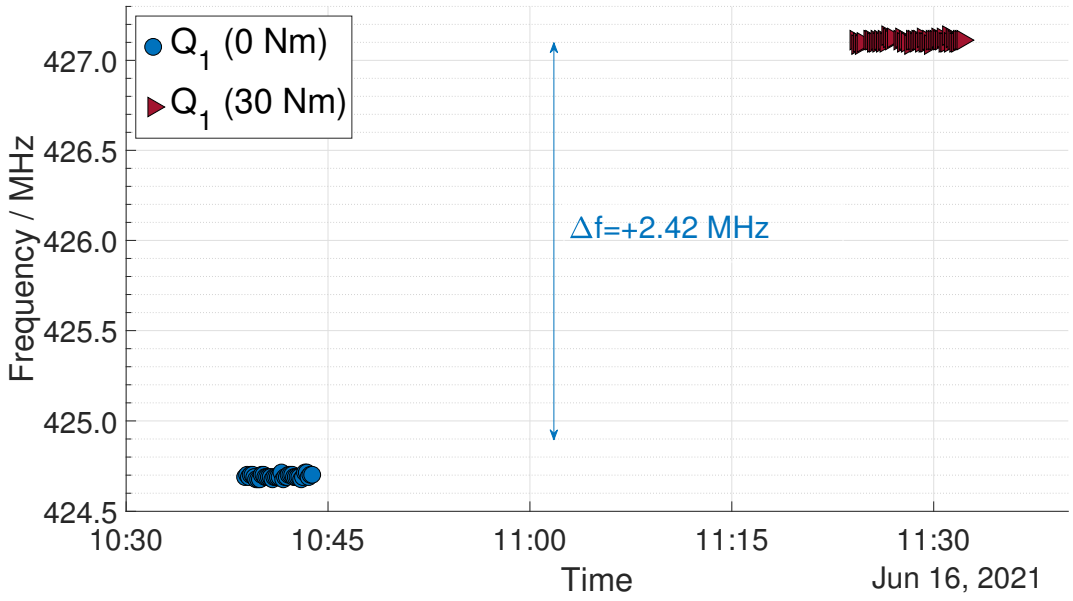

Figure 5.7: Quadrupole mode Q_1 frequency versus time at room temperature. First, the frequency was measured for ten minutes. Then, after reaching a 30 Nm torque on the nuts, it was measured again for the same time period.

Table 5.3: Calculations of the $df/d\text{gap}$ for the quadrupole modes from the experimental results. The frequency difference Δf was divided by the gasket deformation of (420±50) µm.

Mode	$\langle f_{0\,\mathrm{Nm}} \rangle$ / MHz	$\langle f_{30\,\mathrm{Nm}} \rangle$ / MHz	Δf / MHz	$df/d\text{gap}$ / MHz/100 µm
Q_1	424.691±0.002	427.109±0.002	2.418±0.002	−0.576±0.069
Q_2	857.320±0.001	861.501±0.001	4.181±0.002	−0.995±0.118
Q_3	1296.700±0.001	1302.200±0.001	5.449±0.002	−1.297±0.154

The sensitivity $df/d\text{gap}$ for Q_1 obtained from simulations deviates by more than two times compared to the measurements, and the deviation significantly increases for the sensitivities of Q_2 and Q_3 (see Tabs. 4.3 and 5.3). The discrepancies could originate from the setup used to estimate the gasket deformation, see Fig. IV.2, which might not be able to apply the same force on the gasket as the QPR bottom flange. While the materials of the flanges used in the deformation setup and the QPR are the same, the discrepancies in the sensitivities could be attributed to the different geometries, resulting in differences in rigidity. This suggests that the deformation of the gasket may actually be less than the estimated value of (420±50) µm. For instance, using Eq. 4.21 shows that the change in frequency of Q_1 corresponds to a reduction of the gap of 199.83 µm.

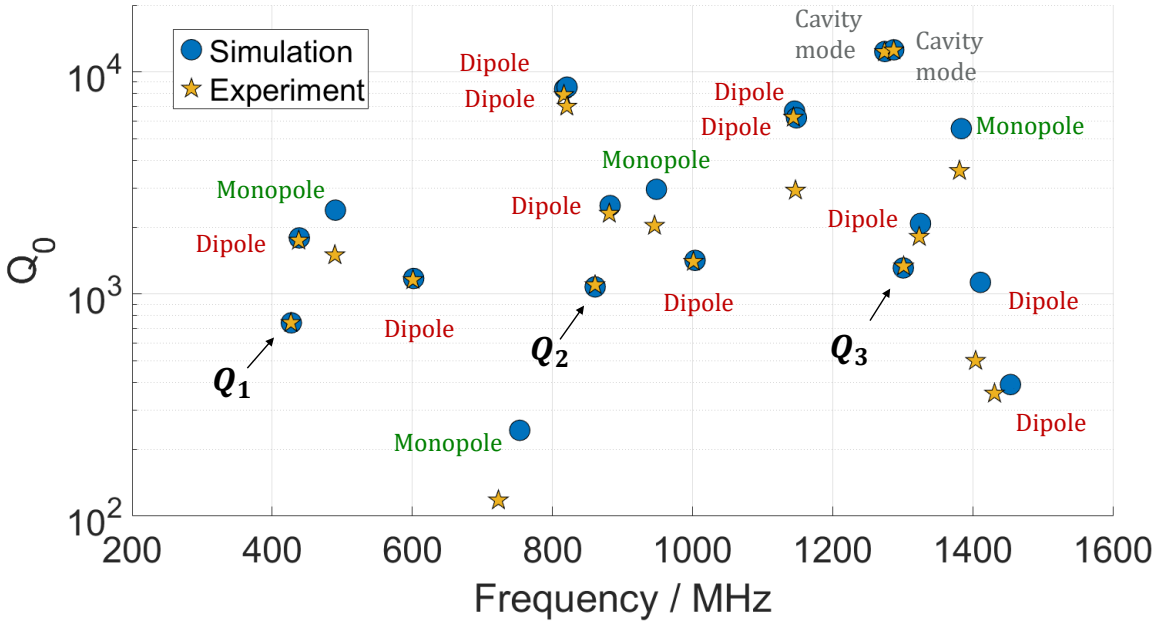

Figure 5.8: Comparison of simulated and experimental quality factor versus frequency of the modes of the QPR at room temperature. Simulated values calculated in CST Microwave Studio®, as shown in Fig. 4.24. Error bars are the same size or smaller than the symbols.

5.2.5 RF Spectrum

By using Eq. 4.21 and the frequency value of Q_1 at 30 Nm as reported in Tab. 5.3, the gap was determined to be 883.55 µm. Therefore, the modes were recalculated accordingly in CST. The RF spectrum was measured with a vector network analyser (VNA) through the transmission coefficient S_{21} between 400 and 1400 MHz, and the results were compared to the simulated values. The comparison of these two spectra is shown in Fig. 5.8. For the measurements and simulations, the input antenna loop, as depicted in Fig. 5.9, was positioned perpendicular to the magnetic field, which corresponds to the zero-angle

orientation shown in Fig. 4.27. Conversely, the pick-up antenna was oriented at 45° to facilitate the coupling and detection of various modes.

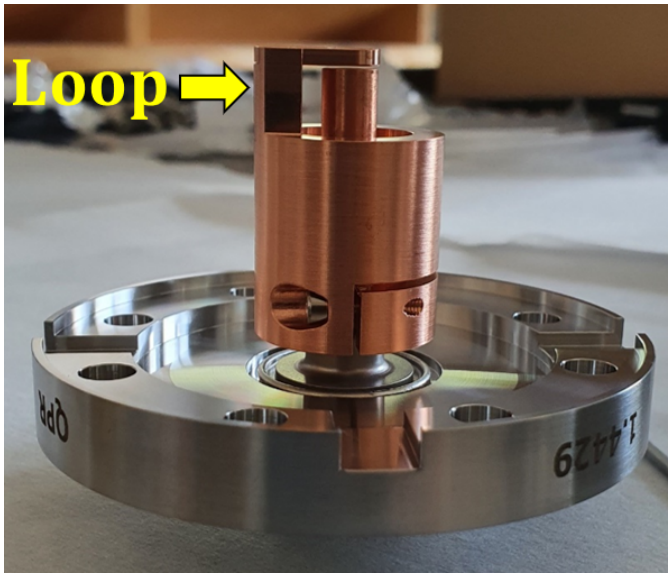

Figure 5.9: Input antenna: the coupling is controlled via the angle between the loop area and the field orientation.

Significant discrepancies were observed in the Q_0 for certain monopole and dipole modes. However, it was noted that the technique to calculate the quality factor, as detailed in Sec. 5.4.2, could not be effectively applied to those modes. At room temperature, some modes became excessively broadened, leading to overlaps with neighbouring modes and insufficient data for the Q_0 calculations. Other modes already had amplitudes on the noise level, which presented the same issue. Conducting simulations and measurements for different antenna couplings could help clarify whether these discrepancies originate from the antennas.

Conversely, the simulated frequency values exhibited a deviation up to 4.2% compared to the measurements. The experimental results showed a minimum and maximum difference of 2.50 and 141.20 MHz between neighbouring modes, respectively (refer to Appx. I to see the frequencies of all modes), and no dynamic mode order swapping was observed. Most importantly, there was an excellent agreement between the simulated and measured frequencies, as well as the quality factors, of the quadrupole modes.

5.2.6 Evacuation Effects on the Gap

After completing the previous test, the QPR was evacuated with the aim of reaching a pressure $\leq 10^{-3}$ mbar. However, due to a leak in the 1 mm indium gasket located on the sample flange, see Fig. 4.3, the pressure achieved was only of 6.0 mbar. The frequency of Q_1 was monitored during the vacuuming process, as shown in Fig. 5.10.

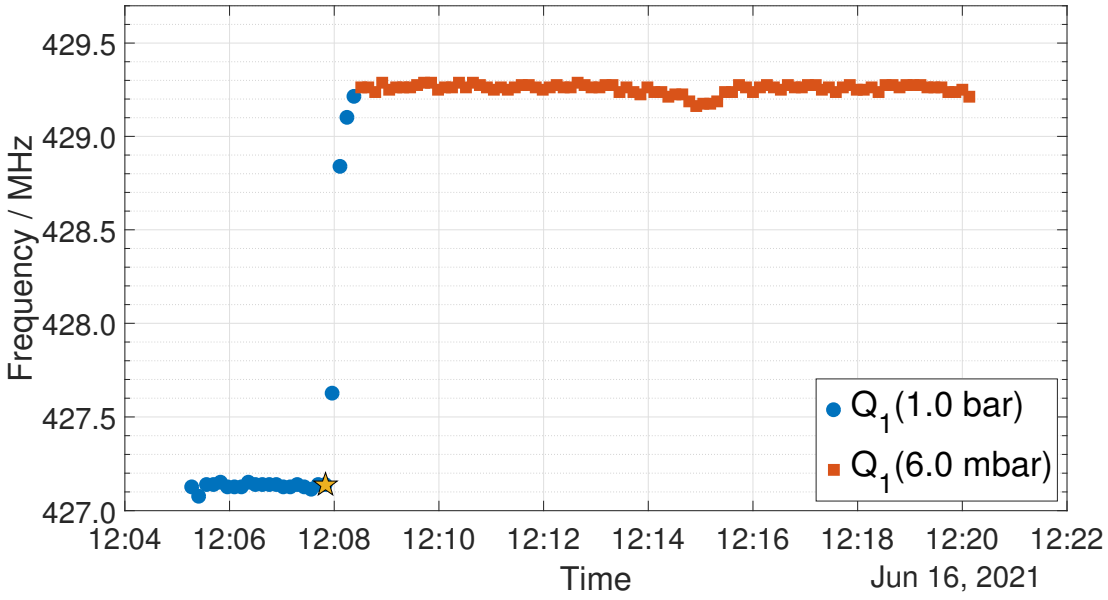

Figure 5.10: Quadrupole mode Q_1 frequency versus time. Mode Q_1 was recorded while pumping down the QPR from ambient pressure to 6.0 mbar. The yellow star denotes the time and frequency at which the evacuation process started.

Fig. 5.11 show the frequency of mode Q_1 recorded at 6 mbar and 1 bar. The modes were initially recorded at low pressure and then at ambient pressure, with each mode recorded for ten minutes. The frequency change of modes Q_2 and Q_3 are shown in Appx. II.

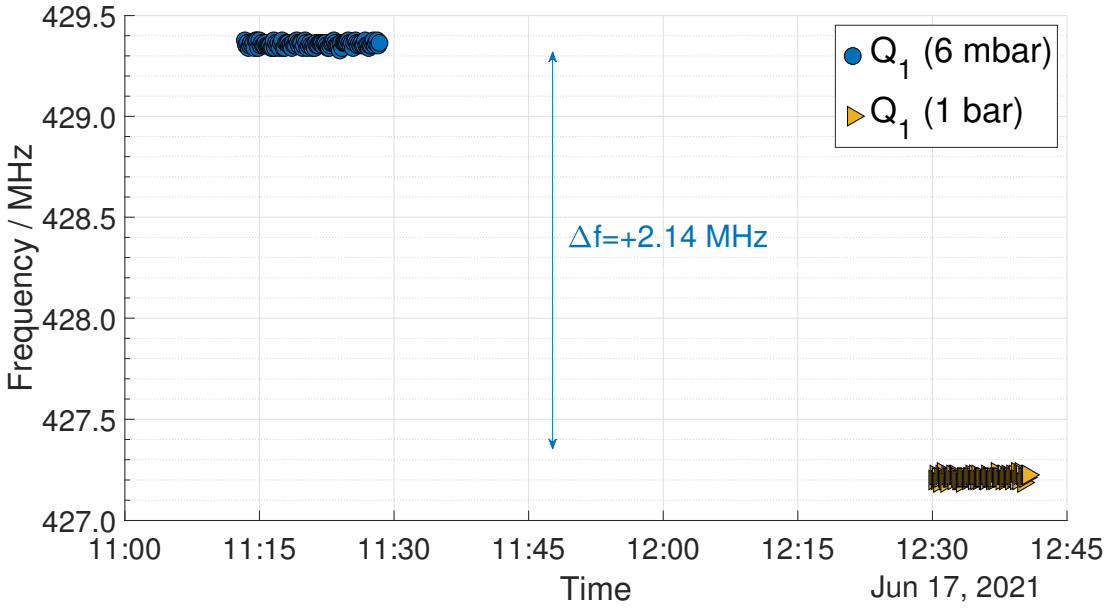

Figure 5.11: Quadrupole mode Q_1 frequency versus time. Initially, the frequency was measured at 6 mbar for ten minutes. Then, the measurements were repeated at ambient pressure for the same time period.

Based on these results, the frequency change with respect to pressure df/dp was determined for the quadrupole modes. The obtained values are reported in Tab. 5.4. These values were derived by averaging the respective data sets at 1 bar and at 6 mbar and then dividing by the pressure difference.

Table 5.4: Experimental results of the df/dp for the quadrupole modes. The change in frequency Δf was divided by the pressure difference between 1 bar and 6 mbar.

Mode	$\langle f_{1\,\mathrm{bar}} \rangle$ / MHz	$\langle f_{6\,\mathrm{mbar}} \rangle$ / MHz	Δf / MHz	df/dp / Hz/mbar
Q_1	427.210±0.001	429.360±0.001	2.143±0.002	2155.792±0.002
Q_2	861.670±0.001	865.310±0.001	3.639±0.001	3661.066±0.001
Q_3	1302.400±0.001	1307.200±0.001	4.833±0.001	4861.902±0.001

Simulations conducted by P. Putek [111] revealed that a pressure difference of 1 bar inside and outside the QPR results in a displacement of the rods-pole shoes in all three dimensions, with their maximum movement (separation) occurring along the y-axis (see Fig. 5.12). These results revealed a maximum displacement at the bottom of the pole shoes of 0.192 mm, which corresponds to a bending angle of each rod of 0.034°. In contrast, the minimum displacement of the pole shoes occurs in the x-axis, with a value of 0.025 mm, which is considered negligible.

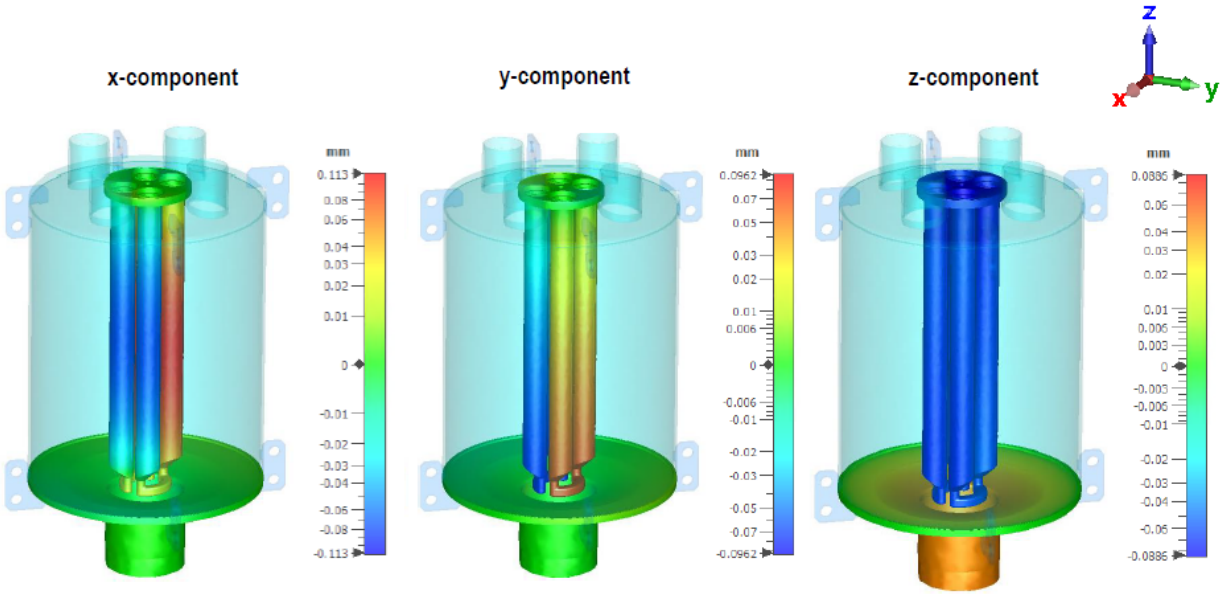

Figure 5.12: Simulation of the displacement of the rods due to a pressure difference inside and outside the QPR of 1 bar. Image shared via private communication with P. Putek.

To understand whether the frequency shift presented in Tab. 5.4 originates from the movement of the pole shoes in the y-axis, as found by Putek, their maximum displacement was compared to the results of a simulation study on the static detuning of the QPR, as detailed in Appx. III. In this study, CST simulations were conducted to investigate the effects of the symmetric bending of the rods within a range of angles from -0.4° to 0.4° around the y-axis. However, these simulations indicate that a bending angle of 0.034° leads to a frequency change in the order of tenths of MHz, whereas in the experiment, a frequency change ranging from 2.14 to 4.83 MHz was observed.

According to Eq. 4.21, the measured frequency change of Q_1 would correspond to a reduction of the gap of 177.69 µm. This observation is supported by the findings of Putek, who demonstrated that under a 1 bar difference, the rod-pole-shoe loops experience a negative displacement of 88.6 µm along the z-axis, while the coaxial tube undergoes a positive displacement of 88.6 µm. These displacements bring them closer to each other, resulting in a total reduction of the gap of 177.20 µm.

5.3 Straightening Process

After the 800 °C annealing - step *ii* of the chemical treatment - measurements with a CMM were conducted on the QPR at Zanon, see Fig. 5.13, to estimate the parallelism of the pole shoes with respect to the bottom flange and the QPR axis. As a first step, a plane (plane 1) was fitted to points and lines on the sealing surface of the bottom flange (see Fig. 5.14) to define the axis and origin of the QPR, following the steps described in Appx. V.

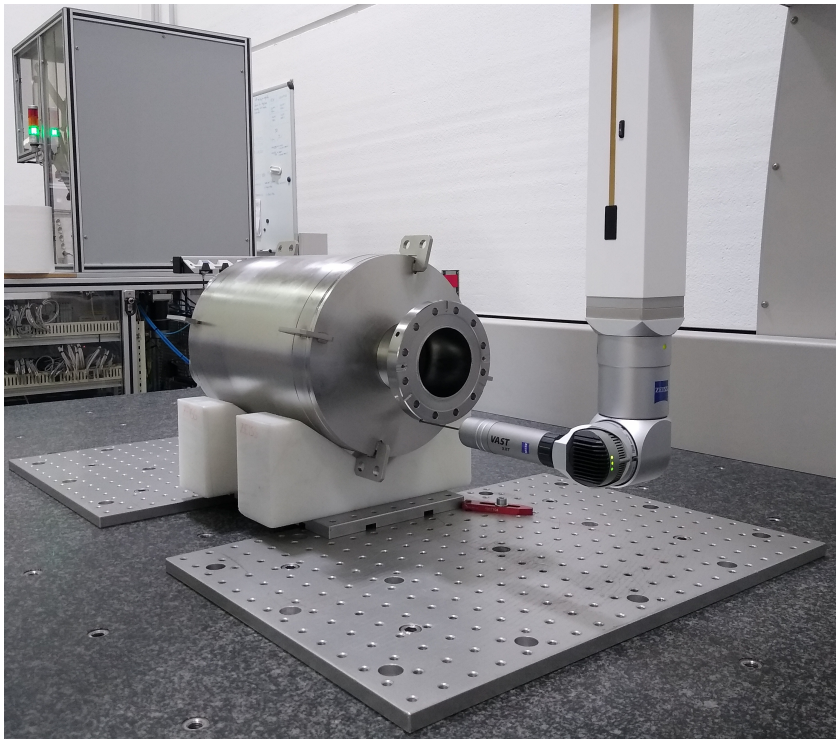

Figure 5.13: CMM measurement of the bottom flange of the QPR with the system at Zanon.

Then, multiple points on both pole shoe planes were recorded, and their distance in the z-coordinate was obtained with respect to the origin. Then, a second plane, plane 2, was defined with the height of these points. Subsequently, the planarity (deviation of the points on the pole shoes from plane 2) and total parallelism of the pole shoes were determined. The total parallelism refers to the deviation the points on the pole shoes, considering their individual offset, from their mean height from plane 1.

The analysis of the CMM data showed a total height difference of 239.69 µm between the closest and farthest points on the pole shoes, $z_{\max}$ and $z_{\min}$, respectively, from the origin of plane 1. Fig. 5.15 illustrates 14 points on the pole shoes with respect to their mean height. This analysis indicated that a corrective straightening procedure was necessary for the QPR in order to meet the requested tolerances for total parallelism. To achieve this, the sample tube of the QPR was actively tilted in order to align it and reduce this difference.

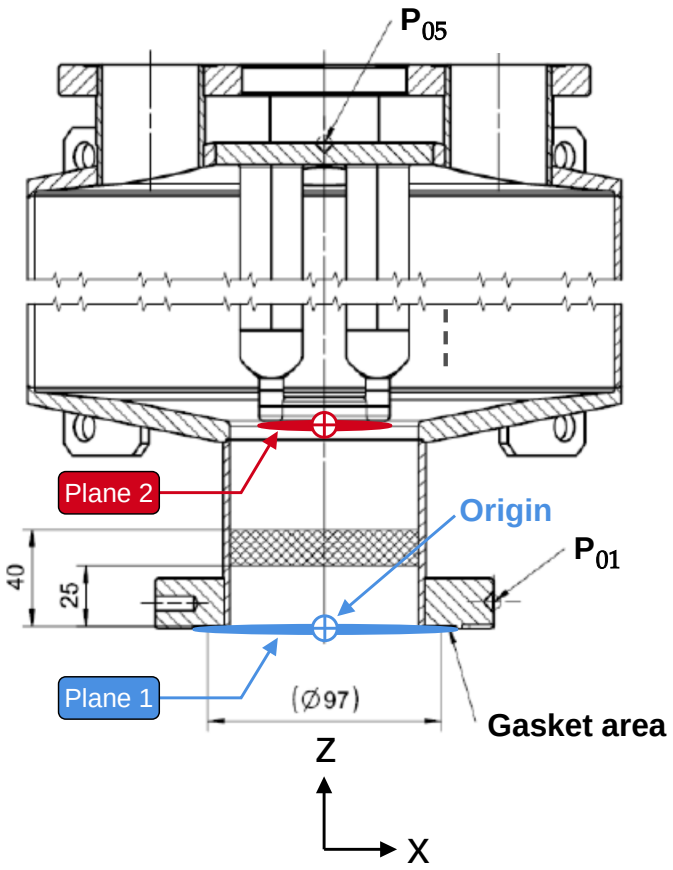

Figure 5.14: Diagram of the QPR coordinate system. Plane 1 is defined on the gasket area of the bottom flange where the origin is also defined. A plane, plane 2, is fitted to the pole shoes with their distance from the origin. Reference points P_{01}, P_{02}, and P_{03} are used to fix the QPR in the same position on the CMM.

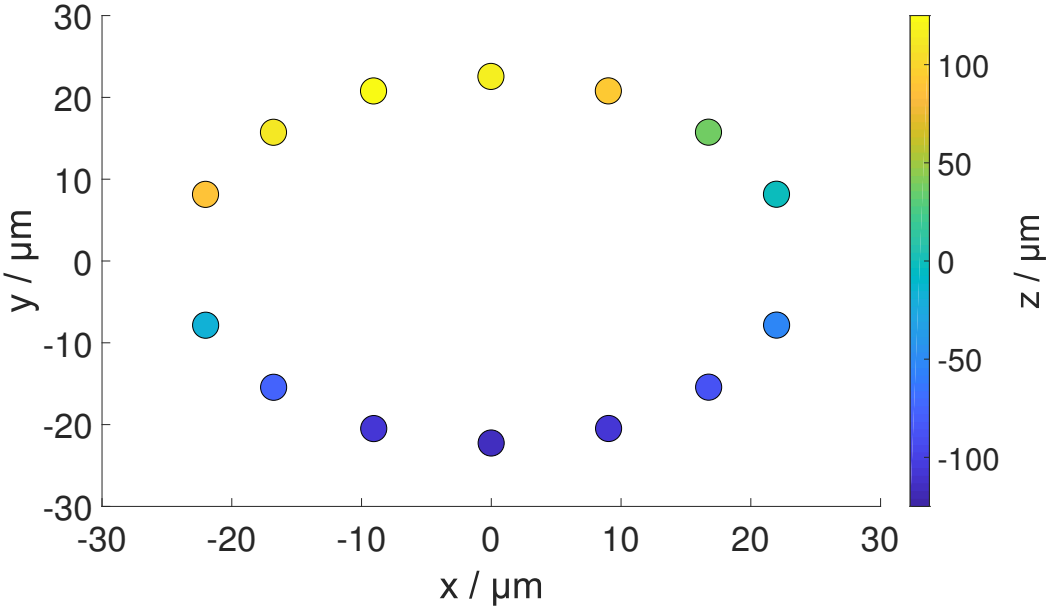

Figure 5.15: CMM measurements on the pole shoes before the deformation steps. Each datapoint is plotted with respect to the average height of the 14 points.

The QPR was placed on a table and secured by the vessel to counteract the force exerted during the deformation process. The bottom flange was deformed in the three dimensions with a flat jack hydraulic cylinder (model Enerpac RSM-50) with force applied manually using a pump. Three dial indicators were used, two for the z-coordinate and one to measure in the xy-plane, to directly estimate the deformation. The QPR was carefully aligned stepwise while exceeding the limit of elastic deformation. The setup used is shown in Fig. 5.16.

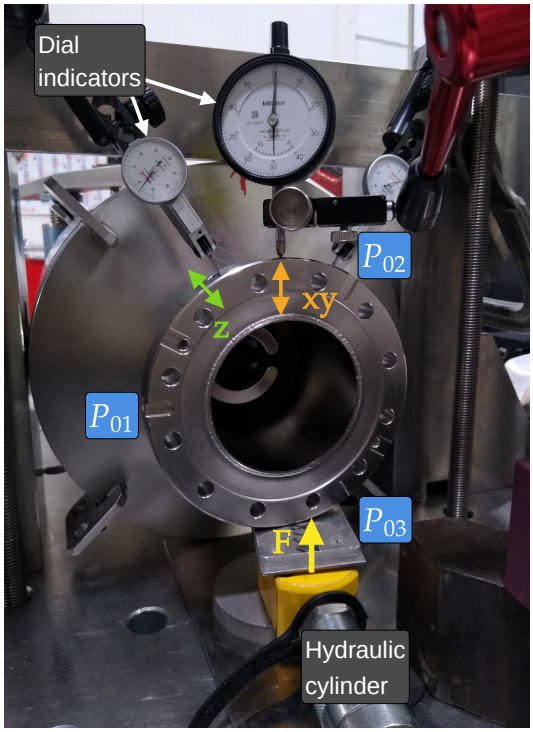

Figure 5.16: Deformation setup used to align the QPR. The hydraulic cylinder is used to apply a force F on the side of the bottom flange. Reference points P_{01}, P_{02}, and P_{03} are used to secure the QPR in the same position on the table.

A total of three deformation attempts were made on the QPR, with CMM measurements recorded in between them to track the necessary corrections in angle and length. The correction length was determined by the formula:

$$\text{Correction} = \frac{z_{\max} - z_{\min}}{2}, \tag{5.1}$$

and the angle was calculated by determining the gradient of plane 2. The results of the CMM measurements after the final alignment are shown in Tab. 5.5. The deformation of the resonator was stopped after the third step due to the increased mechanical force required to observe a change in the parallelism of the pole shoes. This indicated that the hardness increased in the lower area of the vessel, which represented a risk of significant plastic deformation if the deformation had continued. Fig. 5.17 shows the total parallelism after the third step.

In summary, the alignment of the QPR resulted in an improved total parallelism between the surface defined by both pole shoes and the sealing surface of the sample flange. The parallelism was calculated by defining a plane given by the mean distance of 14 points on the pole shoes from the origin of plane 1 and determining the separation of the points from the plane along the z-axis. Prior to the alignment, the distance between the maximum and minimum points was 239.69 µm. After the correction, it was reduced to 91.10 µm. Finally, the planarity was determined to be 43.51 µm.

Table 5.5: Alignment steps of the QPR during the visit to Zanon.

BCM Meas.	$z_{max} - z_{min}$ / µm	Correction / µm	Orientation / deg
Before def.	239.69	119.84	75.39
1st Attempt	133.00	66.50	61.94
2nd Attempt	95.50	47.75	48.38
3rd Attempt	91.10	45.55	35.03

These levels of parallelism and planarity introduce uncertainty contributions to the gap, each given by half of their value. Combining these errors with the bending of the pole shoes determined from the CMM data (as detailed Sec. 5.2.2), and the measurement error in the deformation of the gasket (see Appx. IV), results in an overall uncertainty of the gap of 73.65 µm.

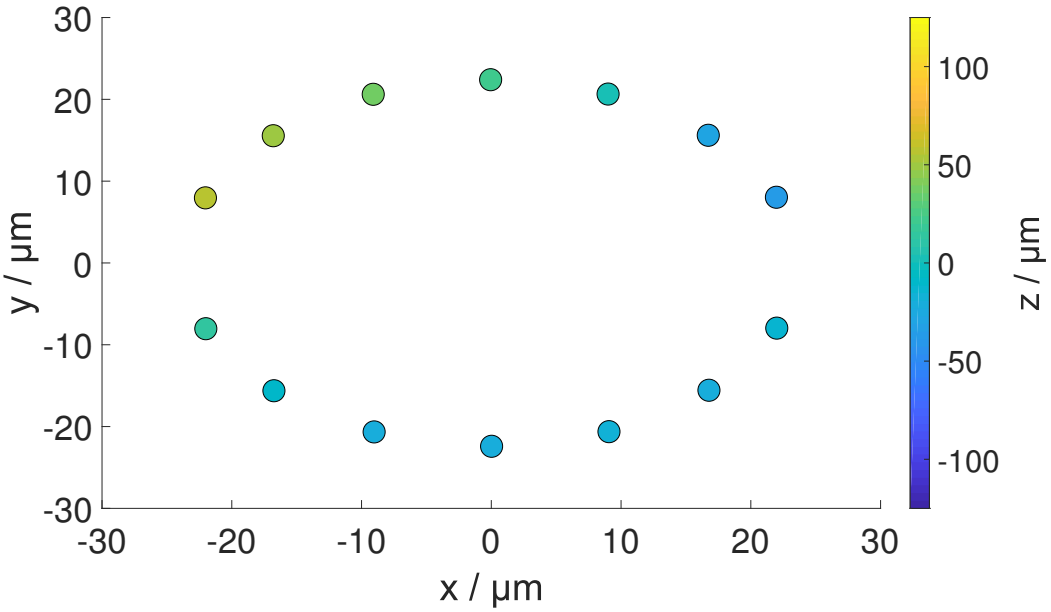

Figure 5.17: CMM measurements after final deformation step.

5.4 RF System

The existing RF and data-acquisition systems employed for the R&D of SRF cavities at DESY [112] were used for the first tests with the QPR. However, an upgrade was carried out on these systems to be able to measure also at frequencies Q_1 and Q_2. The diagram of the RF system of the QPR is shown in Fig. 5.18.

In the RF system, a signal generator initially produces an input signal with frequency ω_F. After passing through different components, such as amplifiers, insulators, and directional couplers, this signal enters and drives the QPR. The signal from the resonator, with frequency ω_T and phase ϕ, is then used for frequency modulation with the frequency of a specific quadrupole mode ω_Q obtained after the cooldown process, as described in Sec. 5.5.3, to generate a new input signal. The system is considered to be "locked" when $\omega_F - \omega_T$. However, when the QPR is immersed in LHe, changes in cryostat pressure and microphonics can lead to frequency variations. The PLL compensates for these variations through a non-zero signal.

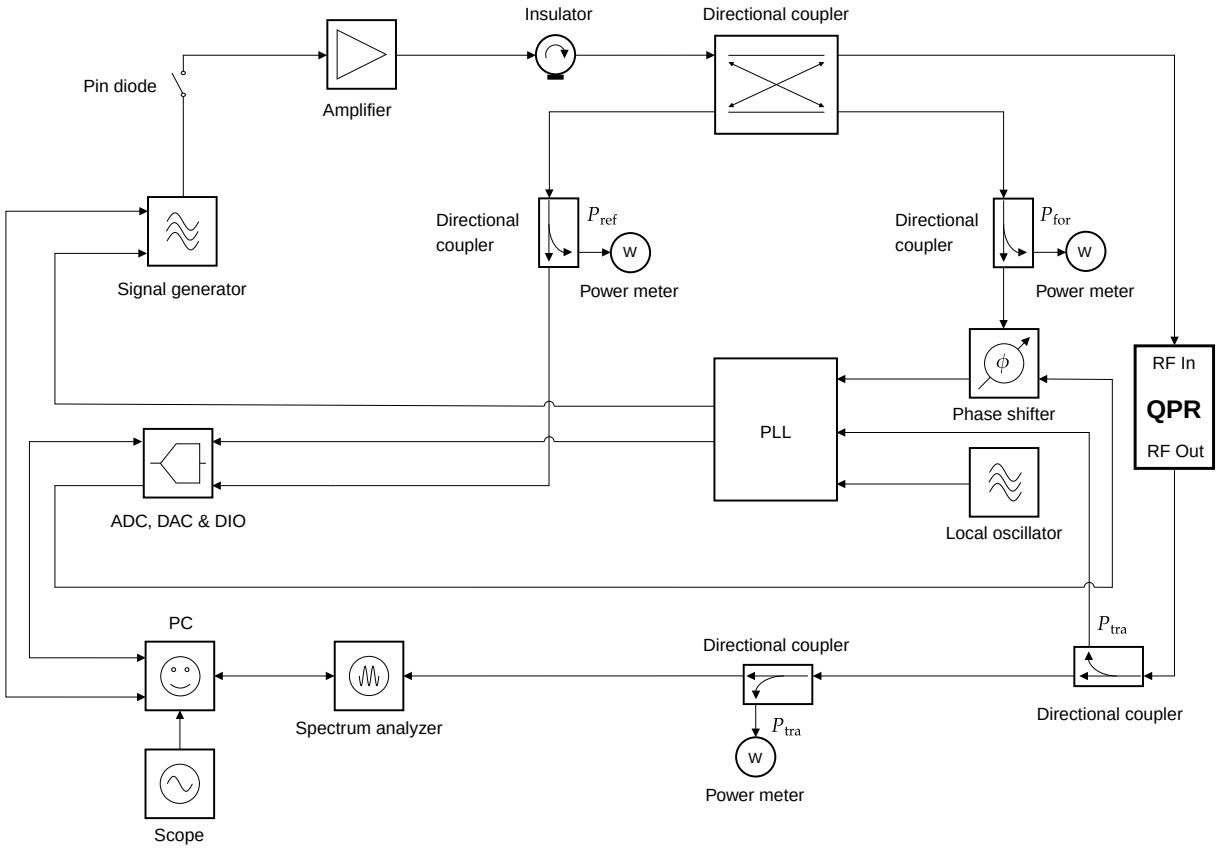

Figure 5.18: Simplified diagram of the RF system of the UHH QPR.

Consequently, the instantaneous frequency of the signal generated by the signal generator after frequency modulation is:

$$\omega\left(t\right) = \omega_{\mathrm{Q}} + K_f \cdot \cos\left[\left(\omega_{\mathrm{F}} - \omega_{\mathrm{T}}\right) t + \phi\left(t\right)\right], \tag{5.2}$$

where t represents time and K_f is the sensitivity of the frequency modulator. The phase shifter is used to adjust ϕ to maximize the transmitted power P_{tran}, ensuring that the system is locked. This means that the QPR is driven with a signal frequency as close as possible to the selected quadrupole mode.

5.4.1 Surface Resistance Measurement

To measure the surface resistance of the sample, the calorimetric measurement technique, described in Sec. 4.4, was implemented. A Lake Shore 336 controller was utilized to control the closed-loop system consisting of a 50 Ω heater and four T-sensors inside the calorimetry chamber. When the maximum current setting is utilized, this controller can provide minimum steps of 30.5 µA in current, 47 nW in heater power, and 1.5 mV in voltage. The powers before and after turning on the RF power, P_{DC1} and P_{DC2}, were determined by measuring the heater voltage and current using the multimeters HP 34401A and Keithley 2100, respectively. The heater current is measured with a resolution of at least 1 µA and an accuracy of 0.3%. The heater voltage is measured with an accuracy of 600 µV.

In order to determine the stored energy U inside the cavities, the decay-time-constant τ_{L} is obtained. The constant τ_{L} can be determined from the traces of the reflected and transmitted powers when the RF power is switched off (see Eq. 3.66). Common values of τ_{L} range between 0.5-1 s, which can be resolved by the existing analog-to-digital converter (oscilloscope) of the setup at DESY.

However, in the QPR, due to its over-coupled input antenna ($\beta_{\text{inp}} \sim 100$) the decay times are much shorter, typically between 1-3 ms. To improve the resolution up to 1 µs, the existing power meters in the setup were replaced with RadiPower RPR2006P power meters. Therefore, in the case of the QPR, the integral over the entire reflected power pulse can be related to the stored energy U as follows:

$$U \approx \sum_{m}^{N} P_{\text{refl}} \Delta t, \tag{5.3}$$

where Δt is the sampling time of the power meter, N is the number of samples, and m is the sample at which the RF power is switched off.

During the antenna Q_{ext} measurements that are presented in Sec. 5.5.2, it was found that when the 1 W RF power is turned off, approximately 10^{-3} J of energy flows out of the input antenna and 10^{-6} J from the pick-up antenna. Therefore, even though the coupling of β =0.01 for the latter was not achieved, the energy flowing out of this pick-up antenna was negligible. Additionally, the decay time constants τ_{L} obtained from the traces were within the range 0.27-2.31 ms, which are significantly lower than the τ_{L} found in cavities of 1 s. Fig. 5.19 shows an example of the power traces before and after P_{forw}=1 W is switched off for Q_3. It is important to note that at $t = 0$ ms, the forward power P_{forw} in on the order of 10^{-2} W, corresponding to the directivity value of the directional coupler (20 dB) used in the RF system.

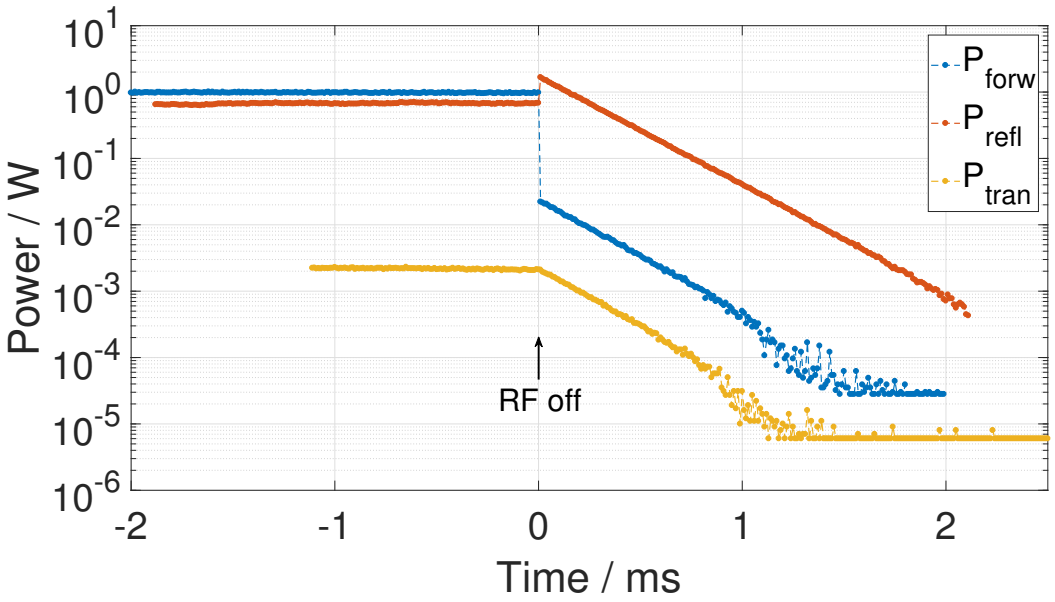

Figure 5.19: Forward, reflected, and transmitted powers, P_{forw}, P_{refl}, and P_{tran} respectively, versus time. At $t = 0$, the power P_{forw} of 1 W is switched off. The y-axis is represented on a log-scale.

The power meters employed to measure P_{refl} or P_{tran} have an accuracy of ±0.25 dB, and an additional ±0.2 dB is added to account for RF losses in the setup cables. This results in an overall accuracy of the power meters of ±0.455 dB. Therefore, currently, this sets the uncertainty of the R_{s} measurements in the worst case of $\sigma_{R_{\text{s}}} = \pm 11.05\%$, which is calculated with the error propagation of Eq. 4.1.

5.4.2 Frequency Measurement and Penetration Depth Determination

Measuring the frequency of the QPR as a function of the temperature of the sample leads to the determination of its near-surface material parameters, such as the London penetration depth at 0 K, mean free path, and effective penetration depth [113]. This relationship is described by Slater [114], who stated that the change in frequency Δf is proportional to the change in stored energy ΔU:

$$\frac{\Delta f}{f} = \frac{\Delta U}{U}. \tag{5.4}$$

In the superconducting state, the London penetration depth varies with temperature, as shown in Eq. 3.20. As a superconductor is heated, its ability to shield the electromagnetic field decreases, resulting in an increase of the RF volume. The time-average fraction of stored energy in a volume ΔV filled with the electromagnetic fields is given by:

$$\frac{\Delta U}{U} = \frac{\frac{1}{4}\int_{\Delta V}\left(\epsilon\left|E\right|^2 - \mu_0\left|H\right|^2\right)dV}{U}. \tag{5.5}$$

Since the contribution of the electric field is negligible for clean metals [115], Eq. 5.5 is approximated as

$$\frac{\Delta U}{U} \approx -\frac{1}{4}\frac{\int_{\Delta V}\mu_0\left|H\right|^2 dV}{U}. \tag{5.6}$$

The integrated volume depends on the penetration depth λ, such that $dV = d\lambda dA$, where A is the surface area. Considering this volume element and using the definition of the geometric factor G, see Eq. 2.49, the fraction of stored energy is

$$\frac{\Delta U}{U} \approx -\frac{\pi\mu_0 f_0}{G}\Delta\lambda. \tag{5.7}$$

Finally, the change in frequency is related to the change in penetration depth as follows:

$$\Delta\lambda = -\frac{G}{\pi\mu_0 f_0^2}\Delta f, \tag{5.8}$$

where $\Delta f = f\left(T\right) - f_0$, $\Delta\lambda = \lambda\left(T,\,\ell\right) - \lambda\left(0,\,\ell\right)$, and f_0 is the nearly temperature-independent frequency between 0 K and 7 K.

The resonant frequency of the QPR was determined using a VNA. The process begins by immersing the QPR in a LHe bath at 1.8-2 K. An Agilent E5061B VNA is utilized to send a low power signal (<10 dBm or 10 mW) to drive the resonator. The sample temperature is gradually increased from 2 K to 20 K or a higher temperature using the heater. The temperature ramping rate is set to the minimum value of 0.1 K/min, resulting in a measurement process that typically lasts around two hours per quadrupole mode. The VNA settings were optimized to enhance the signal-to-noise ratio, allowing for frequency data to be collected every 15 seconds along with recording the shape of the resonance peak[2]. However, the spectrum obtained from the VNA usually exhibits a noisy signal for frequencies at temperatures $T \geq T_c$. To determine the resonant frequency of the QPR with more accuracy, a fitting procedure is applied to the peak using Eq. 5.9:

[2]The peak is obtained from the transmission coefficient S_{21} using the Log Mag type of measurement of the VNA.

$$S_{21}(f) = \frac{S_{\mathrm{M}}}{1 + 2Q_{\mathrm{L}}\left(\frac{f-f_{\mathrm{r}}}{f_{\mathrm{r}}}\right) i}, \tag{5.9}$$

where Q_{L} is the loaded quality factor, f_{r} is the resonant frequency, and S_{M} is the amplitude of the peak at f_{r}. It is important to note that the peak described in Eq. 5.9 exists in the complex space, whereas the peak obtained with the VNA is a real number in units of decibels (dB). The conversion between these two representations is performed through the formula [116]:

$$|S_{21}(f)|^2\,(\mathrm{dB}) = 20 \cdot \log_{10}\left[S_{21}(f)\right]. \tag{5.10}$$

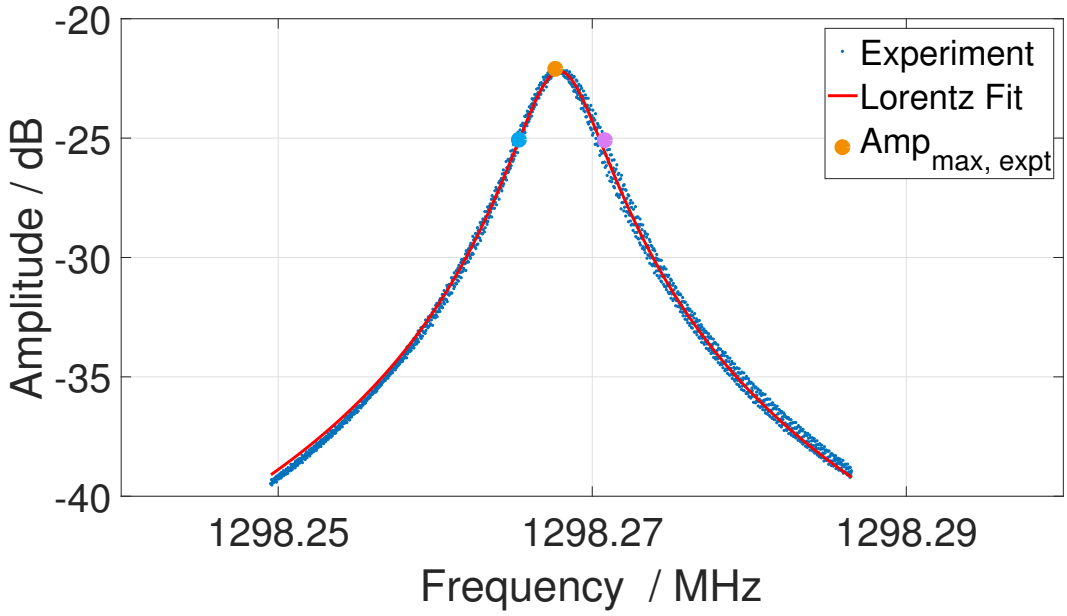

Figure 5.20: Amplitude versus frequency of the third QPR mode at 9.22 K. The orange dot indicates the maximum amplitude of the peak in the experiment, while the blue and purple dots mark the points at 3 dB below the maximum amplitude on both sides of the peak. The red line represents the Lorentz fit based on Eq. 5.11.

Taking the square of the absolute value of Eq. 5.9 gives the equation

$$|S_{21}(f)|^2 = \frac{S_{\mathrm{M}}^2}{1 + 4Q_{\mathrm{L}}^2\left(\frac{f-f_{\mathrm{r}}}{f_{\mathrm{r}}}\right)^2}, \tag{5.11}$$

which is an expression commonly known as the “Lorentz” or “Cauchy–Lorentz” distribution. Furthermore, the loaded quality factor is calculated using the relation:

$$Q_{\mathrm{L}} = \frac{f_0}{2\gamma}, \tag{5.12}$$

where 2γ is the bandwidth of the resonance peak, also known as the “full width at half maximum”. An example of this procedure is shown in Fig. 5.20, where the resonance peak of the third quadrupole mode at 9.22 K was fitted with the Lorentz distribution.

5.4.3 Thermal Conductivity Measurement

The thermal conductivity κ of the sample as a function of temperature was deduced by measuring the DC heating of the sample $\dot{Q}_H$, provided with the heater, and recording the temperature of sensors T_1 and T_4, as observed in Fig. 5.21. Note that the obtained κ value corresponds to that of the sample tube. Therefore, this measurement is facilitated by the QPR for bulk samples only when they are fabricated from the same material batch as the sample tube [100].

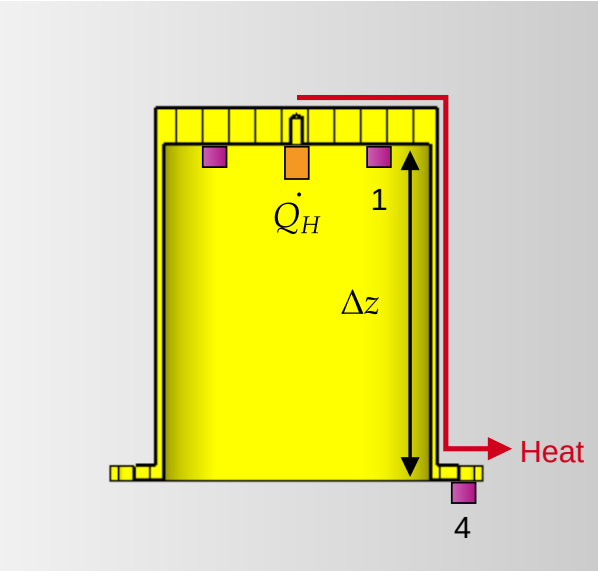

Figure 5.21: Diagram showing the heat path as power $\dot{Q}_H$ is provided to the sample using the heater. The distance $\Delta z = 89\,\text{mm}$ indicates the length of the sample tube.

The thermal conductivity of the sample is obtained from Fourier's law of heat conduction [117], given by Eq. 5.13:

$$\dot{Q}_H = -\kappa\,(T) \cdot A \cdot \frac{\partial T}{\partial z}, \tag{5.13}$$

where A is the cross-sectional area of the sample tube and z is the coordinate indicating the heat propagation path along the sample. For the κ measurements presented in this thesis, heat propagates over a distance of Δz =89 mm between T_1 and T_4. It can be observed in Fig. 5.21 that the length Δz corresponds to that of the sample tube, measured at its maximum inner radius. However, sensor T_1 is positioned below the sample but at a smaller radius. Therefore, the current set up ignores the heat conduction path between the maximum radius and the location of sensor 1. To improve the accuracy of future measurements, temperature sensors will be directly attached to the sample tube as well as to other areas inside the calorimetry chamber.

5.5 Cold Temperature Tests

After the completion of the surface treatment of the QPR at Zanon and its arrival at DESY, the following procedure was implemented to enable the measurements of material properties of the sample at cold temperatures.

5.5.1 Sample Installation

The first sample characterized with the UHH QPR was provided by HZB, and its surface treatment history is shown in Tab. 5.6. This sample is made of Nb with a *RRR* of approximately 300, and it underwent a 110 µm BCP as a final treatment step before delivery. Since no 800 °C annealing was conducted, it was anticipated that the sample would exhibit a Q-disease behaviour. It is worth mentioning that the HZB QPR had not been used to analyse this particular sample before. Therefore, no baseline data was available at the time of its study at DESY.

Table 5.6: Specifications of the HZB sample used in the first cold test of the UHH QPR. Data shared via private communication with Keckert.

Step	Date	Procedure	Results/Remarks	Height (H)/Tilt (T)
1	01.2019	Manufacturing, EB welding, machined by milling	Tilt <60 µm	H 95.13 mm T <49 µm
2	04.02.2019	Mechanical polishing with grinding paper P800	Removed material ∼10-20 µm	H ∼95.12 mm T <35 µm
3	02.2019	BCP RF surface 150 µm		H ∼94.97 mm
4	01.03.2019	800 °C annealing, 4 hours		
5	06.03.2019	BCP full surface 10 µm		H ∼94.96 mm
6	16.05.2019	BCP RF surface 100 µm		H ∼94.87 mm
7	16.12.2021	Height measurement		H 94.80 mm

The sample was attached to the sample adapter flange using a 1.6 mm indium wire to ensure the leak-tightness. This structure was then installed on the bottom flange, employing an Al sealing, in a local cleanroom. Although the nominal design of QPR samples specifies a height of 95 mm, the actual height of the sample was measured to be 94.80 mm, as shown in Tab. 5.6, due to several BCP treatments. With this height and Eq. 4.21, the gap between the sample and pole shoe surfaces was determined to be (1150±74) μm. This gap was used to determine the corresponding constants c_1, c_2, and G for all quadrupole modes in CST. The obtained values of these constants for the three quadrupole modes are presented in Tab. 5.7.

Table 5.7: Frequency f, and QPR constants c_1, c_2, and G corresponding to a gap of $(1150 \pm 74)\,\mu$m. Simulated values obtained in CST Microwave Studio®.

f / MHz	c_1 / 1/m^2	c_2 / T^2/J	G / Ω
424.92	1203.35	0.1202	84.39
856.88	1279.66	0.1184	183.72
1295.59	1414.64	0.1335	272.39

With this gap, the frequencies of the quadrupole modes, measured at room temperature with equal pressure conditions inside and outside the QPR, were found to be Q_1=424.51, Q_2=857.81, and Q_3=1298.54 MHz, respectively.

5.5.2 Installation of the Antennas

In Sec. 4.7.3, it was shown that in order to achieve the coupling of the input antenna β_{inp} of 100 at 2 K, its external quality factor $Q_{\text{ext}}^{\text{inp}}$ is set to 10^7. On the contrary, the external quality factor of the pick-up antenna $Q_{\text{ext}}^{\text{pro}}$ is fixed at a value between 10^{10} and 10^{11}, which results in a coupling β_{pro} in the range of $0.01 - 0.1$. To obtain the desired couplings, the input antenna must be placed in port position A with its loop oriented at 22°, while the pick-up antenna should be installed in position B at 85°, see Figs. 4.28 and 4.29. However, to validate these results, the external quality factors of the antennas were measured.

For the measurements, a forward power P_{forw} of 1 W was supplied to the QPR. After achieving the steady-state, the RF power was switched off, and the traces of the reflected power P_{refl} and transmitted power P_{tran} at the input and pick-up antennas, respectively, were recorded. These traces were analysed to obtain Q_{ext} and β for all of the quadrupole modes, as described in Sec. 3.3.1. The findings are presented in Tab. 5.8. It is worth mentioning that measuring Q_0 is neither required nor possible with the techniques presented in this thesis. Therefore, the quality factors considered for all of the modes are those obtained in simulations, which were provided in Tab. 4.1.

Table 5.8: External quality factors of the input and pick-up antennas, $Q_{\text{ext}}^{\text{inp}}$ and $Q_{\text{ext}}^{\text{pro}}$, and their corresponding coupling constants, β_{inp} and β_{inp}. The coupling was determined considering the simulated intrinsic quality Q_0^{CST} factor at 2 K for the QPR operational modes from the values reported in Tab. 4.1.

f / MHz	Q_0^{CST} (2 K)	$Q_{\text{ext}}^{\text{inp}}$	β_{inp}	$Q_{\text{ext}}^{\text{pro}}$	β_{pro}
Q_1	$1.01{\cdot}10^9$	$6.16{\cdot}10^6{\pm}2.85{\cdot}10^3$	163.96	$7.29{\cdot}10^9{\pm}7.68{\cdot}10^8$	0.14
Q_2	$1.45{\cdot}10^9$	$3.04{\cdot}10^6{\pm}3.83{\cdot}10^3$	476.97	$3.05{\cdot}10^9{\pm}3.78{\cdot}10^8$	0.47
Q_3	$1.70{\cdot}10^9$	$2.17{\cdot}10^6{\pm}3.98{\cdot}10^3$	788.02	$1.61{\cdot}10^9{\pm}2.27{\cdot}10^8$	1.06

It is observed that the simulated $Q_{\text{ext}}^{\text{inp}}$, see Sec. 4.7.3, for the first quadrupole mode is within a 13.60% agreement with the measurements, confirming that the input antenna is over coupled. However, there is a discrepancy between the measured and simulated external quality factor of the pick-up antenna. Nevertheless, the under-coupled condition remains valid for the first two modes. As was mentioned in Sec. 5.4, the energy flowing out of the pick-up antenna is negligible when compared to the energy coupled to the input antenna for all quadrupole modes.

5.5.3 Identification of the Quadrupole Modes

Spectrum measurements of the QPR reveal the presence of 20 resonant modes within the frequency range of 400 MHz to 1400 MHz, as shown in Fig. 4.24. Considering the minimum frequency difference between neighbouring modes is 2.50 MHz, there is a possibility that changes in pressure during cooldown could lead to a swap of mode order. Since the QPR is sensitive to changes in pressure, see Fig. 4.18, the technique established by HZB, mentioned in Sec. 4.6.4, was applied to identify the modes during the cooldown process.

During the first cooldown of the QPR from 300 K to 2 K, the frequencies of Q_1, Q_2, Q_3, and their neighbouring modes were recorded. This process was carried out by filling the cryostat with LHe, decreasing the temperature from 300 to 4.2 K. To reach 2 K, the pressure inside the cryostat was gradually changed from approximately 1100 to 31 mbar. Additionally, a temperature of 1.5 K could be achieved by further reducing the pressure to 4.7 mbar. Fig. 5.22 displays the recorded frequency of Q_1 and the next dipole as a function of cryostat pressure during the cooldown procedure. The tracking of modes Q_2

and Q_3 are displayed in Appx. II. The previous results provided insights into the frequency sensitivity to ambient pressure df/dp, given in Tab. 5.9.

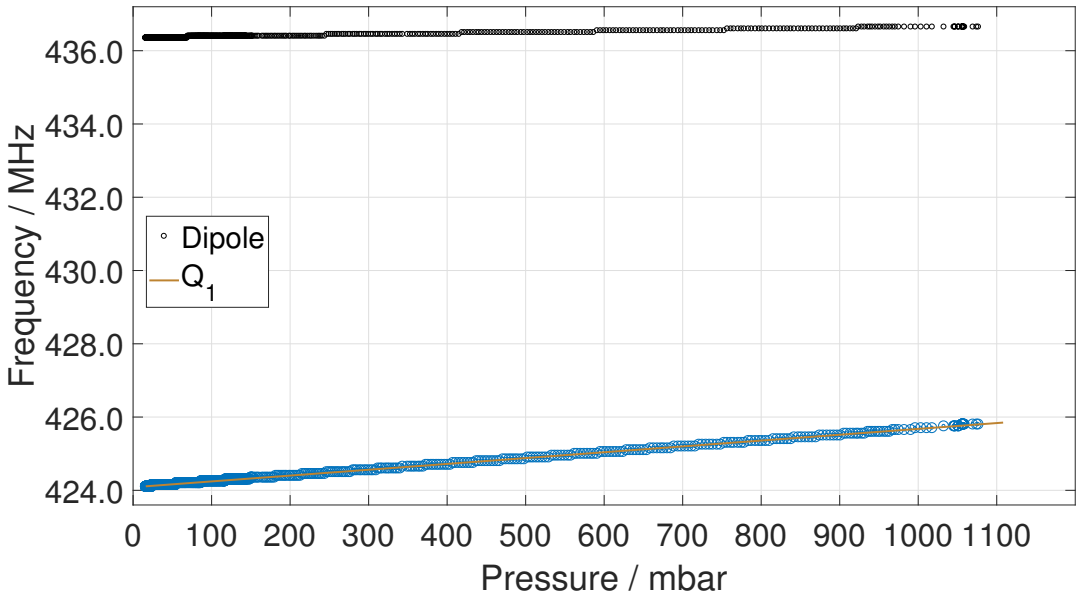

Figure 5.22: Quadrupole mode Q_1 frequency as a function of cryostat pressure during the cooldown process of the QPR from 300 K to 2 K.

It is important to note that the sensitivities of the UHH QPR are comparable to those of the HZB QPR, as reported in Tab. 4.18. However, there is some discrepancy when comparing them to the values of Tab. 5.4. As Keckert [104] mentioned, these values are specific to a particular run, and changes can occur depending on the forces exerted on the QPR by the frame and insert. Therefore, df/dp should be determined again for future runs to ensure accurate data correction.

Table 5.9: Sensitivity of the resonant frequency to the ambient pressure in the cryostat df/dp for the three operational modes.

Frequency at 2 K	424.26 MHz	857.67 MHz	1298.35 MHz
df/dp / Hz/mbar	1592.83±1.24	2536.65±1.22	3162.98±1.23

Finally, under the same pressure inside and outside the resonator at room temperature, the frequency of mode Q_1 is 424.51 MHz, while at 2 K, it is 424.26 MHz. Using Eq. 4.21, this shift in frequency corresponds to an overall increase of the gap of 20 µm due to the shrinkage of the material. This gap change has already been considered in the calculation of constants c_1 and c_2 provided in Sec. 5.5.1.

5.5.4 Cryogenic Pressure Stability and Frequency Changes

During the characterization of the sample, surface resistance measurements were conducted at a temperature of the cryostat of 2 K, while resonance frequency measurements were performed at 1.5 K. The LHe level during these tests was kept at 87%. To maintain a stable temperature of the cryostat of 1.5 K, the average pressure was set at $\langle p \rangle = 4.72$ mbar, with a standard deviation of $\sigma_p = 15.37$ µbar. Using the saturated vapour pressure curve of LHe 4 (see Fig. 5.23) [118], the slope at this temperature is

$$\frac{dT}{dp}\,(1.5\,\mathrm{K}) = 43.69\,\frac{\mathrm{mK}}{\mathrm{mbar}}. \tag{5.14}$$

Therefore, the pressure variation σ_p corresponds to a temperature variation of $\sigma_T = 0.67\,\mathrm{mK}$.

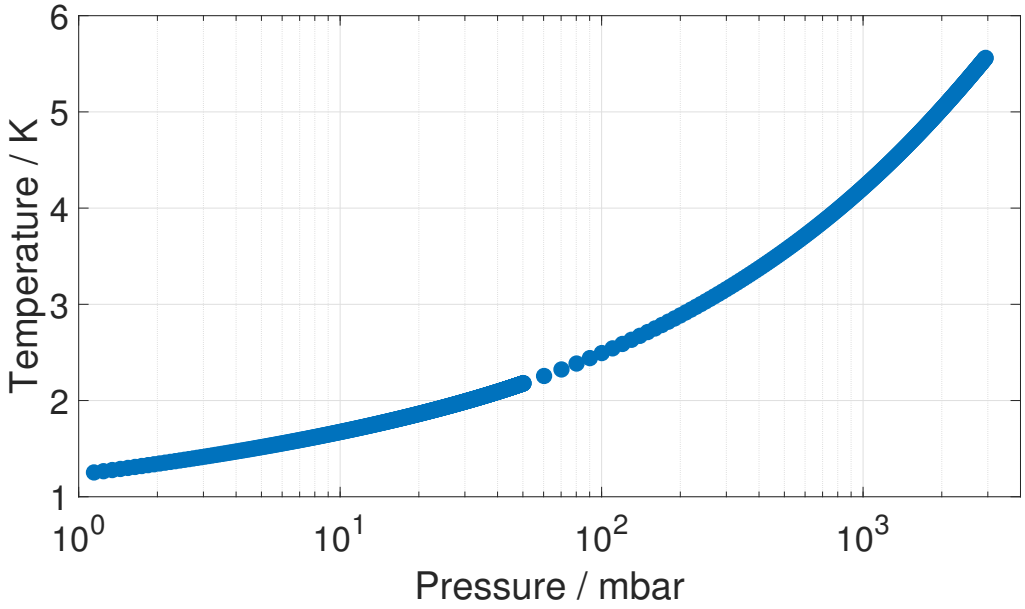

Figure 5.23: Calculated LHe temperature versus saturated vapour pressure. The results were derived from equations given in [118].

Similarly, at 2.0 K, the average pressure of the cryostat was $\langle p \rangle = 31.01\,\mathrm{mbar}$, with a pressure variation of $\sigma_p = 10.17\,\mu\mathrm{bar}$. The slope of the LHe curve at this temperature is

$$\frac{dT}{dp}\,(2.0\,\mathrm{K}) = 10.87\,\frac{\mathrm{mK}}{\mathrm{mbar}}, \tag{5.15}$$

resulting in a temperature change of $\sigma_T = 0.11\,\mathrm{mK}$ due to σ_p. Considering the frequency sensitivity to pressure df/dp of the quadrupole modes, shown in Tab. 5.9, the corresponding frequency variations caused by σ_p are reported in Tab. 5.10.

Table 5.10: Uncertainty or standard deviation resulting from the cryostat pressure variations at 1.5 and 2.0 K, and at a LHe level of approximately 90%.

Mode	σ_f (1.5 K) / Hz	σ_f (2.0 K) / Hz
Q_1	24.48	16.20
Q_2	38.99	25.80
Q_3	48.61	32.17

Furthermore, variations in temperature σ_T resulting from changes in pressure can also lead to fluctuations in heater power P_{DC}. The heater power required to achieve a specific temperature of the sample between 2 and 10 K was measured during the commissioning process, as depicted in Fig. 5.24. Considering the slope of this curve dP/dT for T-sensor 1 at 2 K, the deviation σ_T corresponds to a heater power change of $\sigma_P = 3.89\,\mu\mathrm{W}$. Using Eq. 4.1 for mode Q_1 with σ_P gives the minimum resolvable surface resistance of the QPR (nominal design), resulting in $R_\mathrm{s} = 0.178\,\mathrm{n\Omega}$ at $B_{\mathrm{sample,\,pk}}$ =10 mT and 0.001 nΩ at 120 mT.

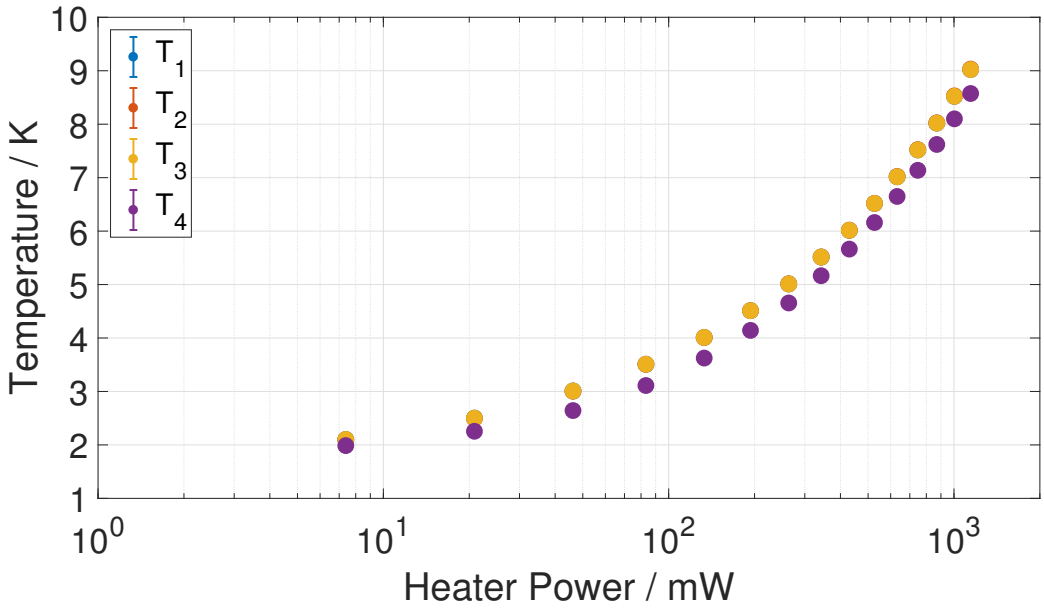

Figure 5.24: Measured sample temperature versus heater power for the four temperature sensors. The error bars are smaller than the symbols.

However, to mitigate the uncertainties in the measurements caused by the cryostat pressure instability, a larger number of data points is considered. This approach reduces the standard error of the measurements, leading to more reliable results.

Chapter 6

First Cold Measurements of a Nb Sample

Within the scope of this thesis, two measurement campaigns were conducted on the same sample. In the first campaign, Test 1, the sample was characterized for the third quadrupole mode, while in the second campaign, Test 2, it was characterized for all three quadrupole modes. This chapter presents the results of the surface resistance of the sample at constant peak magnetic field and temperature for all quadrupole modes. In addition, the frequency and thermal conductivity versus temperature results are discussed.

6.1 Surface Resistance

6.1.1 Surface Resistance at Constant Peak Magnetic Field

The results of the surface resistance versus temperature of the sample at a constant forward power of 1 W (equivalent to a constant peak magnetic field $B_{\mathrm{sample,\,pk}}$ between 10 and 37 mT, depending on the mode) are shown in Fig. 6.1. These measurements confirm that the R_{s} curves follow a dependency consistent with the BCS prediction for the surface resistance for temperatures below T_{c}, which is given by Eq. 3.37. Additionally, it was observed that the sample has a critical temperature of $T_{\mathrm{c}} = 9.27\,\mathrm{K}$.

Although the same forward power was applied, the difference in peak magnetic field $B_{\mathrm{sample,\,pk}}$ on the sample for the different modes is a result of the slightly different field distributions associated with each mode. Furthermore, the difference in R_{s} between the Q_3 curves of Test 1 and 2 is likely attributed to differences in the cooldown rate, although other factors such as multipacting [119] were also considered. However, during the cooldown from 300 to 2 K for Test 1, T_{c} was crossed at a rate of 1.1 K/min, while for Test 2, it was crossed at 0.8 K/min. This suggests that more magnetic flux was trapped (high trapping efficiency) in the sample for Test 2, leading to an increased surface resistance. The development of standardized multipacting processing and cooldown procedures at DESY will be required for future measurements to ensure the reproducibility of the results.

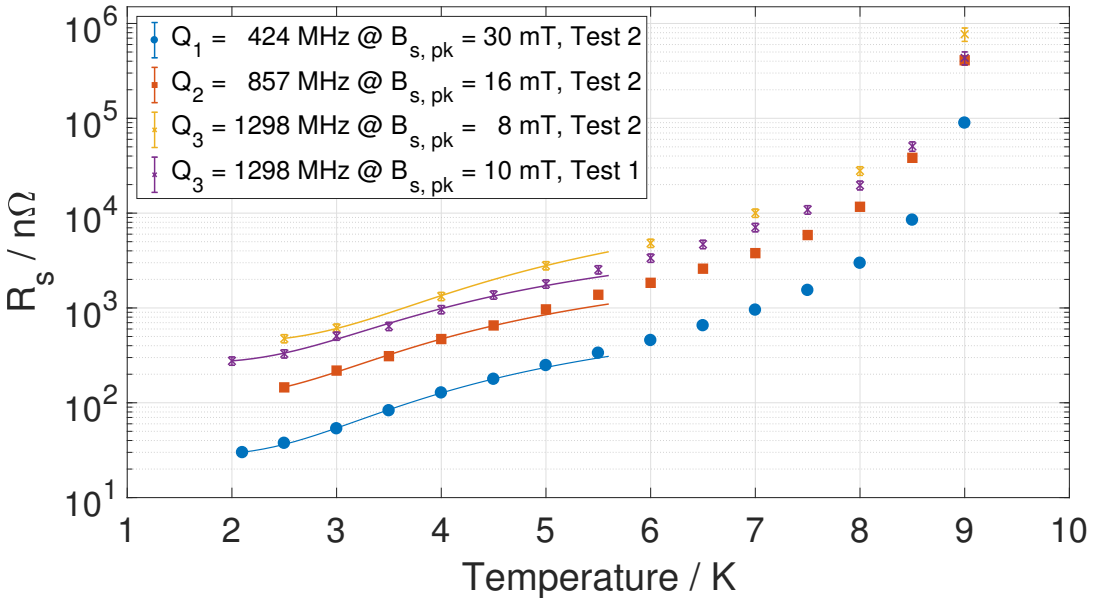

Figure 6.1: Surface resistance R_s versus temperature of a Nb sample for the three operational frequencies at constant peak magnetic field on the sample $B_{\text{sample, pk}}$. Continuous lines correspond to the fitting of the data using Eq. 3.37 valid until $T_c/2$.

The sample surface resistance value for Q_1 at 2 K and 30 mT is (29.93 ± 0.99) nΩ, which is comparable to the measurement at HZB [99] of 28.70 nΩ at 10 mT before the Nb coating of the gasket area of the sample flange, as explained in Sec. 4.3. However, a direct comparison of these two measurements is not straightforward. On the one hand, the HZB measurement corresponds to a Nb thick-film on copper sample and includes the parasitic losses from the normal conducting sample flange, which introduce a systematic bias of R_s. On the other hand, the sample measured at DESY may have been contaminated with hydrogen. The sample R_s at 2.5 K for modes Q_1 and Q_2 of Test 2 and Q_3 of Test 1, as well as their corresponding residual resistance R_{res} and reduced gap $\Delta_{red} = \Delta_0/k_B T_c$, obtained from the fitting of Eq. 3.37 for $T < T_c/2$, are reported in Tab. 6.1. It is observed that the derived values of Δ_{red} are in good agreement with literature values for a Nb sample [120].

Table 6.1: Surface resistance R_s at 2.5 K and other material properties of the sample obtained from fitting of the data using Eq. 3.37, where $k_B = 1.38 \cdot 10^{-23}$ J/K, and $T_c = 9.27$ K.

f / MHz	$R_s(2.5\,\text{K})$ / nΩ	Af^2	$\Delta_{red} = \Delta_0/k_B T_c$	R_{res} / nΩ
424	37.53±1.25	$4.97{\cdot}10^{-5}$	1.95±0.73	27.70±0.54
857	145.35±9.76	$16.30{\cdot}10^{-5}$	1.88±0.43	112.90±3.63
1298	329.52±33.00	$29.68{\cdot}10^{-5}$	1.89±0.57	262.44±11.72

The R_{BCS} for all modes at 2.5 K can be calculated with the first term of Eq. 3.37 or by using J. Halbritter's code (SRIMP) [115], considering a Nb sample with T_c=9.27 K, $\Delta_{red} = 1.90$, $\lambda_L(0) = 39$ nm, $\xi_0 = 38$ nm, and RRR=300 (see Fig. 3.2). In this case, SRIMP was employed, giving the values of 9.23 (Q_1), 32.39 (Q_2), and 67.07 nΩ (Q_3). Subtracting these values from the surface resistance $R_s(2.5\,\text{K})$ of each mode gives the residual surface resistance of Q_1, Q_2, and Q_3 of (28.30±1.25), (112.96±9.76), and (262.45±33.00) nΩ, respectively. These results are consistent with the values obtained directly from fitting the exponential expression of R_s. Furthermore, the obtained reduced gaps, ranging from 1.88 to 1.95 (equivalent to 1.50-1.56 meV), agree with reported values in EP/BCP SRF cavities of 1.95 [121].

However, the residual resistance R_{res} is typically reported without a frequency dependency. As will be shown in Sec. 6.2, the obtained mean free path of the sample falls into the clean limit regime, indicating a frequency-independent sensitivity to trapped flux [122]. Therefore, the behaviour of $R_{\mathrm{res}}(f)$ may suggest RF parasitic heating of the sample flange and coaxial tube as the underlying cause. This phenomenon will continue to be investigated in future tests using different samples or the same one after undergoing chemical or thermal treatments. Nevertheless, accessible studies of the same SRF sample under controlled conditions, such as the analysis of its residual resistance as the function of frequency or applied field, underscore the powerful capabilities of the QPR and its great value in SRF accelerator R&D.

6.1.2 Surface Resistance at Constant Temperature

Surface resistance measurements were conducted to analyse the dependence on $B_{\mathrm{sample,\ pk}}$ at a constant temperature of 4 K, as shown in Fig. 6.2. Noticeably, there was no measurement conducted for mode Q_3 in Test 2. This occurred because the upgrade of the RF system to enable measurements for Q_1 and Q_2 took place during the second test. The improvements implemented reduced the available cryostat time.

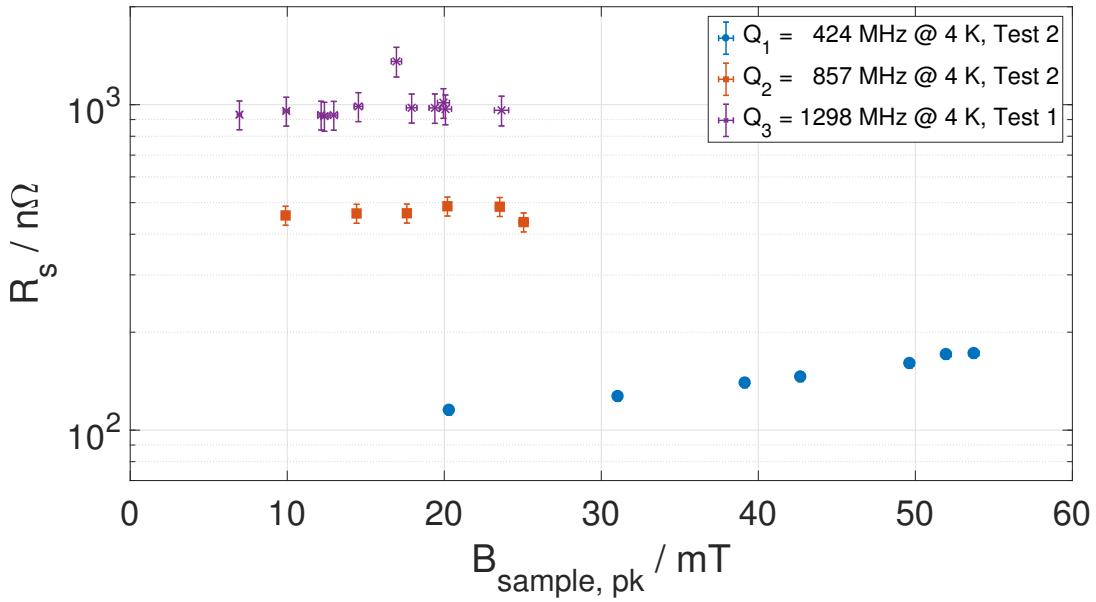

Figure 6.2: Surface resistance R_{s} versus peak magnetic field $B_{\mathrm{sample,\ pk}}$ of a Nb sample for the three operational frequencies at 4 K.

At the peak magnetic field of approximately 20 mT, the R_{s} for Q_1 is measured to be (115.20±3.85) nΩ, while for Q_2 it is (487.54±32.69) nΩ. The difference of these two values satisfies the expected increase of f^2, as shown in Eq. 3.37. The same comparison could not be made for the Q_2 and Q_3 curves since they were measured under different cooldown parameters. However, the R_{s} for Q_3 is (969.43±101.87) nΩ, which is lower than the expected value based on the same scaling. This is attributed to the possibility that less magnetic flux was trapped during Test 1.

The R_{s} measurements presented in this section are limited by thermal quench. During the measurements, it was observed that when setting up the heater power to achieve a stable 4 K temperature on the sample surface, and subsequently switching on the RF power, a rapid increase in temperature above T_{c} took place. This can be expected based on the experience gained from HZB, indicating that the R_{BCS} becomes excessively high at 4 K. This can eventually cause a thermal runaway of the sample when measured at higher B-fields, particularly if Q-disease is present. It should be noted that the reduction of the maximum applicable field is also dependent on the frequency. This observation further supports the

thermal runaway model as the surface resistance scales with f^2. To address this, the next measurements of the sample will involve eliminating the Q-disease by annealing it at 800 °C. This thermal treatment is expected to reduce the surface resistance, making it possible to measure at higher peak magnetic fields.

6.2 Frequency versus Temperature

The frequency of the sample $f\,(T)$ below the critical temperature T_c for the three quadrupole modes was measured in individual thermal cycles. The frequency changes Δf for each data set with respect to 1.5 K are shown in Fig. 6.3. These results confirm, as expected, that the critical temperature of the sample is T_c =9.27 K.

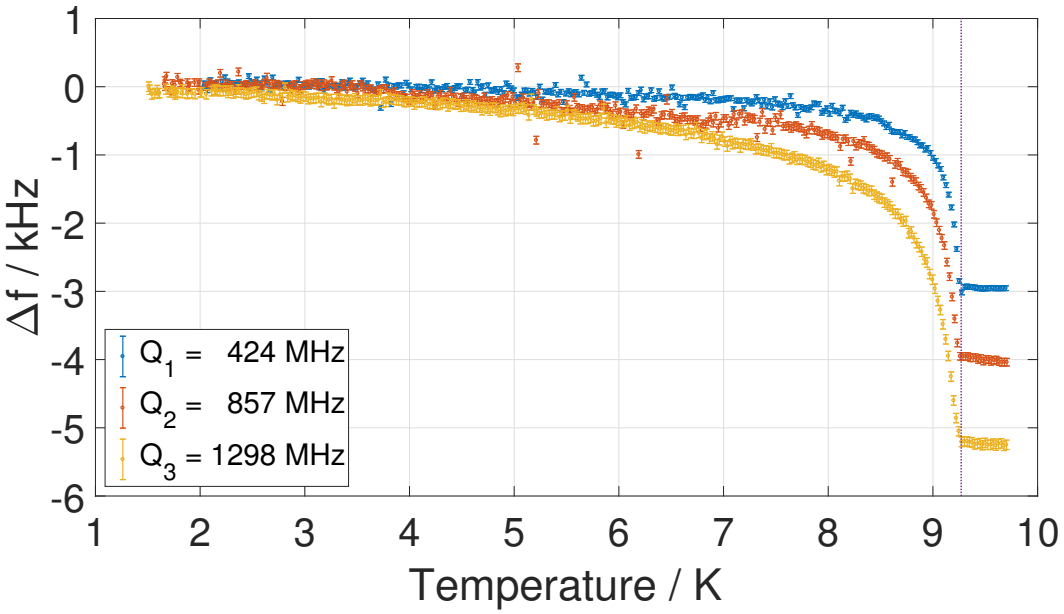

Figure 6.3: Frequency change Δf with respect to $f\,(1.5\,\mathrm{K})$ as a function of temperature for the three operational frequencies. The dotted purple line indicates the temperature of 9.27 K.

The uncertainty of these measurements is primarily influenced by the cryostat pressure stability, as shown in Tab. 5.10. However, some values exhibit significant deviations from the expected curves, likely attributable to errors occurring during the Lorentz distribution fitting procedure of these particular spectra. Such errors may occur if the resonance peak shifts quickly due to rapid pressure changes, leading to an incomplete spectrum data. Nonetheless, this can be solved in future measurements by reducing the recording period to less than the current 15 seconds.

6.2.1 Penetration Depth

The change in penetration depth $\Delta\lambda$ was deduced based on the frequency versus temperature results, as depicted in Fig. 6.4. Notice that the expression of $\Delta\lambda$, given by Eq. 5.8, is expected to be frequency-independent. This is due to the direct dependence of the geometric factor G on frequency, see Eq. 4.5. The curves obtained for $\Delta\lambda$ confirm that the change of penetration depth stays independent of the mode, as shown in Eq. 5.8.

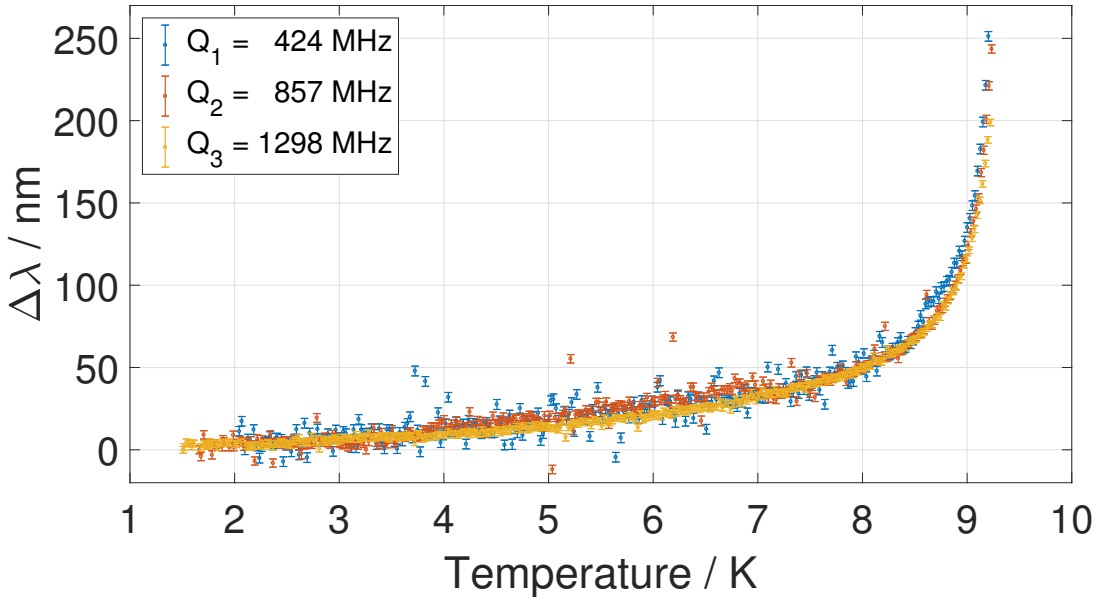

Figure 6.4: Penetration depth change $\Delta\lambda$ versus temperature for the three operational frequencies.

Based on the change in penetration depth, it was possible to determine the *RRR* and the London and effective penetration depths at 0 K, $\lambda_\mathrm{L}(0)$ and $\lambda(0, \ell)$ respectively, of the RF surface of the sample using SRIMP. The mean free path ℓ was determined from the following expression [14]:

$$\ell\,(\mathrm{nm}) = 2.7 \cdot RRR. \tag{6.1}$$

Table 6.2: Calculated material properties of the sample, with $\lambda(0, \ell) = \lambda_\mathrm{L}(0)\sqrt{1 + \xi_0/\ell}$.

f / MHz	424	857	1298
RRR	239.87±20.11	284.95±21.81	292.43±26.68
ℓ / nm	647.65±54.30	769.37±58.89	789.56±72.04
$\lambda_\mathrm{L}(0)$ / nm	38.12±0.01	39.50±0.05	38.77±0.01
$\lambda(0, \ell)$ / nm	40.13±0.11	39.93±0.11	40.28±0.11

Tab. 6.2 shows these material parameters obtained from the fitting routine. The values of the *RRR* align closely with the known value of the sample of approximately 300, with the exception of the 424 MHz mode. However, this discrepancy could originate from the propagation of frequency errors, as indicated in Sec. 6.2, leading to a $\Delta\lambda$ curve for this mode that is more scattered (see Fig. 6.4). Consequently, the SRIMP fitting routine may yield less accurate results. In contrast, the values of $\lambda_\mathrm{L}(0)$ are consistent with values reported in the literature [120] for a Nb sample, where the London penetration depth at 0 K is 39 nm.

6.2.2 Superconducting Surface Reactance

The frequency versus temperature data allows for the determination of the surface reactance in the normal conducting and superconducting states. The normal conducting surface reactance is given by $X_\mathrm{n} = 1.37\,R_\mathrm{n} = 1.37\,G/Q_0\,(10\,\mathrm{K})$, where R_n is the normal conducting surface resistance at 10 K, G represents the geometry factor of each mode, and the factor of 1.37 is deduced from Fig. 6.5. The

calculation of this factor considers the average mean free path of 735.53 nm. The obtained values for the normal conducting surface resistance and reactance are provided in Tab. 6.3.

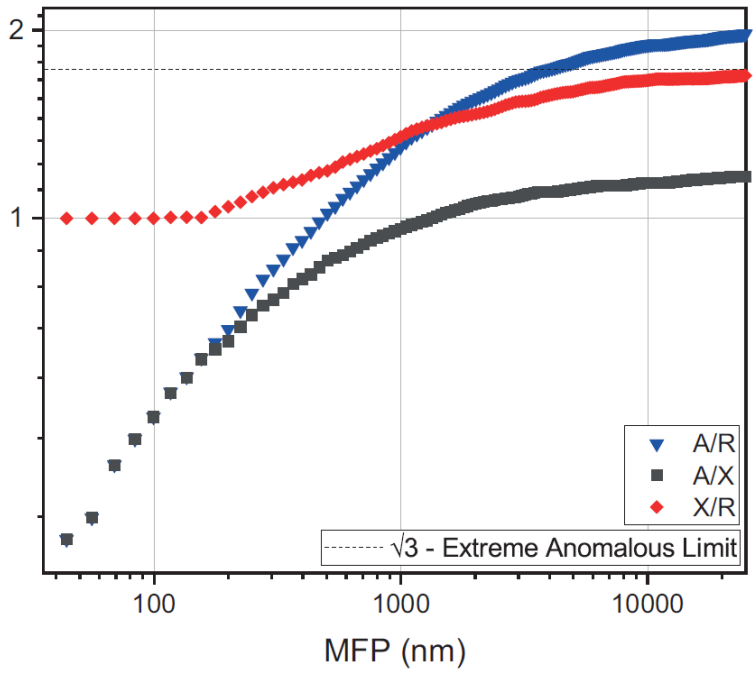

Figure 6.5: Logarithmic plot of normalized resistance (blue down pointed triangles) and reactance (grey squares) for the diffuse reflection case extracted from Figure 1 of G. E. H. Reuter and E. H. Sondheimer in the Proceedings of the Royal Society A [45]. The quotient of the two curves is given in red diamonds. Figure taken from [20].

Then, the superconducting surface reactance is calculated as follows:

$$X_{\mathrm{s}}(T) = -2G \cdot \frac{\Delta f(T)}{f_1} + X_{\mathrm{n}}, \tag{6.2}$$

where $\Delta f(T) = f(T) - f_1$ and f_1 is the frequency at 10 K. The surface reactance of the sample from 1.5 to 10 K for the three quadrupole modes is shown in Fig. 6.6.

The imaginary part of Eq. 3.23 establishes the relationship of the surface reactance with the experimental effective penetration at 0 K, $\lambda^{\mathrm{expt}}(0, \ell)$, which can be expressed as:

$$X_{\mathrm{s}}(0) = \mathrm{Im}[\eta] = \omega\mu_0\lambda^{\mathrm{expt}}(0, \ell). \tag{6.3}$$

However, as observed in Fig. 6.6, the data is available from the temperature of 2 K, but the value of X_{s} appears to be almost temperature independent at lower temperatures. Therefore, to estimate the experimental effective penetration depth $\lambda^{\mathrm{expt}}(0, \ell)$, the value of X_{s} at 2 K is considered. Tab. 6.3 shows these values obtained for all quadrupole modes. In general, the results of $\lambda^{\mathrm{expt}}(0, \ell)$ are in good accordance with values reported in literature and in Tab. 6.2.

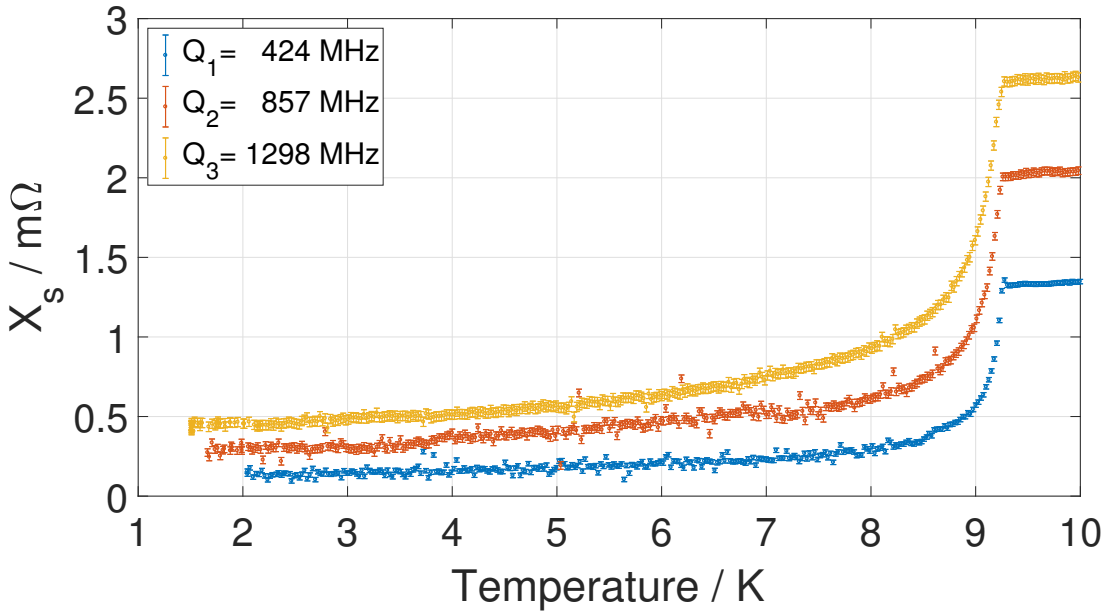

Figure 6.6: Superconducting surface reactance X_s as a function of temperature for the three operational frequencies.

Table 6.3: Normal conducting surface resistance and reactance at 10 K, R_n and X_n respectively, along with the superconducting surface reactance X_s at 2 K, and the deduced experimental effective penetration depth $\lambda^{expt}(0, \ell)$.

f / MHz	424	857	1298
R_n / mΩ	0.98±0.01	1.49±0.02	1.91±0.02
X_n / mΩ	1.35±0.01	2.04±0.02	2.63±0.03
X_s / mΩ	0.14±0.01	0.27±0.02	0.42±0.03
$\lambda^{expt}(0, \ell)$ / nm	41.21±4.11	40.42±3.49	42.91±2.83

6.2.3 Complex Conductivity

Models that describe superconductivity based on the BCS theory often prove to be too simplistic to describe the physics of real materials. This oversimplification is due to the fact that these models neglect Cooper pairs breaking mechanisms, such as current, magnetic impurities, hydrides, and non-stoichiometric regions, all of which exist in real samples. The study of the complex conductivity σ provides insights into the behaviour of quasiparticles and superconducting charge carriers in the presence of pair breaking-factors. D. Bafia [20] gives an expression for σ that involves the surface resistance and reactance in the superconducting state, as follows:

$$\sigma = \sigma_1 + i\sigma_2 = \omega\mu_0 \left[\frac{2R_s X_s}{(R_s^2 + X_s^2)^2} + i\frac{X_s^2 - R_s^2}{(R_s^2 + X_s^2)^2} \right]. \tag{6.4}$$

The real part of the complex conductivity σ_1 exhibits non-monotonic temperature dependence when $\hbar\omega \ll \Delta_0$. This phenomenon is referred to as "coherence peak", and it reaches a maximum around a temperature of $0.90\,T_c$ for Nb at 1.3 GHz. By analysing the height and width of this peak, it is possible to obtain a measure of pair-breaking processes present in the material.

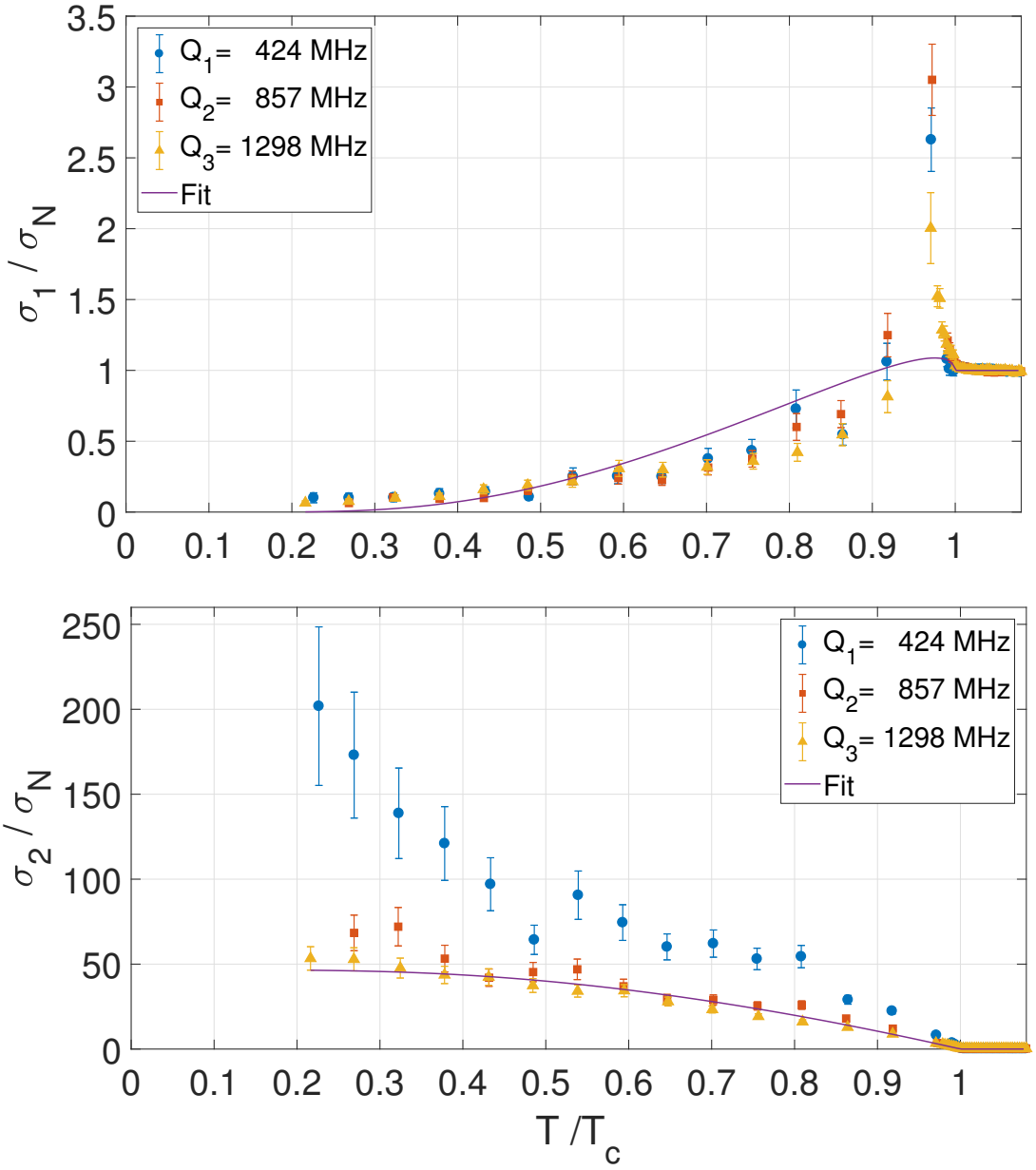

Figure 6.7: Real and imaginary parts of the normalized complex conductivity, σ_1/σ_N and σ_2/σ_N respectively, versus normalized temperature for the three operational frequencies. σ_N is the conductivity in the normal conducting state of the sample at 10 K. The fits displayed were performed following the theory of T. Kubo and correspond to those applied to mode Q_3 [124].

Several authors [20, 123, 124] have proposed models to fit the coherence peak based on the Mattis Bardeen conductivity [125] and on the Eliashberg theory [126]. For instance, T. Kubo introduced a formula for the complex conductivity of a superconductor, which considers the arbitrary concentration of non-magnetic impurities. Within this framework, $\sigma\,(T,\,\omega,\,\Gamma,\,\gamma)$ depends on temperature T, frequency ω, the Dynes inelastic scattering parameter Γ, and the non-magnetic impurity scattering rate γ.

In the case of the QPR sample, the previous R_s and X_s data were used to calculate the normalized complex conductivity σ/σ_N, where σ_N is the conductivity in the normal conducting state at 10 K. The results of the real and imaginary parts of the normalized σ are shown in Fig. 6.7. The coherence peak σ_1/σ_N, was fitted with the model of Kubo to obtain the ratios of γ and Γ with the superconducting gap Δ_0. These values are reported in Tab. 6.4 for all quadrupole modes. Notably, the superconducting gaps Δ_0 of modes Q_1, Q_2, and Q_3 can also be expressed as reduced gaps, with values of 1.95±1.32, 1.96±1.80, and 1.95±1.72, respectively. These results show excellent agreement with the results in Tab. 6.1.

Table 6.4: Material parameters Δ_0, γ/Δ_0, and Γ/Δ_0 obtained from the fitting routine of T. Kubo applied to the coherence peak σ_1/σ_N.

f / MHz	424	857	1298
Δ_0 / meV	1.555±1.036	1.564±1.816	1.560±1.375
Γ/Δ_0	0.040±0.305	0.025±0.180	0.032±0.322
γ/Δ_0	0.055±0.854	0.048±0.421	0.036±0.299

According to Fig. 3.2, the QPR BCP sample analysed fits in the category of moderately clean material, with an average mean free path of approximately 750 nm. Kubo reported that in this category, the condition $\gamma/\Delta_0 \ll 1$ is met. The results obtained from fitting σ_1/σ_N to the sample data show that this condition is satisfied for all the modes. Moreover, the limit $\Gamma/\Delta_0 \ll 1$ characterizes a nearly-ideal superconductor. This is because, when $\Gamma \to 0$, the quasiparticle density of states predicted by the BCS theory is recovered [125]. This additional condition is also met by the results reported in Tab. 6.4, which indicates the absence of nonmagnetic impurities in the material and that the measured R_s fits well with the description of the BCS theory. It is important to highlight that the maxima of the coherence peaks are observed at $0.97\,T/T_c$, while measurements at Fermilab [127] indicate they occur at $0.90\,T_c$. However, according to the values reported in Tab. 6.4, the model of Kubo predicts the maxima at around $0.95\,T/T_c$. In addition, this model shows that height of the peak decreases with increasing frequency, which is consistent with modes Q_1 and Q_3.

Bafia reported the ratios Γ/Δ_0 in the case of EP ($\ell \sim$550±120 nm) and N-Doped ($\ell \sim 70$ nm) cavities, with values of 0.025 and 0.0058, respectively. In the QPR sample, the values of Γ/Δ_0 for all modes fall between 0.028 and 0.037, which are comparable to the reported EP cavity result. Additionally, the superconducting gaps of the sample are in the range of 1.55-1.56 meV, aligning well with the data from the EP cavity, where Δ_0=1.5 meV. The mean free path values were determined using the ratio $\gamma/\Delta_0 = \pi\xi_0/2\ell$, where the coherence length $\xi_0 = 38$ nm, giving the lengths of (852.72±8076.46), (1243.55±9611.58), and (1658.06±13817.20) nm for the coherence peaks of Q_1, Q_2, and Q_3, respectively. While the calculated mean free path for the peak of mode Q_1 closely approximates the previously determined value of 750 nm, the standard errors associated with these measurements are excessively large.

Further studies are required to validate the comparison of the Dynes parameter between BCP and EP samples, as well as with BCP and EP cavities. Additionally, optimising the measurement techniques employed in the QPR will make it possible to increase the number of data points of R_s in order to reduce the standard errors in Tab. 6.4.

6.3 Thermal Conductivity

The thermal conductivity $\kappa(T)$ of the sample was determined with Eq. 5.13, see Fig. 6.8. This experimental result is in accordance with values reported for Nb samples with RRR=300 [128] and 307 [129]. Notably, it is observed that at temperatures below T_c, the thermal conductivity follows the predictions of the BCS theory. According to this theory, at these temperatures, the electrons form Cooper pairs and cannot transport thermal energy as they do not scatter with the lattice. The curve is extrapolated to determine the thermal conductivity at 4.2 K. As mentioned in Sec. 5.4, the measurement of κ corresponds to the sample tube, and it is the same as the sample only when they are fabricated from the same material batch.

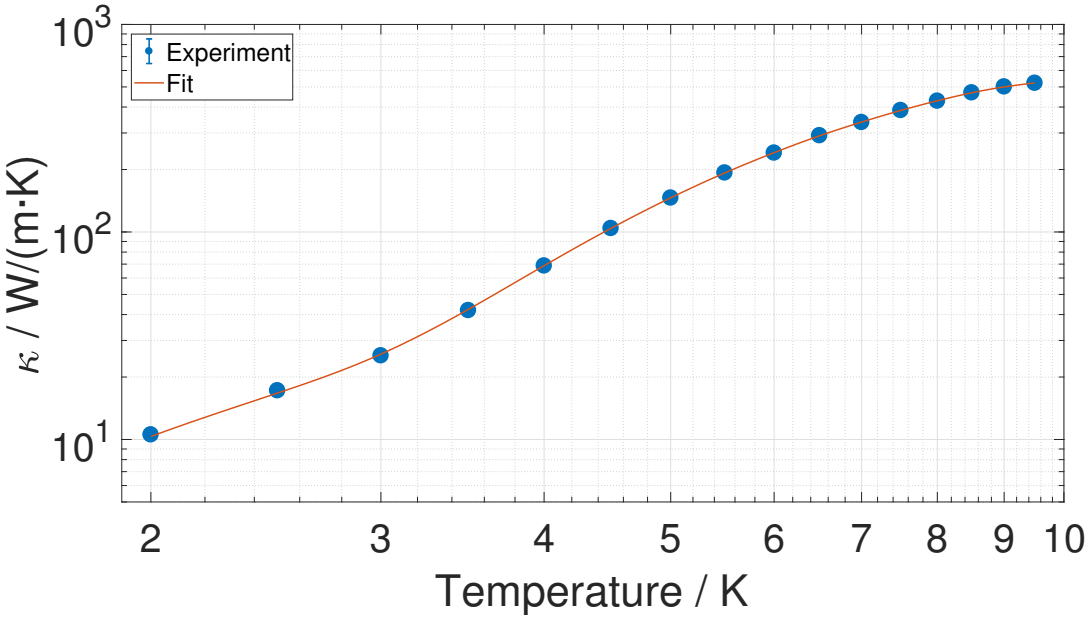

Figure 6.8: Thermal conductivity κ versus temperature of the sample tube.

With this, the RRR and the mean free path ℓ are calculated as follows [14]:

$$RRR = 4 \cdot \kappa\,(4.2\,\mathrm{K}) = 327.93 \pm 2.86 \tag{6.5}$$

$$\ell\,(\mathrm{nm}) = (885.40 \pm 7.73)\ \mathrm{nm}, \tag{6.6}$$

where the uncertainty is determined as the overall standard error of the fit. The RRR appears to agree with the known purity of the sample studied, which is assumed to have a value of 300.

Considerable differences exist between the mean free path ℓ calculated in this section and those reported in Tab. 6.2. This discrepancy occurs because the mean free path, calculated using Eq. 6.5, is associated with that of the RF surface in conjunction with the bulk material of the sample disk and sample tube. Conversely, the values in the table are derived using the SRIMP code applied to the frequency versus temperature data, exclusively probing a nanometric layer from the sample RF surface. The reduction in ℓ observed in the latter is expected, considering that for a $RRR = 300$ Nb sample after a BCP treatment, hydrogen mainly concentrates near the sample RF surface, precisely at the Nb-oxide interface. The hydrogen-rich region (up to 25 at.%) extends over a layer of about 10 nm, gradually decreasing into the bulk, where the content falls below 1 at.% [130].

Despite the cooldown rate of the tests presented in this work being considered sufficiently quickly to prevent the formation of hydrides (see Sec. 6.1.1), there is still a possibility of hydride precipitation at the lattice atoms and defects within the hydrogen-rich layer. This precipitation could potentially cause a reduction in the mean free path. Additionally, other elements like oxygen, nitrogen, and carbon may have entered the sample during its treatment and installation, contributing to this reduction in ℓ. In future measurement campaigns with the QPR, advance surface characterization studies, such as laser confocal microscopy, could be implemented to investigate hydride formation in the samples [82] and assess the content of other elements, thus complementing the material characterization study.

Chapter 7

Summary

Sample characterization plays a crucial role as a preliminary step prior to coating entire SRF cavities made of Nb or implementing new surface treatments. Test devices that enable such studies significantly contribute to the advancement of Nb-alternatives in the field of SRF accelerator R&D. To facilitate systematic studies of superconducting samples across the resonant frequency f, temperature T, and applied magnetic field B, a collaborative effort between Universität Hamburg and DESY has led to the development and construction of a new and improved QPR. This QPR satisfies the requirements for R&D of easier sample test preparation when compared to vertical tests of cavities.

The UHH QPR was designed in a collaboration between Universität Hamburg and Universität Rostock based on the successful system at HZB. This QPR was manufactured and surface treated, as a standard SRF cavity following the Eu-XFEL recipe, at Zanon and successfully commissioned at DESY. Through design optimization, the rigidity of the rods was increased, offering simplified operation thanks to its reduced detuning. In addition, cooling channels were machined into the sample flange to allow for the flow of LHe. This feature minimizes parasitic heat on the gasket area and, consequently, on the RF surface of the sample. The QPR device enables comprehensive investigations of 75 mm superconducting samples at 424, 857, and 1298 MHz, from temperatures of 1.5 K and designed applied magnetic fields up to 120 mT, with the latter to be demonstrated in upcoming measurements.

The characterization of a Nb sample provided by HZB led to the determination of material parameters that exhibit excellent agreement with literature values for Nb. The surface resistance as a function of temperature and peak magnetic field curves follow the prediction of the exponential expression of R_s, which includes the BCS term, for temperatures $T < T_\mathrm{c}/2$. Fitting these curves with this exponential equation yielded the determination of material parameters. These parameters include the reduced gap Δ_red within the range of 1.88-1.95 and the frequency-dependent residual resistance R_res of 27.70, 112.90, and 262.44 nΩ at 424, 857, and 1298 MHz, respectively. Ongoing analysis includes the study of residual resistance dependency on the frequency.

Measurements of the resonant frequency as a function of temperature allowed for determining the critical temperature T_c of 9.27 K, mean-free path ℓ of approximately 735.53 nm, and the London and effective penetration depths at 0 K, $\lambda_\mathrm{L}(0)$ and $\lambda(0, \ell)$ respectively, of 39.50 nm and 40.05 nm. This data also facilitated the determination of the superconducting surface reactance X_s and the complex conductivity $\sigma = \sigma_1 + i\sigma_2$. An analysis of the superconducting surface reactance X_s data led to the experimental effective penetration at 0 K, denoted $\lambda^\mathrm{expt}(0, \ell)$, which aligns well with the previous result. In this thesis, the first frequency-dependent measurement of the coherence peak σ_1 at three modes has been presented. Based on the theory of Kubo, this study resulted in the determination of the normalized

Dynes and impurity rate parameters, Γ/Δ_0 and γ/Δ_0 respectively, ranging from 0.025-0.040 and 0.036-0.055. Additionally, the superconducting gaps Δ_0 were determined and found to fall within the range of 1.55-1.56 meV. These results are consistent with the values found in the work of Bafia in an EP cavity.

Finally, the thermal conductivity κ as a function of temperature was measured, and its value at 4.2 K was determined. This made it possible to obtain the mean free path of the bulk material of the sample, which was found to be 885.40 nm. This value of the mean free path approximately agrees with the known purity of the sample, which is assumed to have a value of 810 nm. Future tests with the QPR will be complemented with advance surface characterization studies, such as laser confocal microscopy, to investigate hydride formation in the sample and estimate other elemental content that may modify the mean free path. These findings highlight the powerful capabilities of the QPR and its valuable role in SRF accelerator R&D.

Outlook

Looking ahead, the following points outline possible measurements with samples and improvements that could enhance the measurement capabilities of the QPR:

In the short term at DESY, the next measurement that can be performed corresponds to the characterization of the available sample after it has been annealed at 800 °C. This characterization would make it possible to observe the differences in its material parameters with and without the "Q-disease" as the annealing procedure degasses the sample. The observed increased surface resistance as a function of peak magnetic field of the sample, which was attributed to the hydrogen contamination, could be reduced by annealing it, allowing for extending the maximum magnetic field applied.

To extend the surface resistance measurements to temperatures of 10 K, it would be required to replace the RadiPower RPR2006P power meters, which have a resolution of 1 µs, with power meters capable of resolving on the nanosecond scale. This is because the decay times τ_L observed during the measurements in this thesis ranged from 0.27 to 2.30 ms. When the RF power is switched off at 9.5 K, the reflected power trace decays faster than a microsecond, making it impossible to fit with the exponential decay equation. Extending the R_s temperature range would benefit the study of the complex conductivity σ as this value requires the intrinsic quality factor at 10 K.

Improvements in the calorimetry chamber setup, such as adding more temperature sensors to the sample tube wall, could lead to a more accurate determination of the thermal conductivity of the sample. Additionally, including a coil system for the controlled application of the magnetic field to the bottom surface of the sample would enable studies of trapped magnetic flux.

Upcoming new samples can be analysed with the QPR after undergoing the standard surface treatment for SRF cavities. Moreover, the QPR is prepared to perform the RF characterization studies of samples subjected to mid-T heat treatments and coated with materials such as SIS and other thin-films.

Bibliography

[1] D. Barak, B. Harrison, and A. Watts. Concepts Rookie Book. *Fermilab Accelerator Division - Operations Department*, 2017.

[2] B. Aune et al. Superconducting TESLA cavities. *Phys. Rev. ST Accel. Beams 3*, 092001, 2000. doi: 10.1103/PhysRevSTAB.3.092001

[3] D. M. Pozar. Microwave Engineering. *Hoboken, NJ: Wiley*, 2012.

[4] D. J. Griffiths. Introduction to Electrodynamics. *Boston: Pearson*, 2013.

[5] D. Proch. Superconducting cavities for accelerators. *Rep. Prog. Phys.* 61 431, 1998.

[6] H. J. Weber and G. B Arfken. Essential Mathematical Methods for Physicists. *ISE London: Academic Press*, 2003.

[7] Wolfram Research, Inc., "Mathematica 13.0," 2021.

[8] D.W. Jordan and D. E. Hughes. Self-induction and the Skin-Effect. *Centaurus*, 26: 123-153, 1982. doi: https://doi.org/10.1111/j.1600-0498.1982.tb00658.x

[9] D. M. Siegel. Electrodynamics from Ampère to Einstein. *Physics Today 55*, 53-53, 2002. doi: https://doi.org/10.1063/1.1461329

[10] https://media.desy.de/

[11] Computer Simulation Technology AG. CST Studio Suite®. Release Version 2021.05, Dassault Systemes Deutschland GmbH.

[12] ANSYS HFSS: Everything to Know - Explore the Future of Engineering: 3D Modeling, CAD and More. 2020-01-04. Retrieved 2022-03-04.

[13] K. Akai, N. Akasaka, K. Ebihara, E. Ezura, T. Furuya, et al. RF systems for the KEK B-Factory. *Nuclear Instruments and Methods in Physics Research Section A: Accelerators, Spectrometers, Detectors and Associated Equipment. Elsevier BV.* 499 (1): 45–65, 2003. doi:10.1016/s0168-9002(02)01773-4. ISSN 0168-9002

[14] H. Padamsee, J. Knobloch, and T. Hays. RF Superconductivity for Accelerators. *Wiley-VCH Verlag*, Weinheim, 2008.

[15] D. A. Edwards and M. J. Syphers. An Introduction to the Physics of High Energy Accelerators. *Wiley-VCH Verlag*, Weinheim, 2004.

[16] T. Inagaki, C. Kondo, H. Maesaka, T. Ohshima, Y. Otake, T. Sakurai, K. Shirasawa, and T. Shintake. High-gradient C-band linac for a compact x-ray free-electron laser facility. *In Physical Review Special Topics Accelerators and Beams* 17.8, p. 080702, 2014.

[17] J. Sekutowicz, V. Ayvazyan, J. Branlard, M. Ebert, J. Eschke, T. Feldmann, A. Gössel, D. Kostin, M. Kudla, F. Mittag, et al. Feasibility of CW and LP Operation of the XFEL Linac. *In Proc. of 35 Free–Electron Laser Conf. (FEL13)*, pp. 189–192, 2013.

[18] M. Wenskat. Automated Surface Classification of SRF Cavities for the Investigation of the Influence of Surface Properties onto the Operational Performance. Ph. D. Thesis, Universität Hamburg, 2015.

[19] A. Romanenko, A. Grassellino, F. Barkov, and J. P. Ozelis. Effect of mild baking on superconducting niobium cavities investigated by sequential nanoremoval. *Phys. Rev. Spec. Top. Accel. Beams*, Vol. 16, p. 012001, 2013. doi:10.1103/PhysRevSTAB.16.012001

[20] D. Bafia. PhD thesis, Illinois Institute of Technology, 2020.

[21] H. Kamerlingh Onnes. *Commun. Phys. Lab.* Univ. Leiden 120b-123b, 1911.

[22] H. Kamerlingh Onnes and J. Clay, *Commun. Phys.* Lab. Univ. Leiden 95d, reprinted in Proc. K. Ned. Acad. Wet. 9, 213, 1906.

[23] H. Kamerlingh Onnes and J. Clay, *Commun. Phys. Lab.* Univ. Leiden 99b, reprinted in Proc. K. Ned. Acad. Wet. 10, 200, 1907.

[24] M. Parizh, Y. Lvovsky, and M. Sumption. Conductors for Commercial MRI Magnets Beyond NbTi: Requirements and Challenges. *Supercond. Sci. Technol. 2017,* Jan. 30(1):014007, 2017. doi: 10.1088/0953-2048/30/1/014007. Epub 2016 Nov 16. PMID: 28626340; PMCID: PMC5472374.

[25] K. Sawada. Outlook of the Superconducting Maglev. *In Proceedings of the IEEE* 97, 1881-1885. 2009.

[26] D. Larbalestier, A. Gurevich, D. Feldmann, et al. High-Tc Superconducting Materials for Electric Power Applications. *Nature* 414, 368–377, 2001. doi: https://doi.org/10.1038/35104654

[27] M. Polini, F. Giazotto, K. C. Fong et al. Materials and Devices for Fundamental Quantum Science and Quantum Technologies. *arXiv preprint* arXiv:2201.09260, 2022.

[28] A. Drozdov, M. Eremets, I. Troyan et al. Conventional Superconductivity at 203 Kelvin at High Pressures in the Sulfur Hydride System. *Nature* 525, 73–76, 2015. doi: https://doi.org/10.1038/nature14964

[29] A. Godeke. Nb_3Sn for Radio Frequency Cavities. *Tech. rep.* 62140. LBNL, 2006. url: https://escholarship.org/uc/item/6d3753q7.

[30] W. Meissner and R. Ochsenfeld. Ein neuer effekt bei eintritt der supraleitfhigkeit. *Physica Naturwissenschaften* 21, p. 787, 1933.

[31] M. Tinkham. Introduction to Superconductivity. *Dover Publications*, 2004. ISBN: 0486435032.

[32] J. N. Rjabinin and L. V. Schubnikow. Magnetic Properties and Critical Currents of Supraconducting Alloys. *Nature* 135, 581–582, 1935. doi: https://doi.org/10.1038/135581a0

[33] A. A. Abrikosov. *Zh. Éksp. Teor. Fiz.* 32, 1442, 1957. [*Sov. Phys.* JETP 5, 1174 (1957)].

[34] L. Ginzburg and L. D. Landau. On the Theory of Superconductivity. *Sov. Phys.* JETP, 20, 1064, 1950.

[35] J. Bardeen, L. N. Cooper, and J. R. Schrieffer. *Phys. Rev.* 106, 162, 1957.

[36] C. J. Gorter and H. B. G. Casimir. *Physik. Z.* 35, 963, 15, 539, 1934.

[37] S. Pal, et. al. Gorter-Casimir two fluid model revisited and possible applications to superconductivity. *International Journal of Innovative research in physics*, 2020. doi: 10.15864/ijiip.1103

[38] M. Wolfke and W. H. Keesom. *Proc. Amst.* 31, 81, 1927. [W. H. Keesom and M. Wolfke, Leiden. *Comm.* 190b, (1927)].

[39] F. London and H. London. The Electromagnetic Equations of the Supraconductor. *Proceedings of the Royal Society A*, 149, 71-88, 1935. doi: https://doi.org/10.1098/rspa.1935.0048

[40] J. D. Jackson. Classical Electrodynamics. *New York:Wiley*, 1999.

[41] J. Turneaure and I. Weissman. Microwave surface resistance of superconducting niobium. *J. Appl. Phys.*, vol. 39, p. 4417, 1968.

[42] A. B. Pippard. The surface impedance of superconductors and normal metals at high frequencies V. Analysis of experimental results for superconducting tin. *Proc. R. Soc. Lond. A,* 203, p. 195, 1950.

[43] A. B. Pippard. An experimental and theoretical study of the relation between magnetic field and current in a superconductor. *Proc. R. Soc. Lond. A* 216, p. 547, 1953.

[44] R. G. Chambers. The Anomalous Skin Effect. *Proceedings of the Royal Society of London. Series A, Mathematical and Physical Sciences* 215, no. 1123: 481–97, 1952. http://www.jstor.org/stable/99095

[45] G. E. H. Reuter and E. H. Sondheimer. The theory of the anomalous skin effect in metals. *Proc. R. Soc. Lond. A* 195 (1042), p. 336, 1948.

[46] P. AO, D.J. Thouless, and X.-M. Zhu. Nonlinear Schrödinger equation for superconductors. *M. Phys. Lett. B.* 09, 755-761, 1995.

[47] C. Benvenuti, S. Calatroni, I. E. Campisi, P. Darriulat, M. A. Peck, R. Russo, and A.-M. Valente. *Physica C* 316, 153, 1999.

[48] W. Singer, A. Ermakov, and X. Singer. RRR-Measurement Techniques on High Purity Niobium. *TTC Meeting 2010.* 27, 49, 50, 51, 61, 2010.

[49] L. P. Pitaevskii and S. Stringari. Bose–Einstein Condensation. *Oxford: Clarendon Press.,* 2003. ISBN 978-0-19-850719-2

[50] L. P. Gor'kov. Microscopic Derivation of the Ginzburg-Landau Equations in the Theory of Superconductivity. *Sov. Phys. JETP*, 36, 1364, 1959.

[51] N. Valles and M. Liepe. The Superheating Field of Niobium: Theory and Experiment. *In Proceedings of the 15th Int. Conf. on RF Superconductivity*, SRF2015, Chicago, IL, USA, 2015.

[52] J. I. Gittleman and B. Rosenblum. *Phys. Rev. Lett.* 16, 734, 1966.

[53] A. Grassellino et al. Nitrogen and argon doping of niobium for superconducting radio frequency cavities: a pathway to highly efficient accelerating structures. *Superconductor Science and Technology*, Vol. 26, no. 10, p. 102001, 2013. doi:10.1088/0953-2048/26/10/102001

[54] A. Grassellino et al. Unprecedented quality factors at accelerating gradients up to 45 MV/m in niobium superconducting resonators via low temperature nitrogen infusion. *Superconductor Science and Technology*, vol. 30, no. 9, p. 094004, 2017. doi:10.1088/1361-6668/aa7afe

[55] S. Posen, A. Romanenko, A. Grassellino, O. S. Melnychuk, and D. A. Sergatskov. Ultralow Surface Resistance via Vacuum Heat Treatment of Superconducting Radio-Frequency Cavities. *Physical Review Applied*, Vol. 13, p. 014024, 2020. doi:10.1103/PhysRevApplied.13.014024

[56] S. Posen and D. L Hall. *Supercond. Sci. Technol.* 30 033004, 2017.

[57] A. M. Valente-Feliciano. Superconducting RF materials other than bulk niobium: a review. *Superconductor Science and Technology*, Vol. 29, no. 11, p. 113002, 2016. doi:10.1088/0953-2048/29/11/113002

[58] A. M. Valente-Feliciano et al. Next-generation superconducting RF technology based on advanced thin-film technologies and innovative materials for accelerator enhanced performance and energy reach. *arXiv*:2204.02536, 073901, 2022.

[59] A. Gurevich. Enhancement of rf breakdown field of superconductors by multilayer coating. *Appl. Phys. Lett.*, vol. 88, p. 012511, 2006. doi:10.1063/1.2162264

[60] A. Gurevich. Theory of RF superconductivity for resonant cavities. *Supercond. Sci. Technol.* 30, 3, 034004, 2017.

[61] J. Nagamatsu, N. Nakagawa, T. Muranaka, Y. Zenitani, and J. Akimitsu. Superconductivity at 39 K in magnesium diboride. *Nature*. 410 (6824): 63–4. Bibcode:2001Natur.410...63N, 2001. doi:10.1038/35065039

[62] M. Eisterer. Magnetic properties and critical currents of MgB_2. *Superconductor Science and Technology,* 20 (12): R47–R73. Bibcode:2007SuScT..20R..47E, 2007. doi:10.1088/0953-2048/20/12/R01. S2CID 123577523

[63] M. Wenskat, G. K. Deyu, I. González Díaz-Palacio, R. H. Blick, R. Zierold, and W. Hillert. Successful Al2O3 coating of superconducting niobium cavities with thermal ALD. *Supercond. Sci. Technol.* 36(1), 015010, 2023.

[64] I. González Díaz-Palacio, M. Wenskat, G. Kacha Deyu, W. Hillert, R. H. Blick, and R. Zierold. Thermal annealing of superconducting niobium titanium nitride thin-films deposited by plasma-enhanced atomic layer deposition. *Journal of Applied Physics,* 134(3):035301, 07, 2023.

[65] C. Schmidt, G. Lichtenberg, W. Koprek, W. Jalmuzna, H. Werner, and S. Simrock. Parameter estimation and tuning of a multivariable RF controller with FPGA technique for the Free Electron Laser FLASH. *In 2008 American Control Conference. IEEE*, pp. 2516–2521, 2008.

[66] T. Powers. Theory and Practice of Cavity RF Test Systems. *12th International Workshop On RF Superconductivity*, N. p. 10-15, Ithaca, New York, United States, 2006.

[67] J. Branland et al. LLRF Design for the HINS-SRF Test Facility at Fermilab. *In Proc. LINAC'10*, Tsukuba, Japan, paper MOP083, 2010.

[68] A. Bellandi. LLRF Control Techniques for the European XFEL Continuous Wave Upgrade. Ph.D. thesis, Universität Hamburg, Hamburg, Germany, 2021.

[69] T. Kubo. Magnetic Field Enhancement at a Pit on the Surface of a Superconducting Accelerating Cavity. *Prog. Theor. Exp. Phys. 2015*, p. 073G01, 2015.

[70] H. Padamsee. Superconducting Radiofrequency Technology for Accelerators: State of the Art and Emerging Trends. *Wiley-VCH Verlag*, Weinheim, 2023.

[71] Yla-Oijala P. *Part. Accel.*, 63, p. 105, 1999.

[72] R. Prakash, A. Ratan Jana, and V. Kumar. Multipacting studies in elliptic SRF cavities. *Nuclear Instruments and Methods in Physics Research Section A: Accelerators, Spectrometers, Detectors and Associated Equipment*, Volume 867, Pages 128-138, ISSN 0168-9002, 2017. doi: https://doi.org/10.1016/j.nima.2017.06.003

[73] P. Yla-Oijala et al. MULTIPAC – Multipacting simulation package with 2D FEM field solver. *SRF 2001*, Tokyo, Japan, 2001.

[74] R. Ferraro et al. Guide to Multipacting/Field Emission Simulation Software, 6th Edition. *Cornell LNS Report SRF/D*-961126/10, 1996.

[75] J. Knobloch, W. Hartung, and H. Padamsee. *In 8th Workshop on RF Superconductivity.* Vol. 09, Padova, Italy, 1997.

[76] B. Bonin. Field emission in RF cavities. *CERN course on Particle Accelerators*, Hamburg, May, 1995.

[77] J. Knobloch. The "Q-disease" in Superconducting Niobium RF Cavities. *AIP Conference Proceedings* 671, 133, 2003. doi: https://doi.org/10.1063/1.1597364

[78] L. Lilje. Buffered Electrochemical Polishing of Niobium. Ph. D. Thesis, University of Hamburg, 2001.

[79] V. Palmieri. Fundamentals of Electrochemistry - The Electrolytic polishing of Metals: Application to Copper and Niobium. *SRF Workshop 2003*, Germany, 2003.

[80] C. Z. Antoine and S. Berry. H in Niobium: Origin And Method Of Detection. *AIP Conference Proceedings* 671, 176, 2003. doi: https://doi.org/10.1063/1.1597367

[81] M. Wenskat, J. Čižek, M. O. Liedke, et al. Vacancy-Hydrogen Interaction in Niobium during Low-Temperature Baking. *Sci Rep* 10, 8300, 2020. https://doi.org/10.1038/s41598-020-65083-0

[82] F. Barkov, A. Romanenko, and A. Grassellino. *Phys. Rev. ST Accel. Beams* 15, 122001 – Published 4 December, 2012.

[83] S. Isagawa. Hydrogen absorption and its effect on low-temperature electric properties of niobium. *J. Appl. Phys.* 51, 4460–4470, 1980.

[84] P. Goudket, T. Junginger, and B. P. Xiao. Devices for SRF material characterization. *Superconductor Science and Technology*, vol. 30, no. 1, p. 013001, 2016. doi:10.1088/ 0953-2048/30/1/013001

[85] E. Haebel et al. Cavity shape optimization for a superconducting linear collider. *In Proc. 15th Int. Conf. on High Energy Acc.* HEACC'92, 2 (Hamburg, Germany, July), 957, 1992.

[86] W. Singer et al. Specification Documents for Production of European XFEL 1.3 GHz SC Cavities. *DESY*, 2009.

[87] T. Raubenheimer. The LCLS-II-HE, A High Energy Upgrade of the LCLS-II. *In Proc. 60th ICFA Advanced Beam Dynamics Workshop on Future Light Sources (FLS 2018)*, Shanghai, China, p 6-11, 2018. doi:10.18429/JACoWFLS2018-MOP1WA02

[88] H. T. Hou. SRF Status of the SHINE Project at Shanghai. *In Proceedings of the 19th Int. Conf. on RF Superconductivity*, SRF2019, Dresden, Germany, SRF19, Dresden, Talk MOFAB2, 2019.

[89] E. Bargalló, R. Andersson, A. Nordt, A. De Isusi, E. Pitcher, and K. H. Andersen. ESS Reliability and Availability Approach. *In IPAC 2015: Proceedings of the 6th International Particle Accelerator Conference* (JACoW, Richmond, 2015), p. 1033, 2015. https://jacowfs.jlab.org/conf/proceedings/IPAC2015/

[90] The CEPC-SPPC Study Group, Machine Layout and Performance. *In CEPC-SppC Preliminary Conceptual Design Report*, Vol. II: Accelerator (Institute of High Energy Physics, CAS, Beijing, China), Chap. 3, p. 39, 2015.

[91] S. Bauer, W. Diete, B. Griep, M. Peiniger, H. Vogel, P. vom Stein, S. Calatroni, E. Chiaveri, and R. Losito. Production of Nb/Cu sputtered superconducting cavities for LHC. *In Proceedings of the 9th Workshop on RF Superconductivity*, Santa Fe, New Mexico, USA, 1999.

[92] S. Keckert, R. Kleindienst, O. Kugeler, D. Tikhonov, and J. Knobloch. Characterizing materials for superconducting radiofrequency applications—A comprehensive overview of the quadrupole resonator design and measurement capabilities. *Rev. Sci. Instrum. 1,* June 2021; 92 (6): 064710, 2021. https://doi.org/10.1063/5.0046971

[93] E. Brigant, E. Haebel, and E. Mahner. The Quadrupole Resonator, Design Considerations and Layout of a New Instrument for the RF Characterization of Superconducting Surface Samples. *In Proc. 6th European Particle Accelerator Conf. (EPAC'98)*, Stockholm, Sweden, paper TUP042B, pp. 1855-1857, 1998.

[94] R. Kleindienst, J. Knobloch, and O. Kugeler. Development of an Optimized Quadrupole Resonator at HZB. *In Proc. 16th Int. Conf. RF Superconductivity (SRF'13)*, Paris, France, paper TUP074, pp. 614-616, 2013.

[95] V. del Pozo Romano, R. Betemps, F. Gerigk, R. Illan Fiastre, and T. Mikkola. Redesign of CERN's Quadrupole Resonator for Testing of Superconducting Samples. *In Proc. 18th Int. Conf. RF Superconductivity (SRF'17)*, Lanzhou, China, pp. 420-422, 2017. doi:10.18429/ JACoW-SRF2017-TUPB016

[96] M. Arzeo. Design, manufacturing and evaluation of the 2nd CERN quadrupole resonator. *Quadrupole Resonator Workshop*, Berlin, Germany, 2019.

[97] P. Putek, S. G. Zadeh, M.Wenskat, and U. van Rienen. Multiobjective design optimization of a Quadrupole Resonator under uncertainties, 2020. *arXiv*:2004.09470

[98] S. Bira. Geometry Optimization for a Quadrupole Resonator at Jefferson. *In Proc. 21th Int. Conf. on RF Superconductivity (SRF'23)*, Grand Rapids, MI, USA, WEPWB048, 2023.

[99] S. Keckert, W. Ackermann, H. De Gersem, X. Jiang, A. Ö. Sezgin, M. Vogel, M. Wenskat, R. Kleindienst, J. Knobloch, O. Kugeler, and D. Tikhonov. Mitigation of parasitic losses in the quadrupole resonator enabling direct measurements of low residual resistances of SRF samples. *AIP Advances*, Vol. 11 (12), pp. 125326, 2021. doi: https://doi.org/10.1063/5.0076715

[100] T. Junginger. Investigations of the surface resistance of superconducting materials. Ph.D. thesis, Ruprecht-Karls- Universität, Heidelberg, Germany, 2012.

[101] D. Boussard. Operational experience with the LEP2 SC cavity system. *In Proceedings of the 5th European Particle Accelerator Conference*, 1996.

[102] R. Kleindienst et al. Commissioning Results of the HZB Quadrupole Resonator. *In Proc. of the 17th International Conference on RF Superconductivity (SRF'15)*, Whistler, BC, Canada, pp. 930–936, 2015. doi: 10.18429/JACoW-SRF2015-WEA1A04

[103] R. Kleindienst. Radio Frequency Characterization of Superconductors for Particle Accelerators. Ph.D. thesis, Universität Siegen, Siegen, Germany, 2017.

[104] S. Keckert. Characterization of Nb_3Sn and Multilayer Thin-Films for SRF Applications. Ph.D. thesis, Universität Siegen, Siegen, Germany, 2019.

[105] R. Monroy Villa, W. Hillert, S. Keckert, O. Kugeler, P. Putek, D. Reschke, D. Tikhonov, U. van Rienen, M. Wenskat, and S. Zadeh. Design and Fabrication of a Quadrupole-Resonator for Sample R&D. *In Proc. 19th Int. Conf. on RF Superconductivity (SRF'19)*, Dresden, Germany, pp. 838-841, 2019. doi:10.18429/JACoW-SRF2019-THP004

[106] R. Monroy-Villa, W. Hillert, M. Wenskat, S. Gorgi Zadeh, P. Putek, M. Lemke, D. Reschke, M. Röhling, and J.-H. Thie. Status of the New Quadrupole Resonator for SRF R&D. *In Proc. 20th Int. Conf. on RF Superconductivity (SRF'21)*, Virtual Conf., pp. 751-755, 2021. doi:10.18429/JACoW-SRF2021-THPFDV001.

[107] https://www.zanonresearch.com/

[108] C. Balanis. Antenna Theory. *Wiley-Interscience*. Third Ed., p. 246, 2005. ISBN 0-471-66782-X

[109] S. Aderhold, S. Chel, E. Elsen, F. Eozenou, L. Lilje, and D. Reschke. ILC higrade cavity process. *Technical Report No.* 2010-005-1 DESY, 2010.

[110] S. Chetri, P. Dhakal, D. C. Larbalestier, P. J. Lee, and Z.-H. Sung. Determination of Bulk and Surface Superconducting Properties of N_2-Doped Cold Worked, Heat Treated and Electro-polished SRF Grade Niobium. *In Proc. 17th International Conference on RF Superconductivity (SRF'15)*, Whistler, Canada, September 13-18, 2015. doi: 10.18429/JACoW-SRF2015-MOPB052

[111] Private communication, *DESY*, 2020.

[112] M. Wiencek, K. Kasprzak, D. Kostin, D. Reschke, and L. Steder. Summary of the Superconducting Rf Measurements in AMTF Hall at DESY. *In Proc. 21th Int. Conf. on RF Superconductivity (SRF'23)*, (THCAA02), Grand Rapids, MI, USA, Jun. 2023.

[113] M. Martinello. PhD thesis, Illinois Institute of Technology, 2016.

[114] J. C. Slater. Microwave Electronics. *Rev. Mod. Phys.* 18, p. 04441, 1946.

[115] J. Halbritter. On electric surface impedance. *Z Physik B* 31, 19–37, 1978.

[116] N. Pompeo, K. Torokhtii, F. Leccese, A. Scorza, S. Sciuto, and E. Silva. Fitting strategy of resonance curves from microwave resonators with non-idealities. *In Proceedings of the IEEE International Instrumentation and Measurement Technology Conference (I2MTC)*, Turin, Italy, 22–25 May, pp. 1–6, 2017.

[117] T. L. Bergman and F. P. Incropera. Fundamentals of Heat and Mass Transfer. *Seventh edition. Wiley*, 2011.

[118] R. J. Donnelly and C. F. Barenghi. The Observed Properties of Liquid Helium at the Saturated Vapor Pressure. *Journal of Physical and Chemical Reference Data* 27, 1217, 1998. doi: https://doi.org/10.1063/1.556028

[119] S. Bira et al. Multipacting Analysis of the Quadripolar Resonator (QPR) at HZB. *In Proc. RF'21*, East Lansing, MI, USA, p. 42, Jun.-Jul. 2021. doi:10.18429/JACoW-SRF2021-SUPCAV013

[120] B. W. Maxfield and W. L. McLean. Superconducting Penetration Depth of Niobium. *Phys. Rev.*, vol. 139, 1965. doi:10.1103/PhysRev.139.A1515

[121] M. Martinello, A. Grassellino, M. Checchin, A. Romanenko, O. Melnychuk, D. A. Sergatskov, S. Posen, and J. F. Zasadzinski. Effect of Interstitial Impurities on the Field Dependent Microwave Surface Resistance of Niobium. *Appl. Phys. Lett.* 109, p. 062601, 2016. doi:10.1063/1.4960801.

[122] M. Checchin et al. Frequency dependence of trapped flux sensitivity in SRF cavities. *Appl. Phys. Lett.*, vol. 112, p. 072601, 2018. doi:10.1063/1.5016525

[123] F. Herman. *In Proceedings of the 20th International Conference on RF Superconductivity (2021),* THPFDV010, 2021.

[124] T. Kubo. Effects of Nonmagnetic Impurities and Subgap States on the Kinetic Inductance, Complex Conductivity, Quality Factor and Depairing Current Density. *Phys. Rev. Appl.* 17, 014018, 2022.

[125] D. C. Mattis and J. Bardeen. *Phys. Rev.* 111, 412, 1958.

[126] F. Marsiglio and J. P. Carbotte. Electron–Phonon Superconductivity. *In Superconductivity*, edited by K. H. Bennemann and J. B. Ketterson (Springer, Berlin, 2008), Vol. 1, 2008.

[127] D. Bafia, A. Grassellino, M. Checchin, J. Zasadzinski, and A. Romanenko. The anomalous resonant frequency variation of microwave superconducting niobium cavities near T_c. *arXiv*:2103.10601, 2021.

[128] W. Wasserbäch. Low-temperature thermal conductivity of pure and impure niobium and tantalum single crystals. *Phys. Stat. Sol. (b)*, 84: 205-214, 1997. doi: https://doi.org/10.1002/pssb.2220840123

[129] T. Schilcher. Wärmeleitvermögen von Niob bei kryogenischen temperaturen. Ph. D. Thesis, Universität Regensburg/DESY, 1995.

[130] A. Romanenko and L. V. Goncharova. Elastic recoil detection studies of near-surface hydrogen in cavity-grade niobium. *Supercond. Sci. Technol.* 24, 105017, 2011.

[131] C. Martens. Berechnung der Nb-Ti-Flanschverschraubungen der supraleitenden Nb-Cavities des VUV-FEL. *DESY*, Hamburg, Germany, 2005.

Appendix I

QPR Modes at Room Temperature

The modes of the QPR were calculated using the nominal design specifications (with zero tolerances) through simulations using CST at room temperature. These modes were identified as monopole (M), dipole (D), quadrupole (Q), and cavity mode (C) and follow the order presented in Fig. 4.24. The numerical values of their frequency f_{CST} and quality factor Q_0^{CST} are presented in Tab. I.1.

Table I.1: Frequencies and quality factors of the QPR nominal design simulated using a model in CST Microwave Studio®.

Mode No.	Type	f_{CST} / MHz	Q_0^{CST}
1	Q	431.99	633.16
2	D	439.27	1719.49
3	M	477.71	2202.06
4	D	563.07	978.21
5	M	771.01	218.44
6	D	817.69	8110.81
7	D	821.07	8302.92
8	Q	870.99	912.42
9	D	883.99	2396.39
10	M	944.09	2069.27
11	D	965.09	1205.13
12	D	1461.17	6276.47
13	D	1490.83	5993.50
14	C	1274.58	12305.41
15	C	1287.24	12539.99
16	Q	1314.69	1072.87
17	D	1328.84	2002.77
18	M	1377.65	4783.57
19	D	1384.70	1231.81
20	D	1461.89	384.94

A direct comparison between the simulated and measured modes was conducted for the gap of

883.55 µm, as detailed in Sec. 5.2.5. The numerical values of both spectra are provided in Tab. I.2. It is worth mentioning that the experimental frequencies f_{exp} and quality factors Q_0^{exp} of the modes were measured when the QPR was not evacuated.

Table I.2: Frequencies and quality factors of the measured RF spectrum with the input antenna in position A and the pick-up in B. The simulated results of the QPR were obtained using a model with a gap of 883.55 µm in CST Microwave Studio®. Their differences are given by $\Delta f = f_{\mathrm{exp}} - f_{\mathrm{CST}}$ and $\Delta Q_0 = Q_0^{\mathrm{exp}} - Q_0^{\mathrm{CST}}$.

Mode No.	f_{exp} / MHz	Q_0^{exp}	f_{CST} / MHz	Q_0^{CST}	Δf / MHz	ΔQ_0
1	426.77	742	427.33	742.09	-0.56	-0.09
2	437.84	1743	438.73	1790.21	-0.89	-47.21
3	489.47	1498	490.28	2386.15	-0.81	-888.16
4	600.92	1158	602.01	1175.82	-1.09	-17.82
5	722.97	118	753.37	243.49	-30.41	-125.50
6	816.42	7884	817.47	8386.36	-1.05	-502.40
7	820.57	6991	820.91	8544.73	-0.35	-1553.73
8	860.90	1098	861.03	1077.10	-0.13	20.90
9	881.23	2304	882.35	2502.87	-1.12	-198.87
10	945.78	2032	948.48	2962.01	-2.70	-930.01
11	1001.36	1400	1003.66	1418.00	-2.30	-18.00
12	1144.05	6242	1145.70	6661.89	-1.67	-419.89
13	1146.99	2928	1148.35	6216.50	-1.37	-3288.50
14	1274.01	12303	1274.49	12362.82	-0.48	-59.82
15	1287.35	12525	1287.28	12580.55	0.07	-55.56
16	1301.41	1334	1300.97	1311.18	0.45	22.82
17	1323.61	1812	1325.51	2078.68	-1.90	-266.68
18	1381.12	3591	1383.75	5555.56	-2.63	-1964.56
19	1404.04	530	1411.01	1129.10	-6.86	-628.10
20	1430.88	321	1453.91	391.33	-22.80	-34.33

Appendix II

Complementary Simulation and Commissioning Results

In this appendix, the simulated and measured results of the quadrupole mode Q_1 frequency are extended to illustrate the behaviour of modes Q_2 and Q_3, considering the different parameters discussed in Secs. 4.7.4, 5.2.4, 5.2.6, and 5.5.3.

4.7.4 Frequency Sensitivity to Gap Changes

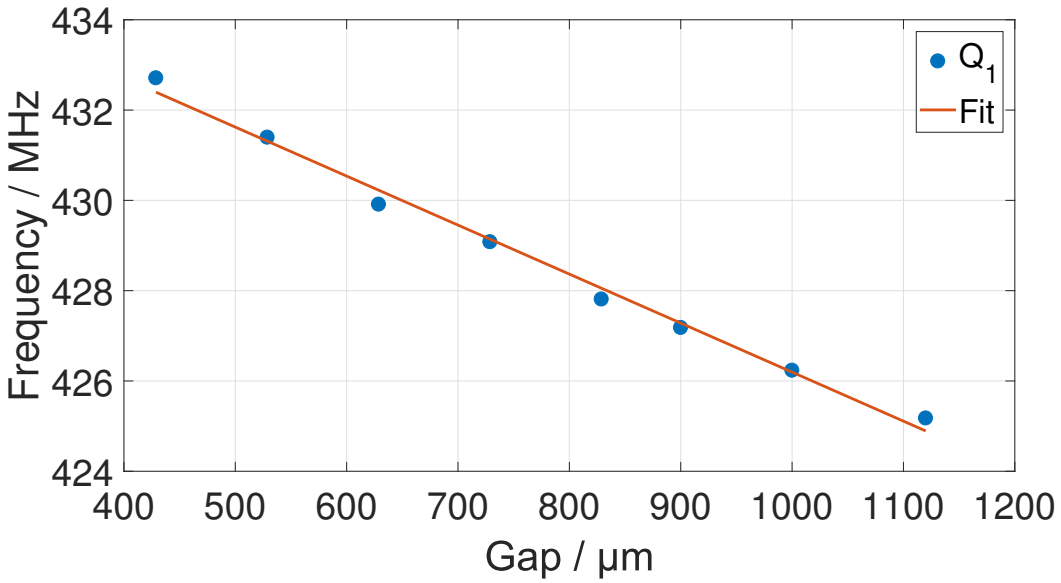

Figure II.1: Quadrupole mode Q_1 frequency versus gap. Simulated frequencies obtained in CST Microwave Studio®.

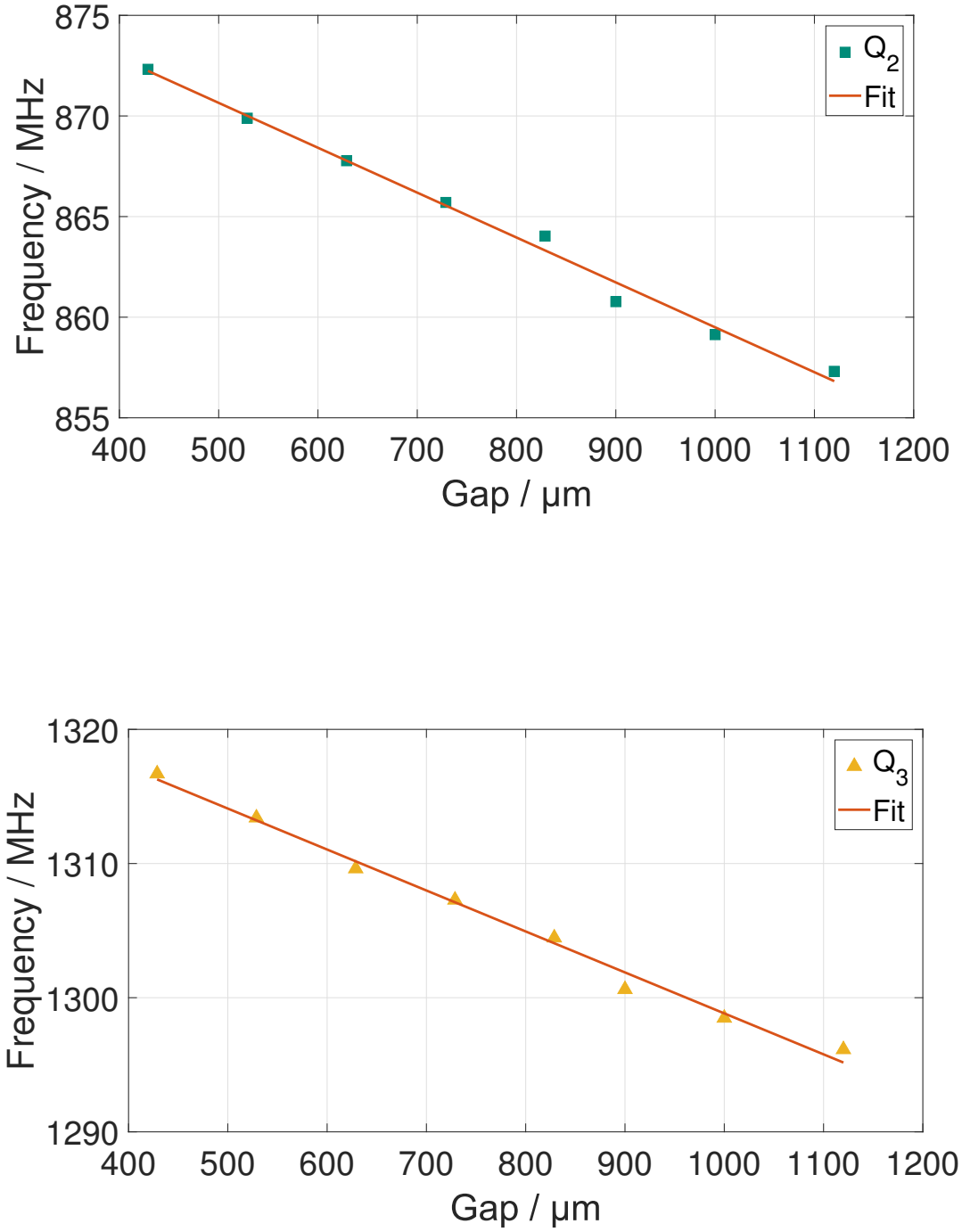

Figure II.2: Quadrupole modes Q_2 and Q_3 frequencies versus gap. Simulated frequencies obtained in CST Microwave Studio®.

5.2.4 Measurement of the Frequency Sensitivity to Gap Changes

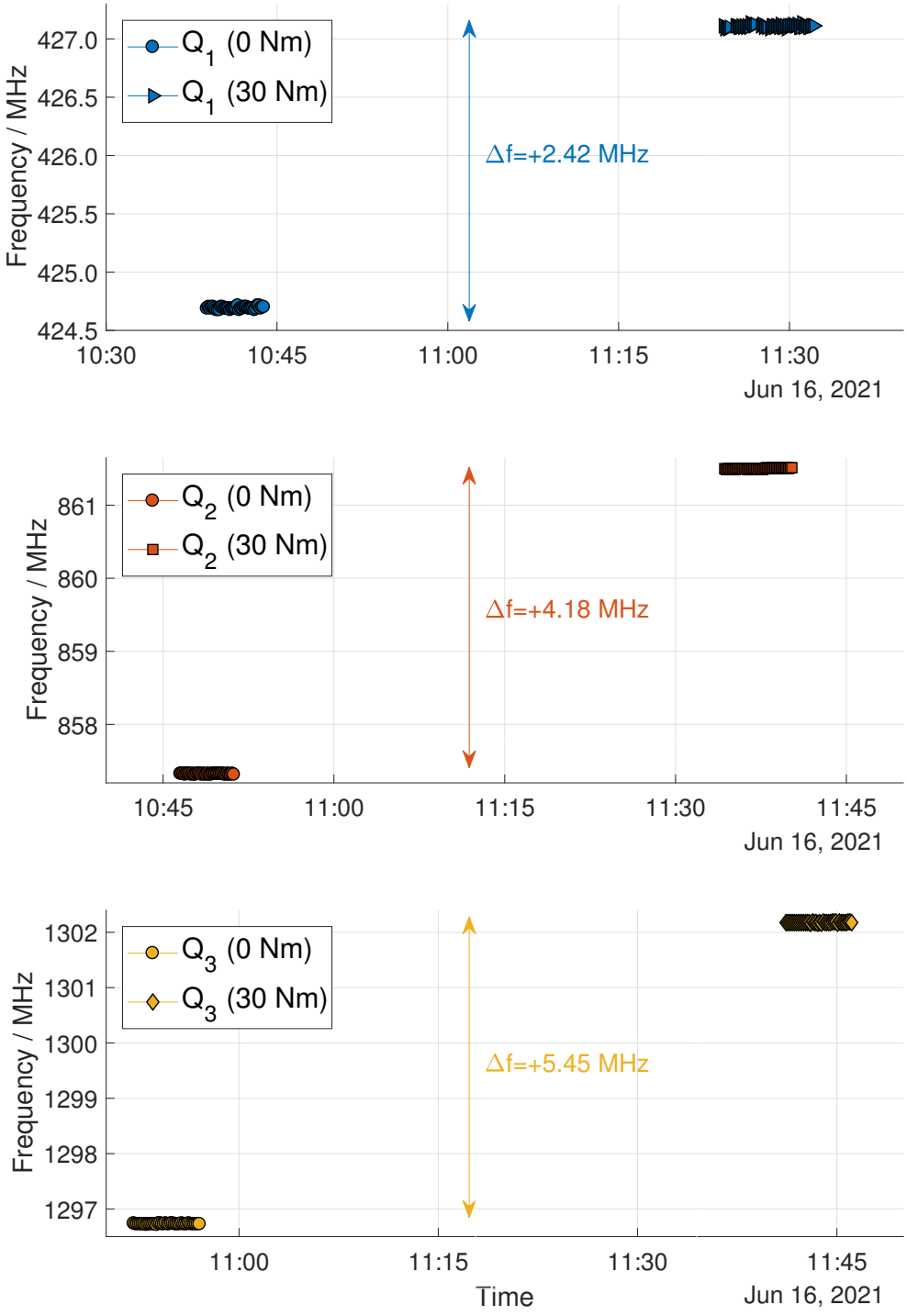

Figure II.3: Quadrupole modes Q_1, Q_2, and Q_3 frequencies versus time at room temperature. First, the frequency was measured for ten minutes. Then, after reaching a 30 Nm torque on the nuts, it was measured again for the same time period.

5.2.6 Evacuation Effects on the Gap

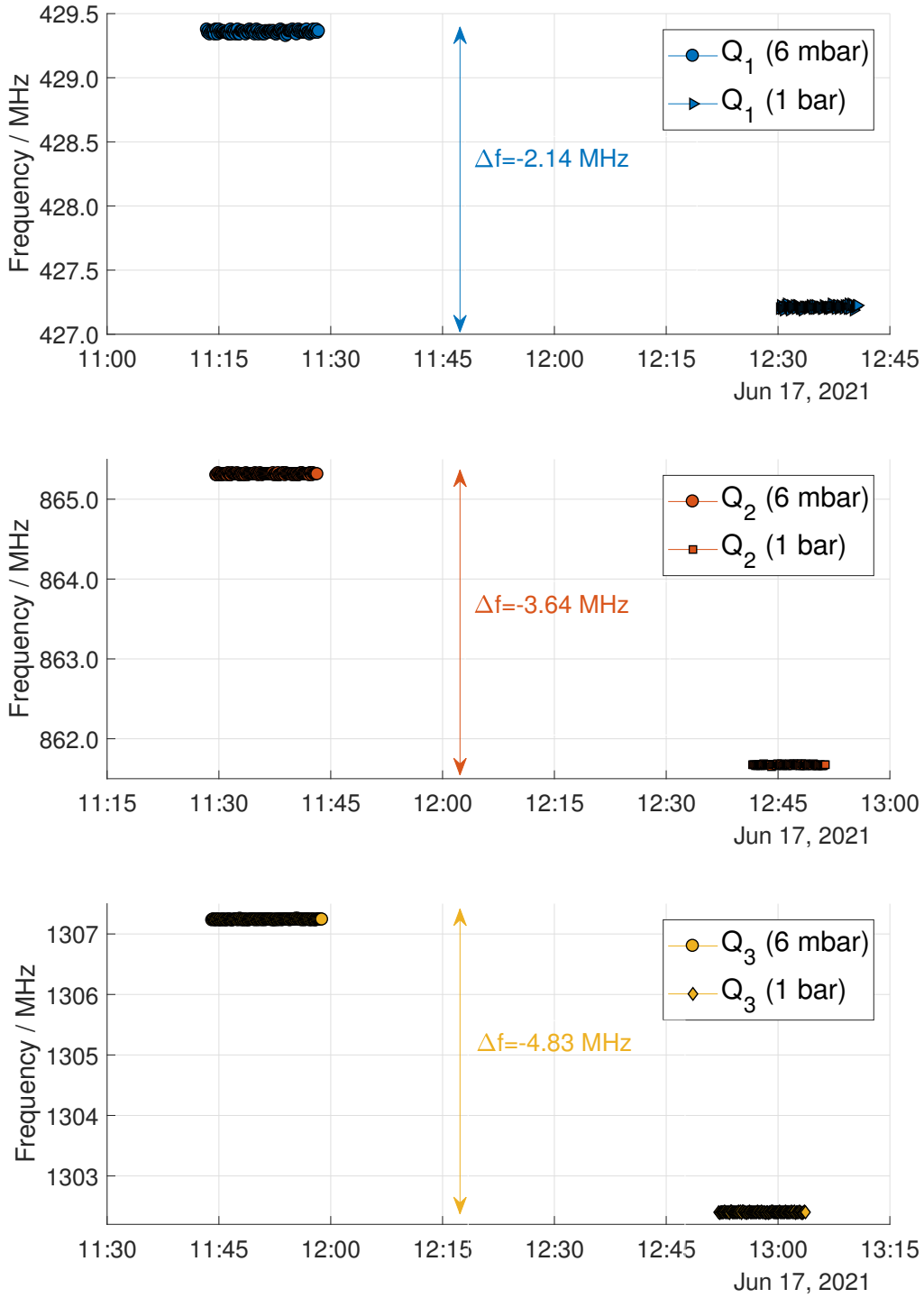

Figure II.4: Quadrupole modes Q_1, Q_2, and Q_3 frequencies versus time with vacuum. Initially, the frequency was measured at 6 mbar for ten minutes. Then, the measurements were repeated at ambient pressure for the same time period.

5.5.3 Identification of the Operation Modes

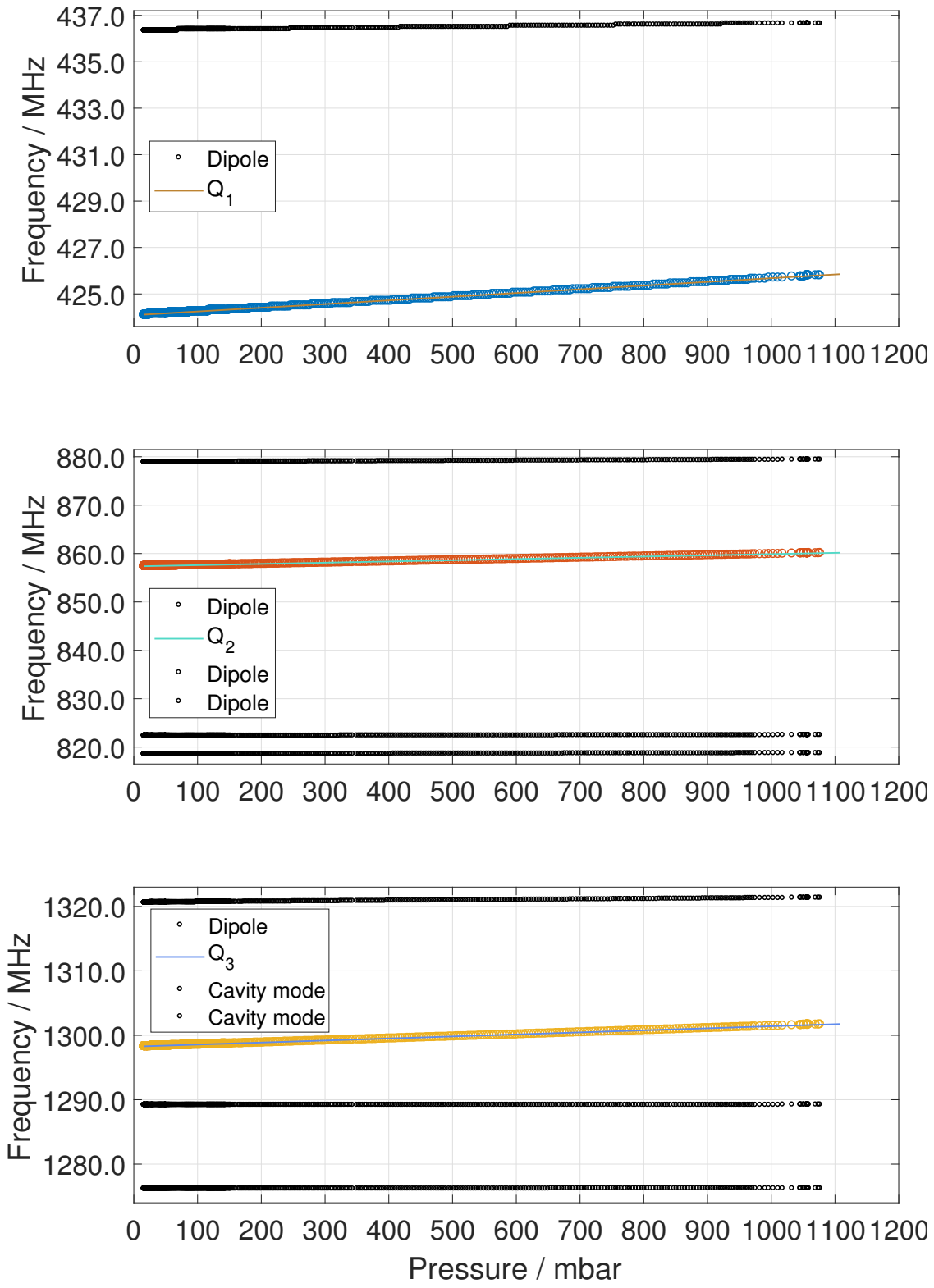

Figure II.5: Quadrupole modes Q_1, Q_2, and Q_3 frequencies versus pressure during the cooldown process of the QPR from 300 K to 2 K.

Appendix III

Static Detuning Study of the QPR

The electromagnetic fields associated with the quadrupole modes of the resonator dampen within the coaxial gap. Therefore, any defects that modify the resonator's symmetry (detuning) can lead to the excitation of unwanted neighbouring modes, such as the monopole or dipole modes, in addition to the desired quadrupole modes. These additional modes can propagate into the coaxial gap, resulting in unaccounted heating of the sample and overestimation of the surface resistance, see Eq. 4.1. In practice, factors like microphonics, deformations after pumping down, or fabrication errors can induce angle deviations in the QPR rods, leading to the simultaneous excitation of multiple modes.

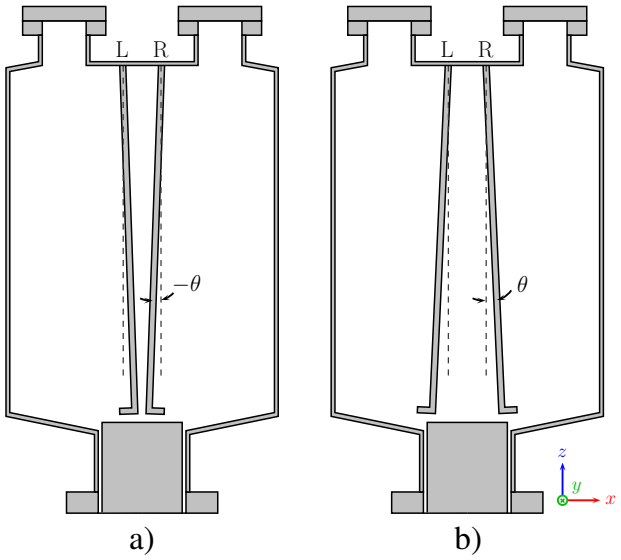

Figure III.1: Schematic diagram of the angle variation of the rods inside the QPR. The rotation of the rods was done around the y-axis with an angle θ that is a) negative when the rods get closer and b) positive when the rods move apart.

Tilting of the Rods

To simulate static detuning caused by fabrication errors, prior to the fabrication of the QPR, the rods were rotated at the point where they are fixed to the top plate. The rotation was performed around the y-axis with the same angle θ ranging from -0.4° and 0.4°. Fig. III.1 illustrates that a negative angle θ brings the rods closer together, while a positive angle results in their separation along the x-axis. Specifically, a tilting of 0.4° for one rod is equivalent to a displacement of 2.28 mm along this axis.

Fig. III.2 displays the spectrum of the 20 modes obtained for different rotation angles. The displacement of the rods predominantly affects a few dipoles and all three quadrupole modes, causing them to spread out from their baseline positions.

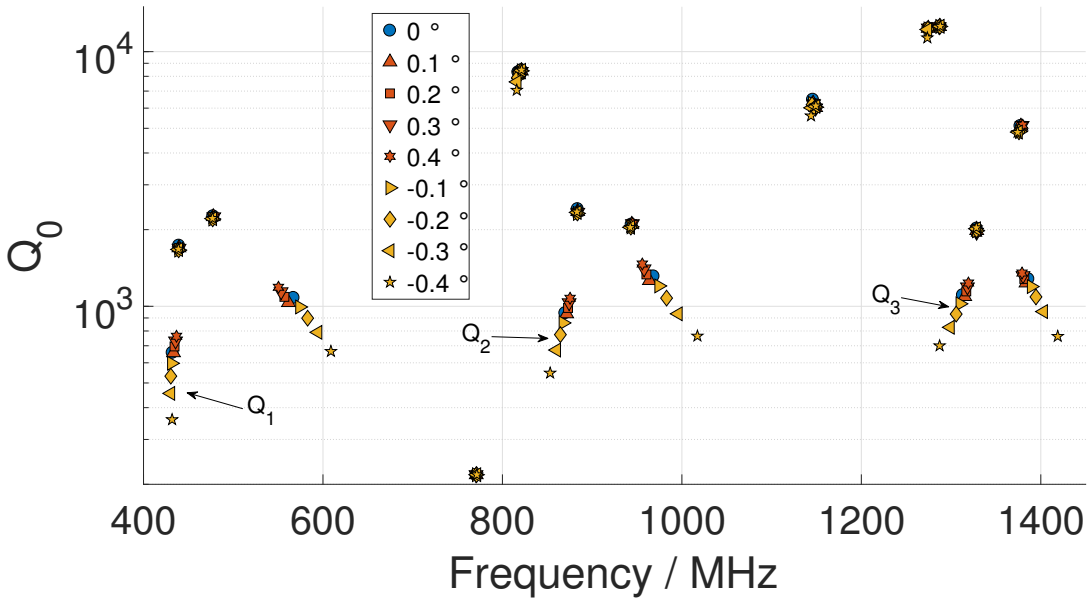

Figure III.2: Quality factor Q_0 versus frequency of the QPR at room temperature with a rotation of the rods around the y-axis with an angle θ between -0.4° and 0.4°.

Fig. III.3 depicts the frequency change of modes Q_1, Q_2 and Q_3, respectively, in relation to the rotation angle of the rods. This plot reveals a linear relation between the frequency and the rotation angle of the rods within the range of 0° to 0.4°. However, surprisingly, a non-linear effect occurs between angles -0.4° to 0°.

From the previous findings, it is evident that the frequency change of Q_2 and Q_3 exhibits a significantly faster rate as the rods move closer to each other, displaying a non-linear behaviour. Additionally, a mode exchange occurs between Q_3 and the previous cavity mode. It can be observed that the quality factor of mode Q_3 at -0.4°(blue star) increases by one order of magnitude compared to the mode calculated at 0° (blue circle). Similarly, for the CM, a -0.4° angle deviation of the rods (red star) results in a decrease of one order of magnitude. The mode exchange was confirmed in CST, where a detailed distribution of the $\vec{E}$-field is visible. However, such mode-exchange behaviour does not occur between Q_3 and the next-higher frequency mode (dipole) for any angle.

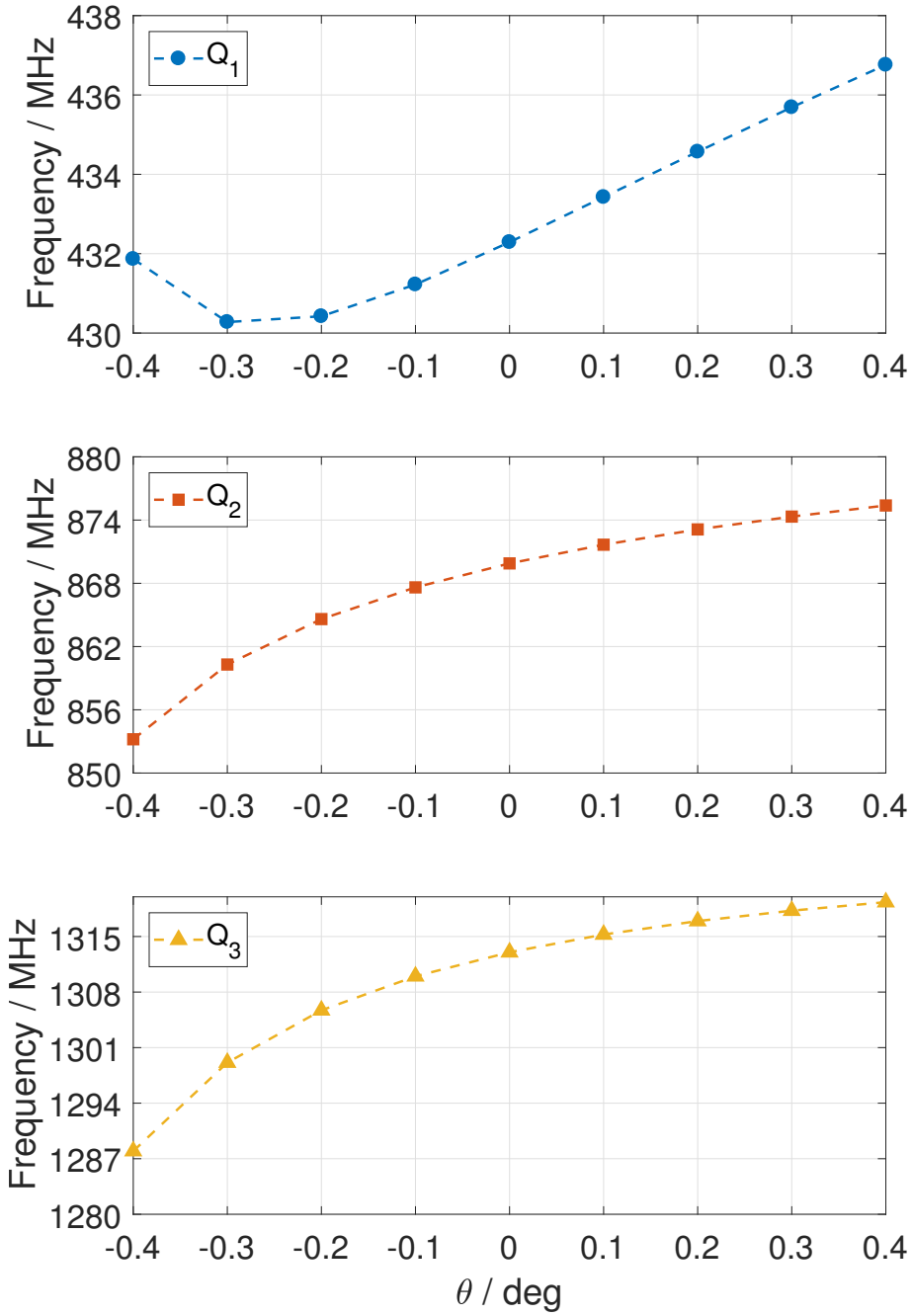

Figure III.3: Quadrupole modes Q_1, Q_2, and Q_3 frequencies versus rotation angle of the rods around y-axis.

Tilting of the Pole Shoes

Another potential cause of static detuning could arise from the rotation of the pole shoes at the point where they are welded to the rods. To simulate this effect, the pole shoes were rotated around the y-axis with an angle ϕ ranging from -1° to 1°. At this point, an angle of 1° corresponds to a displacement of the pole shoes by 0.339 mm along the z-axis. Fig. III.4 illustrates that a negative angle brings the pole shoes closer to the sample, while a positive angle results in their separation.

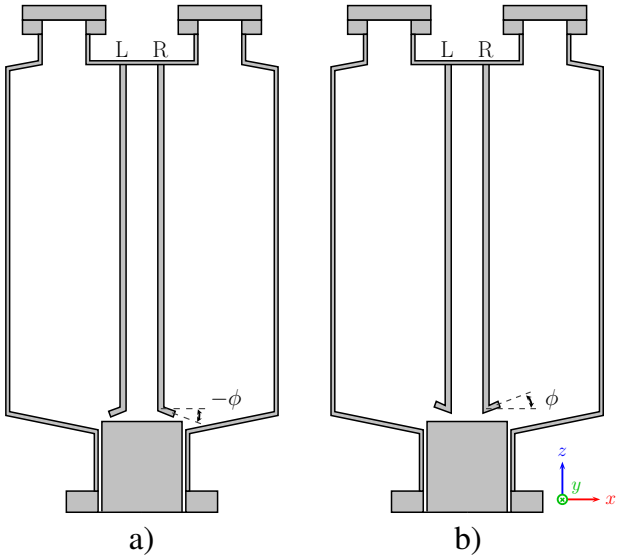

Figure III.4: Schematic diagram of the angle variation of the pole shoes at the point they are joined to the rods. The rotation of the pole shoes was performed around the y-axis with an angle ϕ that is a) negative when the pole shoes get closer to the sample and b) positive when the pole shoes pull away from the sample in the z-axis.

The 20-modes spectrum obtained for various rotation angles of the pole shoes is shown in Fig. III.5. Fig. III.6 depicts the frequency change of modes Q_1, Q_2, and Q_3, respectively.

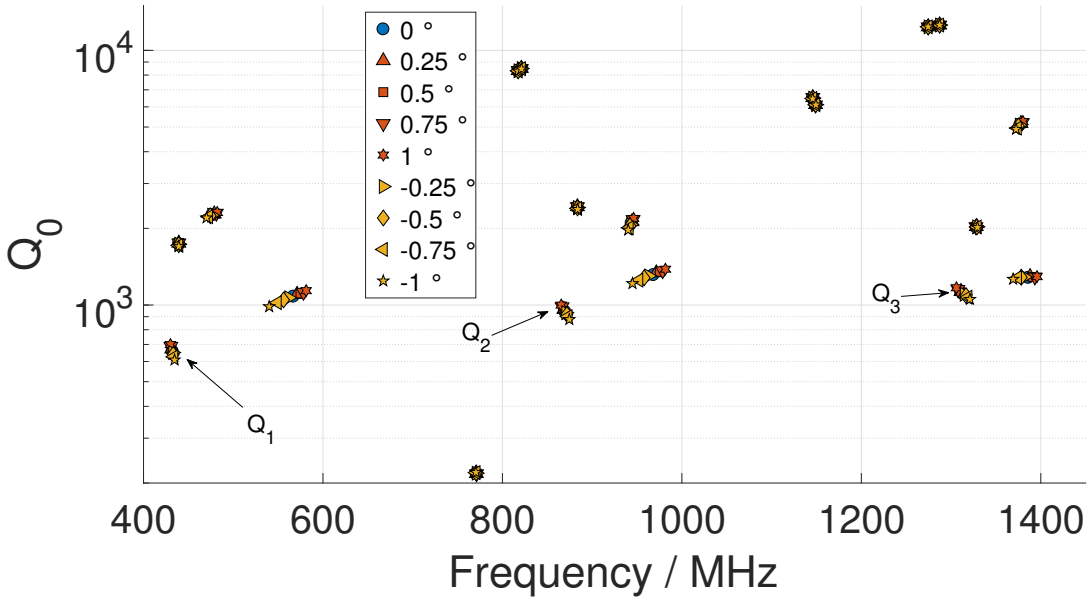

Figure III.5: Quality factor Q_0 versus frequency of the QPR at room temperature with a rotation of the pole shoes around the y-axis with an angle θ between -1° and 1°.

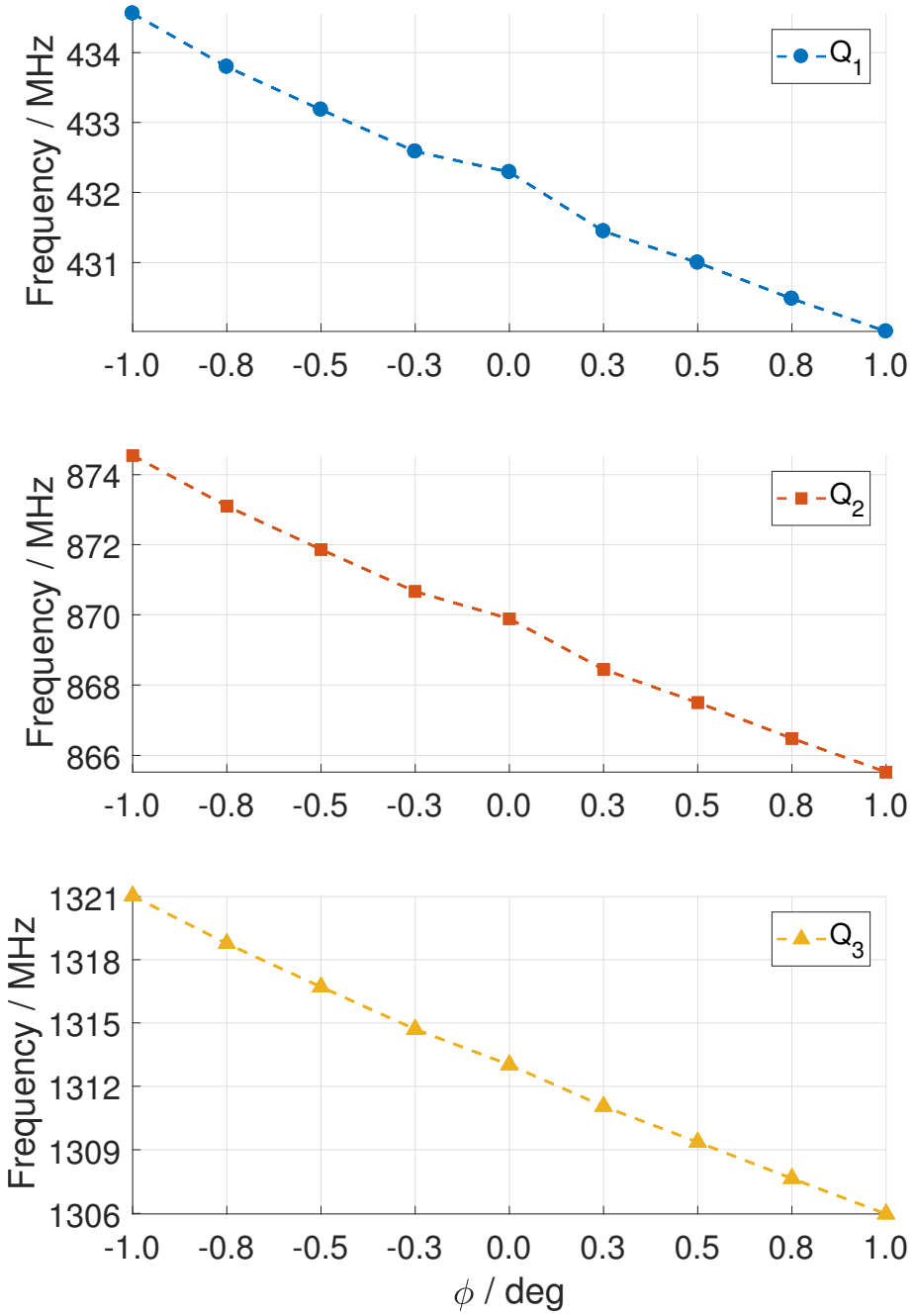

Figure III.6: Quadrupole modes Q_1, Q_2, and Q_3 frequencies versus rotation angle of the pole shoes around y-axis.

Comparing these results with the ones obtained from the rotation of the rods, it is evident that the change of frequency exhibits a negative slope and an approximately linear trend in the case of the pole-shoe rotation. It is clear that within the considered range of angles, the rotation of the rods has a more pronounced impact on the frequency compared to the rotation of the pole shoes, and it can even cause a mode to swap with its neighbouring mode.

Appendix IV

Deformation Investigations of Two Types of Gaskets

Achieving the desired nominal pole-shoes-sample gap with minimal deviations is crucial since the operational frequency of the QPR is highly sensitive to it, see Tab. 4.3. Additionally, the Al gasket (see Fig. IV.1) must provide a leak-tight seal to maintain a pressure $\leq 10^{-9}$ mbar inside the vessel. At DESY, this is typically achieved by applying a torque of 30 Nm to the nuts used to secure both flanges [131]. To characterize the deviations in the gap that can be achieved in the QPR, a gasket-deformation study was conducted using gaskets from two different vendors.

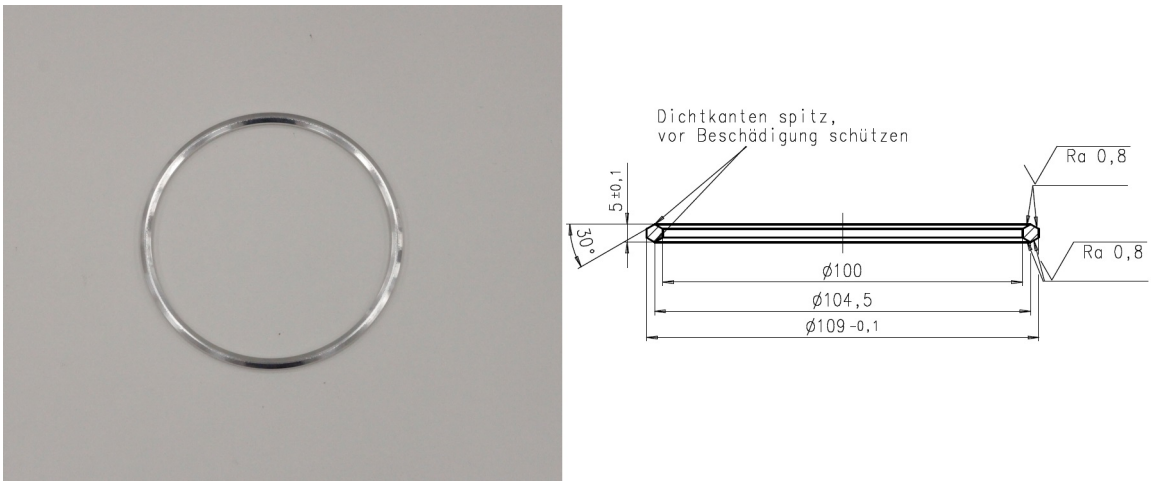

Figure IV.1: Left: Photo of the Al gasket. Right: Schematic drawing of the Al gasket, with dimensions in millimetres.

For this study, a setup was prepared, consisting of a replica of the bottom and sample flanges, as shown in Fig. IV.2.

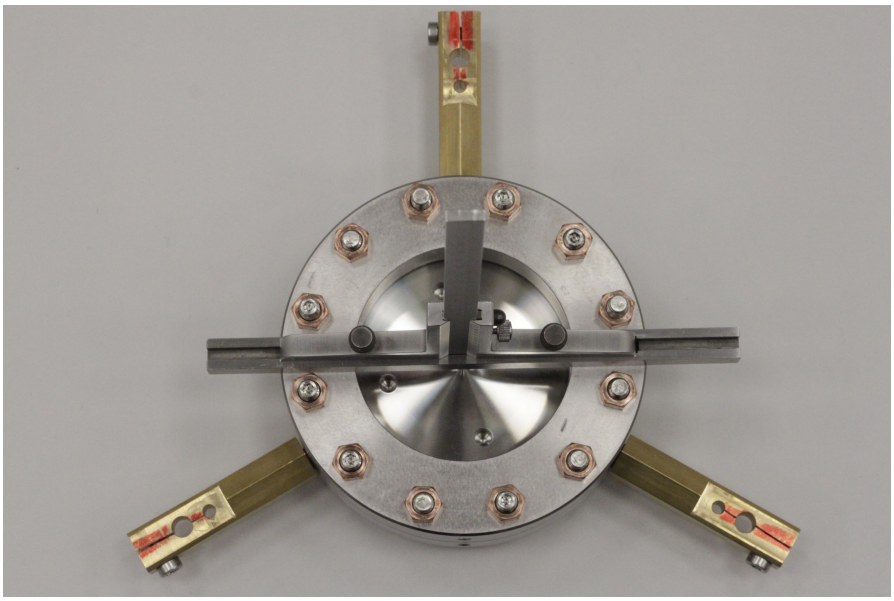

Figure IV.2: Gasket deformation setup.

The NW 78 bottom flange, which is electron beam welded to the cut-off tube of the vessel, is made out of NbTi55, as depicted in Fig. IV.3, while the blind sample flange is fabricated from stainless steel (1.4429-X2CrNiMoN17-13-3).

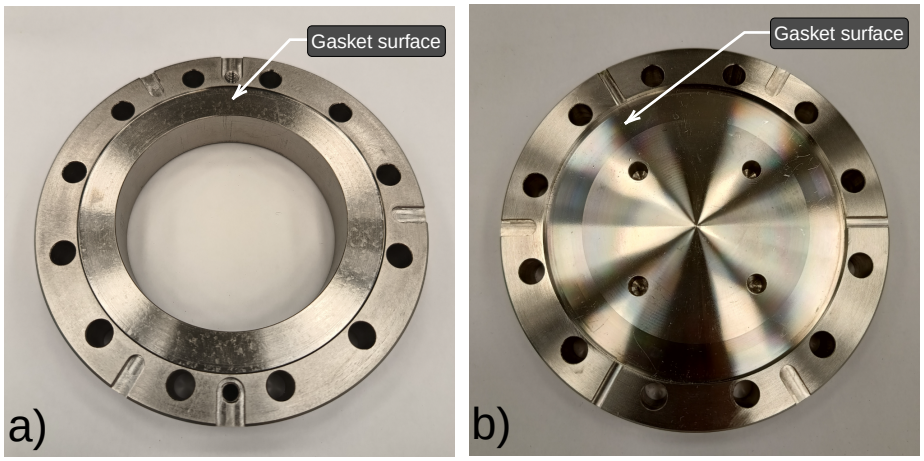

Figure IV.3: Left: Replica of NW 78 bottom flange. Right: Stainless steel blind flange.

The DESY-type Al gasket is positioned between the flanges and undergoes deformation due to the force applied to the set of M8 bolts and hexagonal nuts. Initially, the gasket has a diamond-shaped cross-section with a length of h_i, as illustrated in Fig. IV.4. Then, when the force is applied, the gasket deforms and flattens, reducing its height to h_f.

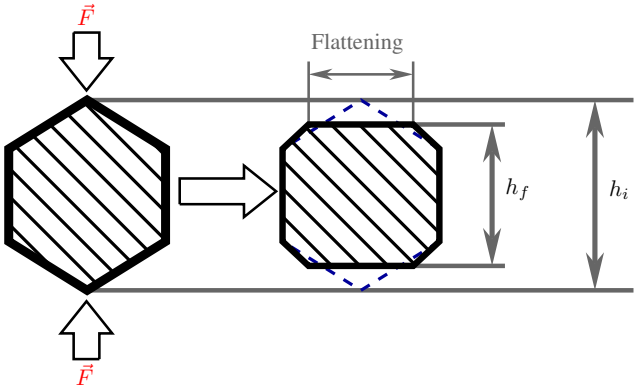

Figure IV.4: Schematic representation of the gasket deformation.

In Fig. IV.3, it can be observed that the bottom flange is hollow, allowing the measurement of its centre height relative to the centre of the sample flange before and after deformation. These measurements correspond to h_i^c and h_f^c. The purpose of this test is to determine the elastic and plastic deformations of several gaskets from both vendors and compare their results.

Vendor A

In the first step of this test, h_i is measured at four equally distant points around the sealing using a Vernier calliper[1]. The average value is then determined. Subsequently, the gasket is mounted in the setup, and a Vernier depth gauge is used to measure centre height by rotating the Vernier 120° to record three values and calculate the average, as depicted in Fig. IV.2. The result of these steps performed on two gaskets from vendor A are show in Tab. IV.1.

Table IV.1: Gasket height before the deformation test.

Gasket No.	0° / mm	90° / mm	180° / mm	270° / mm	$\langle h_i \rangle$ / mm	$\langle h_i^c \rangle$ / mm
1−a	5.06	5.08	5.08	5.1	5.08	25.03
1−b	5.09	5.05	5.07	5.08	5.07	25.03

The third step involves applying a torque σ =30 Nm to the nuts, deforming the sealing with the surfaces of both flanges. Following this, the sealing is disassembled, and h_f is measured using the same method as in step one. The results of these measurements are presented in Tab. IV.2.

Table IV.2: Gasket height after the deformation test for σ =30 Nm.

Gasket No.	0° / mm	90° / mm	180° / mm	270° / mm	$\langle h_f \rangle$ / mm	$\left\langle h_f^c \right\rangle$ / mm
1−a	4.67	4.65	4.69	4.67	4.67	24.63
1−b	4.58	4.6	4.54	4.56	4.57	24.56

In the fourth step, the differences $\Delta h = \langle h_f \rangle - \langle h_i \rangle$ and $\Delta h^c = \left\langle h_f^c \right\rangle - \langle h_i^c \rangle$ are calculated, as shown in Tab. IV.3.

[1] The resolution of this Vernier gauge is of 100 µm.

Table IV.3: Height measurement at centre with Vernier depth gauge after the deformation test for σ =30 Nm.

Gasket No.	Δh / mm	Δh^{c} / mm
1−a	0.41	0.40
1−b	0.50	0.47

Therefore, the elastic deformation ε_{E} and plastic deformations of the gaskets ε_{P} are determined from the previous results using the following equations:

$$\varepsilon_{\mathrm{E}} = \Delta h - \Delta h^{\mathrm{c}} \tag{IV.1}$$

and

$$\varepsilon_{\mathrm{P}} = \Delta h - \varepsilon_{\mathrm{E}}. \tag{IV.2}$$

These equations are justified by the fact that the height h_i is measured without elastically deforming the gasket with the Vernier gauge. Thus, Δh accounts for both the elastic and plastic deformations. By subtracting Δh^{c}, which considers only the plastic deformation, assuming that the weight of the NW 78 bottom flange itself exerts a force strong enough to elastically deform the gasket, from Δh simply gives the elastic deformation. The plastic deformation can be obtained by subtracting ε_{E} from Δh. The results for ε_{E} and ε_{P} are shown in Tab. IV.4.

Table IV.4: Elastic and plastic deformation (strain) for σ =30 Nm.

Gasket No.	ε_{E} / mm	ε_{P} / mm
1−a	0.01	0.40
1−b	0.04	0.47

Finally, with the given setup and the established torque of 30 Nm, the Al gasket is expected to deform on average a total of $(435 \pm 50)\,\mu$m.

Vendor B

A gasket of the same type was tested in the same manner as the gaskets from vendor A, but it was purchased from a different vendor. The results of steps one and two are show in Tab. IV.5.

Table IV.5: Gasket height before the deformation test.

Gasket No.	0° / mm	90° / mm	180° / mm	270° / mm	$\langle h_i \rangle$ / mm	$\langle h_i^{\mathrm{c}} \rangle$ / mm
2	4.98	4.98	4.98	4.99	4.98	24.93

It is worth noting that h_i in this case is more consistent around the gasket when compared to the values of vendor A (see Tab. IV.1). The results of step three are shown in Tab. IV.6. As observed, step three could not be fully performed since, after applying a torque of σ =30 Nm and measuring h_f^{c}, the gasket was further deformed with a torque of 35 Nm.

Table IV.6: Gasket height after the deformation test for σ =30 Nm.

Gasket No.	0° / mm	90° / mm	180° / mm	270° / mm	$\langle h_f \rangle$ / mm	$\left\langle h_f^{\mathrm{c}} \right\rangle$ / mm
2	–	–	–	–	–	24.51

However, step four was partially carried out and reported in Tab. IV.7.

Table IV.7: Height measurement at centre with Vernier depth gauge for σ =30 Nm.

Gasket No.	Δh / mm	Δh^{c} / mm
2	–	0.42

Based on Eq. IV.2, the obtained value for ε_{P} is shown in Tab. IV.8.

Table IV.8: Elastic and plastic deformation (strain) for σ =30 Nm.

Gasket No.	ε_{E} / mm	ε_{P} / mm
2	–	0.42

The total deformation of an Al gasket from vendor B is expected to be approximately $(420 \pm 50)\,\mu$m, assuming that ε_{E} is much smaller than the uncertainty, as observed with the gaskets from vendor A (see Tab. IV.4). It is evident that one or two gaskets do not provide enough data for a statistical study, but the investigation had to be limited due to the cost and availability of the gaskets at the time of the tests. However, gaskets from vendor B were chosen for use in the QPR as the height h_i is more uniform around the gasket when compared to those from vendor A.

Appendix V

QPR Coordinate System and Metrology Measurements

QPR Coordinate System and Metrology Measurements

1. *Introduction*

The Quadrupole Resonator (QPR) is a device to measure rf properties of samples, inserted in the bottom part (sample section) of the rf space. The parallelism and the position of the pole shoes surface with respect to the sample surface and respectively the sample flange as well as the parallelism and position of the rods to each other and within the vessel is of essential for the functionality of the QPR.

2. *Definition of the QPR Coordinate System*

The origin of the coordinate system is defined as followed: Measuring an area of the outer surface of the sample tube, starting 25mm from the bottom up to 40mm from the bottom, will give a cylinder barrel, see Fig. 1. The intersection point of the rotational axis of this cylinder barrel and the plane defined by the sealing area at the sample flange is the origin of the coordinate system.

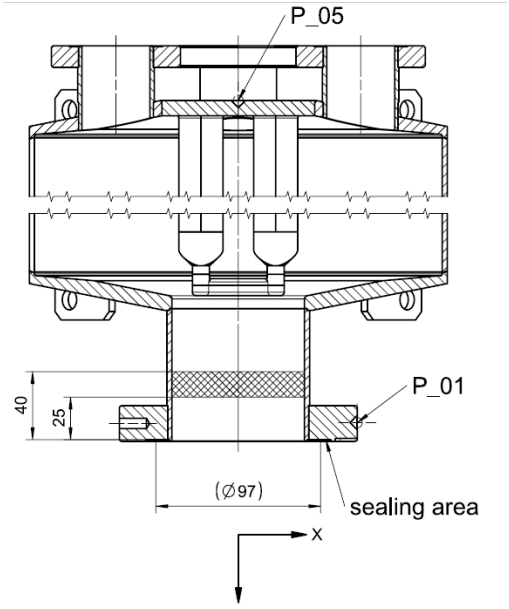

Figure 1 Cross-section of the QPR. The shaded area in the sample tube defines the cylinder barrel which rotational axis is used to define the z-axis, together with P_05 in the cake piece center.

An axis going through this origin point is then extrapolated through the reference point P_05 in the cake piece center of the QPR. This now defined axis is the z-axis of the QPR coordinate

There are three “reference boreholes” outside on the sample flange, see Fig. 2. The z-x plane is defined as the plane which will intersect with this reference borehole P_01. This plane will lie between the pole shoes.

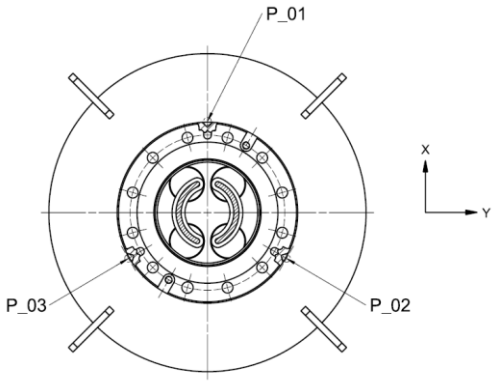

Figure 2 The reference boreholes in the sample flange. P_01 will lie in the z-x plane. This plane will be the mirror plane for the pole shoes.

The y-z-plane will then be perpendicular to the x-axis and will intersect with the pole shoes.

The z-axis direction pointing outside the flange will be the positive direction of z (hence, everything inside the QPR will have a negative z-value w.r.t. the origin) and the x-axis direction pointing towards P_01 will be the positive direction of this axis. The coordinate system will be right-hand oriented, meaning that the reference boreholes P_02 will have a positive y-coordinate and P_03 a negative y-coordinate.

3. *Requested Metrology Measurements*

During fabrication, two sets of measurement and one final measurement after fabrication are requested. The requested measurements are additional to the internal quality control of the manufacturer. The quality control process should not be limited to the requested measurements.

The measurements 3a and 3b have to be carried out with a bridge coordinate measuring machine (e.g. Zeiss Calypso or Accura) and a measuring ball with a diameter of 6mm must to be used as a measurement probe. For the measurement 3c, a smaller diameter of the ball and/or an extension or portable measurement device is allowed.

The measurements have to be documented and the results provided to UHH and DESY. After the measurements 3a and 3b, a hold point of the fabrication is planned

Definition Pole shoe plane: At least 20 points within an area defined in Fig. 3 are to be taken. These points will be used to fit and define the pole shoe plane for each pole shoe.

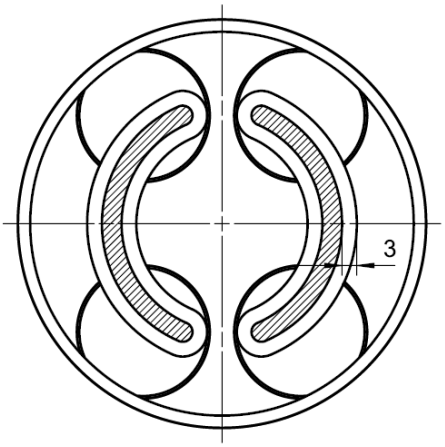

Figure 3 Bottom view through the sample tube into the QPR. Within each shaded area, at least 20 points will be measured to fit and define a plane per pole shoe

a. *To be measured after the fabrication of the pole-unit*
   - The perpendicularity of the four rods with respect to the cake piece weld joint geometry
   - The perpendicularity of the two planes of the pole shoes to the cake piece weld joint geometry
   - The relative distance of the two planes of the pole shoes projected in z-direction to the cake piece weld joint geometry

   The cake piece weld joint geometry is shown in the technical drawing “Pole Unit”.

b. *To be measured after the fabrication of the RF-section*
   - The perpendicularity of the two planes of the pole shoes to the weld joint geometry
   - The distance of the two planes of the pole shoes projected in z-direction relative to the weld joint geometry for sample connector section

   The weld joint geometry is shown in the technical drawing “Radio Frequency Section”.

c. *To be measured after the final fabrication*
   - Position of P_01, P_02, P_03 and P_05 with respect to the coordinate origin
   - The position of the two planes of the pole shoes with respect to the x-y plane through the coordinate origin
   - The relative distance of the two planes of the pole shoes projected in z-axis to x-y-plane

Acknowledgements

Having completed my PhD journey, I want to take a moment to reflect and acknowledge that this work was possible thanks to the dedicated efforts and support of many people, for whom I am sincerely grateful.

First and foremost, I want to thank **Dr. Marc Wenskat** for believing in me and giving me the incredible opportunity to perform high-level scientific research. I am particularly thankful for his mentorship in initiating me into the fascinating research field of RF superconductivity, always being available to teach me new topics and discuss my numerous questions. Beyond his academic duties, what is more important is the fact that he treated me with kindness and supported me during challenging times I faced in my studies.

I extend my gratitude to **Dr. Hans Weise** for giving me a warm welcome into the MSL group, where I always felt well-integrated. His support has been invaluable, ensuring that I had all the resources needed for my PhD work. I also want to thank **Prof. Dr. Wolfgang Hillert** for accepting me into his research group and offering me guidance during my studies at the Universität Hamburg. It is through their decisions and support that I have fulfilled my dream of working in a particle accelerator facility.

I continue by thanking **Dr. Detlef Reschke** for consistently dedicating time to discuss superconductivity topics with me, helping me during conferences, and providing me with valuable feedback on my thesis. **Dr. Lea Steder**, I appreciate your support during my measurements, prioritizing my tests, and assisting me in preparing various talks and publishing conference papers. Special thanks to **Jan-Hendrik Thie** for his kindness in teaching me about the mechanical properties of superconductors and sharing important aspects of his life during the times we worked together. I express my sincere appreciation to **Dr. Mateusz Wiencek** for generously sharing his knowledge in microwave engineering and consistently assisting me with my QPR tests. I am grateful to **Manuela Schmökel** for her patience in teaching me the techniques related to cavity assembly in the cleanrooms. I also express my gratitude to **Thorsten Büttner, Carsten Müller,** and **Lennart Trelle** for their immense support ensuring the timely functionality of the electronics and cleanroom for our test device. I will cherish all the nice moments spent with them and the entire SRF team in the AMTF.

I am truly thankful to **Dr. Oliver Kugeler**, **Dr. Sebastian Keckert**, and **Dmitry Tikhonov** from HZB, **Dr. Tobias Junginger** from the University of Victoria, **Dr.-Ing. Wolfgang Ackermann** from Technische Universität Darmstadt, **Prof. Dr. Ursula van Rienen** and **Dr. Piotr Putek** from Universität Rostock, **Dr. Lorena Vega Cid** from CERN, and **Dr. Anne-Marie Valente-Feliciano** and **Dr. Sarra Bira** from Jefferson Lab for all the enlightening discussions regarding the QPR. Each of you has significantly contributed to my understanding of this remarkable resonator and others, and I appreciate the valuable knowledge gained from our interactions in various online and in-person meetings.

It is important to say "thank you" to **Andre Gössel, Jürgen Eschke, Andrea Muhs, Birte Van Der Horst, Celina Ceylan, Norbert Meyners, Dr. Alexey Sulimov, Dr. Denis Kostin, Dr. Karol Kasprzak, Manuel Mommertz, Ruediger Bandelmann, Cornelius Martens, Swaantje Mette, Dr. Alexey Ermakov, Alexandra Dörner, Katrin Lando,** and **Dimitri Tischhauser,** whom I frequently visited to ask as many questions as I could and requested their assistance in many ways.

My academic journey in Germany has also been a period of personal growth, enriched by the presence of my amazing Bachelor's, Master's, Ph.D. and Postdoc colleagues. I want to extend my gratitude to **Dr. Christopher Bate**, **Jonas C. Wolff**, **Isabel González Díaz-Palacio**, **Dr. Getnet Kacha Deyu**, **Rezvan Ghanbari**, **Cem Saribal**, **Lea Preece**, **Artem Zaidman**, **Tom Harder**, **Chirag Banjare, Marco Voige, Tami Meyer, Thomas Scherbacher, Anton Lorf**, and **Kamila Iskhakova** for creating many nice memories with me, fostering cultural exchange, sharing laughter during lunch time and meetings, and allowing me to learn something new from each of them. Completing my degree would not have been possible without their support.

I also want to express my gratitude to **Ambra Gresele from Zanon R&I Srl** in Schio, Italy for the warm welcome during my visit. It was a total pleasure to get to know their team and work with them in the development of the QPR.

A heartfelt thanks goes to **Stephanie Pampel** for her companionship during this adventure, for her kindness, and for teaching me every day how to be a better person.

Prof. Dr. Daniela Pfannkuche and **Jun.-Prof. Dr. Simon Adrian,** I am grateful for you accepting being members of my examination committee.

Finally, I want to express my earnest appreciation to my family and friends in Mexico. Despite the physical distance, their continuing moral support accompanies me wherever I may be.